N69-78676 (ACCESSION NUMBER)
256 (PAGES)
CR-106136 (NASA CR OR TMX OR AD NUMBER)
FACILITY FORM 602

N69-78682 (THRU)
NONE (CODE)
(CATEGORY)

JET PROPULSION LABORATORY
CALIFORNIA INSTITUTE OF TECHNOLOGY
PASADENA, CALIFORNIA

Project Document 125

SURVEYOR III
PRELIMINARY SCIENCE RESULTS

PD 125 May 15, 1967

Prepared by

The Surveyor Experimenter Teams and Working Groups

National Aeronautics and Space Administration
and
Jet Propulsion Laboratory, California Institute of Technology

JET PROPULSION LABORATORY
CALIFORNIA INSTITUTE OF TECHNOLOGY
PASADENA, CALIFORNIA

Project Document 125

Prepared Under Contract No. NAS 7-100
National Aeronautics & Space Administration

CONTENTS

I. INTRODUCTION AND SUMMARY

T. Vrebalovich, L. D. Jaffe, and S. E. Dwornik

Surveyor III soft-landed on the Moon at 00:04 GMT on April 20, 1967. Data obtained have significantly increased our knowledge of the Moon.

The Surveyor III spacecraft was similar to Surveyor I (Refs. I-1 and I-2); the only major change in scientific instrumentation was the addition of a soil mechanics surface sampler. This device replaced an approach television camera, which was carried but not used on Surveyor I. The soil mechanics surface sampler is essentially the instrument described previously by Scott (Ref. I-3), but without strain gages, accelerometer, or position potentiometers. It consists primarily of a scoop about 12 cm long and 5 cm wide, mounted on a pantograph arm that can be extended about 1.5 m, or retracted close to the spacecraft, by a motor drive. The arm can also be moved in azimuth and elevation by motor drives, or dropped onto the lunar surface, under force provided by gravity and a spring. A door on the scoop can be opened and closed by a motor. The soil mechanics surface sampler can manipulate the lunar surface material in a number of ways, and the results can be observed by the Surveyor television camera. Figure V-2 of the following section by Scott, Roberson, and Clary shows the spacecraft configuration with this instrument aboard.

A minor difference between Surveyors I and III was that Surveyor III carried two auxiliary mirrors, attached to the spaceframe, to permit better survey of selected areas below the spacecraft in its landed position, where interaction between lunar surface and spacecraft might occur. Some small modifications were made in the television survey camera itself. Television was treated as a scientific experiment on Surveyor III.

The spacecraft was launched from Cape Kennedy, Florida, at 07:05:01 GMT on April 17, 1967. An Atlas/Centaur launch vehicle placed the Surveyor into a parking orbit at 165-km altitude and, after a coast of 22 min, 9 sec, injected it into a trajectory intersecting the Moon. The spacecraft mass at injection was 1040 kg; after final touchdown, 302 kg. A midcourse maneuver was performed on April 18. The center of the aiming ellipse chosen for this maneuver was selenographic latitude 2.92°S, longitude 23.25°W. Surveyor III landed at 2.94°S, 23.34°W, within 2.8 km of the aiming point.

The landing site is the southeast portion of Oceanus Procellarum, about 370 km south of the crater Copernicus. The spacecraft rests in a subdued, rounded crater about 200 m in diameter and is inclined 12 to 15° to the horizontal on the eastern slope of the crater. The crater was identified, and the location of Surveyor III within it was determined by comparing features visible from the Surveyor with those found in high-resolution Lunar Orbiter III photographs.

As in the Surveyor I landing, strain gages recorded the loads in each shock absorber during the landing events. Interpretation of these records and other data received from the spacecraft showed that, because the vernier engines did not shut down at the planned height of 4 m above the surface prior to the first touchdown, three separate touchdowns on the lunar surface took place. Since the spacecraft had a lateral velocity of about 1 m/sec, the distance between the first and second touchdown events was about 20 m, and between the second and third impact about 11 m. A final translational movement of about 30 cm occurred following the third touchdown. The vernier engines, which had maintained a stable spacecraft during all of the landing events, shut down prior to the third touchdown.

The marks of the footpads on the lunar surface in the second touchdown, though not in the first, have been identified in the post-landing pictures. Their position correlates with the interpretation of the landing dynamics. There may have been a small amount of soil erosion by the vernier engines during the second touchdown.

Lunar material disturbed by the vernier engines during the unique landing may have coated part of the mirror of the television camera or abraded it, causing the glare evidenced in portions of many television pictures. Temperature measurements indicate no dust layer on Surveyor's thermal compartments.

The television camera could not view the lunar surface outside the crater within which Surveyor III landed, but the sloping walls of the crater allowed it to view nearby features more clearly than would have been possible on a flat terrain. The spacecraft took 6315 pictures from April 20 to May 3, 1967.

Data on the mechanical properties of the lunar surface material were obtained from examination of the depth of the footpad imprints, strain gage records, and computer simulation of the landing, as well as by the soil mechanics surface sampler. The surface sampler made 8 bearing tests and 14 impact tests on the lunar surface, and dug four trenches; it picked up three objects on the lunar surface. One of these, a small rock, was gripped in the surface sampler scoop, which exerted a pressure of at least 10^7 dynes/cm^2 (10^2 psi) on the rock without apparently crushing or breaking it.

In general, the character and properties of the lunar surface at the Surveyor III site seem very similar to those at the Surveyor I site. The position inside or outside a crater or in different mare locations does not seem to make a gross difference in surface characteristics. This similarity includes the mechanical properties of the soil. The static bearing strength, on bearing widths of 2 to 20 cm, is about 2×10^5 to 5×10^5 dynes/cm^2 (3 to 8 psi), the cohesion 10^3 to 10^4 dynes/cm^2 (10^{-2} to 10^{-1} psi), and the angle of internal friction roughly 35°. The elastic rigidity modulus of the top 20 cm or so, as indicated by the frequency of vibration of the spacecraft on the surface, is about 5×10^6 dynes/cm^2. This is much lower than is typical for loose sand, and may represent fine, loosely packed particles. According to present measurements, the penetration of the footpads into the surface material during touchdown did not exceed 5 cm.

The distribution of craters and rock-like features near Surveyor III is not much different than that observed by Surveyor I. Large blocks were more frequent around some of the 10- to 15-m-diameter craters near Surveyor III. Blocks up to 4 m long were visible from the spacecraft; some of these were angular or flat, others were more rounded. Sizes of individual visible particles extended down to the 0.5-mm limit of camera resolution; over 85% of the exposed surface consisted of unresolved finer material. The surface retained a clear imprint of the bottom of a footpad, which had ridges of the order of 60 microns high. The surface material probably contains a considerable fraction of material smaller than 60 microns in diameter, and an appreciable fraction smaller than 10 microns. The fine matrix tends to pile up slightly on the uphill side of the larger blocks, suggesting that it slowly moves downhill.

Television observations with color filters indicate a gray Moon even in disturbed areas. The determinations of photometric functions of the footpad imprints, the areas exposed or disturbed by the soil sampler, and selected areas nearby were considerably uncertain because of glare from the dust or abrasion on the mirror. The local albedo of the fine-grained, undisturbed surface is estimated to be 8.5 ±2%. The larger blocks generally have a higher albedo. The material beneath the surface exposed by the action of footpads and surface sampler is generally darker than the undisturbed surface material. This is also true for disturbed material, as was observed for Surveyor I.

The higher albedo at the surface extends to only a very small depth, perhaps less than the limit of resolution of the Surveyor camera. The surface sampler

results show that the material is appreciably stronger at depths of about 10 cm or so than at the surface, although granular material extends to depths of at least 15 cm with no obvious change in particle size. The shapes of small craters suggest that the surface layer has a depth of several meters; the material below is probably more cohesive.

Thermal properties of the lunar surface surrounding Surveyor III differ somewhat from those obtained with Surveyor I and also with those from Earth-based observations in that Surveyor III measurements showed a higher thermal inertia during a solar eclipse; the thermal parameter was about 400 cgs units. Some directionality was noted in thermal emission from the sunlit surface; this disappeared rapidly during the eclipse.

Electrical properties of the surface, as determined from Surveyor III radar measurements, did not differ appreciably from the Surveyor I results.

In addition to lunar observations, color pictures of the Earth were taken during the eclipse and some time after the eclipse. The eclipse pictures should provide data on scattering of sunlight in the terrestrial atmosphere. A picture of Venus was obtained.

The following sections list the scientific groups most concerned with Surveyor III and give preliminary findings by some of the groups. These sections have been written essentially independently of each other; little effort has been made to resolve differences in interpretation that may exist among them.

Individual pictures taken by Surveyor, and presented in this report and elsewhere, are best identified by the day of the year and Greenwich Mean Time at which they were taken. April 20, 1967, was Day 110; May 3 was Day 123. Mosaics are best identified by catalog number.

REFERENCES

I-1. Surveyor Scientific Evaluation Advisory Team, "Surveyor I: Preliminary Results," Science 152, pp. 1737-1750, 1966.

I-2. Jaffe, L. D. "Lunar Surface Exploration by Surveyor Spacecraft: Introduction," Journal of Geophysical Research 72, pp. 773-778, 1966.

I-3. Scott, R. F. "Soil Mechanics Surface Sampler Experiment for Surveyor," Journal of Geophysical Research 72, pp. 827-830, 1967.

ACKNOWLEDGMENT

Special appreciation is extended to Robert Steinbacher for valuable assistance in organizing and carrying out the scientific effort for Surveyor III; and to Stephen Gunter for responsibility in video data handling for the scientific groups associated with Surveyor III, and providing photographs in the various forms needed for analysis.

II. SCIENTIFIC PERSONNEL

The following groups were cognizant of various scientific aspects of the Surveyor III mission:

A. Surveyor Scientific Evaluation Advisory Team

L. D. Jaffe, Chairman	Jet Propulsion Laboratory
S. A. Batterson	Langley Research Center
W. E. Brown, Jr.	Jet Propulsion Laboratory
E. M. Christensen	Jet Propulsion Laboratory
S. E. Dwornik	NASA Headquarters
D. E. Gault	Ames Research Center
J. W. Lucas	Jet Propulsion Laboratory
R. H. Norton	Jet Propulsion Laboratory
R. F. Scott	California Institute of Technology
E. M. Shoemaker	U. S. Geological Survey
G. H. Sutton	University of Hawaii
A. Turkevich	University of Chicago

B. Television Investigators

E. M. Shoemaker, Principal Investigator	U. S. Geological Survey
R. A. Altenhofen	U. S. Geological Survey
R. M. Batson	U. S. Geological Survey
H. E. Holt	U. S. Geological Survey
G. P. Kuiper	University of Arizona
E. C. Morris	U. S. Geological Survey
J. J. Rennilson	Jet Propulsion Laboratory
E. A. Whitaker	University of Arizona

C. Soil Mechanics Surface Sampler Investigators

R. F. Scott, Principal Investigator	California Institute of Technology
R. Haythornthwaite	University of Michigan
R. Liston	Detroit Arsenal

D. Lunar Mechanical Properties Working Group

E. M. Christensen, Chairman	Jet Propulsion Laboratory
S. A. Batterson	Langley Research Center
H. E. Benson	Manned Spacecraft Center
L. D. Jaffe	Jet Propulsion Laboratory
R. H. Jones	Hughes Aircraft Company
R. F. Scott	California Institute of Technology
E. N. Shipley	Bellcomm, Inc.

R. L. Spencer	Jet Propulsion Laboratory
F. B. Sperling	Jet Propulsion Laboratory
G. H. Sutton	University of Hawaii

E. Lunar Thermal Properties Working Group

J. W. Lucas, Chairman	Jet Propulsion Laboratory
J. E. Conel	Jet Propulsion Laboratory
R. B. Erb	Manned Spacecraft Center
R. R. Garipay	Hughes Aircraft Company
W. A. Hagemeyer	Jet Propulsion Laboratory
H. C. Ingrao	Harvard College Observatory
B. P. Jones	Marshall Space Flight Center
J. M. Saari	The Boeing Company

F. Lunar Electrical Properties Working Group

W. E. Brown, Jr., Chairman	Jet Propulsion Laboratory
R. A. Dibos	Hughes Aircraft Company
G. B. Gibson	Manned Spacecraft Center
D. O. Muhleman	Cornell University
W. H. Peake	Ohio State University
V. J. Peohls	Ryan Aeronautical Company

G. Lunar Theory and Processes Working Group

D. E. Gault, Chairman	Ames Research Center
R. J. Collins	University of Minnesota
T. Gold	Cornell University
J. Green	Douglas Aircraft
G. P. Kuiper	University of Arizona
H. Masursky	U. S. Geological Survey
J. A. O'Keefe	Goddard Space Flight Center
R. A. Phinney	Princeton University
E. M. Shoemaker	U. S. Geological Survey

H. Astronomy Working Group

R. H. Norton, Chairman	Jet Propulsion Laboratory
J. E. Gunn	Jet Propulsion Laboratory
W. C. Livingston	Kitt Peak National Observatory
G. A. Newkirk	High Altitude Observatory
H. Zirin	Mt. Wilson and Palomar Observatories

I. Program and Project Scientists

S. E. Dwornik	Program Scientist
L. D. Jaffe	Project Scientist
T. Vrebalovich	Associate Project Scientist
R. H. Steinbacher	Assistant Project Scientist
S. Z. Gunter	Assistant Project Scientist

J. Cognizant Scientists and Scientific Staff

F. I. Roberson	Cognizant Scientist, Soil Mechanics Surface Sampler Experiment
T. H. Bird	Cognizant Scientist, Television Experiment
J. J. Rennilson	Television Experiment
J. A. Dunne	Television Experiment
D. L. Smyth	Television Experiment
D. E. Willingham	Landing Sites and Television
A. L. Filice	Landing Sites
C. H. Goldsmith	Surveyor Experiment Test Laboratory

K. Instrument Development

D. H. Le Croissette	Manager, Surveyor Instrument Development
M. I. Smokler	Supervisor and Cognizant Engineer, Television Experiment
L. H. Allen	Television Experiment
C. E. Chandler	Supervisor, Surveyor Instrument Group
E. Rouze	Cognizant Engineer, Soil Mechanics Surface Sampler Experiment
M. C. Clary	Soil Mechanics Surface Sampler Experiment

L. Space Science Analysis and Command

J. N. Lindsley	Director
D. D. Gordon	Assistant Director
R. C. Heyser	Director, Television Performance Analysis and Command
T. H. Bird	Director, Television Science Analysis and Command
F. I. Roberson	Director, Soil Mechanics Analysis and Command

III. LUNAR SURFACE ELECTRICAL PROPERTIES

W. E. Brown, R. A. Dibos, G. B. Gibson, D. O. Muhleman,
W. H. Peake, and V. T. Peohls

Radar (Radar Altimeter and Doppler Velocity Sensor, RADVS) preliminary results for Surveyor III indicate that the radar cross sections (rxs)[1] for the 25° off-normal and vertical beams were approximately the same as those obtained by the Surveyor I data (Ref. III-1) and Earth-based measurements (Ref. III-2). The rxs values of -12 db for a 25° angle and -8 to -4 db for the vertical beam yield an estimate[2] of the relative dielectric constant as $\epsilon = 3.5 \pm 0.7$. These values apply to regions external to the crater in which Surveyor III landed; the echo data from within the crater have not as yet been related to surface slope variations and gain switching transient conditions.

The values -12 db and -4 db for the 25° rxs and 0° rxs, the computed value of ϵ, coupled with Earth-based measurements of the factors, microwave phase lag angle (40°), thermal parameter[3] ($\gamma = 1420$) and specific heat ($c = 0.2$) allow a value for the ratio of electrical loss tangent to density to be computed as

$$\frac{\tan \phi}{\rho} = 2.5 \times 10^{-2} \pm 20\%$$

---

[1] The symbol σ is used throughout the literature for radar cross section; it is also used for conductivity, which will be discussed in subsequent reports. In addition, radar cross section is often confused with reflectivity; therefore, it is considered worthwhile to designate a separate and less ambiguous symbol, rxs, for radar cross section.

[2] The estimate of dielectric constant may be determined by many different methods. The wide uncertainties (± a factor of 2) in the published values of rxs lead to a wide range of values for dielectric constant as calculated by any single method. Thus, the significance of any estimate of dielectric constant (permittivity) from the rxs is somewhat questionable. This estimate would agree with Ref. III-4 if the back-scatter gain were about 0.7 rather than unity. Evidence for back-scatter gain less than unity for a dielectric sphere is given in Ref. III.5.

[3] Please refer to Section VI of this report for additional definition of this parameter.

This ratio tends to be invariant with packing factor and could possibly aid in the identification of the surface material. Quartz-like minerals found on the surface of the Earth have a value of approximately 1.5×10^{-2} for this ratio (Ref. III-3).

REFERENCES

III-1. Brown, W. E. Jr., "Lunar Surface Surveyor Radar Response", J. Geophys. Res. 72, No. 2, p. 791, January 15, 1967.

III-2. Evans, J. V., "Radio-Echo Observations of the Moon at 3.6 cm Wavelength", Lincoln Laboratory Technical Report 256, February 19, 1962.

III-3. Troitsky, V. S., "Radio Emission of the Moon, Its Physical State and the Nature of its Surface," The Moon, p. 475, Academic Press, 1962.

III-4. Evans, J. V. and Pettengill, G. H., "The Scattering Behavior of the Moon at Wavelengths of 3.6, 68 and 784 Centimeters," J. Geophys. Res. 68, No. 2, p. 439, January 15, 1963.

III-5. Kerr, D. E., "Propagation of Short Radio Waves," Vol. 13, Rad Lab Series, p. 613, McGraw-Hill Book Co., Inc., New York, 1951.

IV. LUNAR SURFACE MECHANICAL PROPERTIES

E. M. Christensen, S. A. Batterson, H. E. Benson, R. Choate,
L. D. Jaffe, R. H. Jones, H. Y. Ko, R. L. Spencer,
F. B. Sperling, and G. H. Sutton

Interpretation of the lunar surface mechanical properties, as discussed in this preliminary report, is based on observations associated with the landing impacts, telemetry data of Surveyor III, and a comparison with Surveyor I data. The data[1] consist primarily of:

(1) Loads in the landing gear shock absorbers recorded throughout the entire landing sequence.

(2) Photographs of the spacecraft, the spacecraft/lunar interactions, and the lunar surface disturbed by the landings.

(3) Various analytical and laboratory simulations.

The landing of Surveyor III was different from that of Surveyor I, which landed on a relatively flat surface with its three landing legs contacting the surface about the same time, and in which the spacecraft experienced a single landing event (Ref. IV-1). In contrast, Surveyor III made three distinct landings on a sloping crater wall. During the first two landing events the three vernier engines, which controlled the spacecraft attitude and velocity during its final descent to the Moon, were in operation generating an upward force almost equal to the lunar weight of the spacecraft. Prior to the third landing event, however, the vernier engines were shut down, and the spacecraft contacted the surface in a free-fall condition. Nominally, the spacecraft should have had a free fall from an altitude of 4 m after a normal shutdown of the vernier engines.[2]

Figure IV-1 is a photograph of a Surveyor III spacecraft model showing the components and structures discussed in this report. The three legs are designed to rotate upward against the resistance of a shock absorber during a landing impact in order to protect the spacecraft (Figs. IV-2 and IV-3). When the landing loads are relieved, the shock absorbers return to their pretouchdown position. For additional

[1] Data obtained from the soil mechanics surface sampler are, in general, not considered here; see Section V of this preliminary report.

[2] Values will be given in the centimeter-gram-second units. To convert to feet-per-second units, the following factors may be used: 1 m = 3.28 ft; 1 cm = 0.39 in.; 1 newton = 0.225 lb; 1 dyne/cm^2 = 1.46 x 10^{-5} lb/in.^{2}.

protection, the footpads are made of a crushable material (Figs. IV-4 and IV-5); crushable blocks are located on the underside of the spacecraft inboard of each of the legs.

A. Observations

1. Landing

The spacecraft initially touched down on the inner slope of a crater. Because the continued thrusting of the vernier engine and the elasticity of the landing gear, the spacecraft rebounded off the lunar surface and landed again on the crater slope 24 sec later. The third landing event occurred further down the crater slope (Fig. IV-6), 36 sec after the initial contact. During these events, the spacecraft maintained attitude control and stopped approximately half-way down in the crater. A comparison of the features of this crater obtained from Surveyor III's camera with those obtained from Lunar Orbiter III's camera shows that the spacecraft is resting on the eastern slope of a 200-m crater (see Section VII of this report). The comparison also indicated that Surveyor III's landing leg 2 is now oriented in the uphill direction. Consistent with these facts, footpad 2 contacted the lunar surface first in each of the three landing events. This suggests that, at initial touchdown, the spacecraft was essentially level with respect to the true lunar vertical and that, during the interval between landings, the spacecraft flight control system brought the spacecraft to essentially the same level attitude and also prevented significant angular motions about the spacecraft vertical axis. After the final landing, the angle between the spacecraft vertical axis and the true lunar vertical was 12 to 14°, with the spacecraft dipping approximately in the direction of the downhill slope of the crater wall (Fig. IV-7).

The direction of spacecraft travel during landing events can be inferred from photographs of the imprints of footpads 2 and 3 and of the disturbed lunar material around the footpads (Figs. IV-8 and IV-9). A television search for surface marks from the first and second landing events was guided by these data. The suspected landing areas are to the east of the spacecraft. Unfortunately, the camera glare during the lunar morning prohibited obtaining intelligible pictures of these areas until Day 116 when the Sun angle was 77°. Pictures taken on Day 116 revealed distinctive marks, which are spacecraft imprints (Fig. IV-10) of the second landing

event. These marks are estimated to be between 11 and 14 m from the spacecraft at an azimuth of 90° (from north). As yet, no other positive indications of a spacecraft landing have been detected. There are no visible spacecraft-made distinctive marks between the second landing site and the spacecraft. Yet this area is a relatively uniform, uncratered slope on which spacecraft marks should be visible if they were there.

Figure IV-6 is a sketch of the landing sequence of Surveyor III, as interpreted from the data available to date. It shows the three separate landing events. Each event consists of a number of individual impacts of the footpads. Landing Events 1 and 2 occurred before the vernier engines cut off; during these events they were providing a lift equivalent to about 0.9 of the lunar spacecraft weight. In addition, the engines reoriented the spacecraft vertical parallel with the lunar vertical after Landing Events 1 and 2. The vernier engines were shut down before Landing Event 3. Using an estimated horizontal velocity of 0.9 m/sec, the distances between the three landing areas would be 22 m (between Landing Events 1 and 2) and 11 m (between Landing Events 2 and 3). However, the estimate of the horizontal velocity between Landing Events 1 and 2 is tentative at present. The rebound heights attained by the spacecraft are difficult to estimate, since the lift applied by the vernier engines is not well defined.

Figure IV-11 shows the complete time records of the landing forces, as measured by an axial strain gage on each landing leg shock absorber, from the time of initial surface contact until the spacecraft came to rest. It is an accurate record of the times between the first, second, and third landings. During most of the time between landings the axial loads were zero, indicating that the spacecraft was not in contact with the lunar surface. Following the last landing, the magnitude of the axial loads was consistent with the value required to support the static weight of the spacecraft. This indicates that the spacecraft came to rest on its three footpads after the third landing, and that no thrust was being developed by the spacecraft vernier engines.

Figure IV-12 shows an expanded time scale record of the shock absorber axial loads developed during the first landing event. It indicates that footpad 2 impacted first and then rebounded clear of the surface. The next footpad to impact was footpad 3, which occurred about 260 msec after the initial impact of footpad 2, and then leg 1 touched down about 290 msec after initial impact. The load on footpad 2 was completely relieved for about 150 msec and then built up again. The second load

indication of footpad 2 started at about the time the loads on the other two footpads were near their maximum values. Loads on all three footpads reached a zero value at about the same time, indicating that the spacecraft was normal to the lunar surface at the instant it lifted off.

The time records of the axial loads in the shock absorbers during Landing Event 2 are shown in Fig. IV-13 and are quite different in character than those obtained during the first landing event. Again, footpad 2 made contact first and remained on the surface for about 200 msec; footpad 3 made contact about 370 msec after the initial footpad 2 contact, and after footpad 2 had left the surface. Footpad 1 contacted 440 msec after initial footpad 2 contact, and about 50 msec before landing gear 3 experienced its maximum axial load. It can be seen that the maximum axial load in leg 1 was considerably less than the other initial loadings. The second impact of footpad 2 occurred 900 msec after its initial contact, and footpads 1 and 3 were clear of the surface for about 300 msec prior to this impact.

The axial loads developed in the shock absorbers during the third landing event are shown in Fig. IV-14. They are similar in character to those observed in the first landing, although the maximum loads are somewhat higher. Again, initial surface contact occurred on footpad 2, followed by the impact of footpad 1 240 msec later; footpad 3 contact occurred about 270 msec after the initial impact of footpad 2. The surface contacts of footpads 1 and 3 occurred during a short period in which there was no axial load measured in the shock absorber of leg 2. The second impact of footpad 2 occurred when the axial loads in leg 1 and leg 3 were at about their maximum value. All three footpads then left the surface at about the same time, and a much smaller impact was recorded between 400 and 500 msec later. This final rebound was due to the landing gear elasticity. A similar rebound was experienced by Surveyor I.

Table IV-1 gives the maximum axial forces in each shock absorber for all three events as well as the initial contact times, as reduced from the data recorded at Deep Space Station 14 (210-ft antenna) at Goldstone, California.

Table IV-1. Maximum shock absorber axial forces for the three landing events

Leg	Axial force, newtons; initial contact time, min/sec/msec, GMT		
	Event 1	Event 2	Event 3
1	2970 04:18.36	1420 04:42.51	3860 04:54.66
2	3060 (1820) 04:18.07	2800 (930) 04:42.07	2440 (1950) 04:54.42
3	3680 04:18.34	2350 04:42.45	4120 04:54.70

Note: Values in parentheses are peak forces of the second impact of leg 2 within each landing event. Due to considerable noise in the data, the peak force readings are considered accurate within ±20%. Times are accurate within ±10 msec.

Following the last impact of Landing Event 3, a small amplitude oscillation, visible for about 2 cycles and with a frequency of about 6.5 Hz, can be observed in the three strain gage records. The peak-to-peak amplitudes of these oscillations are on the order of 450 newtons. Several similar, but considerably larger oscillations (over 1000 newtons) were observed on the landing of Surveyor I. For both landings, these oscillations are interpreted as a vertical mode of oscillation of the spacecraft, which is related to the elastic properties of the spacecraft and is also influenced by the elastic properties of the lunar surface material. This is further discussed in Section IV-B.

A narrow-angle mosaic of the second landing event area of the spacecraft is shown in Fig. IV-10. Imprint 1 was made by footpad 1. Footpad 2 touched down at 2 and then at 2'. Imprint 3 was made by footpad 3. A trench-like mark can be observed at V. It has been verified that 1, 2, 2', and 3 correspond to the relative positions of the spacecraft's three footpads, and that item V lies in the area under vernier engine 3 during that landing. The spacecraft's azimuth position, as defined by 1, 2, 2', and 3, is very nearly the same as that of the spacecraft's final position. In identifying the landing event which produced surface marks at 1, 2, 2', and 3, the following factors were considered:

(1) Spacing between points 2 and 2' (considered to be two footpad 2 imprints) is 0.6 to 1 m. During the first landing event, the time between the two contacts of footpad 2, from load relief to load buildup, was approximately 0.15 sec. To travel 0.6 m, a horizontal velocity of about 4 m/sec would have been necessary during Landing Event 1. It is unlikely that the horizontal landing velocity was this high.

(2) Time separation between the two contacts of footpad 2 during the second landing event was 0.7 sec. The resulting horizontal velocity for this period would have been between 0.9 and 1.2 m/sec, a more reasonable value.

(3) The time interval between Landing Events 2 and 3 is 12 sec. Thus, during this time a horizontal velocity of approximately 1 m/sec would be required if the spacecraft were to travel between 11 and 15 m. The footpad 2 off-the-Moon time between the second and third impacts of the third landing event is 0.5 sec; the footpad 2 travel distance from its second impact to its final position is 33 to 35 cm. Thus, the average horizontal velocity during this interval was less than 0.7 m/sec. The spacecraft was being slowed down during this interval, and it is reasonable to expect that the velocity could have been 1 m/sec prior to the third landing.

(4) The distance from the marks 1, 2, 2', and 3 (Fig. IV-10) to the spacecraft was computed by triangulation. The footpad impressions are calculated to be between 11 and 14 m from the spacecraft.

These considerations lead to the conclusion that Fig. IV-10 shows the second landing site of Surveyor III.

Footpad/Surface Interactions

The direction and distance of the lateral displacement during the third touchdown event has provided some very good photographic data on the interaction between the footpads and the lunar surface material.

The imprint area in front of footpad 2, formed during the third touchdown landing event, is seen in Figs. IV-15 and IV-16. The imprint is composed of two truncated conical depressions superimposed one on another, the bottom of the imprint being

quite flat. Based on the dimensions of the imprint at the bottom, which correspond to the dimension of the bottom of the footpad (20 cm), and of the imprint at the rim, the depth of the imprint is estimated to be between 1 and 3 cm. The distance between the center of the imprint and the center of footpad 2 is estimated to be about 33 to 35 cm. Results of simulations of this geometry are given in Section IV-B-3.

Figure IV-15 shows that the pushed out and thrown out material displaced by footpad 2 during the third landing event has a darker appearance than the undisturbed material. The rather wide distribution of this material, extending for a meter or so, is the combined displacement from all of the impacts of footpad 2 during the third event.

In afternoon pictures of the imprint area (Fig. IV-16), a feature not apparent from the morning pictures is found. The edge of another imprint is noticed just beyond and to the right of the center of the top of the footpad. The top of this imprint, which is located in the thrownout soil of the first imprint, is a few centimeters from the edge of the footpad. It appears from strain gage data that footpad 2 made four distinct impacts with the lunar surface during the third landing event. The imprint seen over the top of the footpad could then be the one made by the third impact. The first two imprints, which are superimposed on one another, and the fourth imprint underneath the footpad at its present position fall more or less on a straight line, whereas the third one appears to be offset a few centimeters from this line. The movement of the footpad is further complicated by the stroking of the shock absorber on the leg of the spacecraft. The throwout pattern of the disturbed soil is unsymmetrical, with more soil deposited to the right of the footpad and its imprints, indicating that footpad 2 was moving with a lateral velocity in the direction toward the right. This observation is further supported by the smoothness of the top edge of the first imprint at a position corresponding to the lagging edge of the footpad. The scalloped top edge of the left side of the two first imprints are estimated to be 7 to 10 cm apart, but there is no distinction between these two imprints on the right side. These factors indicate that the spacecraft was not moving along a straight line during this third landing event.

In general, the soil near footpad 2, both disturbed and undisturbed, looks generally similar to that found near footpad 2 on Surveyor I. The disturbed soil consists of irregular-shaped clods of materials plus a spray of fine particles; however, the clods appear to be somewhat more flat-sided than those in the Surveyor I pictures. In the pictures of the Surveyor III footpad 2 imprint, taken in the early

lunar morning, a honeycomb or waffle pattern is seen on the bottom of the depression (Fig. IV-8). This indicates that at least some particles in the lunar soil are quite fine-grained. The waffle pattern is an impression of the bottom of a typical footpad (Fig. IV-5). The depressions between the ridges shown in Fig. IV-5 are slight deformations of the bottom skin, which was made of 25-micron-thick aluminum alloy sheet. The ridges are the edges of the aluminum alloy honeycomb that constitutes the interior of the footpad. The ridges are spaced about 1 cm apart, are 0.5 to 1 mm wide, and are estimated to be 40 to 80 microns high. (See Section IV-B-3 for a discussion of the imprint simulation.)

The ridge of soil between the second and the third imprints appears to have crumbled slightly; on the flat bottom of the second imprint of footpad 2, there appear to be some soil particles near the footpad. During the third impact, if the touchdown was very close to the second imprint then some of the material on the common ridge could have been displaced onto the second imprint. The nature of the imprints and the disturbance of the lunar material indicate that the lunar material is not very compressible.

A footpad imprint was also found near footpad 3, as shown in Fig. IV-9. Figure IV-17 is a narrow-angle view of a section of the footpad 3 impression. The pattern of throwout material resulting from the impacts of footpad 3 is shown in Fig. IV-18. The relative directional position of this imprint with respect to footpad 3 is the same as that of the first imprint of footpad 2 with respect to footpad 2. From leg 3 strain gage data of Landing Event 3, it appears that footpad 3 slightly lifted off the ground after the first impact and that, after the second impact, it oscillated without leaving the ground again. This means that footpad 3 moved directly from the position of its imprint to its final current position, while footpad 2 was making four distinct impacts not on a straight line. This would indicate a slight roll in the motion of the spacecraft during this touchdown event.

The small leg 1 shock absorber force during the second landing event can be explained by the fact that the inner edge of the pad hit on the inner slope of a small crater, which resulted in a smaller horizontal constraint than for a flat surface (Fig. IV-10, item 1). Note that the imprint (Fig. IV-19) is flat with no ridge on the edge away from the spacecraft centerline.

There is no evidence that footpad 2 or 3 crushed during the landing sequence (Figs. IV-8, IV-9, and IV-16). For the low landing velocities, which were encountered during all three landing events, no crushing would be expected as long as the

footpad loading was uniform, based upon landing analyses and tests. The footpads are designed to crush at a loading greater than 6.9×10^5 dynes/cm^2. (Analyses of footpad imprints are discussed in Section IV-B-4 and IV-B-5.)

3. Effects of Vernier Engine Firings

The vernier engines continued to operate throughout the first and second landing events and near to touchdown of the third event. A trench-like mark on the lunar surface has been tentatively identified as a disturbance caused by vernier engine 3 during the second landing event (item V, Figs. IV-10 and IV-20). The bottom of this shallow trench is elongated in the general direction of the spacecraft movement when in close proximity to the Moon. The bottom of the trench is lighter or brighter in appearance than the surrounding material. This appearance could be analogous to that of the compressed or packed material in the bottom of the footpad imprints made during the third landing event (see Section IV-B-3).

During the second landing event, the crushable block 3 could have been contacted, disturbed, and imprinted the lunar surface in the area of the trench. However, the block imprint would probably be approximately 30 cm in length (footpad 3 was in contact with the lunar surface for only 300 msec), whereas the trench appears to be over 1 m in length. If the block did make an imprint, the latter might have been erased by the erosion as the vernier engine moved over the block imprint area. The material ejected by the block impact could be blown away by the vernier engine exhaust gases, while the engine itself was also causing erosion of the lunar surface.

Darker thrownout material was observed next to the trench on the uphill side and to the left. Other erosion features from the second landing are not yet clearly defined.

Potential soil erosion marks under the spacecraft, created during the third landing event, as yet have not been detected. Difficulty was experienced in searching for under-the-spacecraft lunar surface disturbances created during the third touchdown event because of the television camera glare, limited camera operation, and the high Sun illumination angles when pictures were taken, thereby resulting in many spacecraft shadows. The estimated height (75 to 105 cm) above the Moon of the vernier engine nozzle at the time of engine cutoff may have caused shallow marks that would be difficult to photograph at high Sun angles.

Apparently, some contamination or degradation of the spacecraft surface finishes occurred during the lunar landing. This is evident by the glare effect caused by a fogging of the television camera mirror which was positioned facing footpad 3, the particles of material observed on footpad 2 (Fig. IV-21), and a suspected fogging of the auxiliary mirrors. Suspected visible lunar material on the side of Compartment A near a vernier engine was proved by comparison with photographs of a duplicate spacecraft on Earth to be a sunlight reflection from the specular finishes on nearby spacecraft components. There appears to be no significant amount of particles on the Surveyor III thermally sensitive mirrors on top of Compartments A and B. Had large amounts of material been deposited on the compartment tops the spacecraft thermal balance would have been destroyed.

The contamination or degradation of the television camera mirror might be due to impingement by lunar material carried by exhaust gases from vernier engine 3. This material, however, could originate either from the erosion by the vernier engine or from the disturbance caused by the crushable block, or both. The contamination could also be due to deposition of vernier engine exhaust gases. If lunar material has been deposited on the spacecraft; it is expected much of it would be a thin coat of fine material below the resolution capability of the television camera.

Prior to the flight, it had been anticipated that the firing of Surveyor vernier engines as close to the lunar surface as occurred during the first and second touchdown events might deposit lunar material on the spacecraft and that potentially the spacecraft operation could be jeopardized. The fact that Surveyor III survived suggests that the erosion hazard during a lunar landing of future spacecraft is not as severe as had been anticipated.

4. Auxiliary Mirrors

Some of the lunar surface areas under the spacecraft that might have been disturbed by the crushable blocks and/or by the operation of the vernier engines cannot be seen directly by the television camera. To provide some visibility of these areas, two auxiliary mirrors were mounted inside the spaceframe on Surveyor III opposite to the camera mounting position. The large mirror provides a view of the bottom portion of crushable block 3, the lunar surface area directly below block 3, and the surface area directly below vernier engine 3. The smaller mirror gives a view of the surface area below vernier engine 2.

As part of the camera calibration and alignment testing performed at Cape Kennedy, Florida, before the launch of Surveyor III, both wide- and narrow-angle pictures of the mirrors were taken by the spacecraft camera. Figure IV-22 is a wide-angle view of the mirrors on Surveyor III. The positions of the imprint areas and the scale on the surface are indicated by the floor pattern of lines and circles.

Figure IV-23 is a wide-angle picture of the same area, taken by Surveyor III after landing on the Moon. The glare present in many of the mission pictures is also noticeable here. However, the various imprint areas can be located by comparing these two wide-angle pictures. A series of narrow-angle pictures was also taken to permit a more detailed study of the several potential imprint areas. Preliminary studies have not shown conclusive evidence of surface disturbance by the crushable blocks. However, there may be no block imprints under the spacecraft, because the crushable blocks normally would not contact a flat, hard landing surface that is level during a landing at the estimated third event touchdown velocity of approximately 1.5 m/sec.

5. Attitude Control Jet Experiment

Prior to launch it was planned that an attitude control jet would be operated after the spacecraft was on the Moon in an attempt to determine lunar soil erosion characteristics. This experiment was unsuccessfully conducted with Surveyor I (Ref. IV-2). The experiment requires good pictures, possibly at low Sun angles, of the lunar surface area beneath the jet prior to and after operation of the jet, because the soil disturbance might be small. It was almost lunar noon before clear pictures, but with small contrast, were obtained of the potential impingement area under the Surveyor III attitude control jet on leg 2. At that time the probability of detecting a jet-created soil disturbance was small because of the lack of lunar surface shadows. Within 48 hr, the shadow of leg 2 would cover the area for the remainder of the lunar day. Because of these reasons and the undesirability of firing the jets when the flight control electronics were overly hot, the jets were not fired during the first lunar day.

B. Analyses and Simulations

1. Simulated Landing Studies

Computer landing simulation studies are being performed to estimate mechanical properties of a surface material that will yield surface penetrations and shock absorber axial loads similar to those obtained during the Surveyor III landings. In the first two landing events, with the vernier engines thrusting and the flight control system in operation, the simulations also will establish time histories of thrust levels and surface proximity of the vernier engines.

Preliminary computer simulations have been made of the third landing event, and reasonable correlations between analysis and flight data have been achieved. Representative analytical shock absorber force/time histories for a landing on a rigid surface are compared with Surveyor III flight data in Fig. IV-24. The impact velocities used in the three analyses conducted to date were 1.5 m/sec vertical and 0, 0.6, and 0.9 m/sec horizontal. (Figure IV-24 shows a landing with 1.5-m/sec vertical and 0.6-m/sec horizontal initial velocities.) Although the comparison is fairly good, further simulations are being conducted in order to obtain a better fit to the data.

The 0.9-m/sec horizontal velocity is consistent with the contention that the distance between the second and third landing events is 11 m, since the time duration between these events is 12 sec. From the computer simulations to date, it is considered that, during Landing Event 3, the maximum normal force exerted against the lunar surface by a spacecraft footpad was approximately 1450 newtons. Based on a measured surface penetration of approximately 2.5 cm, this force would correspond to a pressure level of approximately 2.8×10^5 dynes/cm^2.

The landing simulation program was used to establish the relative angle between the spacecraft x-y plane (horizontal plane with respect to the spacecraft) and the ground (the plane established by the three footpad/ground contact points) for all three landings; and also the roll orientation of the spacecraft was determined with respect to the direction of ground slope. The spacecraft is nominally close to level at the time of initial impact, and the attitude control system retained this attitude throughout the landing sequence except for transients during the actual touchdowns. Thus, the calculated angles constitute approximations to the lunar surface slopes at the three landing sites. The numerical values obtained are:

Landing Event	Surface slope, deg	Angle between leg 2 and uphill direction, deg
1	10.2	+4.5
2	14.9	+7.4
3	10.4	-9.2

With respect to the uphill direction, the angle is defined positive if leg 2 deviates in a clockwise direction, looking down at the spacecraft.

Landing simulations of Surveyor III have indicated that the landing legs have not stroked sufficiently for the body blocks to make contact with a planar landing surface in all three landing events. It can therefore be assumed that the body blocks never touched the lunar surface, unless a local surface protuberance was encountered.

Most landing simulations performed so far assume a rigid surface, i.e., a static bearing strength larger than 6.9×10^5 dynes/cm^2. Various bearing strength values and profiles, as well as various effective friction coefficients will be investigated until an optimum match with the flight data is achieved with respect to axial shock force histories and footpad penetrations. However, a preliminary evaluation of these data indicates that the conclusions regarding mechanical properties of the lunar surface material are likely to be similar to the conclusions obtained from the Surveyor I touchdown data (Ref. IV-3).

2. Elastic Properties of Lunar Soil

Oscillations on the strain gage records following the final impact were observed on Surveyors I and III. In both cases, the observed frequency was near 6.5 Hz. An approximate analysis of the effective spring constant for the unstroked Surveyor landing legs indicates that the spacecraft oscillates at a frequency of 8.0 Hz (with an uncertainty of about ±0.8 Hz) in a vertical translational mode when supported by its landing legs on a rigid surface. The fact that the ring-out observed on the Moon is at a lower frequency indicates that the elastic properties of the lunar surface material are affecting the oscillations. Assuming that the equivalent springs of the spacecraft and of the lunar surface are acting in series and using 8 Hz and the observed 6.5 Hz, the effective spring constant of the lunar surface material averaged over a depth of the order of the footpad diameter is $K \approx 4.9 \times 10^8$ dynes/cm. From

Timoshenko and Goodier (Ref. IV-4), the effective stiffness K for an isotropic medium uniformly loaded over a circular area is

$$K = \pi^2 Er/4(1 - \nu^2)$$

where

E = Young's modulus
r = radius of loaded area (12.7 cm)
ν = Poisson's ratio

From the preceding equation and relations among elastic constants

$$4K/\pi^2 r = E/(1 - \nu^2) = 2\mu/(1 - \nu)$$

where μ = rigidity modulus. Using the value obtained for K and taking various values for ν, we can determine a range of values for μ. Further taking a range of values for the bulk density, ρ, of the lunar surface material, we can obtain a range of values for the shear wave velocity, V_s, and the compressional wave velocity, V_p. Table IV-2 is a summary of results of these calculations.

It is seen from the table that this type of observation provides a rather narrow range of rigidity modulus and, for a given assumed density, a rather narrow range of shear wave velocities and a lower bound for the compressional wave velocity. The shear wave velocities are about an order of magnitude lower than those obtained on Earth in loose sand; they are near the values found for fine ocean bottom sediments near the water-sediment interface. It is planned to obtain more precise estimates of the resonant frequencies of the spacecraft and to obtain more reliable estimates of the possible ranges of average shear and compressional wave velocities of the upper 20 cm or so of the lunar surface material. The above estimates are for a lunar surface loaded by the approximate 3.4×10^4 dynes/cm^2 static pressure exerted by the Surveyor footpads.

3. Footpad Imprint Simulations

Preliminary measurement of the depth, attitude, and position of the landing imprints of footpads 2 and 3 during Landing Event 3 has been performed with the aid of a full-scale Surveyor spacecraft model. This model, located at JPL's Surveyor

Table IV-2. Preliminary estimates of μ, V_p, and V_s for assumed values of ν and ρ

		ρ = 0.5 g/cm^2		ρ = 1.0 g/cm^2		ρ = 1.5 g/cm^3		ρ = 2.0 g/cm^3	
ν	μ(dyne/cm^2 x 10^6)	V_s(m/sec)	V_p	V_s(m/sec)	V_p	V_s(m/sec)	V_p	V_s(m/sec)	V_p
0	7.8	39	55	28	40	23	33	20	28
0.4	4.7	31	76	22	56	18	46	15	38
0.45	4.3	30	100	21	70	17	56	14.5	48
0.5	3.9	28	∞	20	∞	16	∞	14	∞

Experiment Test Laboratory (SETL), was operated in conjunction with a collimated light source simulating the Sun. Television pictures that reasonably duplicate the shadow patterns and footpad imprints seen in Surveyor III pictures have been made by use of this equipment. Figures IV-25, IV-26, and IV-27 are pictures of footpad 2 imprints simulated in three soils with different ranges of particle size. The simulated imprints of footpad 2 best duplicate Surveyor III pictures at a location 35 cm out from the present position of footpad 2, along the centerline of leg 2; and 2 to 3 cm perpendicular to the leg 2 centerline (toward footpad 3). Because small variations in imprint location (±0.5 cm) can be observed in the television pictures, the above dimensions are considered accurate within ±3 cm.

The simulated imprints of footpad 2 in Figs. IV-25 to IV-27 are all made with crushed basalt. Soil particle size ranges in the soil models are: Fig. IV-25, clay-size particles; Fig. IV-26, a mixture of 50% clay-size particles and 50% sand-size particles; and Fig. IV-27, sand-size particles[3]. The 14° illumination angle in Figs. IV-25 to IV-27 duplicates the lunar morning Sun/Surveyor III landing site conditions at 08:00, Day 110. All three simulations reproduce the honeycomb texture of the bottom of the footpad as seen in Fig. IV-8; however, at a 14° light source elevation angle, this pattern shows up clearly only in the pictures of the clay-size and the sand/clay-size models. Of these two models at that Sun angle, the mixed particle size soil reproduces the light reflecting characteristics seen in Surveyor III pictures better than the clay-size soil. In Surveyor III pictures, the observed brightness of the bottom surface of the footpad imprint is somewhat greater than that of the undisturbed lunar surface at this lighting angle. In the simulated models (Figs. IV-25 and IV-26), the observed brightness of the imprint in the sand/clay mixture is slightly greater than that of the undisturbed surface, whereas the brightness of the imprint in the clay-size soil is much greater than that of the undisturbed surface at the same lighting angle. It is recognized that other phenomena besides grain-size variation may explain the above described brightness effects on the Moon.

The imprint of footpad 3 from Landing Event 3 is shown in Fig. IV-9. Television pictures of simulated footpad imprints indicate that the centerpoints of the present location of footpads 2 and 3 are both 30 to 40 cm from the first imprints of Landing Event 3 and in the same direction. Lines connecting the centers of the initial

[3] In the MIT system of grain-size classification, clay-size particles are <0.002 mm; silt-size particles have diameters >0.002 and <0.06 mm; and sand-size particles have diameters >0.06 and <2.0 mm.

impacts and those of the final positions of footpads 2 and 3 point along an azimuth of 280° from north. This azimuth should represent the general direction of spacecraft movement during Landing Event 3. If so, then Landing Event 2, and possibly Landing Event 1, should have occurred along an azimuth of 100° from the Surveyor III present position. This value compares well with the estimate of due east obtained from the photographs of the second landing event.

Depth of footpad 2 and 3 penetrations during Landing Event 3 have been obtained from measurements of the model imprints at SETL that best duplicate Surveyor III pictures, as well as from measurements on Surveyor III pictures. The most accurate measurement of penetration could be made for footpad 2 because of better picture quality and more photographic coverage of imprint area. Model imprint simulations indicate that the depth of penetration across each imprint was not uniform. The footpads can rotate during the landing about a horizontal axis perpendicular to the spacecraft leg. Pictures indicate that the at-rest orientation of the footpads, relative to the spacecraft x-y plane, are:

(1) Footpad 2: outer edge tilted downward 12 ±2°.

(2) Footpad 3: outer edge tilted downward 10 ±2°.

From simulation studies, a preliminary estimate of the average depth of penetration of footpad 2 in making the dual imprint is between 1 and 3 cm; for footpad 3, the imprint is approximately 3 to 5 cm deep.

4. Analysis of Footpad Imprint Pictures

Analysis of pictures of footpad imprints has included a study of the spacecraft shadows on the lunar surface material. Using the size and location of spacecraft features and the direction of the Sun, calculations can be made about the footpad penetrations and about the topography of the disturbed material around the footpads.

Preliminary results have indicated that the average footpad penetration for footpads 2 and 3 in their final resting positions is less than 2.5 cm. However, both of the footpads appear to be tilted, outward edge down, to an angle of 8 to 12°. These results are in good agreement with those obtained in the simulations (Section IV-C-3).

The imprint produced by the first two impacts of footpad 2 during Landing Event 3 has an estimated average depth of 2.5 cm. The deeper imprint caused by footpad 3 is surrounded by some of the ejected material that forms a sloping wall

several centimeters high. The depth below the original level is estimated to be about 5 cm. The extent of the area over which the material was ejected indicates that much of the material was removed from the impact hole. The relative height of footpad 3 in its final position indicates that possibly it is resting on a patch of the throwout material. Some of the clumps of soil beyond the footpad form a ridge a few centimeters lower than the top of the footpad.

Figure IV-19 shows a narrow-angle view of the imprint formed by footpad 1 during Landing Event 2. The depth of penetration at the left edge is 4 cm; the angle of the left imprint edge to the horizontal is about 60°.

5. Estimations of Soil Parameters

Because of the horizontal velocity and surface slope associated with the landing of Surveyor III, the vertical loads on the surface during landing are more difficult to estimate than for Surveyor I, which landed nearly vertically on a near horizontal surface. However, it is quite certain that the vertical dynamic loads developed during Landing Event 3 were lower than those for Surveyor I. Preliminary estimates of the vertical landing loads when compared with estimated footpad penetrations indicate that, at least as far as dynamic penetration of the material is concerned, the soils at the two Surveyor landing sites are similar. For Surveyor III, a maximum dynamic pressure level of 2.8×10^5 dynes/cm^2 was estimated from the simulated landing studies (Section IV-B-1).

The imprint in front of footpad 2 (Figs. IV-16 and IV-8) is estimated to be 2.5 cm deep. If the material were completely frictionless, then the cohesion required to support the 45° slope edge of the imprint would be at least 30 dynes/cm^2. If the material were cohesionless, its angle of internal friction would be at least 45°. The left rim of the impression attributed to footpad 1 during Landing Event 2 (Fig. IV-19) is estimated to have a slope of about 60° to the horizontal with a height of about 4 cm. If the material were frictionless, the cohesion would be at least 10^2 dynes/cm^2 to support this slope under lunar gravity; if the material were cohesionless, then its angle of internal friction would be at least 60°.

An upper bound for the cohesion can be obtained from the bearing strength. For a frictionless material, the contribution of cohesion to bearing strength is approximately six times the cohesion if soil failure is by general shear and four times the cohesion if failure is by local shear. Thus, with a bearing capacity of

where ρ_2 is the soil density after local shear. During the initial stages, with an assumed initial velocity of 150 cm/sec, then $p_i < 7 \times 10^4$ dynes/cm^2, h = 0, and $\dot{h}^2 = 2.25 \times 10^4$ cm^2/sec^2, so

$$\frac{\rho_2 \rho}{\rho_2 - \rho} < \frac{7 \times 10^4}{2.25 \times 10^4} = 3.1 \text{ g/cm}^3 \qquad (3)$$

If it is assumed that the density of the compressed soil after failure is 2 g/cm^3, the density of the undisturbed material at the surface is 1.2 g/cm^3 or less. Or if it is assumed that the density of the compressed soil after failure is 1.7 g/cm^3, the density of the undisturbed material at the surface is 1.1 g/cm^3 or less. This analysis applies only to the top 0.5 cm of the lunar surface material, and is sensitive to the assumed initial velocity. Somewhat lower limits were estimated earlier for the Surveyor I site (Ref. IV-7).

Particle size of most of the lunar soil beneath and close to the spacecraft is less than the resolution of the television camera (approximately 1.0 mm at footpad distance). For rock particles larger than 1.0 mm seen throughout the entire field of view of the television camera, particles appear to be relatively well graded, i.e., the particles have a continuous size gradation from the 1.0-mm minimum resolution up to the maximum size present. It is expected, therefore, that particles with diameters less than 1.0 mm are also well graded.

As with Surveyor I, the appearance of the disturbed lunar material in the vicinity of the footpads is suggestive of material similar in mechanical properties to a moist terrestrial soil containing a fair amount (>10%) of fine silt or clay-size particles (less than about 10 microns).

6. Strength Estimate of Lunar Rock

Figure IV-28 is a photograph of a rock fragment of about 1.2 cm in diameter held in the jaws of the surface sampler. Scott, Roberson, and Clary (Section V) give dimensions and applied forces and pressures for the rock fragment. During this time, the rock fragment apparently popped out of the jaws of the surface sampler between television picture frames and was not subsequently located on the ground. The maximum force available (25 newtons) was applied to this rock fragment in an attempt to determine its strength. Maximum force was applied to the rock fragment for

10 to 15 min before it was lost. Therefore, the breaking strength was equal to or greater than the stress applied. Maximum pressure was applied to the rock fragment along the edge of the sampler scoop (1 mm thick). Assuming a contact length of 1.2 cm, Scott et al. estimated a pressure of about 2×10^7 dynes/cm^2. This is in the range of crushing strength for rather weak rocks such as some tuffs, siltstones, and claystones. Thus, the rock fragment must be at least as strong as these types of terrestrial rocks.

Rocks are generally an order of magnitude (or more) weaker in tension than in compression. Their shear strength is also generally much lower than their compressive strength. Therefore, it is possible that local tensile or shear stresses developed in the rock fragment were large enough to fracture stronger rocks than the terrestrial rocks mentioned above. Analyses will continue on the stresses developed in the rock fragment, and experiments will be conducted with a model of the surface sampler jaw using various rock types in order to improve the estimate of minimum strength for the rock fragment.

D. Summary

In addition to the expected data, the unplanned triple landing of Surveyor III provided other unique information. Based upon these preliminary data, the mechanical properties of the lunar surface at the Surveyor III landing site appear to be similar to those at the Surveyor I site. The fact that the estimates are similar, although derived from two different landing conditions (lunar mare vs lunar crater) lends credence to these estimates.

The three landings were progressively further down into a crater, the last two separated by a distance of 11 to 14 m. Footpad imprints of the second landing have been detected and verified by various techniques.

The preliminary estimate of the lunar soil static bearing capability, as determined by the Surveyor III spacecraft landing interactions with the Moon, appears to be in the same range as that of Surveyor I, i.e., 2×10^5 to 5.6×10^5 dynes/cm^2 (3 to 8 psi) for a depth of penetration of 2.5 to 5 cm and for an area equivalent to that of a footpad. This range of values will be narrowed as the computer simulations of the landing are refined. However, there appears to be a difference in bearing capability of the lunar soil between the locations of footpads 2 and 3.

A trench-like disturbance in the second landing event area is attributed to the vernier engine erosion of the lunar surface. The small amount of lunar material

deposited on the spacecraft and the fogging of the television camera are possibly the effects of such erosion, which did not result in serious mission operational limitations or failure.

Pictures of the areas around footpads 2 and 3, in the final resting position, show several imprints and skid marks which afford the following interpretation of soil properties:

(1) Footpad imprint simulations suggest that the lunar surface material contains a substantial amount of particles finer than sand size (0.06 mm). The particle size distribution appears to be relatively well-graded for sizes above the camera resolution (1.0 mm); therefore, it should be reasonable to extrapolate this size distribution down to 0.01 mm.

(2) Imprints and soil throwout patterns suggest a low compressibility of the lunar surface material.

(3) Difference in footpad 2 and 3 penetrations may be the result of the complex landing dynamics or of soil inhomogeneity.

(4) An upper bound can be determined for the lunar soil cohesion from the bearing strength by assuming that the material is frictionless. For a 5.6×10^5 dynes/cm^2 (8 psi) static bearing capacity on the surface, the average cohesion down to a depth of about 20 cm should be less than 1.4×10^5 dynes/cm^2 (2 psi). A lower bound for the average cohesion for the top few centimeters of soil obtained from the height of standing slopes of imprints is 10^2 dynes/cm^2 (1.5×10^{-3} psi), assuming the material is frictionless. If it were cohesionless, an angle of internal friction of at least 60° is indicated.

Preliminary estimates of the minimum strength of a lunar rock fragment picked up by the surface sampler indicate that it is at least as strong as weak terrestrial rocks, such as some tuffs, siltstones, and claystones.

Ranges for the elastic moduli of the upper few centimeters of the lunar surface were obtained from analysis of spacecraft oscillations following the landing. These preliminary estimates indicate a rigidity modulus and a shear wave velocity lower than those for loose terrestrial sand.

REFERENCES

IV-1. Surveyor Scientific Evaluation Advisory Team, Surveyor I Preliminary Results, National Aeronautics and Space Administration Five-Day Science Report, Project Document 97, Jet Propulsion Laboratory, June 30, 1966, also in Science 152, 3730, 1737-1750, 1966.

IV-2. Surveyor I Mission Report, Part Two: Scientific Data and Results, Technical Report 32-1023, Jet Propulsion Laboratory, Pasadena, Calif., September 10, 1966.

IV-3a. Sperling, F., and Garba, J., A Description of the Surveyor Lunar Landing Dynamics and an Evaluation of Pertinent Telemetry Data Returned by Surveyor I, Technical Report 32-1035, Jet Propulsion Laboratory, Pasadena, Calif., 1967.

b. Alderson, R. G., and Wells, D. A., "Final Report on Surveyor Lunar Touchdown Stability Study", Report No. MM-66-19, Analytical Mechanics Department, Bendix Corp., South Bend, Indiana, 1966.

c. Deitrick, R. E., and Jones, R. H., Touchdown Dynamics Study for Lunar Landing Phase of Surveyor Project, NASA Report CR52080, 1963.

IV-4. Timoshenko, S., and Goodier, D., Theory of Elasticity, 2nd Ed., p. 367, McGraw-Hill, New York, 1951.

IV-5. Scott, R. F., "Problem of the Penetration of a Projectile into Soil or Soil-Like Medium, or Compressible Rock", four reports to Space-General Corp., El Monte, Calif., 1962.

IV-6. Chandaysson, P. L., unpublished work, 1966.

IV-7. Jaffe, L. D., "Surface Structure and Mechanical Properties of the Lunar Maria," J. Geophys. Res. 72, 1727-1731, 1967.

ACKNOWLEDGMENT

Appreciation is extended to Ronald Scott, California Institute of Technology, for reading the article and offering suggestions; Charles Goldsmith, Alex Irving, William Peer, Jet Propulsion Laboratory, for assistance in simulating the footpad imprints and performing spacecraft shadow predictions; Daniel Bookstein, Jet Propulsion Laboratory, for assisting in the landing dynamics simulations; and E. N. Shipley, Bellcomm, Inc., for participating in the early portion of the first lunar day operations.

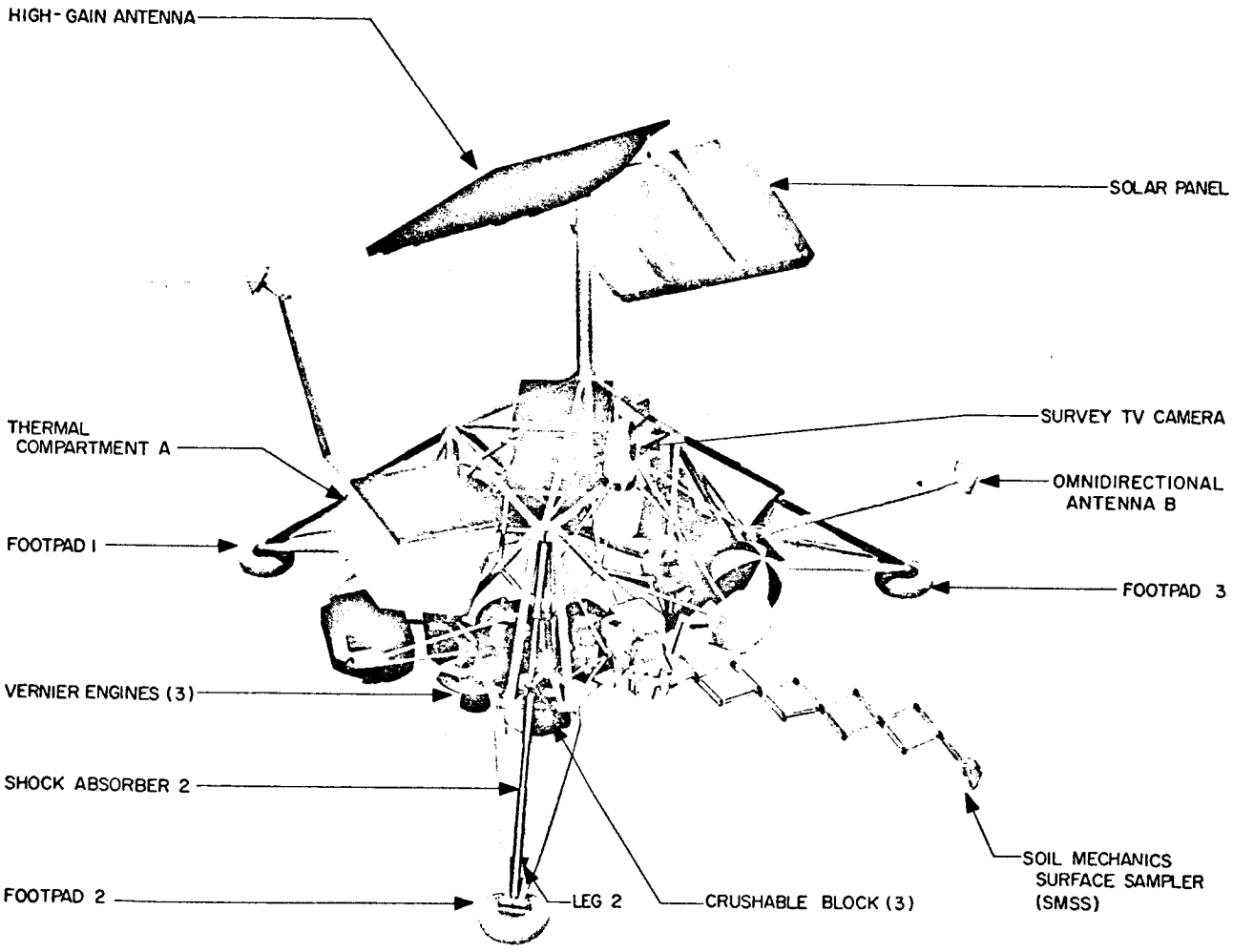

Fig. IV-1. Surveyor III spacecraft model

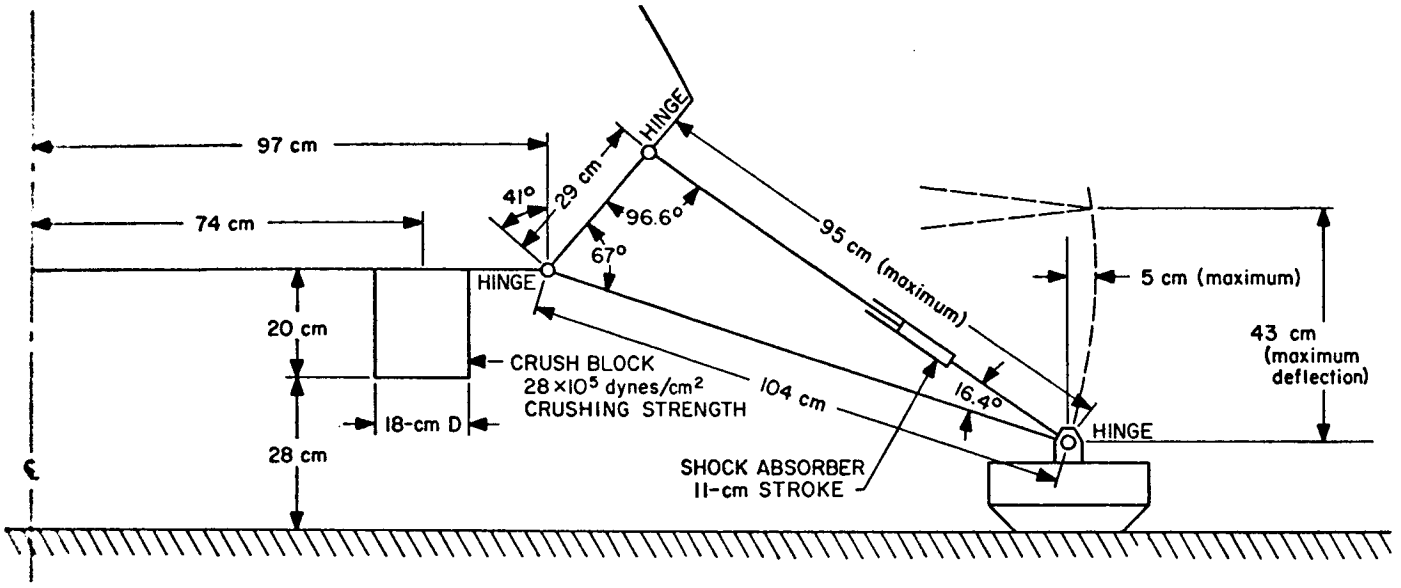

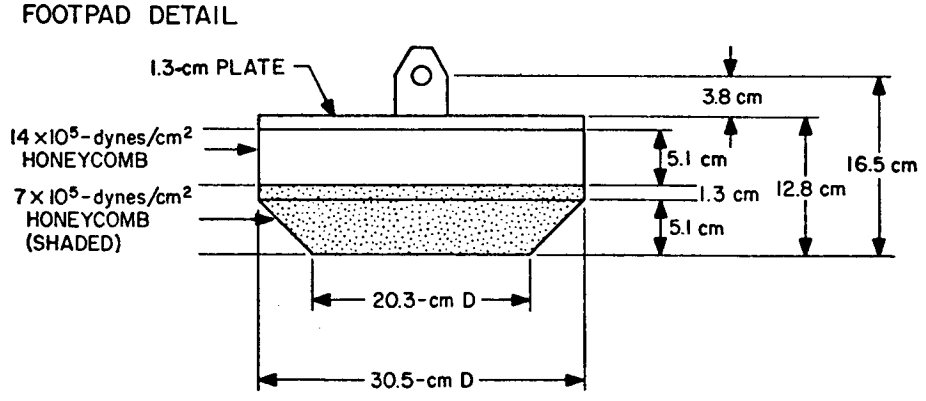

Fig. IV-2. Dimensions of landing gear assembly

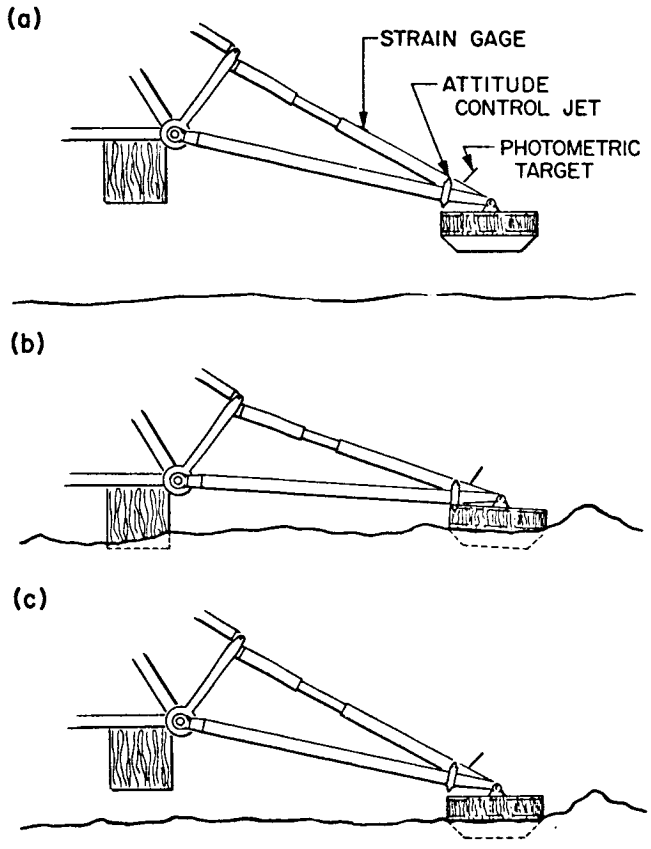

Fig. IV-3. Sequence of landing gear positions during a landing. Assembly is shown fully extended in (a); during landing, the shock absorber compresses and the footpad moves up and away from the spaceframe, as shown in (b); assembly is shown re-extended after landing in (c).

Fig. IV-4. Photograph, taken before launch, of footpad 2. Ballast weights are visible on top of footpad.

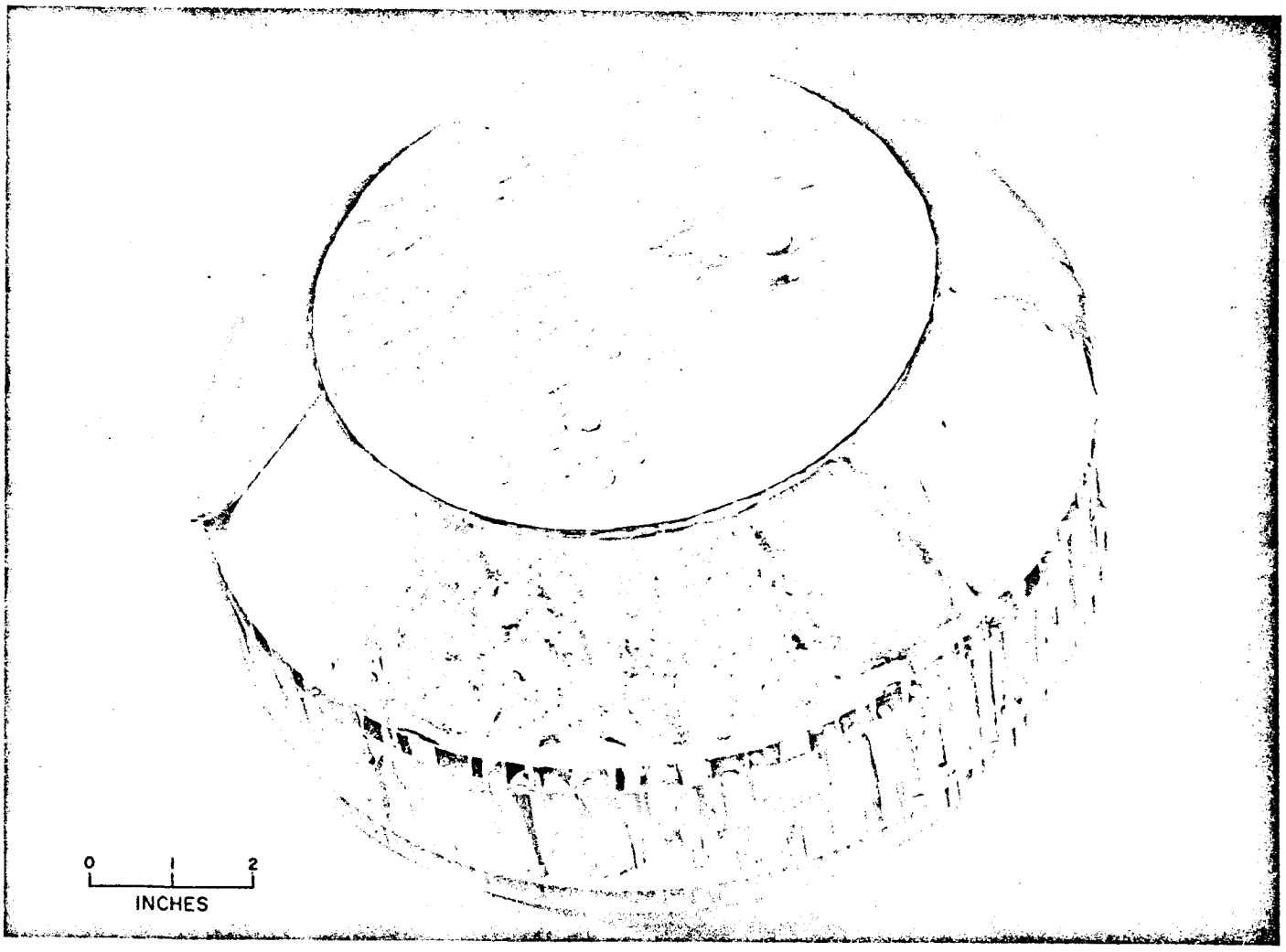

Fig. IV-5. Photograph of bottom of a Surveyor footpad. Footpad has been lightly loaded in vertical compression, thereby exposing the honeycomb pattern.

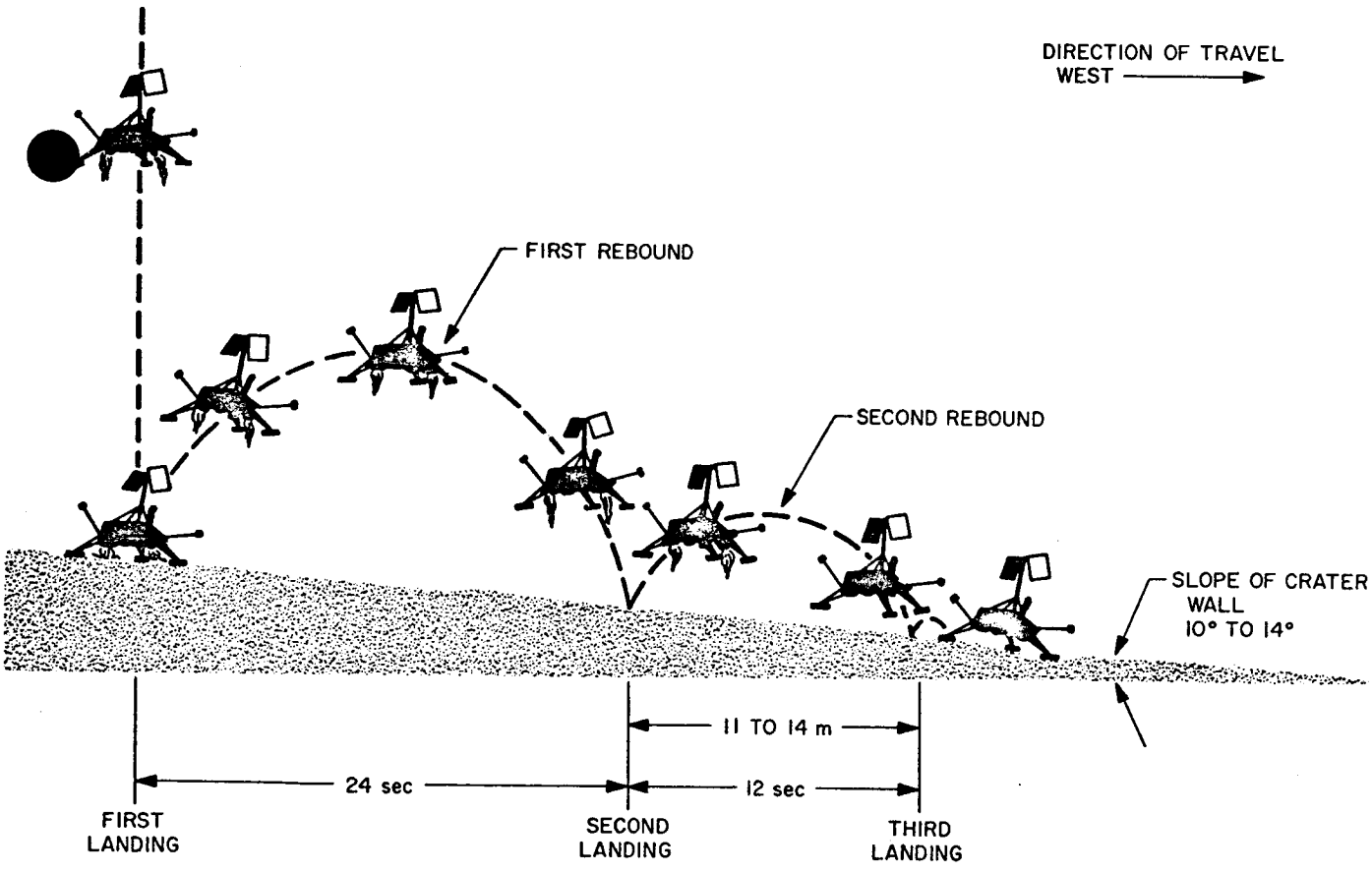

Fig. IV-6. Sketch showing events during landing of Surveyor III on the Moon

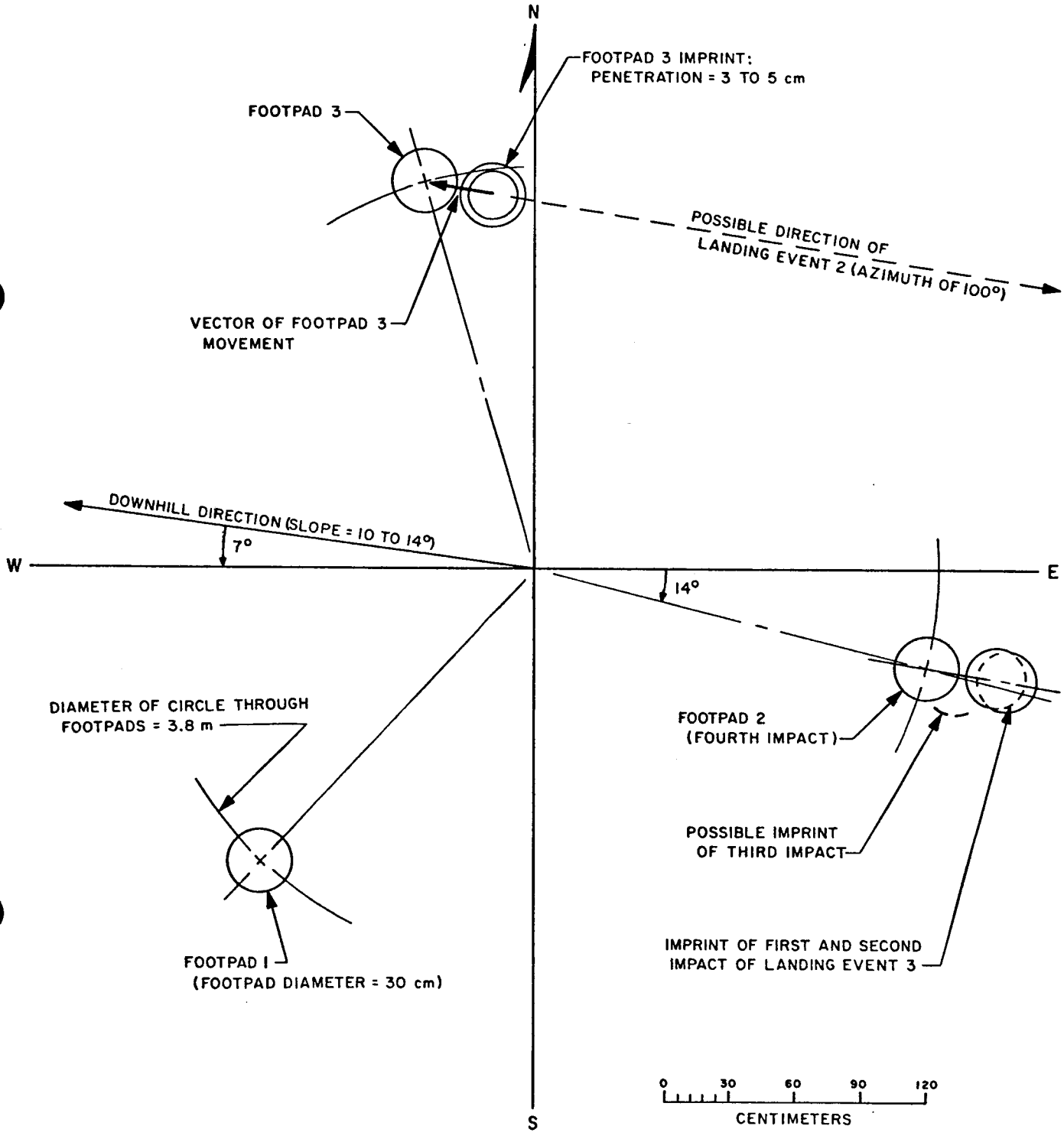

Fig. IV-7. Preliminary evaluation of relationships during and after Landing Event 3

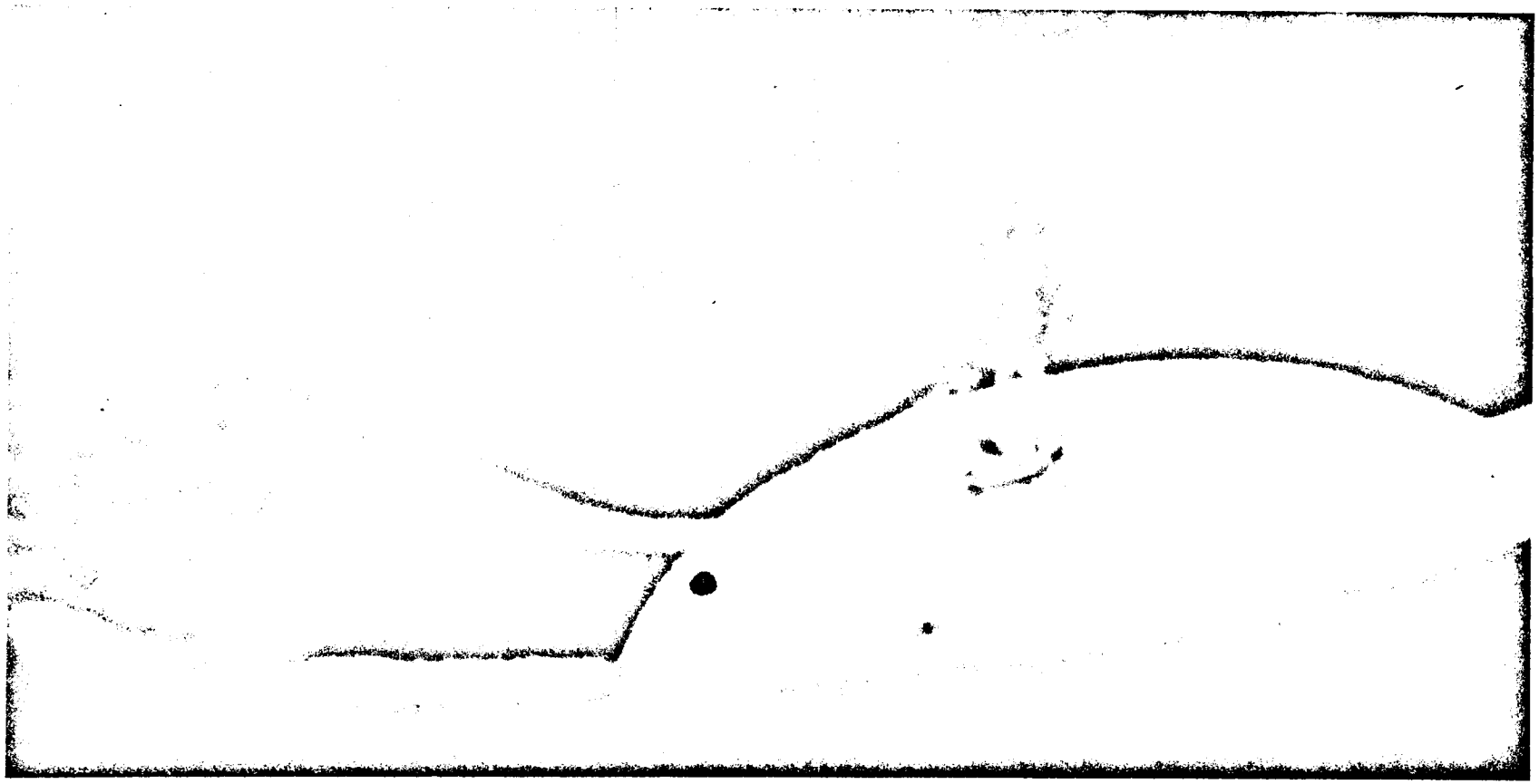

Fig. IV-8. Imprint in lunar surface just outboard of footpad 2. Note honeycomb pattern on bottom. Imprint is attributed to first and second impact of footpad 2 during third landing event. Note reflection off conical part of imprint. White top of footpad is at lower right. Black area in lower part of frame and white streak between this and footpad are images of camera housing. Sun angle was 14° (Day 111, 08:24:20 GMT).

Fig. IV-9. Lunar surface near footpad 3, with portions of Surveyor III spacecraft. Image of footpad top is white ellipse at left center. Imprint attributed to first impact of footpad 3 during third landing event is to lower right of footpad, below boom of omnidirectional antenna (Day 120, 13:42:24 GMT).

Fig. IV-10. Narrow-angle mosaic of the second landing area to the east of the spacecraft. Imprints of the footpads are indicated by numerals (Day 116, between 07:06:46 and 09:27:06 GMT).

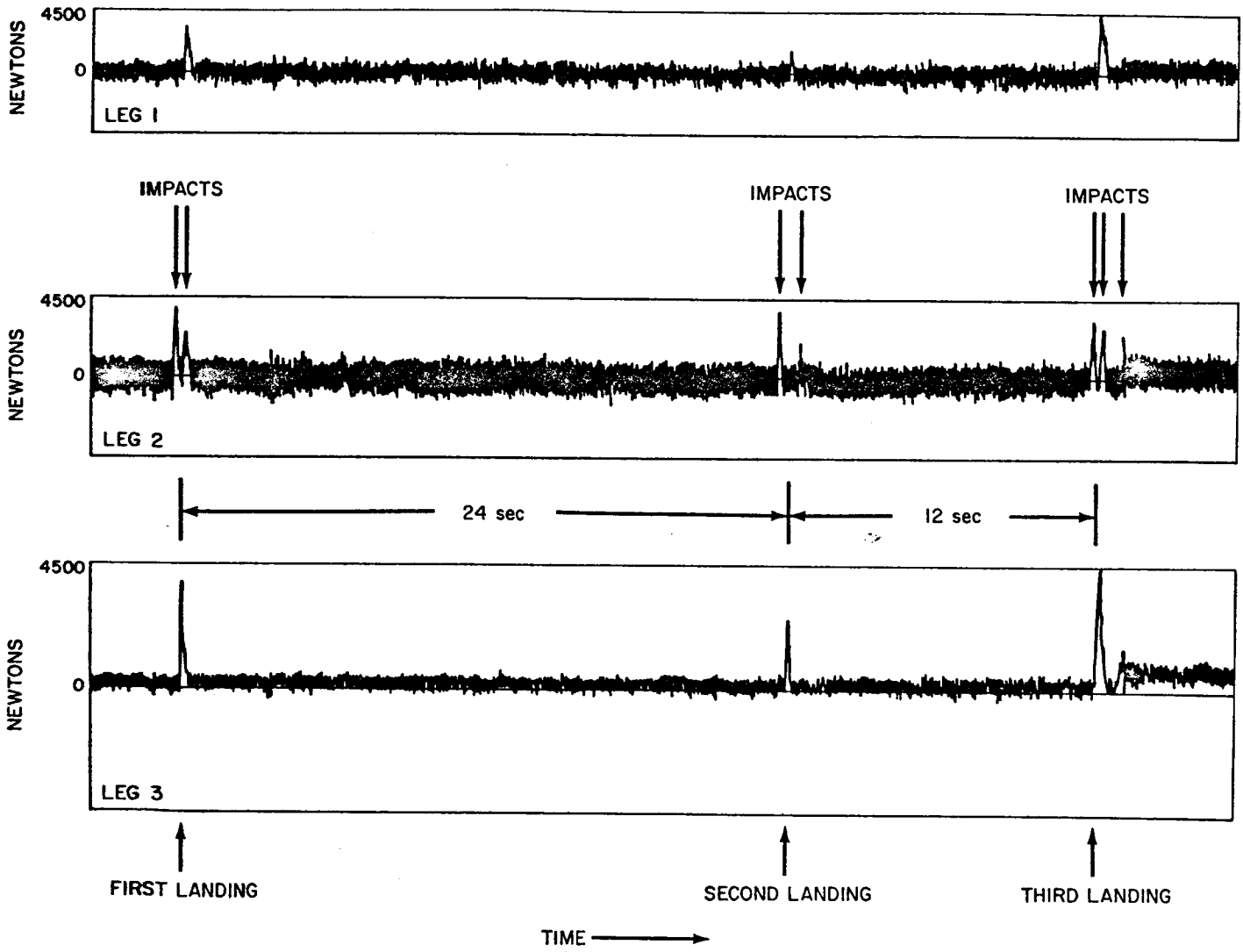

Fig. IV-11. Histories of the axial forces in the shock absorbers of the three landing legs of Surveyor III during the entire landing sequence, touchdown to final rest

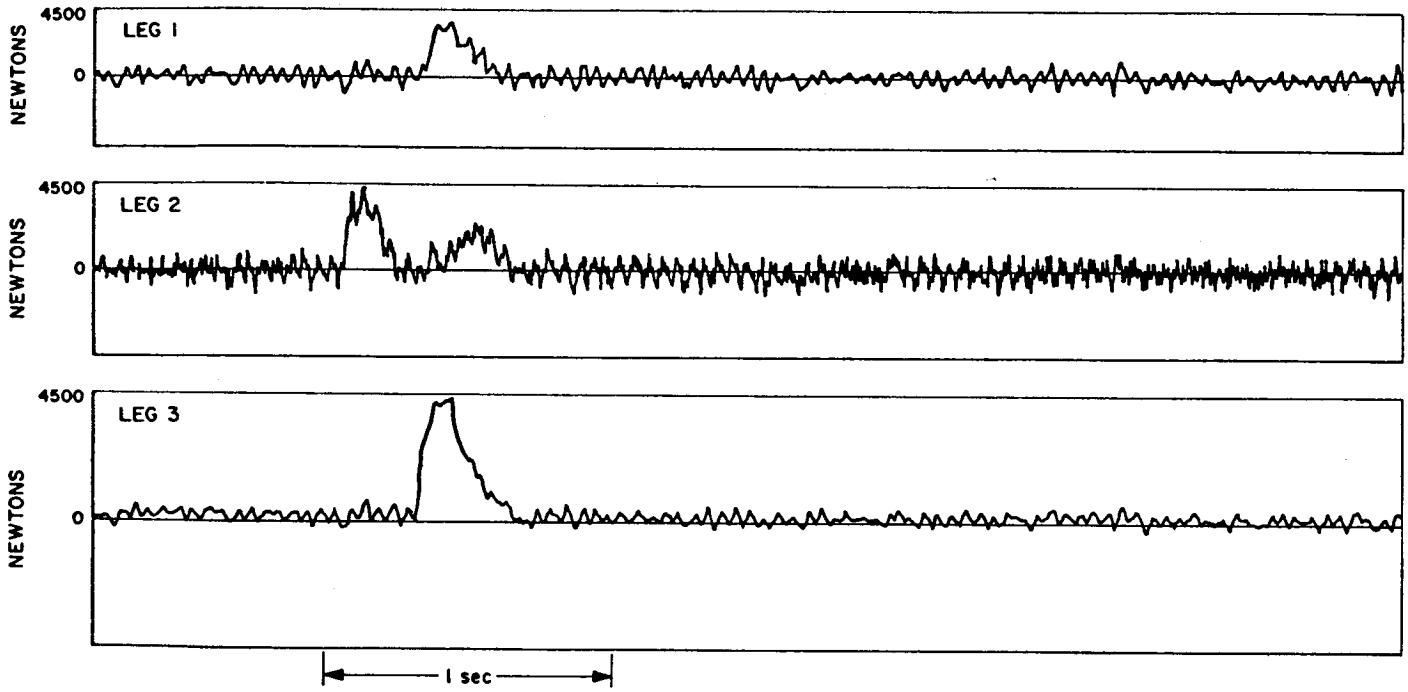

Fig. IV-12. Histories of the axial forces in the shock absorbers of the three landing legs of Surveyor III during the first landing event. (Time proceeds to the right.)

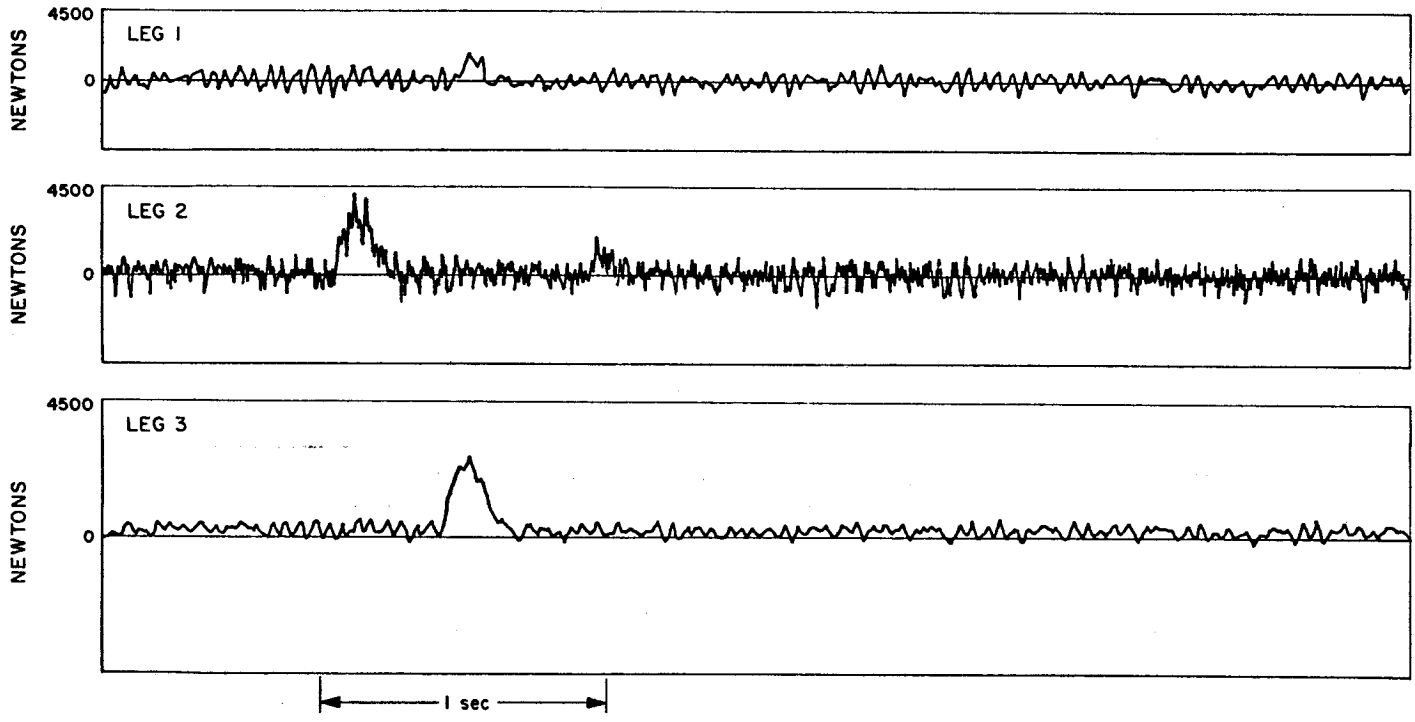

Fig. IV-13. Histories of the axial forces in the shock absorbers of the three landing legs of Surveyor III during the second landing event. (Time proceeds to the right.)

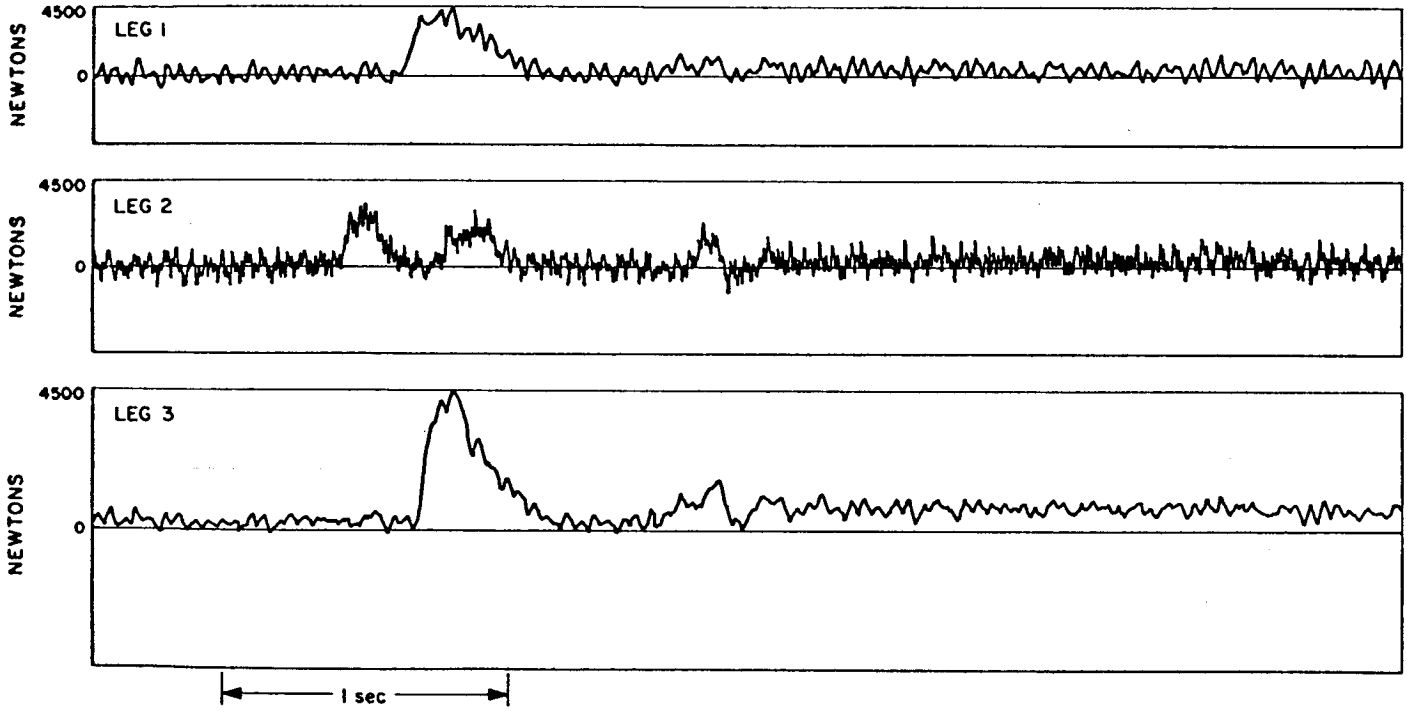

Fig. IV-14. Histories of the axial forces in the shock absorbers of the three landing legs of Surveyor III during the third landing event. (Time proceeds to the right.)

Fig. IV-15. Mosaic of wide-angle frames showing ejected material around footpad 2 (Day 120, 09:52:27 and 11:09:10 GMT).

Fig. IV-16. Narrow-angle mosaic of footpad 2 and of the imprints made during the third landing event (Day 116, between 07:06:46 and 09:27:06 GMT).

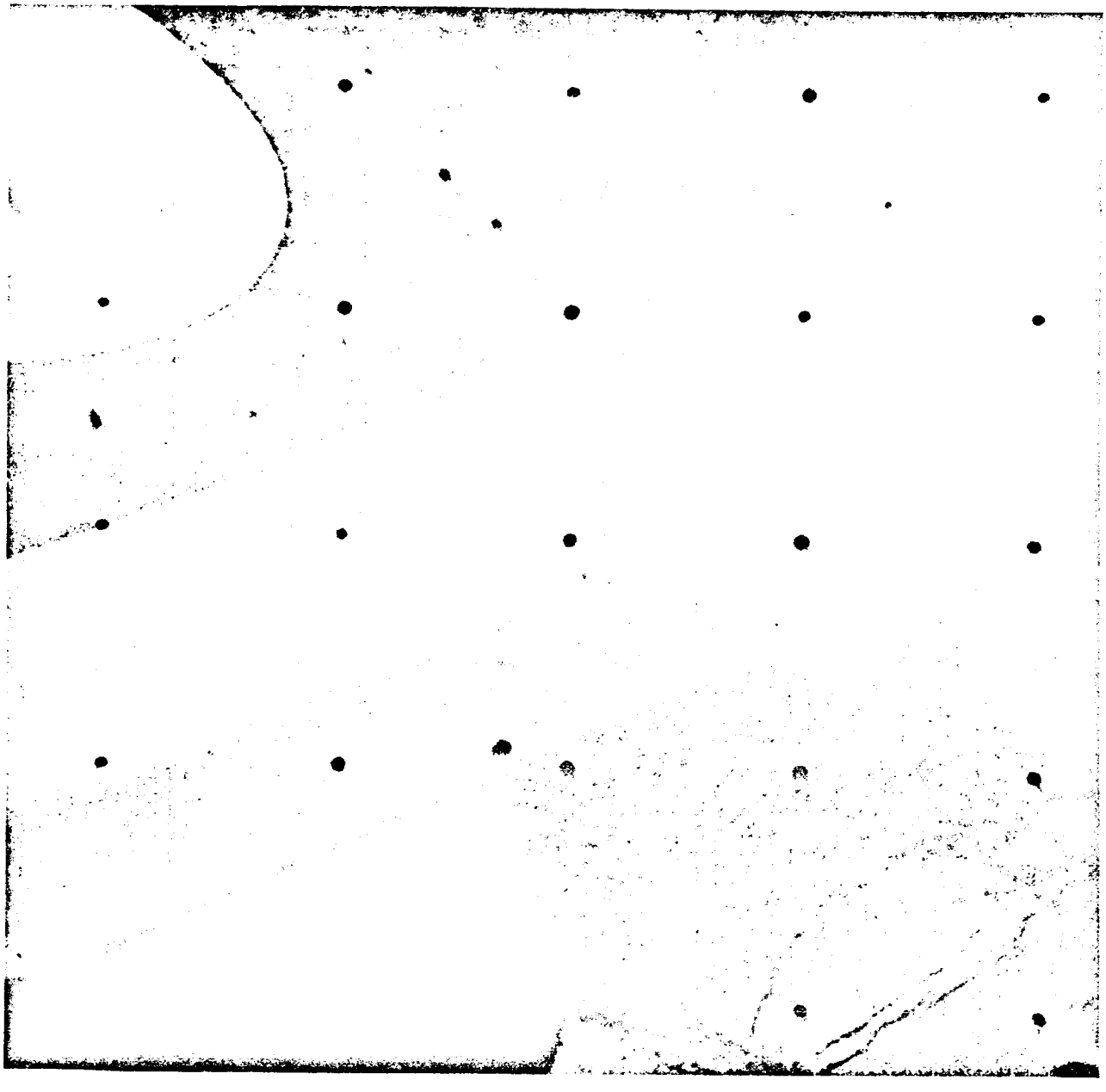

Fig. IV-17. Narrow-angle view of a portion of the imprint attributed to footpad 3. Imprint is at lower right. This photograph shows part of the area covered in wide angle by Fig. IV-9 (Day 120, 14:56:04 GMT).

Fig. IV-18. Wide-angle view of surface area looking over leg 3. The clumps and pattern of darker material indicate the extent of the throwout around footpad 3, which can be seen at lower right (Day 121, 12:12:09 GMT).

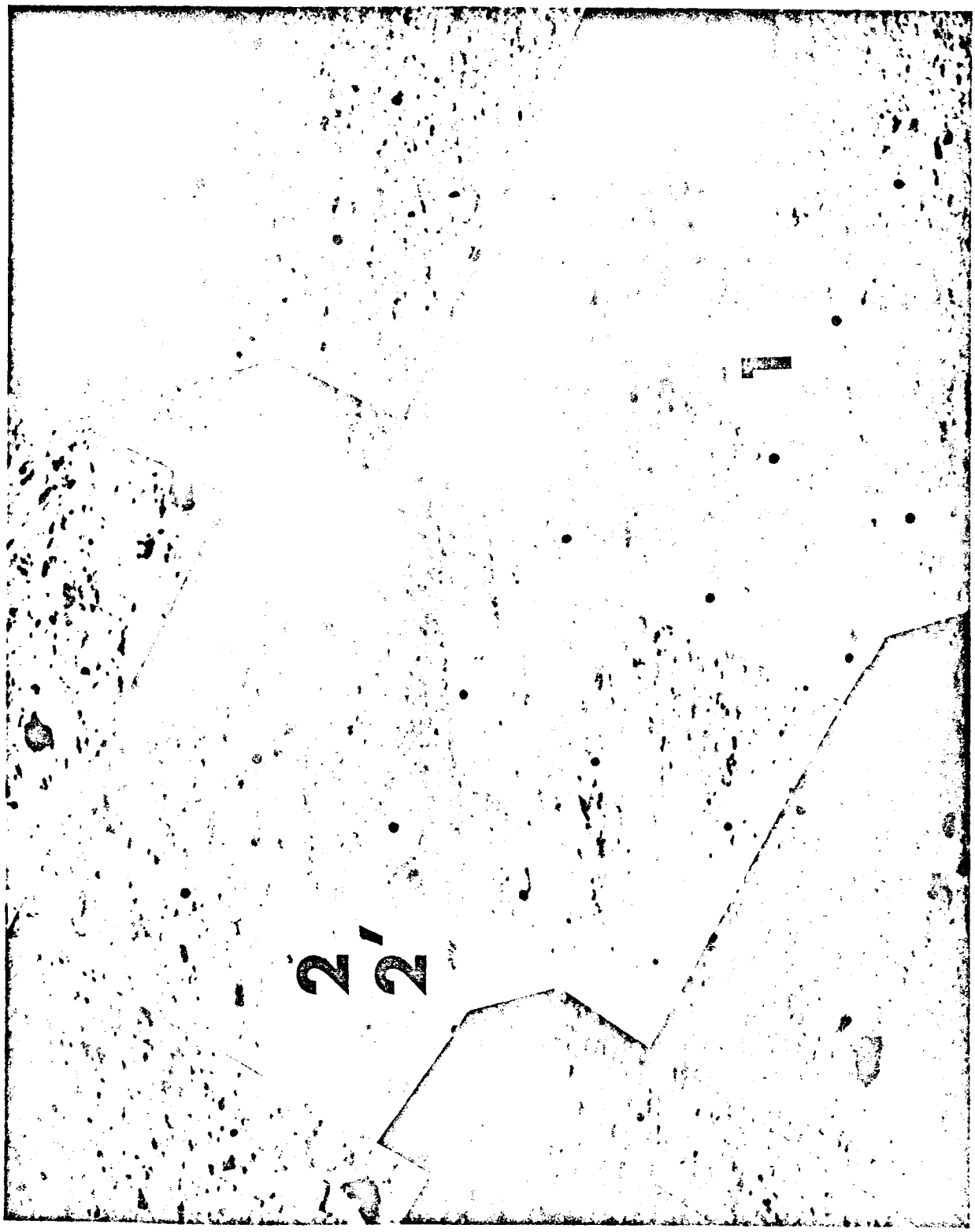

Fig. IV-19. Narrow-angle photograph of Landing Event 2 imprints of footpads 1 and 2. This figure is an enlargement of portion of Fig. IV-10 (Day 116, 08:37:36 GMT).

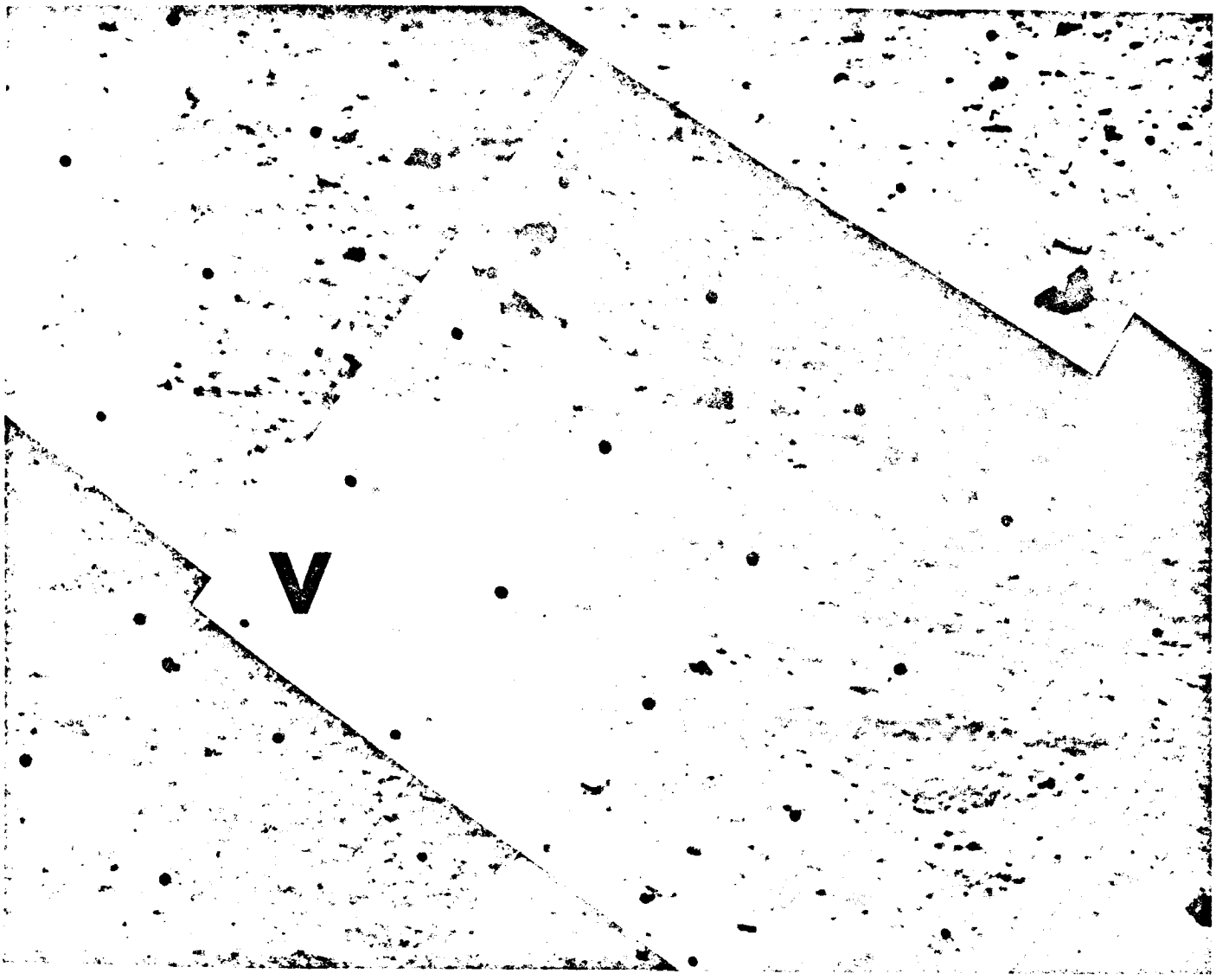

Fig. IV-20. Narrow-angle mosaic of lunar surface that was exposed to erosion by vernier engine 3 during the second landing event. This is an enlargement of a portion of Fig. IV-10 (Day 116, 08:37:36).

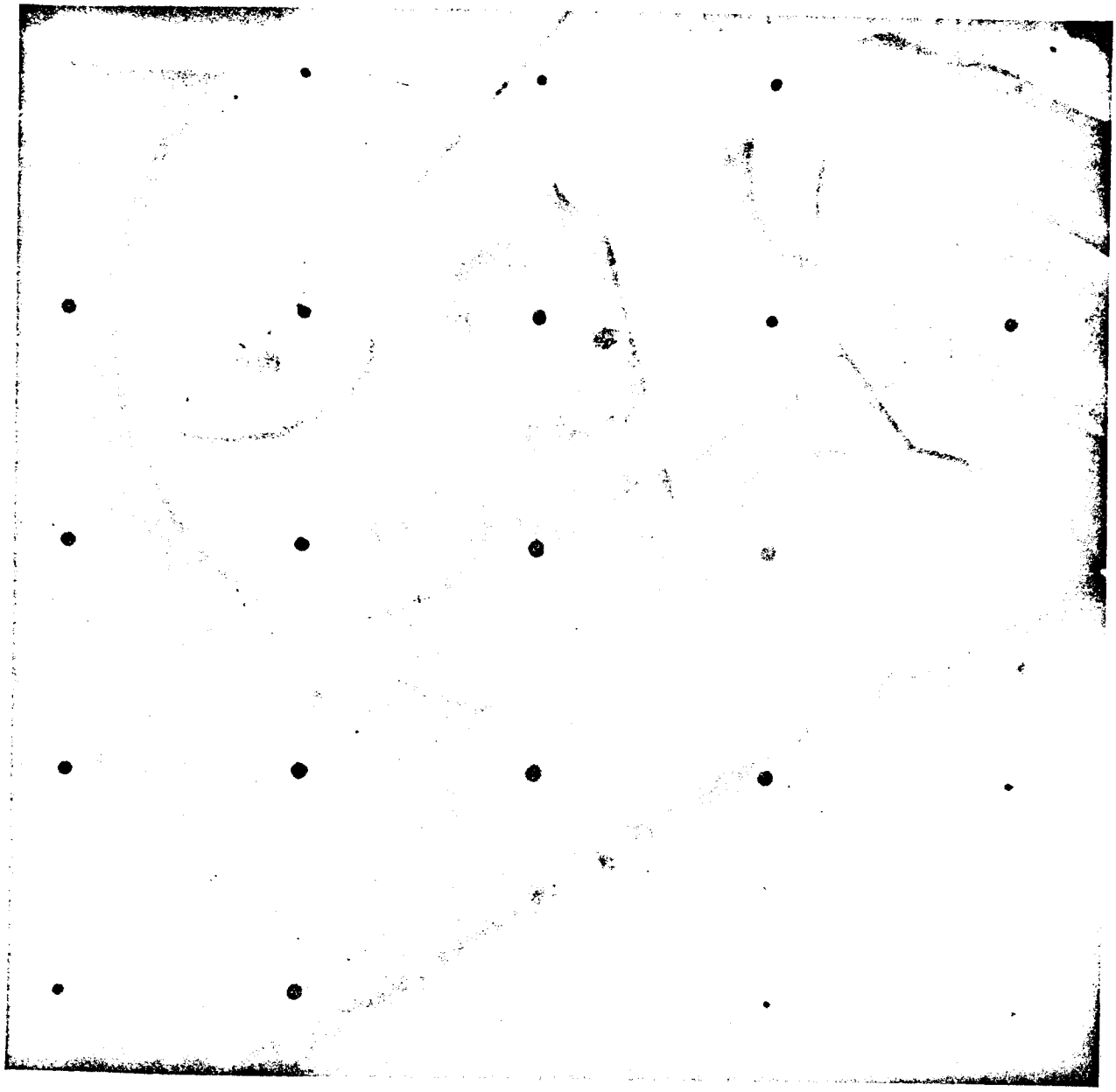

Fig. IV-21. Narrow-angle view of the top of footpad 2. Small particles of lunar material can be seen on the pad surface. The two disks and lockwires are part of the ballast weight assembly, attached to the footpad at Cape Kennedy, Florida, before launch (Day 111, 07:39:59 GMT).

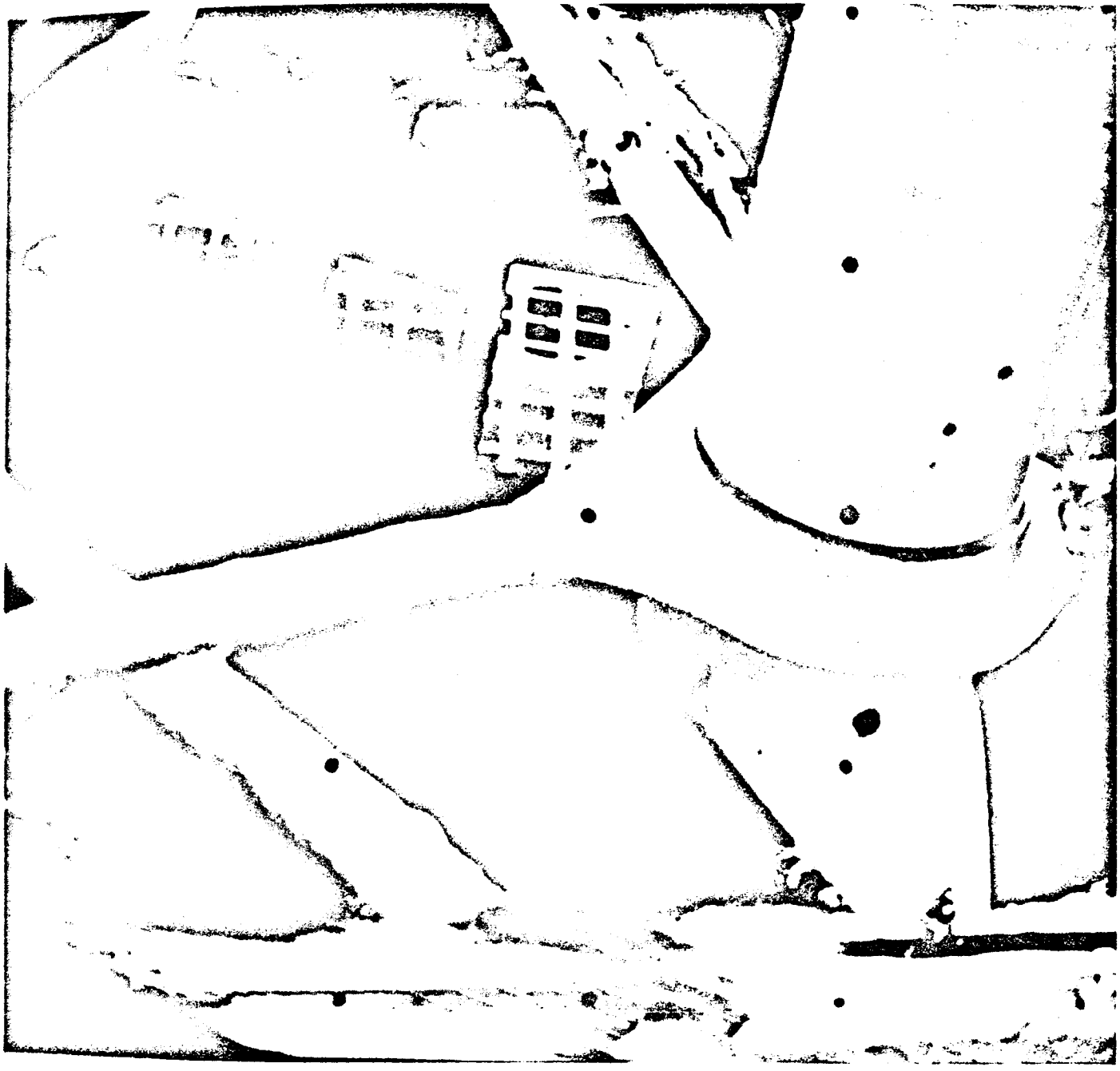

Fig. IV-22. Wide-angle view of the two auxiliary mirrors mounted to the spaceframe of Surveyor III. The dark circles overlain by grids indicate the surface areas directly below crushable block 3 and vernier engines 2 and 3. This picture was taken before launch using the spacecraft television camera.

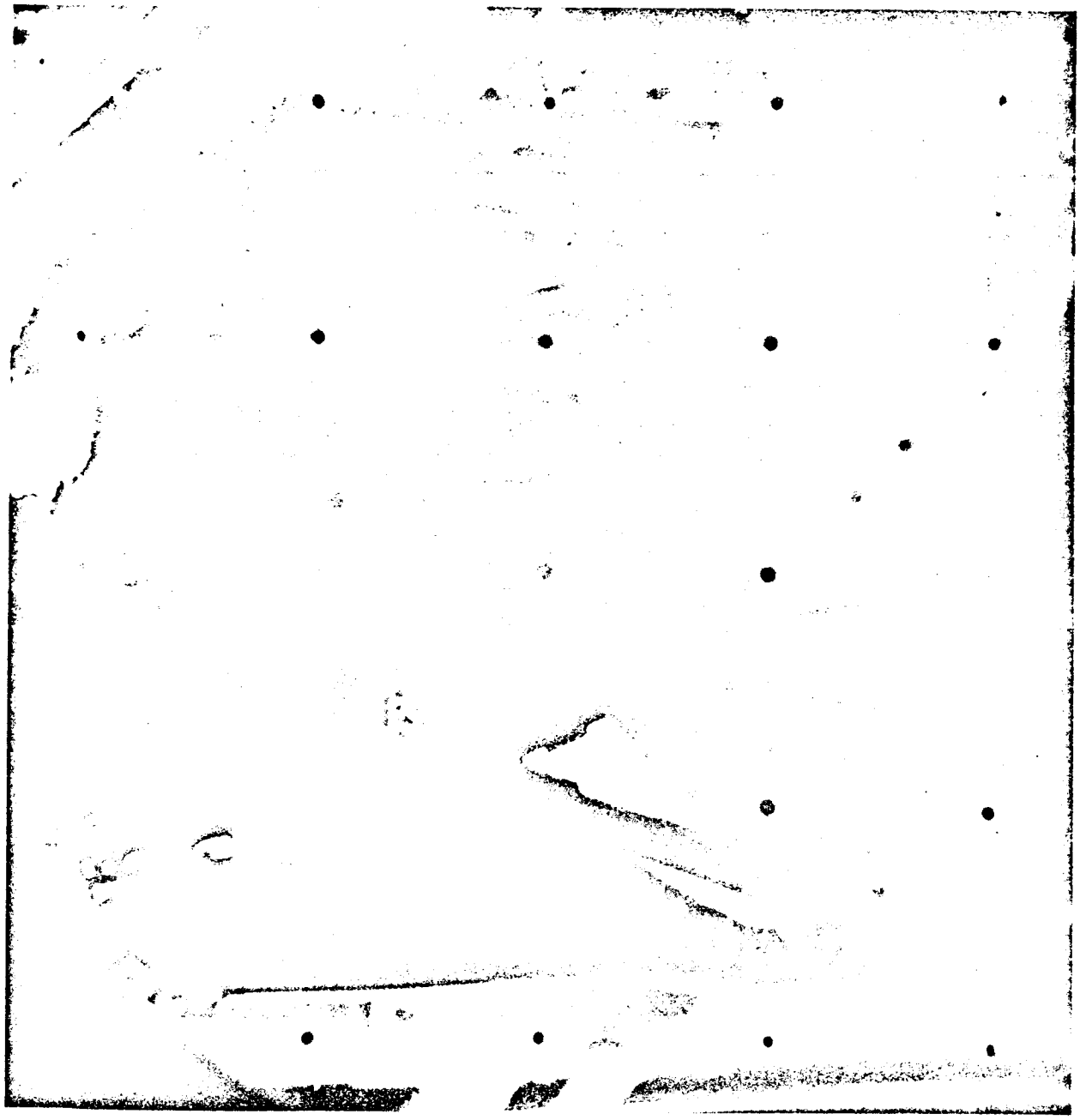

Fig. IV-23. Wide-angle view of the auxiliary mirrors on Surveyor III. The shadowed areas under crushable block 3 and the vernier engines are visible in this frame (Day 117, 11:17:45 GMT).

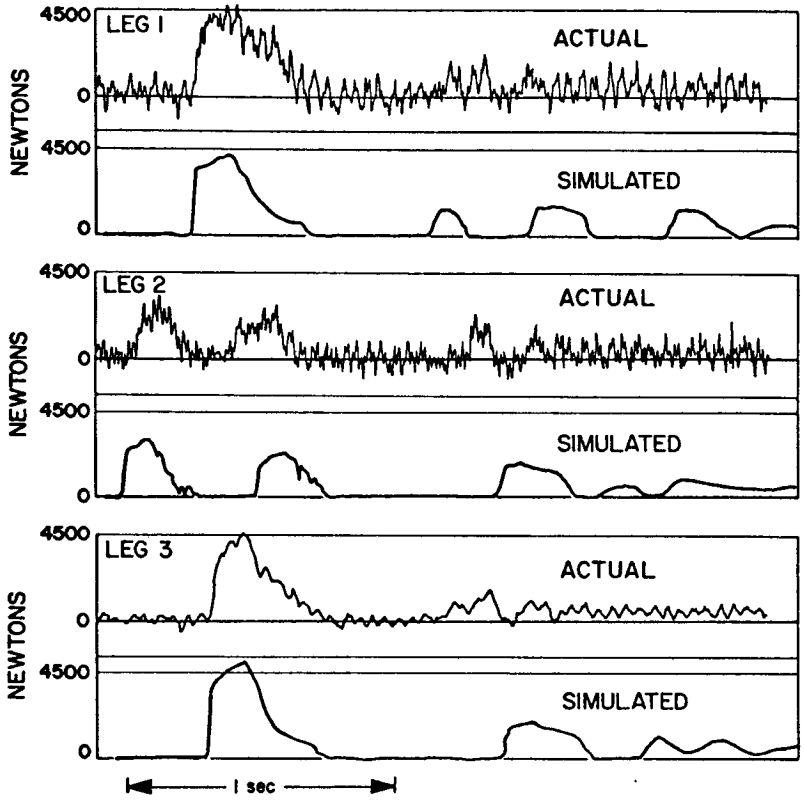

Fig. IV-24. Comparison of histories of axial forces in the three landing legs of Surveyor III during the third landing event, with corresponding data obtained from an analytical landing simulation. Conditions for the simulated landing are: horizontal landing velocity, 0.6 m/sec; vertical landing velocity, 1.5 m/sec; landing surface slope, 10.4°; effective friction coefficient between ground and footpads, 1.0.

Fig. IV-25. Laboratory simulation of footpad and imprint, made on Earth with full-scale model of Surveyor. Surface material: finely crushed basalt, particle size in clay range. Lighting angle similar to that in Fig. IV-8.

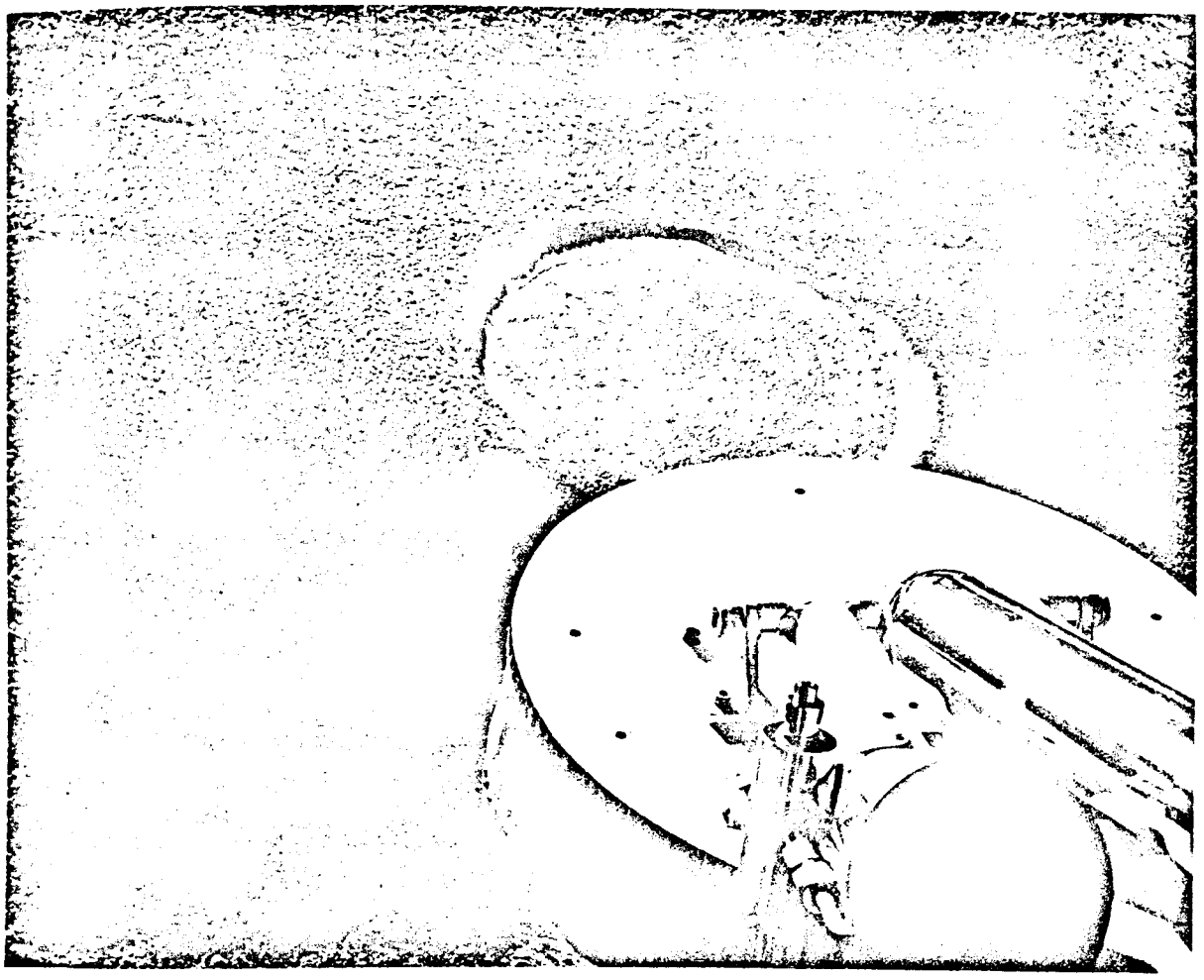

Fig. IV-26. Laboratory simulation of footpad and imprint, made on Earth with full-scale model of Surveyor. Surface material: crushed basalt, 50% fine particles (in clay range) and 50% coarse (in sand range). Lighting angle similar to that in Fig. IV-8.

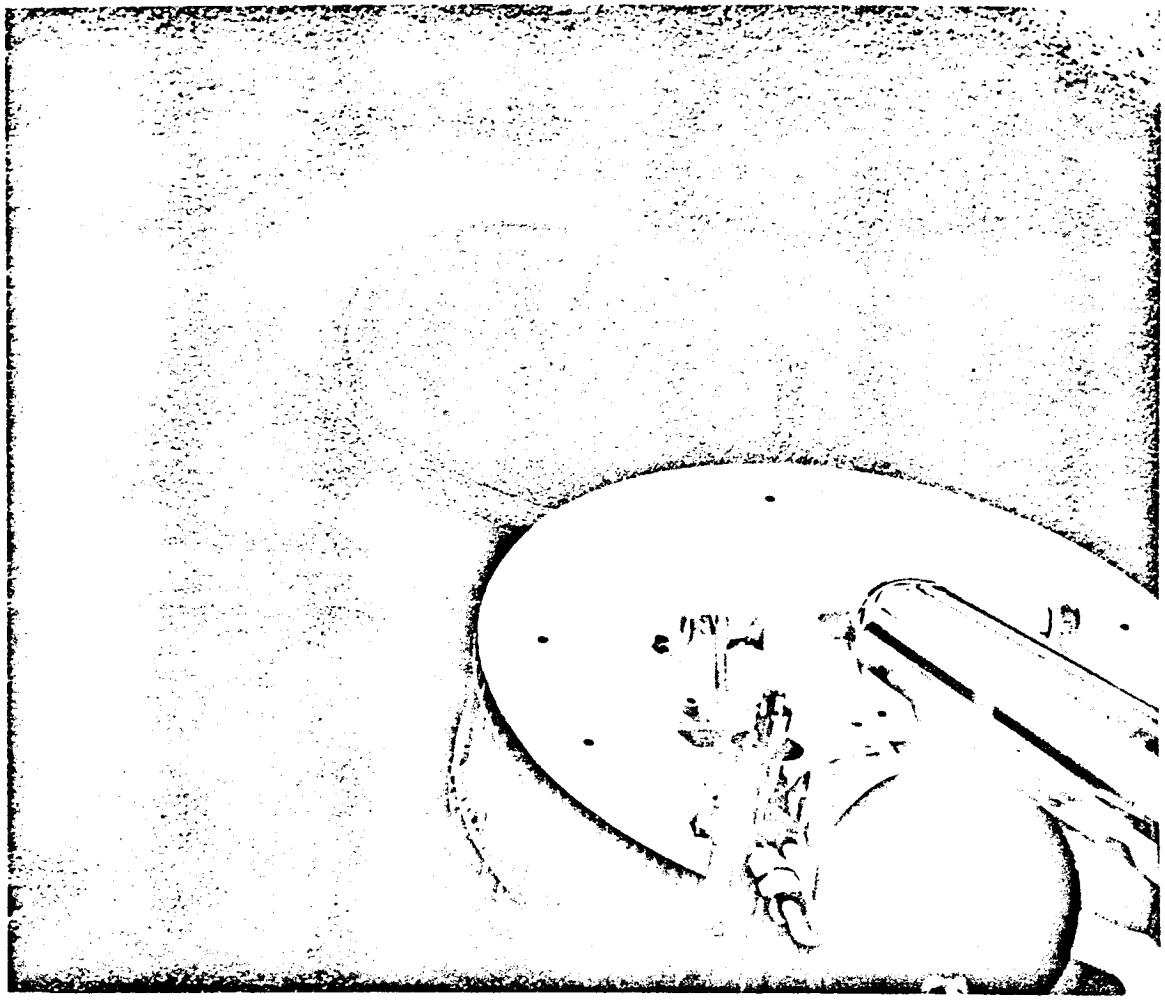

Fig. IV-27. Laboratory simulation of footpad and imprint, made on Earth with full-scale model of Surveyor. Surface material: crushed basalt, particle size in sand range only. Lighting angle similar to that of Fig. IV-8.

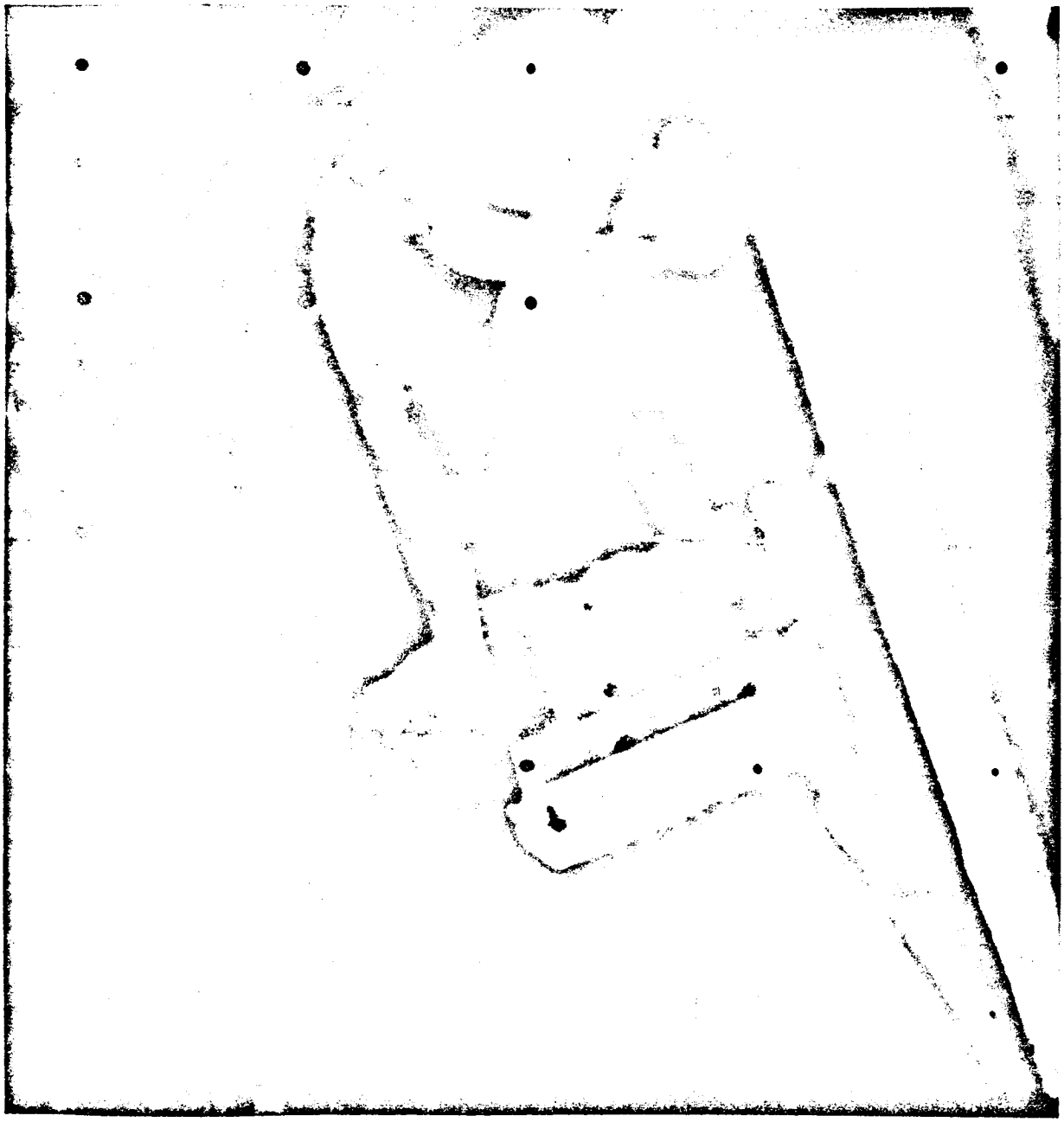

Fig. IV-28. Narrow-angle photograph of lunar rock in jaws of surface sampler (Day 121, 15:21:05 GMT)

JPL Project Document 125

V. SOIL MECHANICS SURFACE SAMPLER: LUNAR SURFACE TESTS AND RESULTS

R. F. Scott, F. I. Roberson, and M. C. Clary

After the success of Surveyor I in meeting the objectives of the engineering flight series, selection from among candidate experiments led to the inclusion of the Soil Mechanics Surface Sampler (SMSS) on the payload. Though originally planned for later Surveyors, the SMSS was modified to fit the reduced telemetry and commanding capability of the earlier spacecraft. Specifically, the SMSS was adapted to the mounting location and the electronics interface of the approach television camera. This required a concentrated, short-term effort to modify, build, and test the SMSS to meet the demanding interface requirements.

Modifications to the SMSS included removal of the strain-, acceleration-, and position-measuring systems originally planned, and incorporation of a means for measuring current drawn by the motors during operation. A description of the modified device, its performance on Surveyor III, and some conclusions regarding the lunar surface material drawn from the experiment are presented.

A. Subsystem Description

The SMSS subsystem consists of a mechanism, an electronics auxiliary, installation substructure, and wiring harnesses. The mechanism is an electromechanical device that can pick, dig, scrape, and trench the lunar surface, and transport lunar surface material. The electronics auxiliary provides command decoding, data buffering, power management, squib firing, and control of the mechanism, motors, and clutch. The installation substructure supports the mechanism and the auxiliary on the spacecraft, while the wiring harnesses provide the electrical interconnections with the spacecraft and between units within the subsystem.

1. Extension/Retraction Mechanism

The extension/retraction mechanism is designed to support and to position the scoop and to permit operations within the space envelope shown in Fig. V-1. The

mechanism rotates about azimuth and elevation pivot points so as to provide movement in spherical coordinates.

2. Drive System

Three electrical motors operating through appropriate drive trains furnish mechanical energy to manipulate the SMSS in extension/retraction, azimuth, and elevation. An electromechanical clutch disengages the elevation drive train upon Earth command, allowing the mechanism to be impelled downward by a pretensioned elevation torque spring to strike the lunar surface. A fourth electric motor opens and closes the scoop. The motors and clutch draw electrical power from the spacecraft unregulated bus through the electronics auxiliary, which also provides switch control.

3. Scoop

The scoop consists of a container, a sharpened blade, and an electrical motor to open and close the container. A small footpad is attached to the scoop door to present a flat surface to the lunar surface. The scoop is capable of holding solid lunar material up to approximately 3.2 cm (1.25 in.) in diameter, and up to 100 cm^3 (6 $in.^3$) of granular material.

Before the flight of Surveyor III, an SMSS motor current versus force calibration test was performed on the spacecraft at Cape Kennedy, Florida. The test was performed under ambient temperature conditions at an unregulated voltage of 22 v. The purpose of this test was to accumulate information that would be used to draw conclusions regarding the lunar surface mechanical properties. The results of this test are not tabulated, since a spacecraft malfunction prevented measurement of motor currents on the Moon.

4. Motor Control

Either a 2-sec or a 0.1-sec period of operation of any of the motors can be selected by Earth command. The angle or distance through which the SMSS moves by these commands depends on the motor involved, its condition, temperature, voltage, and the working load.

B. Functional and Operational Description

The SMSS, as modified for Surveyor III, is mounted in the location formerly occupied by the approach television camera. This position lies below the survey television camera, between the auxiliary battery and leg 2, as seen in Fig. V-2. The area of operation, for a nominal surface plane through the three footpads, is shown in Fig. V-1. Since the azimuth axes of the SMSS and the camera are not collinear, the viewing angle, through the television system, of the scoop varies with the scoop's position. When the scoop is positioned near footpad 2, the camera looks directly down the extension arm, which largely obscures the scoop itself. When positioned near the auxiliary battery, a slight side view of the scoop is afforded.

As the SMSS is extended, the angle that the scoop makes with the test surface varies. The extension arm drawing in Fig. V-1 illustrates the effect; the photographs of the scoop in contact with the surface [Fig. V-3(a) and (b)] show the resulting angle for two extension positions on a nominal, flat surface. The flat surface of the scoop door is normal to the tangential elevation motion at maximum extension.

To make optimum use of operating time during a mission, a standard sequence of testing events has been established. Automatic, taped sequences of spacecraft commands have been prepared and provide the proper motion based on preflight tests to accomplish the planned operations. Corrections for variations in motion sizes occurring on the Moon are provided by manually commanding the mechanism after a given taped sequence is complete. Table V-1 lists the size of each of the motions indicated by preflight calibration. These motion increments occurred at a motor voltage of 22.0 v and a motor temperature of 70°F. For comparison, the size of motion increments estimated during Surveyor III lunar operations also are listed. More precise calibrations will be made later.

The originally planned initial standard sequence of tests included six static bearing tests and a single trench. Provisions were made for performance of optional tests, based on decisions made during lunar operations. Such optional tests were to include: impact tests, picking up rocks, trenching deeper, and bearing tests on subsurface material.

A static bearing test is performed by exercising the extension and azimuth motions until the scoop is positioned above the desired surface point, then, with the scoop door closed to provide the flat surface for contact, driving the scoop downward

Table V-1. SMSS motion increments (no load)

Motion, sec	Test value[a]	Value on lunar surface[b]
2.0 (extend)	8.6 cm (3.4 in.)	4.4 cm (1.75 in.)
2.0 (retract)	8.1 cm (3.2 in.)	3.8 cm (1.5 in.)
0.1 (right azimuth)	1.5°	1.5°
0.1 (left azimuth)	1.5°	1.5°
2.0 (up)	6°	6°
2.0 (down)	9°	9°

[a]Nominal value, based on unit and system level tests at three extension distances.

[b]Preliminary estimate based on television observation.

with the elevation motor until the desired penetration is achieved, or until the motor is stalled. An open scoop static test can also be carried out.

For an impact test, the scoop is again positioned above the desired surface point, and the elevation drive clutch is actuated, allowing the scoop to drop to the surface, accelerated by gravity and the torque spring attached at the elevation axis. An impact test can be performed with the scoop open or closed, as desired.

A trenching operation is performed by driving the scoop down into the surface with the door open, then drawing it toward the spacecraft with the retraction motor. Material can be removed from the trench by retracting the scoop until it is clear of the surface, forming a pile of soil at the foot of the trench, or by closing the scoop and lifting the material out of the trench.

The operations of the SMSS experiment must be closely monitored by the survey television camera, since position-indicating telemetry is not available. Sequences and priorities for tests are therefore dependent upon viewing conditions, spacecraft shadow patterns, and the performance of the television system.

C. Mission Description

1. SMSS Engineering Performance

During the flight phase of Surveyor III, a heater was employed in the SMSS electronics auxiliary, in spite of which the temperature of the auxiliary reached -33°F. The designed survival temperature for the unit was -67°F.

After touchdown, during the spacecraft assessment period, the heater remained off for 2.5 hr, allowing the electronics auxiliary temperature to drop to an estimated -130°F. Thermal power was restored, and the temperature of the auxiliary remained within operating limits from initial turn-on on Day 111 (GMT)[1] until operations were concluded on Day 122.

During the 18 hr, 22 min, of total "on time" for the SMSS auxiliary in the first lunar day, 5879 spacecraft commands were sent to it. All commands were correctly coded, and 1898 SMSS commands were generated. The SMSS and its electronics auxiliary responded correctly to each throughout this period.

[1] All times of SMSS events are given in Greenwich Mean Time. All SMSS experiments were performed during periods of lunar visibility from the Deep Space Station at Goldstone, California.

Following touchdown, it was found that some of the Surveyor III telemetry was not reliable so that no valid SMSS motor current data could be obtained.

2. Lunar Surface Operations

Determination that the temperature of the SMSS electronics auxiliary was high enough for operation occurred late in the Goldstone view period of Day 111. The decision to turn on the SMSS power was followed by a short series of tests to assess the condition of the electronics and to attempt a solution of the spacecraft telemetry problems. This section will briefly describe SMSS operations on Day 111 and subsequently. The locations of all tests are shown in Fig. V-4.

a. Day 111. Initial operations began according to the standard sequence, and included firing of the pyrotechnic locking device (to release the SMSS from its stored position) and transmission of four commands to extend in the 2-sec timing mode. A television picture to verify operation of the extension motor showed that extension had occurred, but that the distance extended was less than expected.

The sequence of four commands was repeated, and television verified that the SMSS scoop was then at the originally intended position. A standard sequence was next initiated and included commands to extend; retract; move right, left, up, and down. Completion of these motions showed other SMSS motors to behave as specified. The scoop door motor and the clutch actuator were not tested at this early time.

Glare in the television optical system due to Sun angle had prevented a complete television survey of the area of SMSS operations. Since narrow-angle coverage was available only for the area near the auxiliary battery, a departure from the standard sequence was decided upon, and the scoop was next extended and positioned above the surface near the auxiliary battery, in preparation for the first static bearing test.

The Goldstone view period ended as the bearing test sequence was being initiated, with the result that the SMSS scoop did not contact the surface. The final position of the deployed mechanism on this day is shown in Fig. V-5.

b. Day 112. It had been intended at the end of Day 111 operations that the first bearing test would be performed on Day 112 at the final Day 111 position of the SMSS. Prior to further SMSS operations on Day 112, television surveys were conducted, including a narrow-angle survey of the SMSS operations area. However, during the

television operations, a malfunction occurred in azimuth stepping when the camera was stepping clockwise, or to the right azimuth. Accordingly, it was decided to move the SMSS into the field of view of the TV camera and to start testing the lunar surface. The SMSS was stepped right twelve 0.1-sec steps, extended five 2-sec steps, and down two 2-sec steps to locate it at the surface. Another 2-sec down command drove the closed scoop into the surface at Bearing Test 1, shown as point A in Fig. V-4. After elevating the scoop clear of the surface, it was moved right and extended, in preparation for a trenching operation. The scoop was opened for the first time and driven down into the surface, using three 2-sec lower commands. A total of sixteen 2-sec retract commands, with television observation verifying performance, were used to drag the scoop in forming Trench 1, located at point B in Fig. V-4.

Because of the difficulty encountered in the camera stepping, it was positioned at +15° azimuth, and the SMSS was moved left to this position, near the auxiliary battery. There the camera could follow the retraction motion of the SMSS by stepping its mirror in elevation only. A trench was started by lowering the scoop (door open) into the surface, and retracting eighteen 2-sec steps, allowing the camera to record the operation without use of the aximuth stepping drive.

At the completion of this trenching operation, which constituted the first pass through Trench 2, shown at point C in Fig. V-4, the SMSS was elevated, extended to the head of the trench, and driven down into the surface in preparation for the second pass through the trench. After 18 retract commands, television observation revealed that the scoop had traveled only 10 cm (4 in.), indicating that it was stalled near the head of the trench.

A narrow-angle survey of Trench 2 completed the activities for the Day 112 period. Figure V-6 shows, in a wide-angle photograph, the condition of the operation at the end of the pass, with Bearing Point 1 and Trenches 1 and 2 visible.

c. Day 113. Objectives for this day's operation of the SMSS experiment were to continue in Trench 2 to the maximum depth possible.

To clear the scoop of the stalled condition at the head of the trench, it was extended once and elevated twice, all in the 2.0-sec timing mode; then, two retraction and two down commands placed the scoop back in the trench, on the spacecraft side of the point of obstruction. Eighteen 2.0-sec retract commands were transmitted; after a television survey, twelve additional transmissions completed the second pass through Trench 2.

A television survey of the trench preceded repositioning of the scoop to the head of the trench in preparation for the next drag. The scoop was driven down, again at the head of the trench, and a series of thirty 2.0-sec retraction commands given. Television observation showed the scoop traveled less than in the previous trenching pass, indicating loading at the limit of its retraction capacity. The thirty commands were repeated, followed by an extension step and three 0.1-sec elevation steps. An additional fifteen 2.0-sec retraction steps brought the total to 75 retraction commands for the third pass through the trench. The Goldstone view period ended with narrow-angle television surveys of the trench, and the SMSS remained in position at the foot of Trench 2.

d. Day 114. A survey of Trench 2 was the only operation related to SMSS. Solar eclipse studies were made.

e. Day 115. High temperatures precluded SMSS operations during this Goldstone view period.

f. Day 116. It was decided to restrict SMSS operations to the area near footpad 2 to avoid unnecessary stepping of the camera mirror.

Study of pictures from the Day 113 survey of Trench 2 revealed a solid object (contact 1, point D, in Fig. V-4), felt possibly to be a rock, directly beneath the scoop in its last position. Some experiments with a full-scale model spacecraft with an SMSS attached provided a workable sequence of commands to pick up the object without the aid of television, since the camera position precluded narrow-angle viewing of the scoop. The scoop was visible in wide-angle television without violating the stepping constraint. Operations for Day 116 began with this sequence, which resulted in closing the scoop door on the object.

Elevation of the scoop revealed that the object had apparently been crushed in being retrieved. It was decided, however, to place the material in the scoop on the surface of footpad 2. The SMSS was extended eight 2.0-sec steps, rotated right thirty-six 0.1-sec steps, and viewed through the television system. Because of an uncertainty in the precise extension distance, the scoop was moved left, clear of the footpad, and lowered to the surface, to make a mark indicating its position. After elevating the scoop clear of the surface, study of the mark indicated further extension was required. The SMSS was extended two 2.0-sec steps, moved against the right

azimuth stop in five 0.1-sec steps, and lowered to the surface of footpad 2. The scoop door was opened, the scoop elevated and lowered to jar loose the material, and the scoop moved up and to the left, clearing the television view of the footpad. The position of the SMSS at the end of the operation, as well as the lunar surface material on the footpad is shown in Figs. V-7 and V-8. A narrow-angle, color filter survey of the material was conducted before the end of the Goldstone view.

g. Day 117. Operations on Day 117 consisted of moving left from footpad 2 and extending the SMSS. Bearing Test 2 was performed by driving the scoop down four 2.0-sec steps. Bearing Test 3 was subsequently performed after moving further right and still further out in extension. These two bearing tests are located at points E and F in Fig. V-4.

The SMSS scoop was then positioned left, driven into the surface with the scoop open and Trench 3 was started. This trench, shown at G in Fig. V-4, was dug by retracting the SMSS in the 2.0-sec mode a total of 26 steps. A special series of 26 television pictures was taken during this trenching operation, one frame after each retraction step. Figure V-9 shows the completed Trench 3 and Bearing Point 2.

h. Day 118. At the close of SMSS operations on Day 117, an object of higher albedo than the surrounding surface was observed near Trench 3, at Contact Point 2 (item H in Fig. V-4). Operations for Day 118 began by placing the scoop with the door open, over the object (Fig. V-23), and with close coordination between narrow-angle television viewing and SMSS commanding, the object was picked up in the scoop.

After positioning the scoop over footpad 2, and opening the scoop door, a short series of 0.1-sec elevate and lower commands were issued to ensure that the object was freed from the scoop. This motion freed a portion of soil that had remained in the scoop since the last trenching operation. Subsequent television observation of the footpad showed the pile of material with the deposited object apparently covered.

Attempts to uncover the object, by placing the scoop tip on the footpad and retracting it, succeeded in removing some material from the footpad, leaving an object on the footpad tentatively identified as the one picked up.

Items J and K in Fig. V-4 represent further trenching operations at Trench 3. The scoop was positioned near the head of the trench, to the left, and retracted, widening the trench to three scoop widths. Figure V-10 shows the widened trench,

just prior to conducting Bearing Test 4, shown at item L, in Fig. V-4, in the bottom of the trench.

i. Day 119. A series of impact tests, shown as items M through R (Fig. V-4) were performed starting with a drop from a single 2.0-sec elevation above the surface at Impact Test 1. After assessing the impact result, the tests that followed were performed by releasing the scoop from higher positions. Impact Tests 2 and 3 were performed by elevating the scoop two 2.0-sec steps above the surface; Impact Tests 4, 5, and 6 were accomplished by elevating the scoop four 2.0-sec steps.

At the conclusion of operations, the SMSS was exercised in several of its operating modes to record the size of motion increments provided by the motors, to see whether any changes had occurred to this time. There were none observed on the basis of preliminary estimates.

j. Day 120. On Day 120, SMSS operations were again shifted to the area near the auxiliary battery. The SMSS was extended to near maximum extension, the scoop closed, and Bearing Tests 5, 6, and 7 were performed at a single azimuth position, retracting the scoop between tests. During this bearing test sequence, contact was made with a small surface object at item T in Fig. V-4, in which the three bearing tests are shown as items S, U, and V.

By stepping the SMSS right two 2.0-sec steps and performing Impact Tests 7, 8, and 9, with extension motions between, the three impact points shown at W, X, and Y on Fig. V-4 were placed on a line parallel to that of the bearing tests. Stepping right two more 0.1-sec steps, Impact Test 10 was performed. Elevations of two 2.0-sec steps for Impact Tests 7 and 8, and four 2.0-sec steps for Impact Tests 9 and 10 were used.

k. Day 121. Initial activities involved coordinating the position of the scoop through narrow-angle television, and picking up the "rock" turned up on the previous day. The "rock" was gripped in the side of the scoop. The scoop was repositioned to afford the best view of the rock (see Fig. V-11), and a complete color filter survey was performed. While positioning the scoop to place the "rock" on the surface nearby (since the camera could not at this time be moved to view footpad 2) the "rock" slipped out, and thereafter was not visible on the surface in the immediate area.

Three new trenching passes were made through Trench 2, using twenty, thirty-three, and twenty-four 2.0-sec retraction commands, respectively. Before the last pass, four impacts with the scoop open were performed in the trench floor to loosen the material. Figure V-12 shows the SMSS scoop with the "rock" in the door, as well as Bearing Tests 5, 6, and 7 from previous operations.

1. Day 122. Sun angles for Day 122 dictated moving of SMSS operations to the right, where available light permitted tests, and minimum camera stepping would be required to follow sunset shadows. The television camera was moved successfully.

Impact Test 11 at position b in Fig. V-4 was performed on the undisturbed surface with the scoop open, following a 2-sec elevation movement. Another test from the same height, Impact Test 12, was repeated at position c because material deposited from the scoop on the surface in Impact Test 11 obscured the surface at point b. A short trench was dug at point d, followed by Impact Test 13 at location e in the trench floor on subsurface lunar material. Final position of the SMSS, with Trench 4 and several impact points visible on the surface below, is shown in Fig. V-13.

D. Tests on Lunar Surface Material

Results of tests performed by the SMSS on the lunar surface and conclusions on the mechanical properties of the surface material, as deduced from the test results, are presented here.

1. Tests Performed

Using the SMSS, many mechanical tests were performed from which calculations of varying degrees of refinement can be made. In this report only the most preliminary estimates of material properties are given, based on a very brief evaluation of the SMSS behavior and the photographic results. A summary of the tests from which mechanical properties can be derived is given in Table V-2.

Table V-2. Summary of SMSS bearing and impact tests

Test	Time (GMT)	Force, dynes x 10^5	Scoop closed (c), open (o)	Penetration, cm	Drop height, cm
Bearing 1	Day 112, 05:07:01	49	c	2.5	
Bearing 2	Day 117, 08:45:20	27	c	2.5	
Bearing 3	Day 117, 09:21:55	22	c	1.9	
Bearing 4	Day 118, 13:32:44	27	c	0.6	(in trench bottom)
Bearing 5	Day 120, 15:35:31	27	c	2.2	
Bearing 6	Day 120, 15:45:42	4.5 to 9	c	Compressed clod	
Bearing 7	Day 120, 15:48:50	27	c	2.9	
Bearing 8	Day 120, 15:59:18	29	c	1.9	
Impact 1	Day 119, 09:27:02		c	1.3	15
Impact 2	Day 119, 09:42:02		c	3.3	30
Impact 3	Day 119, 09:49:04		c	2.5	30
Impact 4	Day 119, 10:08:29		c	3.8	60
Impact 5	Day 119, 10:16:45		c	4.3	60
Impact 6	Day 119, 10:26:40		c	3.8	60
Impact 7	Day 120, 16:17:06		c	1.3	30
Impact 8	Day 120, 16:24:57		c	1.6	30
Impact 9	Day 120, 16:32:45		c	1.6	60
Impact 10	Day 120, 16:41:30		c	1.6	60
Impact 11	Day 122, 12:38:33		o	6.3	15
Impact 12	Day 122, 13:03:40		o	6.3	15
Impact 13	Day 122, 13:30:37		o	1.3	15
Impact 14	Day 122, 14:07:29		c	5.1	78

2. Bearing

There were eight bearing tests made with the SMSS door in the closed position so that an area 5 by 2.5 cm was presented to the lunar surface. As seen in Fig. V-3(a) and (b), the angle that the flat base of the scoop makes with the lunar surface varies with the extension distance of the sampler. Only in the extreme extension position is the flat base aligned approximately parallel to the surface. Consequently, as the scoop is pushed into the surface in the bearing tests, the material under the scoop is forced down and the surface toward the spacecraft is observed to rise as the soil is displaced, as shown in Fig. V-14(b).

When each trench was begun, the scoop was pushed into the lunar surface with the door wide open so that a much smaller area was presented to the surface; consequently, greater penetration depths were obtained. These tests have not been analyzed, and no results from them are shown in Table V-2, although general penetrations of 3.8 to 5 cm (1.5 to 2 in.) were obtained.

As a result of varying temperatures during the lunar day and different distances of extension of the SMSS, a range of forces can be applied to the lunar surface by the tip of the scoop. It was originally intended that these forces be obtained directly by measuring the motor currents and using the preflight calibration data. However, the lack of usable telemetered information on spacecraft motor currents precluded this. No temperature sensors were provided on the motors, and it was necessary to estimate their temperatures from those measured on the spacecraft and temperature differences assumed from preflight tests. The information on forces in the bearing tests shown in Table V-2 was obtained from such estimates of motor temperatures and the known extension distances of the sampler.

After each test of the SMSS scoop in the lunar surface and of the disturbed surface upon removal of the scoop, pictures were obtained by the television camera. Other pictures were obtained of each disturbance at various Sun angles on succeeding days. These photographs have been used to obtain the penetration distances given in Table V-2 for both bearing and impact tests.

Prior to some bearing and impact tests, the SMSS was lowered to the lunar surface by means of 0.1-sec down commands to determine the surface location at the point. The commands were repeated until no downward motion was detected after several 0.1-sec commands. Although these operations imposed loads of 10^5 dynes on the surface, only a small amount of disturbance caused by the blade tip was observed.

3. Trenching

Three trenches were dug in the lunar surface with the SMSS. The first trench was excavated with only a single pass of the sampler, whereas Trenches 2 and 3 were subjected to repeated passes. A bearing test was made on the floor of Trench 3. A fourth small trench was performed for the purpose of carrying out an impact test at a depth of 5 to 7.5 cm (2 to 3 in.) below the surface.

In general, the first pass of the sampler across the lunar surface for the purpose of making a trench produced an excavation about 5 to 7.5 cm deep; the second pass deepened the trench to a depth of 10 to 12.5 cm (see Fig. V-15), and a third pass produced a trench 15 to 17.5 cm in depth. The motion increments produced by a 2-sec retraction command of the surface sampler vary with the load acting on the sampler. When the force reaches a limit determined by temperature and spacecraft voltage, the retraction motor stalls and no retraction is obtained. It was found that the first pass in a trenching operation produced a trench of 38 to 50 cm long with about twenty 2-sec retraction commands. In the second (see Fig. V-16) and third pass in each trench stalling of the motor was observed, and as many as 75 commands were required to complete the third pass through Trench 2, for example. There are two reasons for this behavior:

(1) When a trenching operation is begun at the surface, the material is free to displace sideways out of the way of the advancing scoop. When the trench has been excavated to a depth of several inches, the soil scraped from the trench floor accumulates and is not easily able to get out of the way of the advancing fully-packed scoop, as can be seen in Fig. V-15.

(2) There is a possibility that the lunar material becomes stronger or denser with depth.

Two tests were specifically designed to clarify this latter reason. In the first, a bearing test was performed on the material at the bottom of Trench 3 at a depth of 5 to 7.5 cm below the surface (Bearing Test 4). In the second, two open-scoop impact tests were performed on the undisturbed lunar surface adjacent to a trench (Impact Tests 11 and 12), and an open-scoop impact from the same drop height above the impact surface was made in the bottom of the trench at a depth of 5 to 7.5 cm below the lunar surface (Impact Test 13).

It is not possible at this time to make calculations regarding the lunar material properties based on the trenching operation. Further evaluations of the lunar data must be carried out in combination with laboratory tests with the SMSS. The reason for the small motion increments of the retraction motor observed under no load must be understood before the retraction forces can be estimated.

4. Impact

The bearing tests provide information on the static strength properties of the lunar soil, and thus involve primarily its shearing strength in which the soil's density plays a part. Impact tests were conducted in an attempt to obtain further information on the density of the soil in the absence of the motor current data which would have enabled the weight of a scoopful of soil to be measured. In such tests, the penetration of the surface sampler into the lunar soil is resisted by both the static strength of the soil and by the density of the material. The contribution of the soil's density is greater as the impact velocity increases.

The SMSS is a flexible arm whose vibrations are excited both by the release of the clutch which initiates an impact test and by the impact itself, so that a complete analysis of the motion of the SMSS during impact is complicated. At this time, only approximate comparisons with terrestrial laboratory experiments can be employed to evaluate the soil's density from the impact tests. Fourteen impact tests from a variety of drop heights were carried out at different locations within the reach of the sampler on and below the lunar surface. The results of those tests are presented in Table V-2; their location is shown in Fig. V-4. The drop height given in Table V-2 is at present approximate. For illustration, the result of Impact Test 3 is shown in Fig. V-17.

5. Material Handling and Dumping

Following a trenching operation, it was frequently found that some of the lunar soil remained adhering to the inside of the SMSS even when the soil was considerably disturbed. On occasion, this material fell out unintentionally on the undisturbed lunar surface leaving patches or trails of excavated material as seen in Fig. V-18.

In the process of excavating the second trench, a lump of lunar material was found below the scoop, whose door was closed on the lump in order to find out if

the material was solid or composed of an aggregate of finer particles. Since the scoop door closed through the material with no observable difficulty, it was concluded that the lump was in fact an aggregate. As a check, that portion of the lump pinched off and enclosed in the scoop was transported to footpad 2 and dumped on the footpad for television observation. The material disaggregated on dumping, as seen in Figs. V-7 and V-8.

At another location as shown at point H on Fig. V-4, a small object about 1 cm in diameter with higher albedo than the lunar surface was picked up and transported to footpad 2 in order to determine whether it was solid. During the dumping operation on the footpad, more soil fell out of the scoop and buried the object, which was, however, subsequently identified on the footpad. A third object, also of higher albedo and approximately 2.5 cm in diameter, was located embedded in the lunar soil adjacent to the head of the second trench. It was excavated and picked up in the left side of the scoop, as shown in Figs. V-10 and V-11. In clasping it, the scoop door exerted a force of about 2.5×10^6 dynes (6 lb) on the object, which was restrained by the edge of the scoop, which is 0.1 cm thick. If it is assumed that the bearing area on the object was 1.2 cm long by 0.1 cm wide, then the scoop door exerted a stress in the order of 2×10^7 dynes/cm^2 (300 lb/in.^{2}) on the object. More of the lighter surface of the object was apparent after it was picked up than when it was embedded. The lower surface, as seen in Fig. V-11, is darker. The scratch in this lower surface was probably made by the scoop in excavating the object and may indicate that the lower surface is covered with the darker soil.

6. Homogeneity of Lunar Soil

It can be seen from penetrations recorded during the bearing tests that, considering the probable variation in the force applied to the lunar surface, the lunar material appears relatively homogeneous over the test area of 1.9 m^2 (20 ft^2), as seen, for example, in Fig. V-19.

However, with reference to the impact test data, it appears that somewhat less penetration occurred for Impact Tests 7 through 10 in the vicinity of the auxiliary battery than took place in Impact Tests 1 through 6 at similar drop heights in the area closer toward footpad 2, as seen in Fig. V-20. It should be pointed out that this variation may be due to changes in the drop heights caused by surface sampler elevation motor changes and due to the spacecraft attitude, rather than

developing as a result of differing lunar surface properties. In addition, Impact Test 4 may have been too close to a previous test. However, if differences result from the properties of the soil, they can be effected by either a change in the strength or the density of the material.

No substantial differences were observed in the resistance of the soil encountered in the different trenching operations.

7. Depth Variation of Lunar Soil Properties

In the bearing tests, the SMSS was lowered by one 2-sec command into the lunar soil in general; it was then given successive 2-sec commands, which resulted in small additional penetrations. When the movement ceased, the bearing test was terminated. In the absence of motor current measurements, a detailed evaluation of the force versus depth relation is not possible. Characteristically a penetration of 1.9 to 2.5 cm was achieved in a bearing test at the lunar surface. However, a bearing test (4) carried out at the bottom of the third trench at a depth of approximately 5 to 7.5 cm below the lunar surface, and probably somewhat in disturbed soil, gave a penetration of about 0.6 cm as shown in Fig. V-21. This fact, together with the difficulties observed in making the second and third passes through a trench, even considering the effect of trench confinement mentioned above, appears to indicate that the lunar soil is firmer or denser below this depth. The comparison of the open-scoop Impact Tests 11 and 12 on the undisturbed surface with Impact Test 13, carried out on the material at a depth of 5 to 7.5 cm below the surface, confirms that the material is indeed stronger or denser below a depth of 5 to 7.5 cm.

When the scoop was rested on the lunar surface under a vertical force of an estimated 4.5×10^5 to 9×10^5 dynes (1 to 2 lb), little penetration was observed, so that it appears that an extremely soft upper layer does not exist in the immediate vicinity of Surveyor III. Under the high Sun at lunar noon, the detailed texture of the rough surface is no longer visible, and a clear picture of the distance to which the soil is disturbed by a bearing test can be obtained, as seen in Fig. V-22. The cracks that appear in the ground surface are the surface manifestations of the underground displacement caused by the test. They are not the result of the presence of a surface crust of stronger or more brittle material.

The higher albedo of the undisturbed lunar surface compared to that of the disturbed material in trenches appears to be an extremely shallow effect as seen in Fig. V-23(a) and (b).

As far as can be determined from the SMSS operations, any change in the soil grain size with depth takes place below the resolution of the camera. There is no obvious albedo change with depth, once the lighter surface material has been disturbed. The albedo of the smoothed surface caused by Bearing Test 4 on the undisturbed surface in a trench floor will be studied.

8. Properties of Lunar Soil

a. Bearing tests. Excluding Bearing Test 1, which was carried out at an unfavorable angle to the lunar surface, all other SMSS bearing tests appear to indicate a failure of the surface material to a depth of 5 to 7.5 cm at a pressure of about 2×10^5 dynes/cm^2 (3 psi) on the 5 by 2.5-cm size of the flat base of the SMSS. This value is consistent with the size of the SMSS bearing area and with the lunar soil properties, which were postulated to explain the data observed in the Surveyor I landing, i.e., material with a cohesion of about 1×10^3 to 3×10^3 dynes/cm^2 (0.02 to 0.05 psi) an angle of internal friction between 30 and 40°, and a density about 1.5 gm/cm^3 (3 slugs/ft^3).

In bearing tests of this type, the soil is typically uplifted and disturbed on the surface to a distance that depends on the angle of internal friction of the material. For the 2.5-cm (1-in.) width of the SMSS base, a material with an angle of friction of 30° would be disturbed to a distance of about 7.5 cm (3 in.) from the edge of the base, and a material with an angle of friction of 40° to a distance of about 17.5 cm (7 in.). It is observed in the SMSS bearing tests under high Sun angle (Fig. V-22) that soil disturbance takes place to a distance of 10 to 12.5 cm (4 to 5 in.), indicating an angle of internal friction of about 35°. The nature of the displacement phenomenon observed in the bearing tests seems to indicate that the soil does not change appreciably in density during the test. Below a depth of 7.5 cm (3 in.), the lunar soil is considerably stronger or denser, but no calculation of its properties has yet been made. They will be estimated from the SMSS tests.

b. Impact tests. A complete analysis of the impact tests is lengthy and cannot be given at this time. However, the velocity of the surface sampler at contact with the lunar surface from a drop height of 60 cm (corresponding approximately to four

2-sec elevation steps) can be estimated to be about 2.1 to 2.5 m/sec (7 or 8 ft/sec). Laboratory tests have been carried out on Earth with a prototype sampler striking various soils at a range of velocities. For a slightly higher impact velocity than that given above for the SMSS Moon impacts, laboratory tests on densely packed dry sand (density about 1.7 to 1.8 gm/cm^3) with the scoop closed have given penetration depths of 1.6 to 1.9 cm (5/8 to 3/4 in.). Such a soil has a friction angle of about 40° and is essentially cohesionless. Comparison of the SMSS lunar impact tests with the terrestrial tests indicates that the material densities are comparable, although preliminary analyses indicate that penetration depths at these impact velocities are not very sensitive to density. Such a density (about 1.5 gm/cm^3) would be compatible with the static test results described above. The effect of the stronger or denser lunar soil layer below a depth of 5 to 7.5 cm on the impact test results remains to be investigated. It would tend to lessen the penetrations.

c. Material handling. Since the disturbed lunar soil remains in the open SMSS scoop above the lunar surface, it can be calculated that it possesses a cohesion greater than about 3×10^2 dynes/cm^2 (0.005 psi) for an assumed density of about 1.5 gm/cm^3. Since the walls of the trenches have not collapsed at a depth of 15 to 17.5 cm, it appears that the cohesion may be at least 1×10^3 dynes/cm^2 (0.02 psi). In one impact test carried out with the scoop open, a quantity of soil was dumped on the lunar surface almost equal in volume to the capacity of the scoop as best as can be estimated. In such an impact test, the maximum deceleration is in the range of 5 to 10 Earth g so that the upper limit of the cohesion of the disturbed soil to the scoop can be estimated as being about 1×10^4 dynes/cm^2 (0.2 psi).

In one bearing test, an object [see Fig. V-19(b)] resting on the lunar surface was depressed and found to crumble under a relatively gentle pressure (contact 3, item T in Fig. V-4). It is concluded that this naturally occurring object was an aggregate of smaller particles as was the clod of material broken by the scoop door at the foot of Trench 2. One of the objects of higher albedo picked up seemed to have a substantially greater strength than these clods, and may be termed a rock.

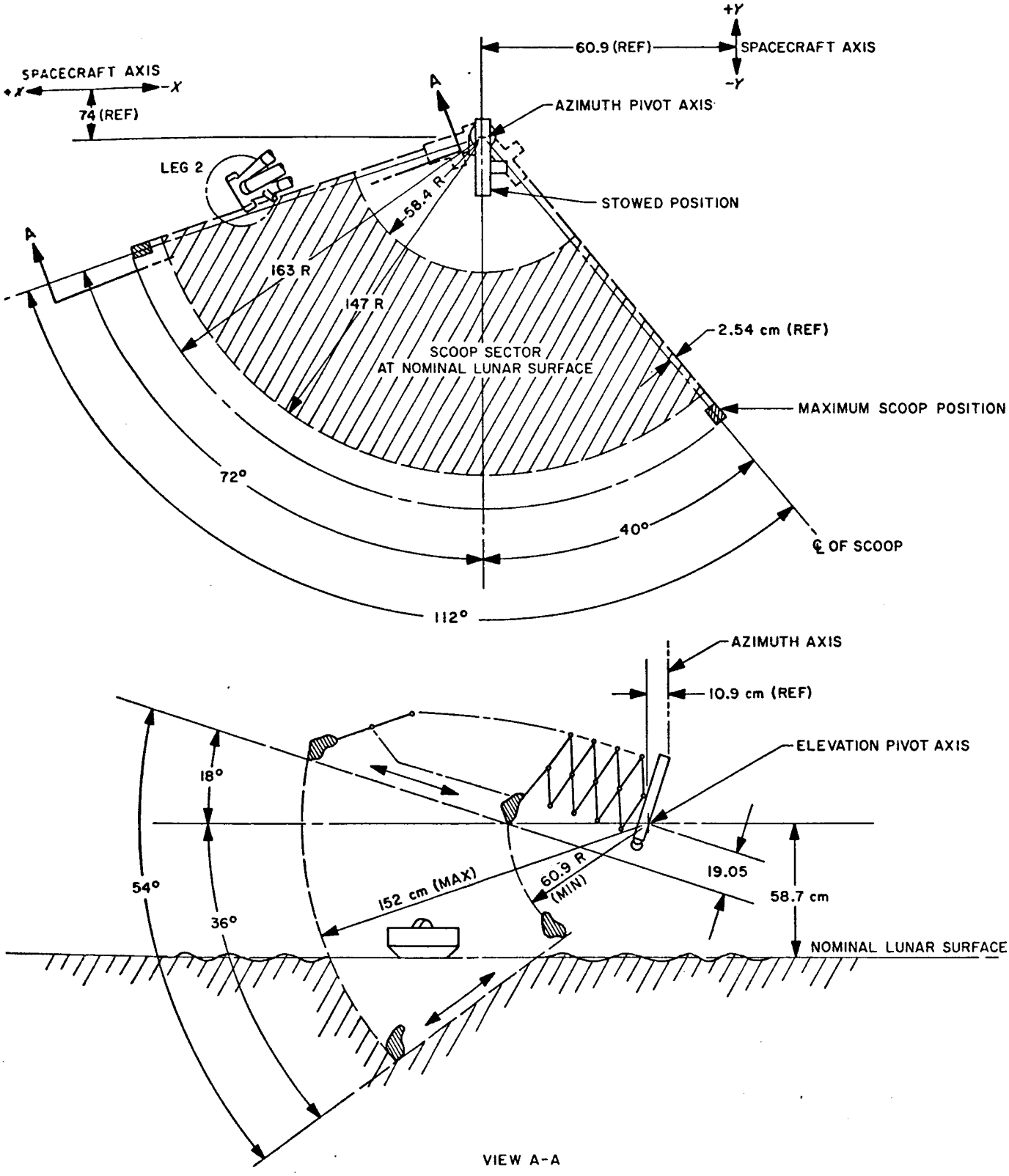

Fig. V-1. Space envelope of operation, SMSS mechanism

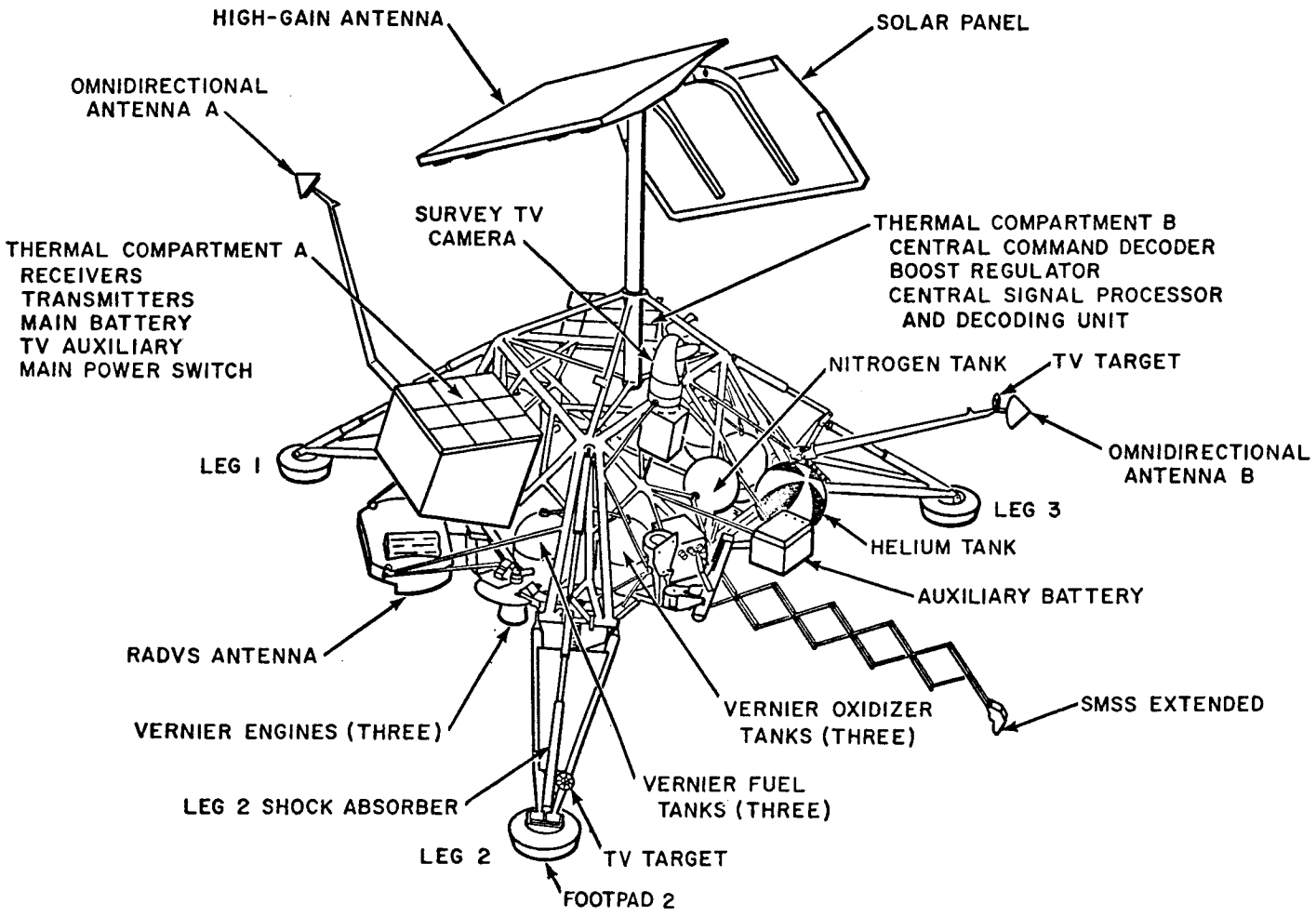

Fig. V-2. Surveyor spacecraft, showing SMSS mounted at approach camera location

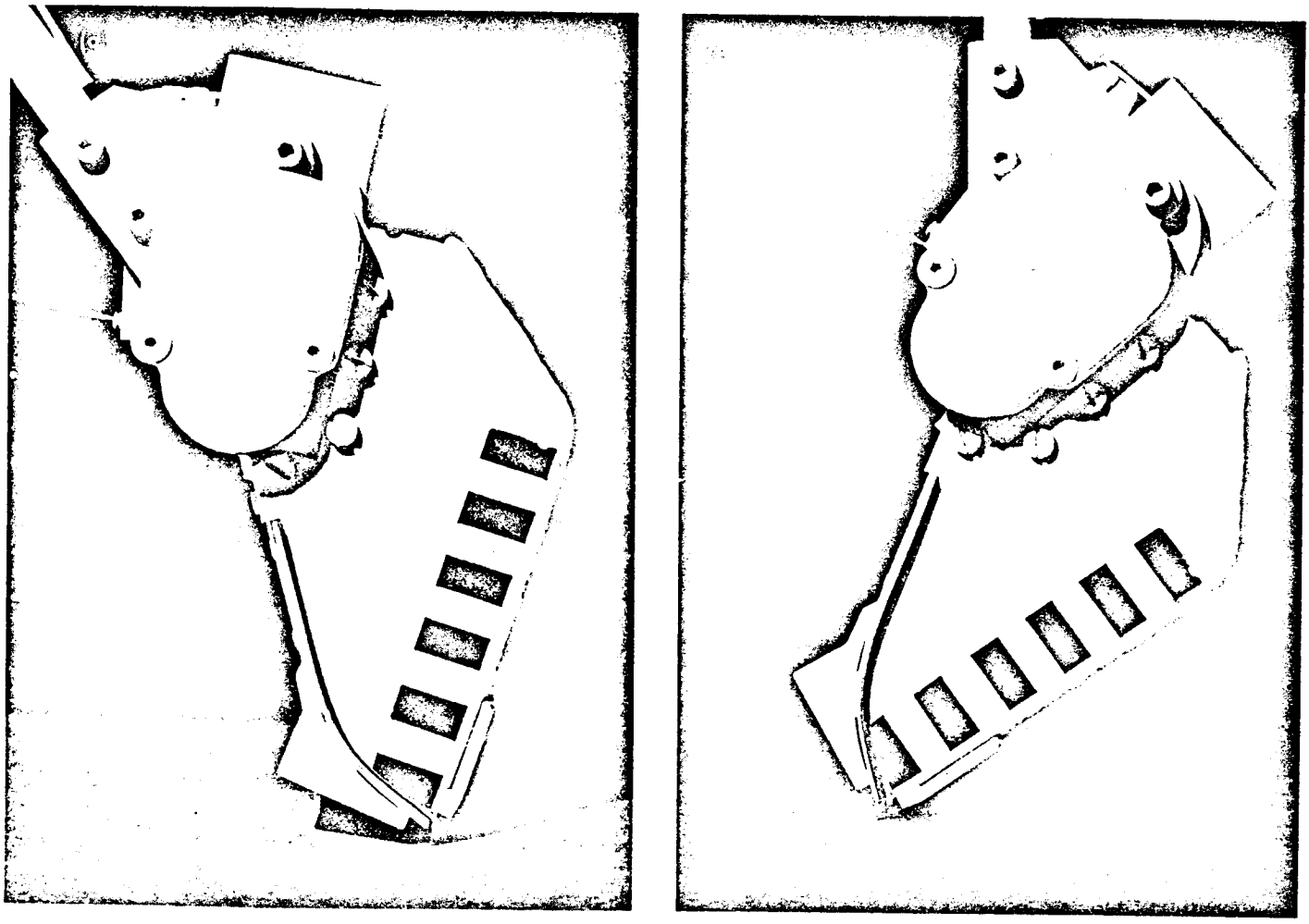

Fig. V-3. Photographs showing angle that SMSS scoop door makes with a nominal surface at (a) maximum extension distance and (b) minimum extension distance at which surface can be reached

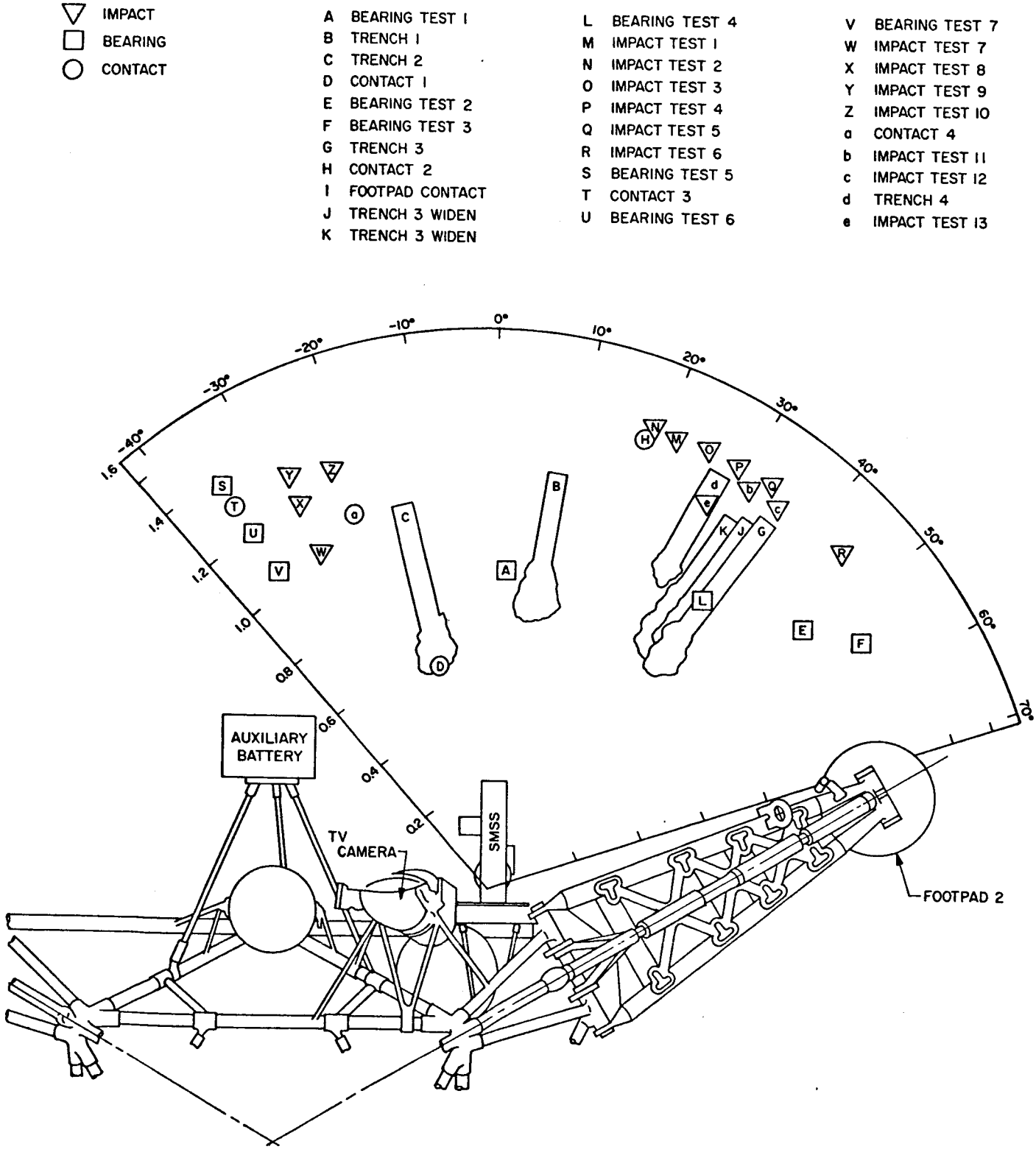

Fig. V-4. Plan view of SMSS area of operations, showing location of all surface tests performed during first lunar day of Surveyor III mission. Angles are referenced to SMSS axis in stowed position.

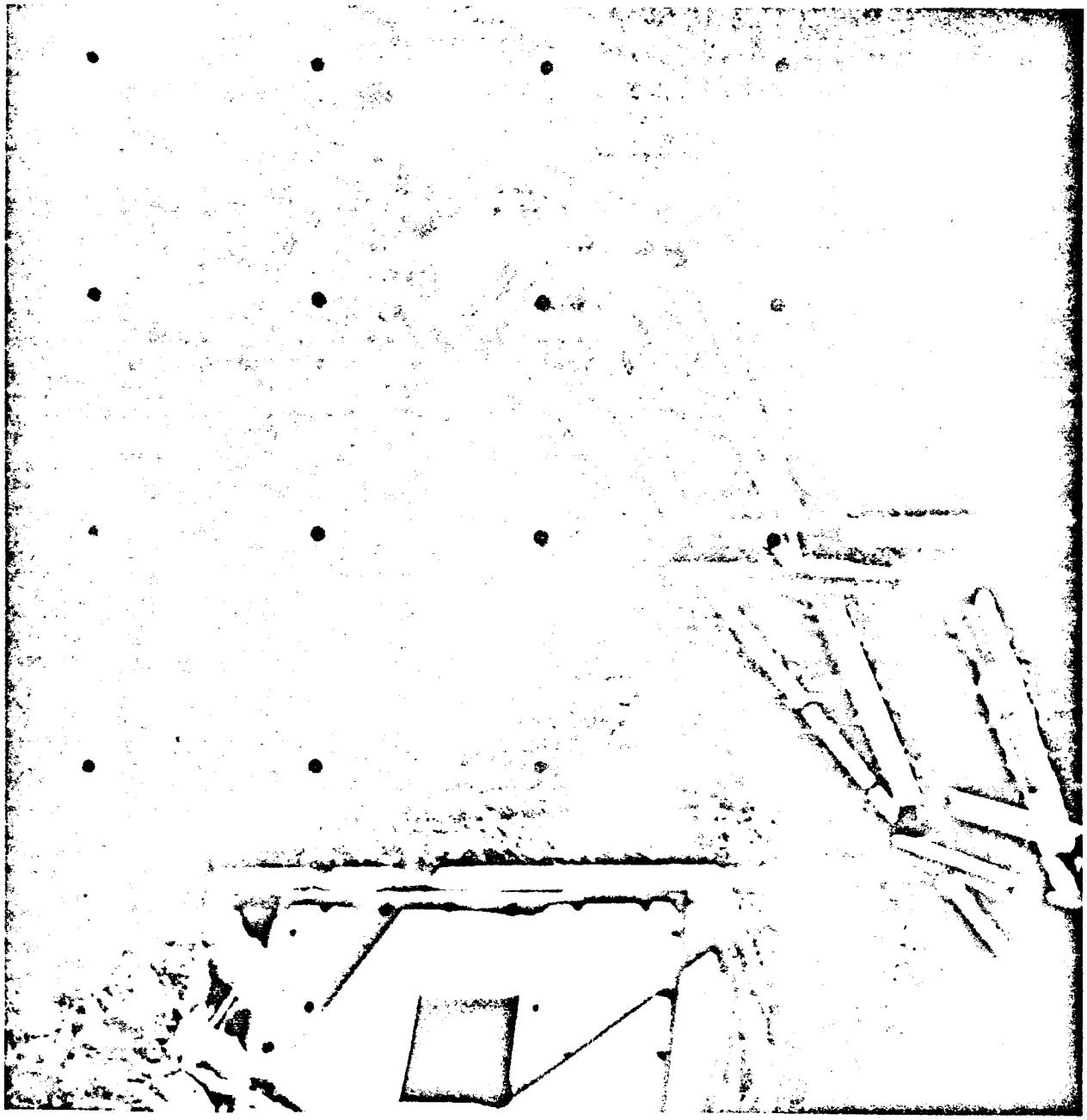

Fig. V-5. SMSS deployed and ready for bearing test as Goldstone view ended on Day 111 (Day 111, 10:43:30 GMT)

Fig. V-6. Final picture of SMSS at completion of operations for Day 112. Trench 1 is visible at right edge of photograph, and Trench 2 is directly below SMSS mechanism (Day 112, 11:34:29 GMT).

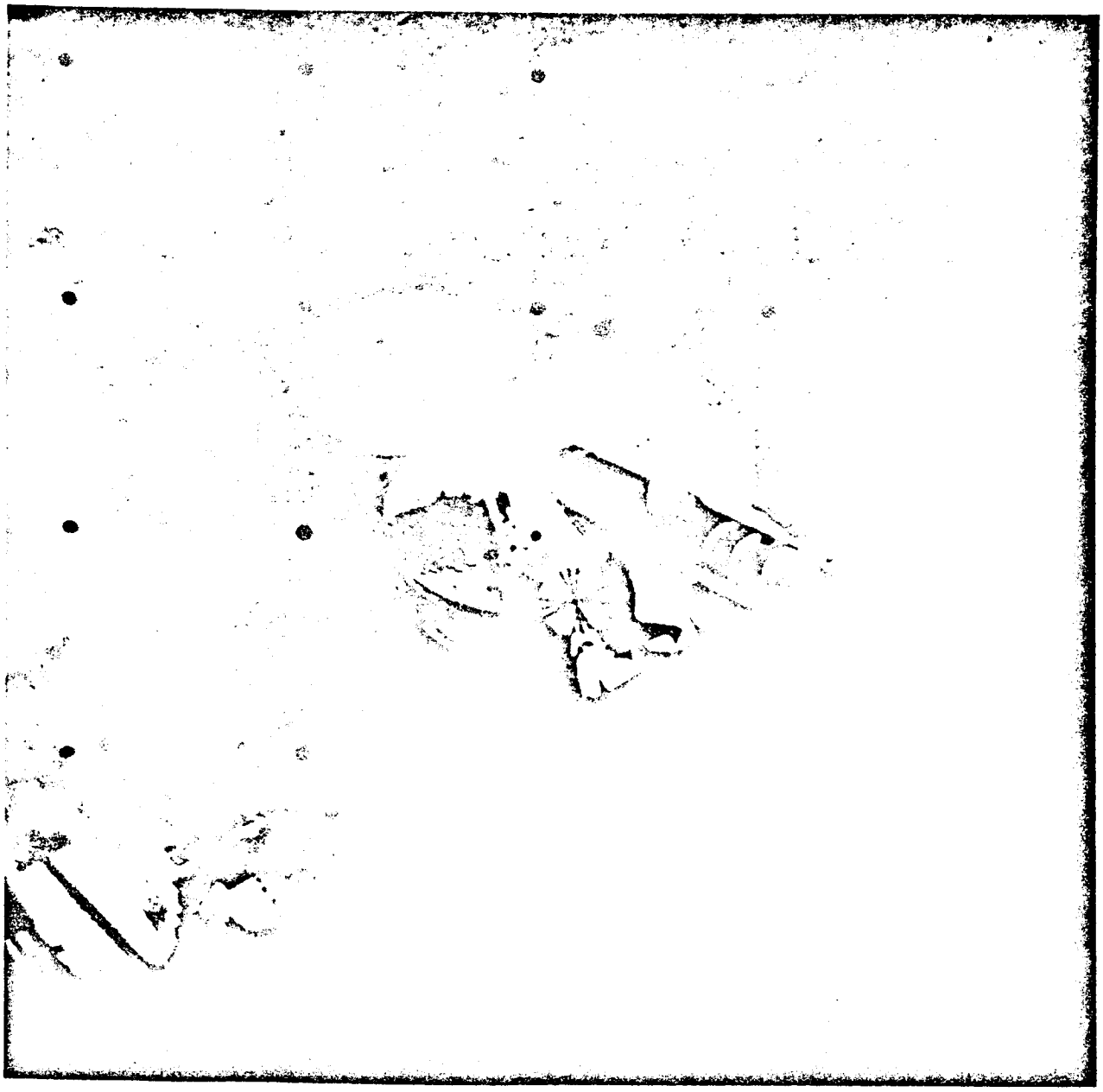

Fig. V-7. Wide-angle view of SMSS and footpad 2. Note pile of lunar surface material on top of footpad (Day 116, 11:53:26 GMT).

Fig. V-8. Material dumped on footpad 2 by SMSS. The color calibration chart is in foreground (Day 116, 12:00:54 GMT).

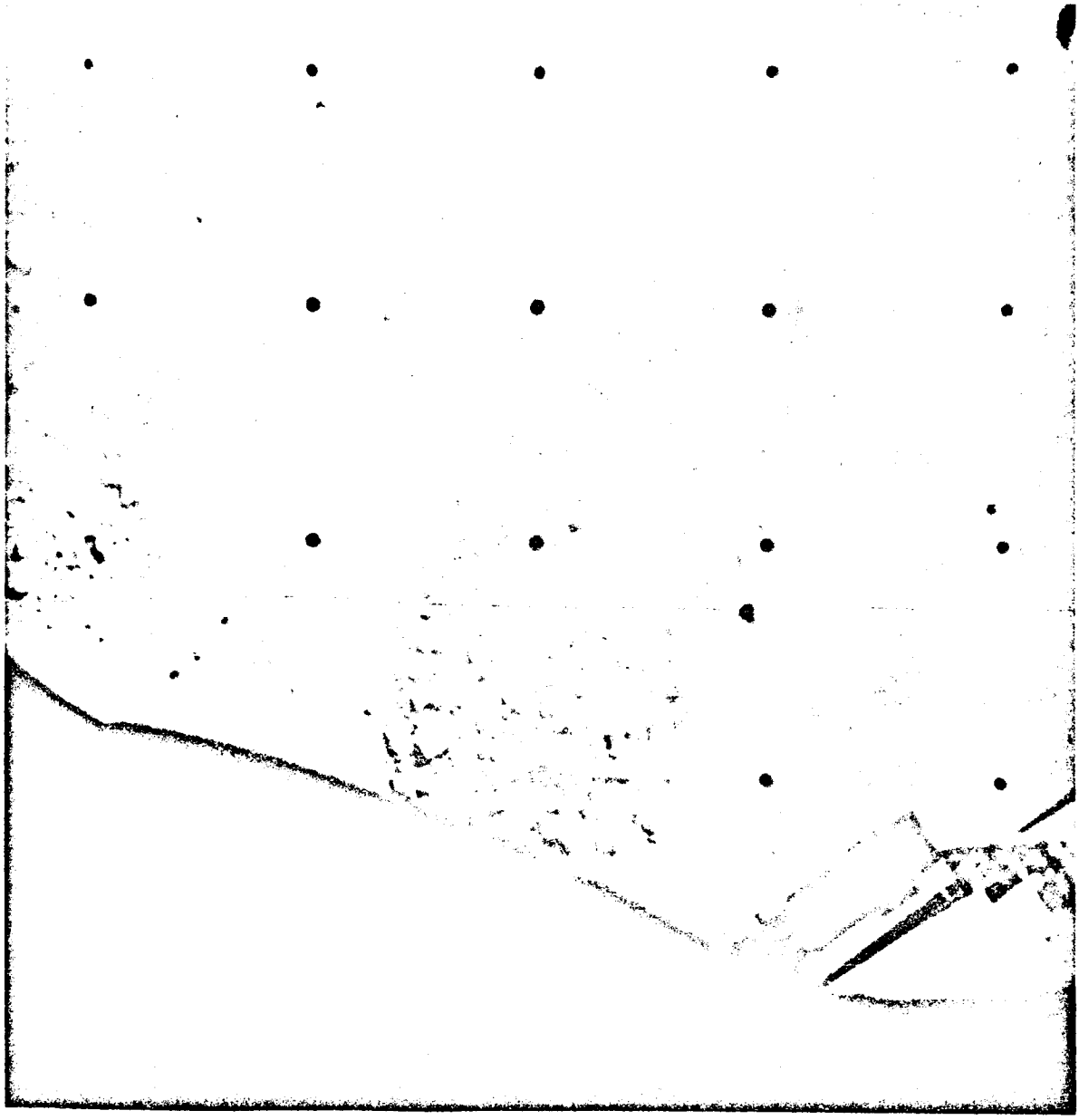

Fig. V-9. Wide-angle view of SMSS at end of Day 117 operations. Trench 3 and Bearing Test 2 are visible on the surface (Day 117, 10:34:53 GMT).

Fig. V-10. Trench 3, widened, with SMSS scoop poised and ready for Bearing Test 4 in trench bottom. SMSS appears blurred due to motion when picture was taken (Day 118, 13:21:33 GMT).

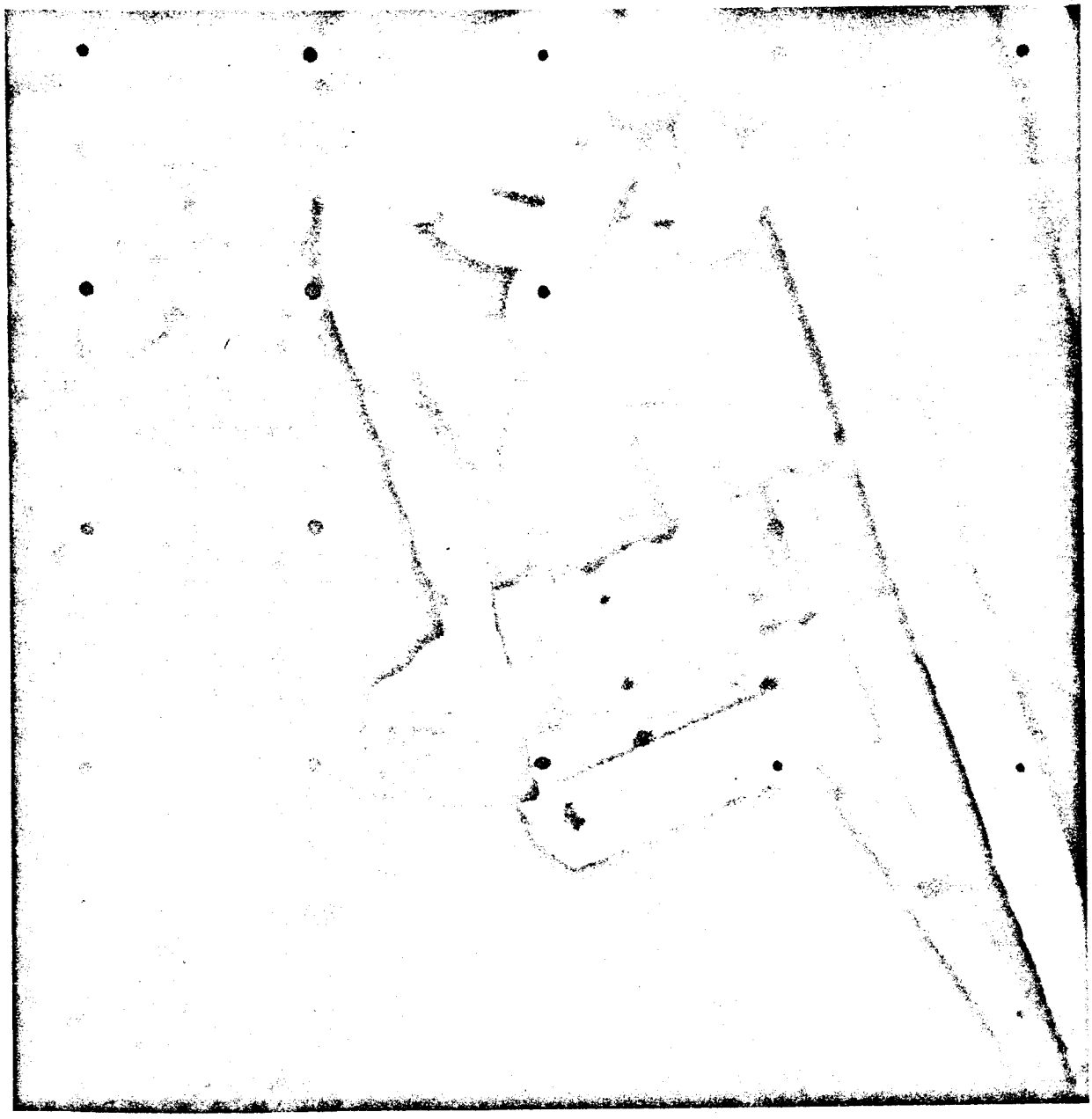

Fig. V-11. Close-up picture of "rock" extracted from lunar surface and being held by SMSS (Day 121, 15:18:39 GMT)

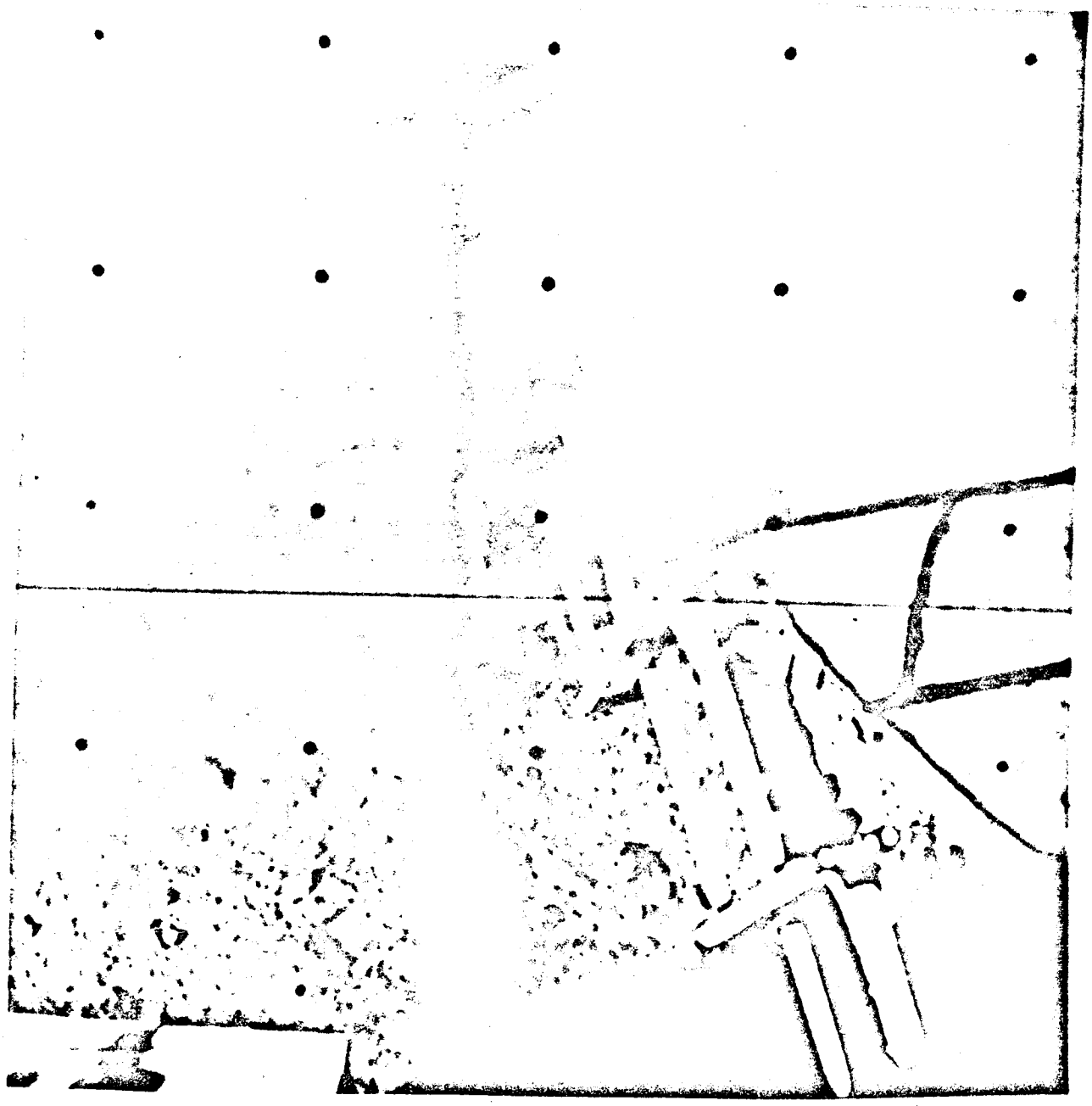

Fig. V-12. SMSS with small "rock" in scoop. Rock was picked up on Day 121. On the surface below, several bearing test points are visible (Day 121, 14:56:38 GMT).

Fig. V-13. Final position of SMSS at conclusion of lunar operations. Trench 4 and several impact points are visible on the lunar surface (Day 122, 14:20:11 GMT).

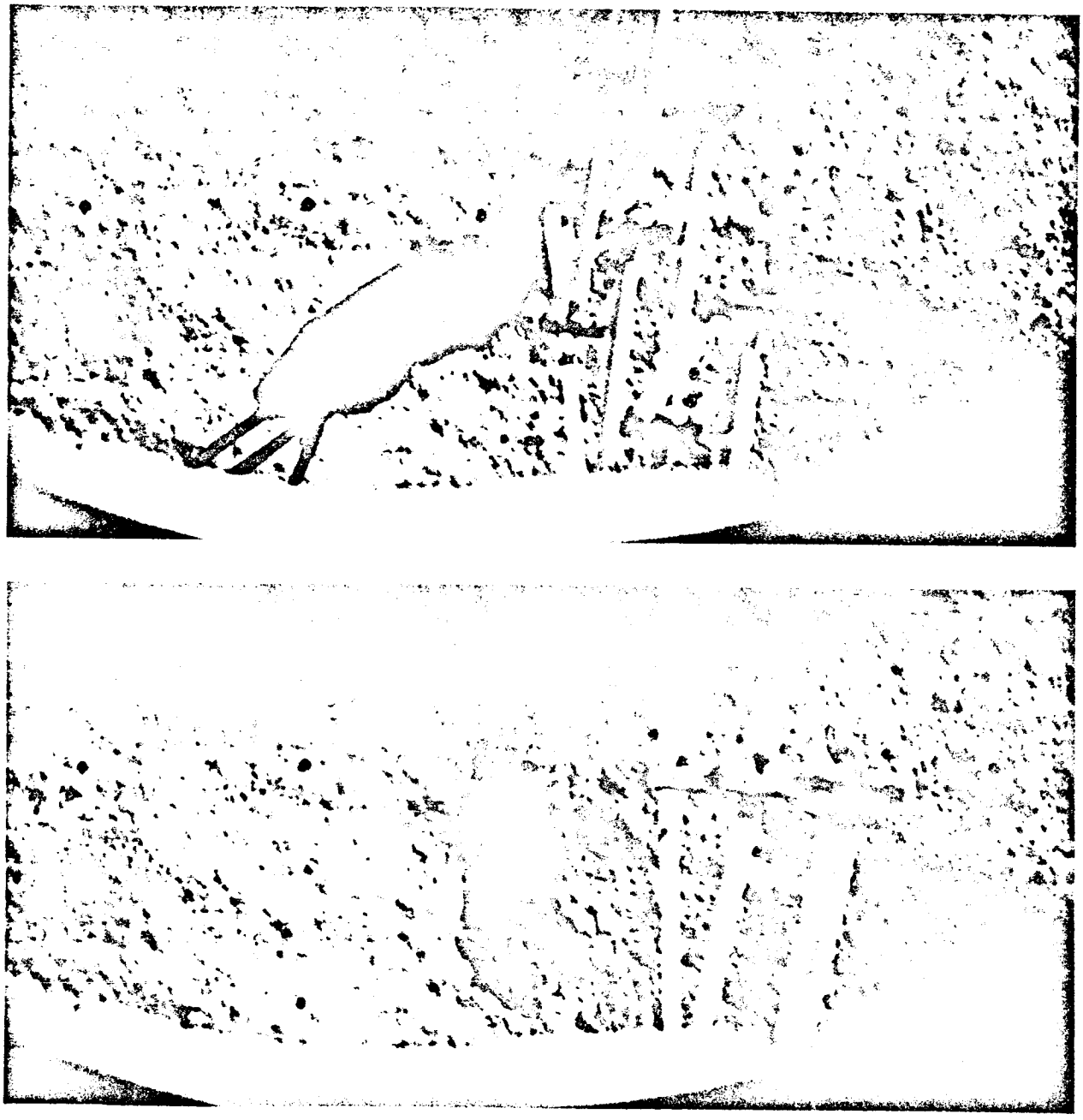

Fig. V-14. Photograph showing SMSS on Day 112 (a) before (05:07:01 GMT) and (b) after completion of first lunar surface bearing test (05:17:27 GMT)

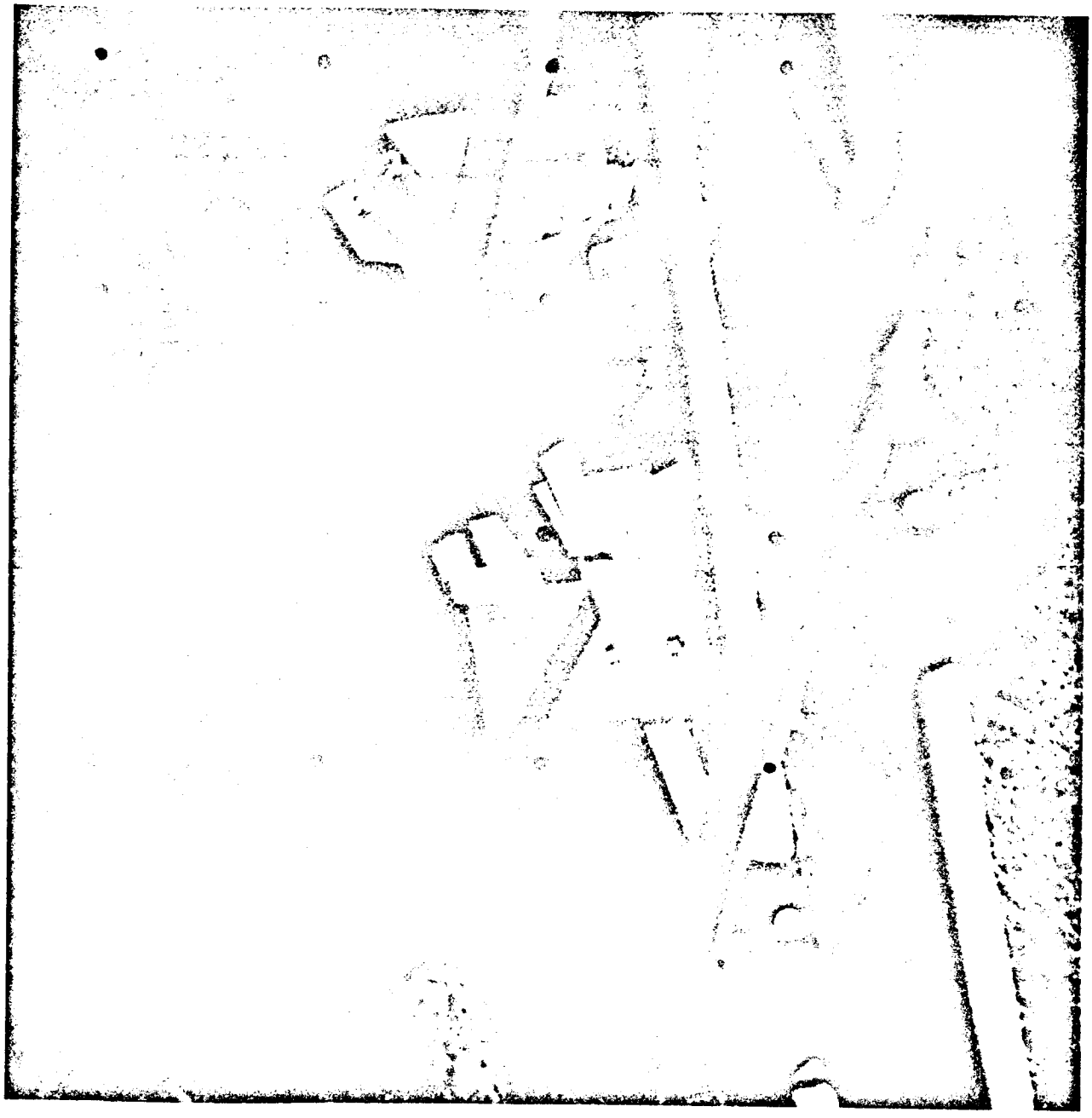

Fig. V-15. Second pass of sampler in Trench 2. Note material ahead of scoop as it is drawn toward spacecraft (bottom of picture) (Day 113, 07:22:04 GMT).

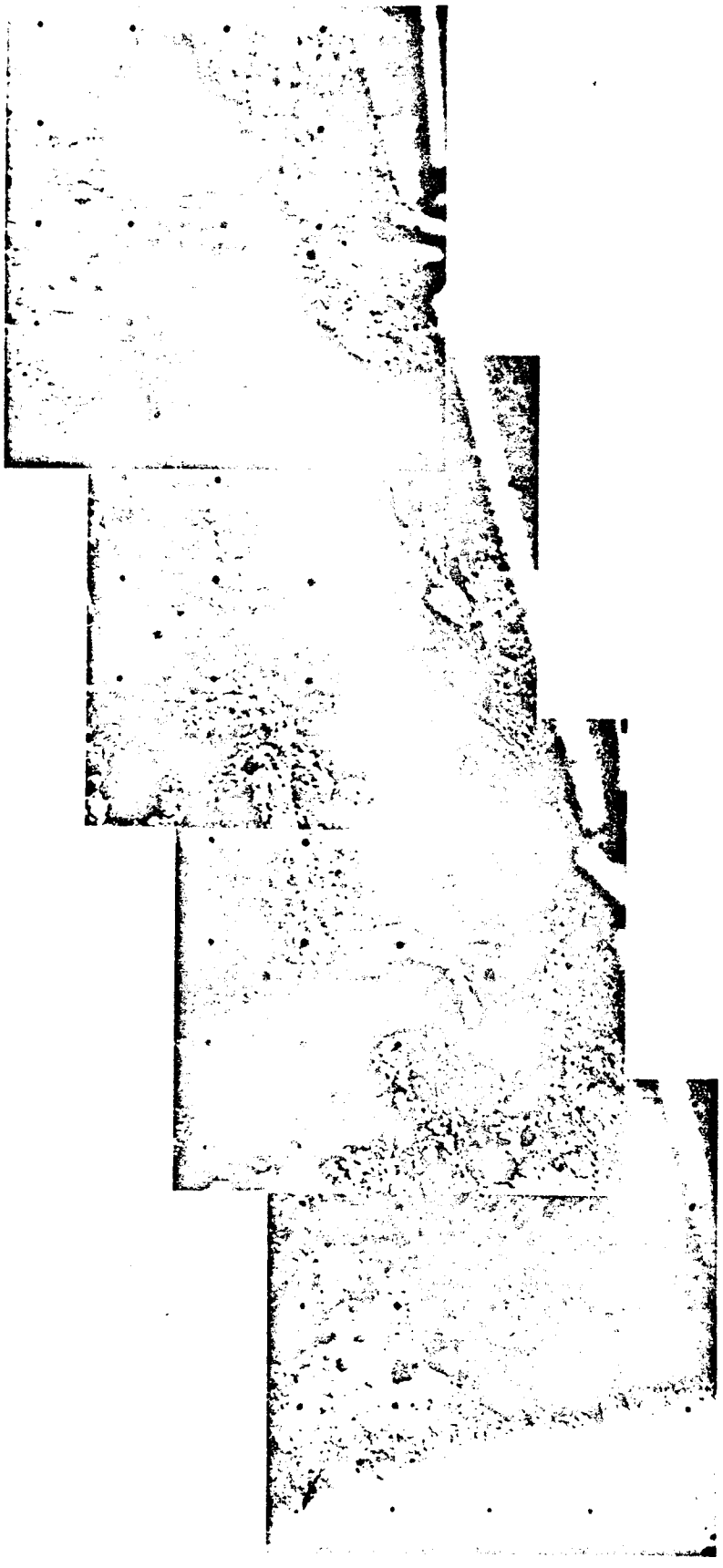

Fig. V-16. Mosaic of Trench 2 after sampler has been removed following stalling at far end, where material from scoop has been dumped (Day 113, Catalog No. 91 SI. 06:39:01, 06:40:05, 06:40:38, and 06:41:08 GMT)

Fig. V-17. SMSS scoop is shown embedded in the lunar soil following a drop from a height of about 30.5 cm in Impact Test 3. A previous SMSS impact impression is shown in top left corner of picture (Day 119, 09:49:45 GMT).

Fig. V-18. Sampler in position to begin picking up object. In moving sampler to this position, material from a trenching operation has fallen from scoop to leave a dark trail across the lunar surface. Bearing Tests 2 and 3 are seen to the right of the SMSS; Trench 3 is obscured by it (Day 118, 09:48:08 GMT).

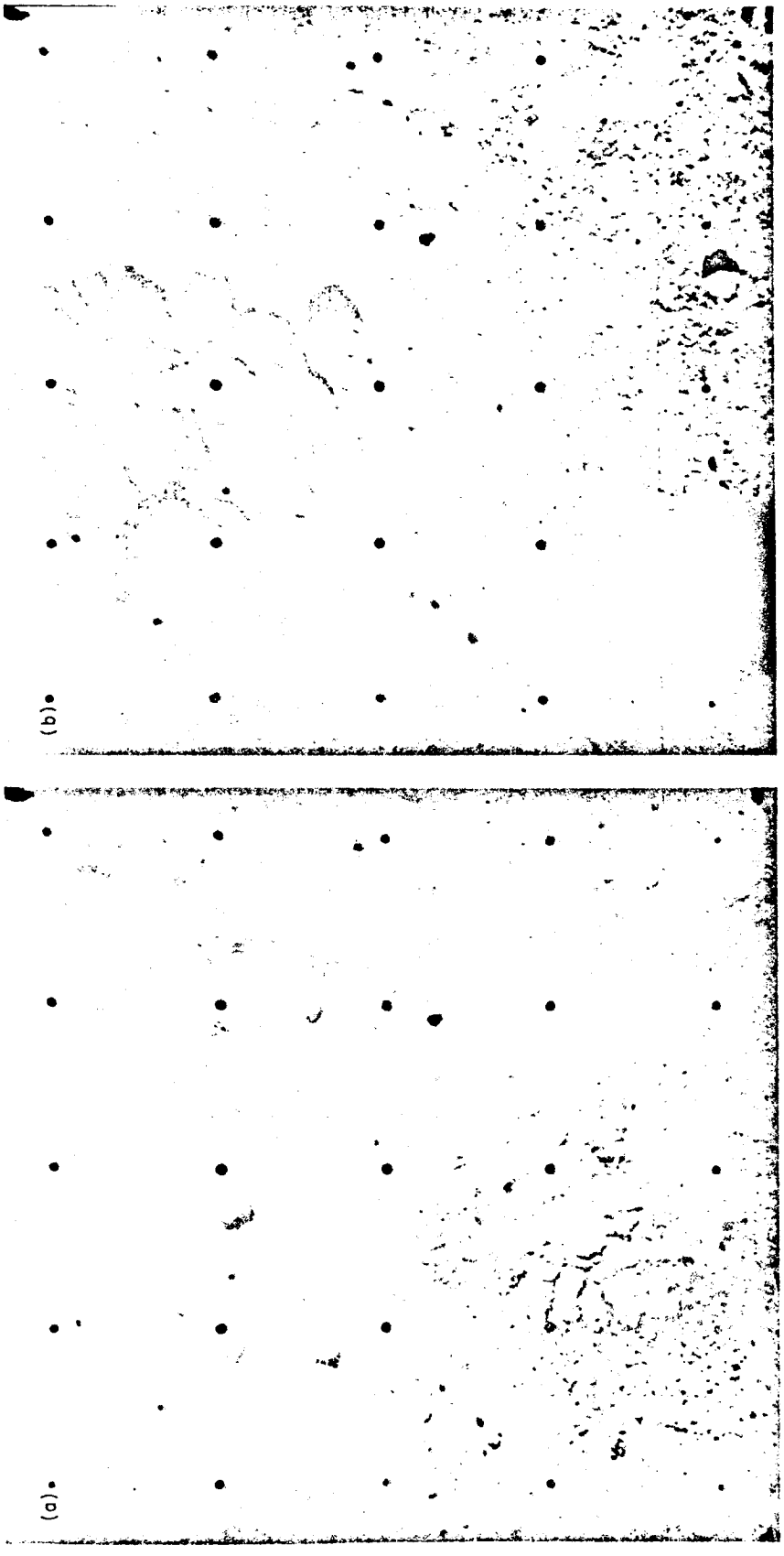

Fig. V-19. (a) Bearing Test 3 near footpad (Day 117, 09:30:12 GMT); (b) Bearing Test 5 near auxiliary battery (Day 120, 15:40:08 GMT). There is an obvious similarity in the imprints of these two tests, which are separated by a distance of several meters. Note small object below imprint in photograph (b).

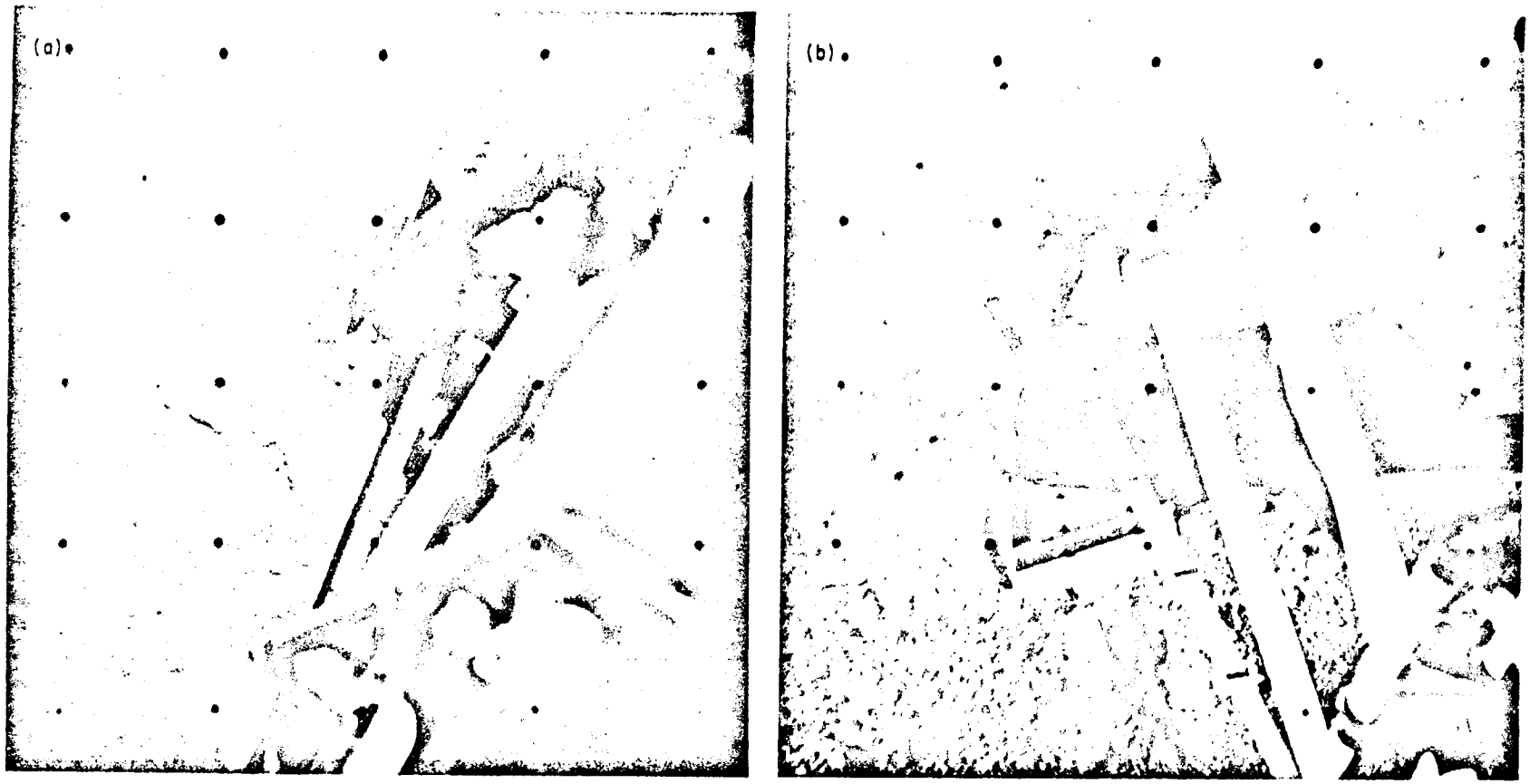

Fig. V-20. (a) Impact 4 from a height of about 60.9 cm near footpad 2 (Day 119, 10:08:29 GMT); (b) Impact 10 from a height of about 60.9 cm near auxiliary battery (Day 120, 16:41:30 GMT). There is a difference in the depths of penetration in these two tests.

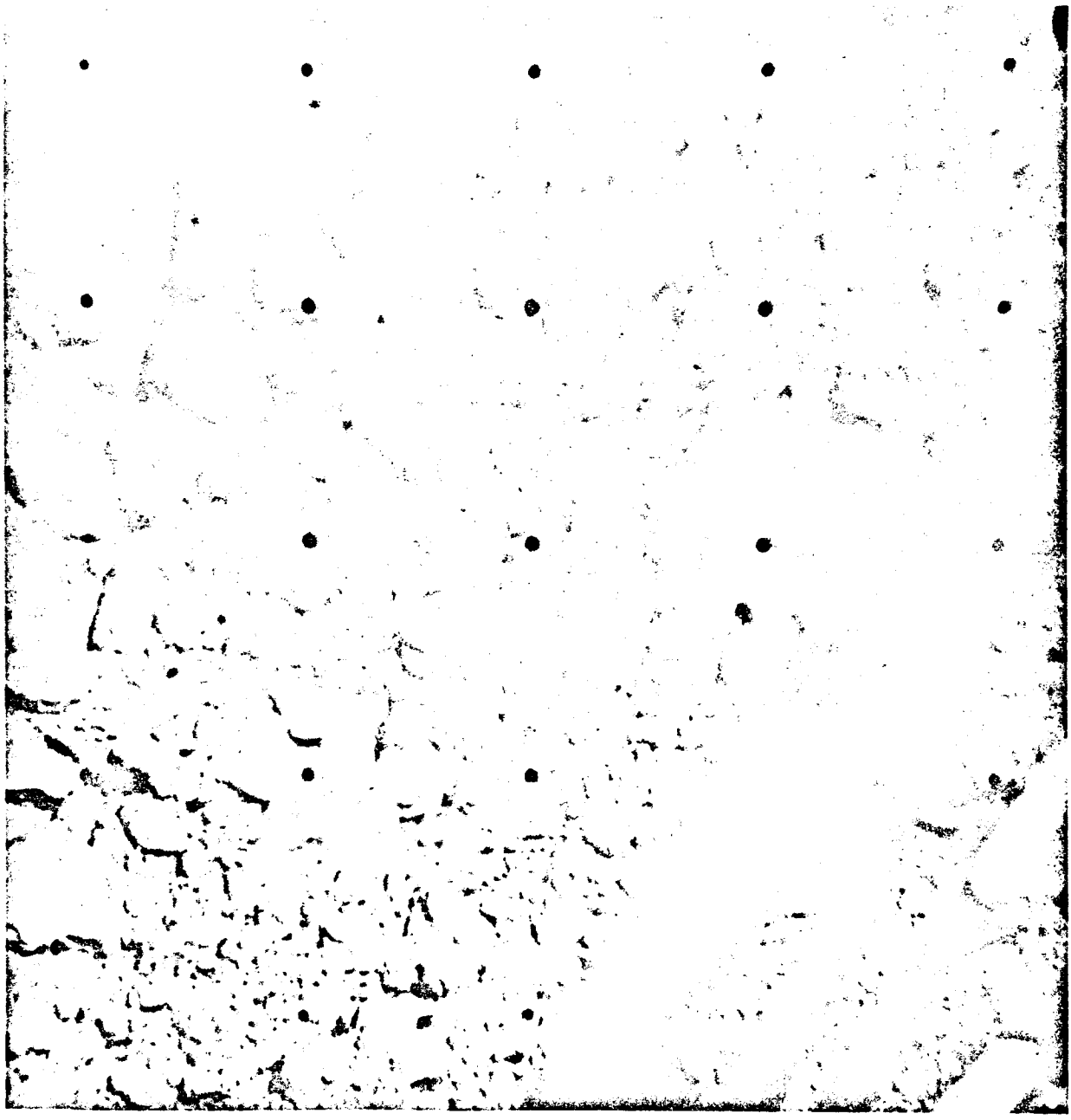

Fig. V-21. Bearing Test 4 impression in bottom of Trench 3 at a depth of 5.1 to 7.6 cm below lunar surface. Depth of impression estimated from shadow. Broken-up soil from trenching operation is visible (Day 118, 13:35:22 GMT).

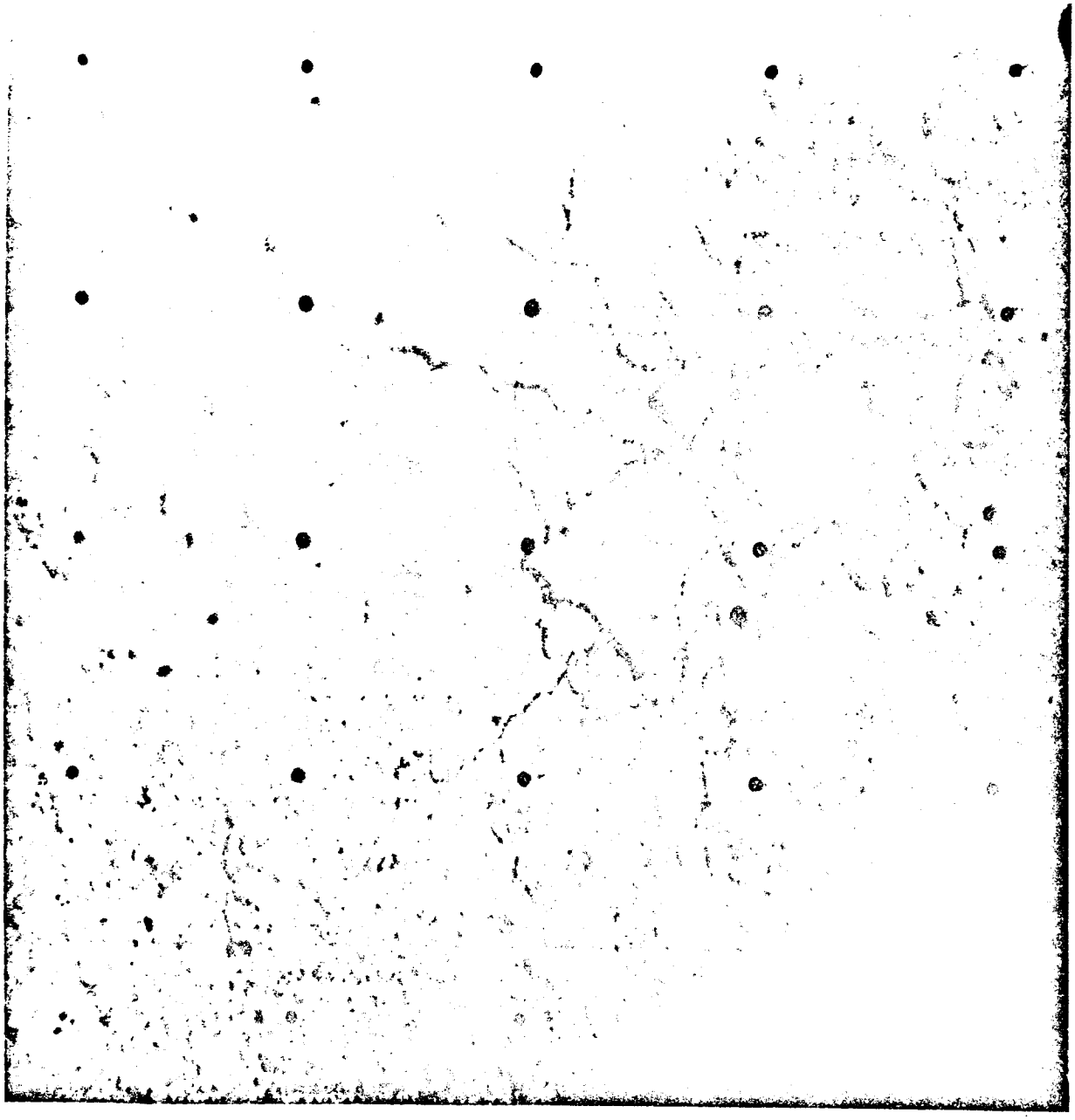

Fig. V-22. Imprint of Bearing Test 2 observed at high Sun. The cracks caused by the test and extending to the surface of the soil are clearly seen (Day 117, 08:56:45 GMT).

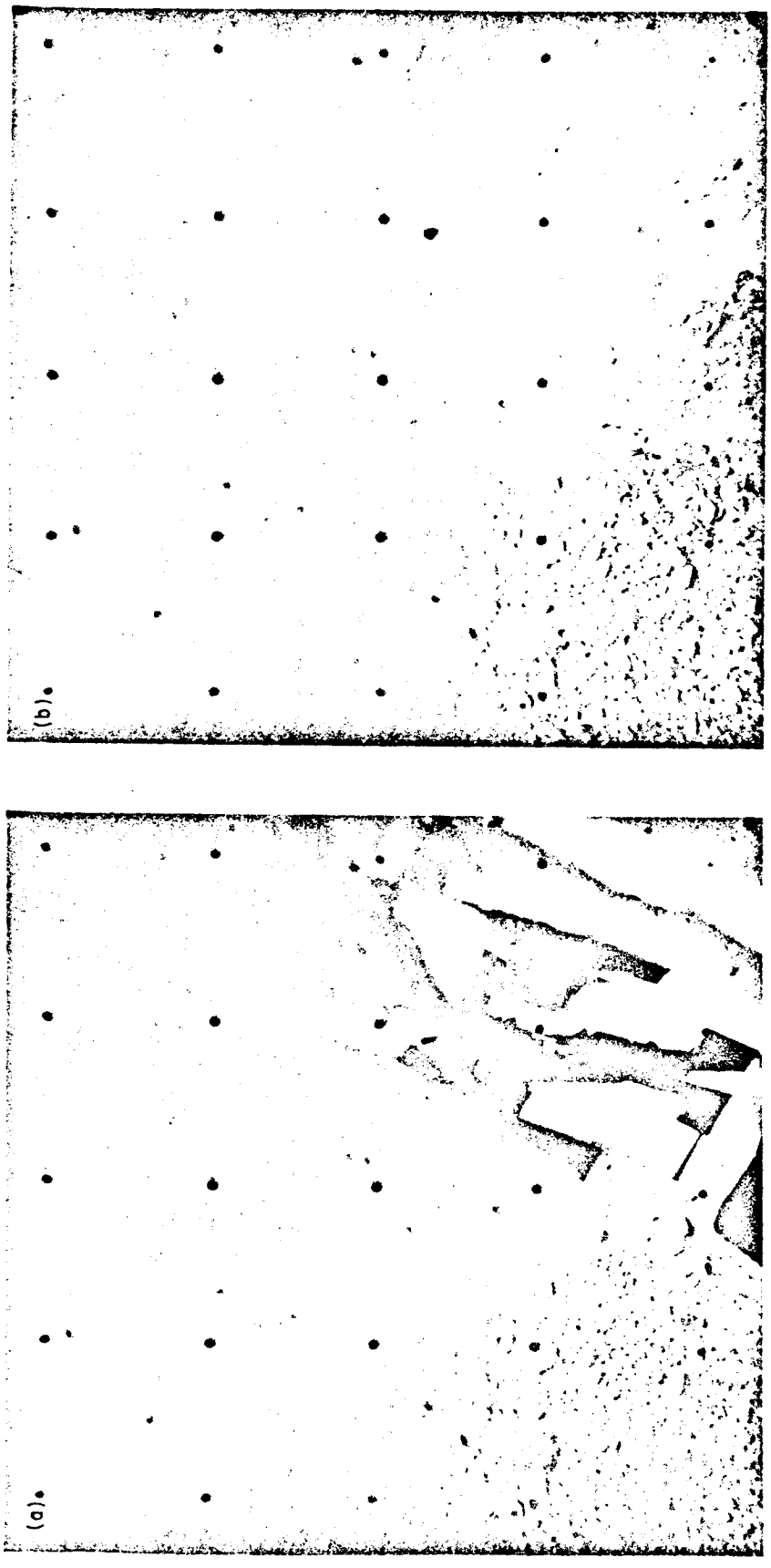

Fig. V-23. (a) SMSS approaching to pick up lighter object. Darker material in bottom left corner fell out of scoop in previous movement (Day 118, 10:20:10 GMT). (b) Surface after removal of object in (a) (Day 118, 10:49:08 GMT). The work of the SMSS is clearly seen. Also note that the lighter shade of the surface is lost in the very small disturbance made by the SMSS.

VI. LUNAR TEMPERATURES AND THERM[illegible] CHARACTERISTICS

J. W. Lucas, J. E. Conel, W. A. Hagemeyer, C. B. Jones,
J. M. Saari, and J. T. Wang

Data on lunar surface temperatures and thermophysical characteristics, and on spacecraft thermal performance on the lunar surface were provided by Surveyor III. This spacecraft carried no instrumentation, as such, to measure lunar surface temperature and was, like Surveyor I, designed to be thermally independent of its environment, both in flight and when landed. Following the Surveyor I analysis, outer canister temperatures of electronic Compartments A and B were used to estimate average brightness temperatures of portions of the surface viewed by the compartments.

The spacecraft landed at 00:04 GMT on Day 110 (April 20), 1967, at the coordinate 2.94°S latitude, 23.34°W longitude. Temperature data for Compartments A and B were obtained until 23:45 GMT on Day 130 (May 3) or about 2 hr after sunset at that longitude. Temperature records during the eclipse of Day 114 (April 24), which occurred between 09:48 and 14:06 GMT, were also obtained.

A. Thermophysical Properties of the Surveyor III Site as Determined From Earth-Based Data

Thermal measurements on the lunar surface were made from Surveyor III under three conditions: (1) during the day, (2) during the total eclipse of Day 114, and (3) until shortly after sunset. For comparison, results from Earth-based measurements are available for conditions (1) and (2) for the Surveyor III site.

During lunar daytime, the observed lunar surface temperature is dependent on Sun angle, surface albedo, and directional effects in infrared emission. The Sun angle can be calculated exactly for a level surface; however, because Surveyor III rests in a shallow crater, the temperature may be expected to vary from place to place in the depression due to variations in topography. The total solar albedo, i.e., the fraction of solar insolation reflected into space, is required for calculating daytime temperatures. This quantity may, in principle, be obtained by integration of the photometric function (scaled by the normal albedo) over a hemisphere, and with wavelength throughout the solar spectrum; a simpler method is to use the

simultaneous infrared and photometric scan data of Shorthill and Saari (Refs. VI-1 and VI-2). Of particular interest is the scan made over the full Moon (phase angle of -2°) just prior to the December 19, 1964, eclipse. For this scan, the change in brightness temperature with change in photometric brightness, B, has been studied. One can write

$$\sigma T_L^4 = (1-A)\, S \sin \psi \tag{1}$$

where σ is the Stefan-Boltzmann constant, T_L is the Lambertian temperature of the surface, A is the total solar albedo, S is the solar insolation, and ψ is the elevation angle of the Sun to the surface. For a full Moon scan, the observed brightness temperature, T_b, differs from the Lambertian temperature because of directional effects (discussed later) such that

$$T_b(\psi) = D(\psi)\ T_L \tag{2}$$

where $D(\psi)$, the directional factor, is defined by this equation. Assuming that the total solar albedo of a small element of surface is proportional to the full-Moon brightness of the same element, one can write

$$A = KB \tag{3}$$

where K is a constant to be determined. If measurements are made on two areas, 1 and 2, of differing albedo at the same ψ

$$\left.\begin{aligned} \left(\frac{T_{b,1}}{D(\psi)}\right)^4 &= (1 - KB_1)\, S \sin \psi \\ \text{and} \\ \left(\frac{T_{b,2}}{D(\psi)}\right)^4 &= (1 - KB_2)\, S \sin \psi \end{aligned}\right\} \tag{4}$$

Eliminating $D(\psi)$ between these two equations and solving for K,

$$K = \frac{T_{b,2}^4 - T_{b,1}^4}{B_1 T_{b,2}^4 - B_2 T_{b,1}^4} \tag{5}$$

Since K could possibly be a function of ψ, a large number of pairs of points of different brightness was measured over the disk; the results showed that k was independent of ψ. The photometric brightness of the Surveyor III site was measured on this full-Moon scan; multiplying by the constant K determined as above, gave a value of 7.6% of the total solar albedo. Since the telescopic measurements were made to a resolution of 10 sec of arc (18 km at the center of the lunar disk), the local albedo of the Surveyor III site may depart considerably from this value.

Predicted lunar surface (Lambertian) brightness temperatures, (shown in (Fig. VI-1), were computed using the program described in Ref. VI-3 for an equatorial site and several different values of the thermal parameter. The thermal parameter, gamma, equals $(k\rho c)^{-1/2}$, where k is thermal conductivity, ρ is density, and c is specific heat. The total solar albedo was taken equal to 0.076. Note that, during the day, surfaces with a gamma greater than 500 have essentially the same temperatures.

Thermal measurements were made with Surveyor III during the Day 114 total eclipse. Figure VI-2 shows a predicted eclipse cooling curve for the site based on measurements obtained by Saari and Shorthill (Refs. VI-4 and VI-5) during the December 19, 1964, eclipse. By assuming that directional effects persist during totality to the same degree as observed just prior to the start of the eclipse, it was possible to infer from the telescopic data a value for gamma of 1420 (cgs units) using the theoretical eclipse cooling curves for a homogeneous model (Ref. VI-6). This is close to a value of 1350 obtained in the same manner for the Surveyor I site. Values of gamma in this range are representative of the highly insulating material that characterizes much of the lunar surface. The warming curve in Fig. VI-2 represents calculated equilibrium surface temperatures corresponding to the insolation at each time.

Infrared measurements made during the December 19, 1964, eclipse showed that the lunar surface exhibits a great deal of thermal inhomogeneity (Ref. VI-4). Because extensive spatial temperature fluctuations were found on features as small

as 4 km, it would not be surprising if they would exist to a scale comparable to that of the Surveyor III site. Thus, the thermal characteristics of this site may be considerably different than observed from Earth with a resolution of 18 km. Isothermal contours of the Surveyor III site obtained during totality of that eclipse are shown in Fig. VI-3. The region is relatively bland; the nearest hot spot is associated with Fra Mauro C at about 21.6°W and 5.4°S. A very mild enhancement is noted closer to the site at 24° W and 3.5°S.

B Directional Effects of Lunar Infrared Emission

It has been determined (Ref. VI-7) that, when the lunar surface is illuminated by the Sun, the observed brightness temperature is not constant for different angles of observation; i.e., the surface does not behave like a Lambertian surface. This effect, ascribed to surface roughness, causes the brightness temperature to be higher when the phase angle is small (i.e., when the Sun-surface-compartment angle is small) than when it is large. Qualitatively, the emission is greater in the direction of the Sun. It is clear that such directionality will have an effect on the radiation received by the compartments on Surveyor.

To correct for directional effects, measurements from over the lunar disk for three Sun angles were used. For a Sun elevation angle of 90°, we take the measurements of Sinton (Ref. VI-8, p. 409), which give the variation in radiance from the subsolar point as a function of the elevation angle of the compartment.

For the two other Sun angles of 30 and 60°, the infrared scan data for different phases made by Shorthill and Saari were used. For these scans, each made at a different phase angle, the brightness temperature was determined at points where the Sun elevation angle was 30 and 60° (Ref. VI-7) and every 10° in thermal longitude. (With reference to a latitude/longitude system where the subsolar point is the north pole and the terminator the equator, thermal longitude is measured from the great circle passing through the subsolar point and the disk center.) Albedo corrections for each point were made from the full-Moon photometric data. The directional factor was calculated from Eq. (2) using calculated values of Lambertian temperatures at each point.

Directional factors obtained in this manner were referenced to a local coordinate system with azimuth and elevation angles for the direction of observation defined as follows. Azimuth angles are measured from the normal projection of the

Sun direction onto the surface. Elevation angles are measured from the surface in the plane of observation. Directional factors obtained over the globe were referenced to this azimuth/elevation angle system. A least-squares spherical harmonic fit, symmetrical with respect to plus and minus azimuth angles, was then computed for the data. A contour plot of the directional factor for a Sun elevation angle of 60° is shown in Fig. VI-4. The spherical harmonic fit was then used to compute the directional factor for elements of the scene viewed by the compartments for the calculation of an effective Lambertian temperature. Directional factors were, of necessity, obtained from global measurements made on a variety of features. It is possible, therefore, that a small area such as the Surveyor III site could have different directional effects than the "average" surface if local roughness or surface configuration differed significantly from the average.

C. Spacecraft View of Lunar Scene

The assumed orientation of Surveyor III with respect to lunar coordinates is given in Fig. VI-5. The azimuth of leg 1, the Y axis, is given as 46.1° southwest (S46.1°W); the -Z axis is taken to be tilted 12.4° from vertical in an azimuth direction of 6.4° northwest (N83.6°W). The normal to the Compartment A outer canister face lies in a vertical plane of azimuth 9° southeast (S9°E) and is inclined at an angle of 65° to local vertical. The normal to the Compartment B outer canister face has an azimuth 16° northwest (N74°W) and is inclined at an angle of 81° to local vertical. If the spacecraft -Z axis approximates the direction of the local surface normal, both compartment normals are inclined at 69° to this direction.

The landing site of Surveyor III (about 45 m southeast of the crater center) is depicted in Fig. VI-6. The general sectors of lunar surface viewed by each compartment are indicated. Compartment A views a scene to the southeast of the spacecraft where the horizon is -5 to +12° (with an approximate average of 0°) above a flat Moon from a level spacecraft (Fig. VI-7). Compartment B looks generally to the northwest, where the horizon is 2 to 12° (with an approximate average of 11°) above the horizontal. The portions of surface viewed by both compartments overlap in a 65° sector looking southwest.

The surface area viewed on each compartment is limited by the canister face orientation and crater rim. On this basis, Compartment A views a maximum projected surface area of 1.3×10^4 m^2, and Compartment B an area of 2.6×10^4 m^2.

In Fig. VI-6, the region enclosed by a dotted line is either totally or partially obscured by the spacecraft structure in television coverage of the surface. Detailed descriptions of observable portions are given in Section VII.

D. Spacecraft Description

For the purposes of this preliminary report, the description of Surveyor I given in Ref. VI-9 applies because, from a thermal standpoint, Surveyors I and III were essentially identical at launch. As with Surveyor I, the telemetered temperatures of the center of the outboard face of Compartments A and B (Fig. VI-8) are used to compute lunar surface temperature.

E. Spacecraft Raw Data

The following environmental parameters and spacecraft thermal properties are significant to compute lunar surface temperatures by the methods used:

(1) Spacecraft landing site: 2.94°S latitude, 23.34°W longitude.

(2) Angle between normal to outboard face and -Z axis: 68° 30' ±30" for Compartment A; 68° 40' ±30' for Compartment B.

(3) Compartment canister properties

  (a) Infrared hemispherical emittance: $\varepsilon = 0.87 \pm 0.02$.

  (b) Solar normal absorptance: $\alpha_S = 0.20 \pm 0.02$.

(4) Temperature data accuracy: further engineering analysis of telemetry data is necessary because of nonstandard behavior of the spacecraft data system.

The angle between a normal to the canister outboard face and the direction of the Sun is presented in Figs. VI-9 and VI-10. It should be noted that, for the computations shown, the Sun was assumed to move in a plane passing through the landing site and tilted 3° to the north.

Representative raw temperature data for the lunation are plotted in Figs. VI-11 and VI-12. Expanded temperature data for the eclipse are plotted in Figs. VI-13 and VI-14. All data given has been corrected on the basis of preliminary calibration curves furnished by Hughes Aircraft Co., El Segundo, Calif.

F. Shading Effects on Compartments

On Day 116 (April 26) stepwise solar panel and planar array positioning maneuvers were conducted to determine the effects of shading on Compartment B temperature measurements (Fig. VI-15). Conduction heat transfer effects between elements of the compartment canister, as well as radiation heat transfer between the canister and the RADVS antenna, were obtained from differentially shading these elements.

The solar panel and planar array positioning sequence was performed on Day 116 (April 26), as listed below:

Phase	Time (GMT)	Experiment
I	04:03 to 04:23	Unshade RADVS, face and top of Compartment B
	04:23 to 12:18	Hold
II	12:18 to 12:55	Shade RADVS, face and top of Compartment B [Fig. VI-15(c)]
	12:55 to 14:00	Hold
III	14:00 to 14:30	Unshade RADVS [Fig. VI-15(b)]
	14:30 to 16:00	Hold
IV	16:00 to 16:10	Unshade face of Compartment B [Fig. VI-15(a)]
	16:10 to 18:00	Hold
V	18:00 to 18:07	Unshade top of Compartment B
	18:07 to 20:00	Hold

1. Experimental Results

Results of the thermal experiment are shown in Fig. VI-16. Initial temperature, with Compartment B and RADVS antennas unshaded (Phase I), was found to be 324°K (124°F). Shading Compartment B and RADVS antennas (Phase II) introduced a ΔT of -6.7°K (-12°F). Unshading the RADVS (Phase III) raised the Compartment B temperature 0.6°K (1.0°F). The rise in the curve between C and D is accounted for by a temporary unshading of the Compartment B outboard face during the positioning maneuvers necessary to unshade only the RADVS antennas. Unshading the compartment outboard face (Phase IV) introduced a ΔT of 6.1°K (11°F).

Unshading the top of Compartment B (Phase V) resulted in a ΔT of 0.8°K (1.5°F) in the canister sensor temperature. The 1.7°K (3°F) increase in base temperature (unshaded) from Point A, beginning of shading, to 20:00 GMT end of experiment, is due to the greater Sun angle incident to the canister outboard face at the end of the experiment.

The thermal experiment provided excellent data for evaluating shading effects on the spacecraft thermal compartments. The measured temperatures indicate that heat transfer effects between the center of the outer face of the compartments and other elements of the spacecraft are negligible. The observed changes in temperature agreed very well with predictions, although the absolute temperatures predicted were slightly lower (Fig. VI-16). Since the predictions were based on preliminary calculations as to spacecraft orientation, these differences in absolute temperatures are not felt to be significant. Because of the excellent data received for Compartment B, it was decided not to duplicate the experiment with Compartment A.

G. Lambertian Lunar Surface Temperature Calculations

Calculations were performed using the following equation [taken from Ref. VI-9, Eq. (2)].

$$\sigma T_2^4 = \frac{\sigma T_1^4}{\varepsilon_2 (F_{12} - F_{13})} - \frac{F_{13}}{F_{12} - F_{13}} \sigma T_3^4 - \frac{\alpha_1 S^S}{\varepsilon_1 \varepsilon_2 (F_{12} - F_{13})}$$

$$\times \left[(F_{12} - F_{13}) \rho_2 \sin \phi + \cos \beta \right] - \frac{\dot{q}}{\varepsilon_1 \varepsilon_2 (F_{12} - F_{13})} \qquad (6)$$

where

T_1 = compartment surface temperature

T_2 = lunar surface brightness temperature

T_3 = lunar surface brightness temperature in shadow, $T_3^4 \ll T_2^4$ is assumed

S = 1386 w/m^2(440 Btu/ft^2-hr)

F_{12} = geometric view factor from 1 to 2

= 0.31 for Compartment A for 0° horizon (Sect. VI-C of this report)

= 0.41 for Compartment B for 11° horizon (Sect. VI-C of this report)

F_{13} = geometric view factor from 1 to 3

$\dot{q}$ = conduction heat flux between inside and outside of compartment wall

= 3.5 w/m^2

σ = Stefan-Boltzmann constant

= 5.675 x 10^{-8} w/m^2 °K^4 (1.713 x 10^{-9} Btu/ft^2-hr °F^4)

ϵ_1 = compartment surface emittance

= 0.87 ±0.02

ϵ_2 = lunar surface emittance

= 1.0

α_{1S} = compartment surface solar absorptance

= 0.20 ±0.02

β = angle between direction of Sun and normal to compartment surface, from Figs. VI-9 and VI-10

$\emptyset$ = Sun angle (between lunar surface and direction of Sun)

ρ_2 ≡ A = 0.076 = lunar reflectivity to solar irradiations

The view factor F_{13} from Compartment B is plotted in Fig. VI-17; F_{13} from Compartment A is negligible.

Figure VI-18 represents the lunar surface brightness temperature for the lunar day as calculated using Eq. (6) from Compartment A and Compartment B telemetered temperatures. It is suggested that Compartment B indicates a higher lunar surface temperature early in the day than Compartment A because Compartment B senses (1) a higher lunar surface temperature on the western portion of the crater due to relatively greater Sun elevation angle there and (2) a higher directional lunar surface temperature at that time, since Compartment B views the lunar surface more directly along the Sun line direction. In the afternoon, the reverse is true.

In Figs. VI-19 and VI-20, lunar surface temperatures indicated by Compartments A and B are shown separately. Also shown are the computed curves

previously given in Fig. VI-1, but shifted to the right 10° in Sun angle to account for local lunar surface tilt toward the west at the Surveyor III landing site (see Sect. VII of this preliminary report). There is fair agreement in the morning, good agreement at noon and fair agreement in the afternoon with predicted Lambertian temperatures.

Lunar surface brightness temperatures derived from Compartment B data on Surveyors I and III are compared in Fig. VI-21. The curves are plotted for corresponding Sun angles, but with the Surveyor I curve shifted to the right by 10° for the reason given previously. The strong correspondence between the two curves shows that essentially identical lunar surface brightness temperatures were observed for Sun elevation angles above 30°. This is not surprising since a wide range of gamma values yield the same daytime temperatures. The correspondence indicates no thermally significant dust on either Surveyor I or III compartment faces.

Figure VI-22 represents the lunar surface temperature data indicated by Compartments A and B during the eclipse. Except for the initial portion of the first penumbral stage and the final portion of the second penumbral stage, both compartments sensed the same lunar surface temperatures during the eclipse. This indicates that (differing) directional lunar surface temperatures, which are sensed by the two compartments when under full illumination, are not present at low, as well as zero, insolation. Note also that both compartments sensed the same lunar surface temperature when communication with the spacecraft was terminated shortly after sunset (Figs. VI-19 and VI-20).

Also included in Fig. VI-22 is the predicted lunar surface temperature during the eclipse given in Fig. VI-2. The spacecraft sensed a lunar surface temperature that lagged and did not fall as low as predicted. Using eclipse cooling curves of Jaeger (Ref. VI-6), it is estimated that a lunar surface with an effective gamma of about 400 would exhibit the observed cooling curve. It was determined that the heat capacity of the compartment cover could contribute a negligible portion of the observed lag between compartment temperatures and expected lunar surface temperature.

It should be noted that the cause of the elevated cooling curve cannot be accounted for by a heat transfer cavity effect in the crater. A possible cavity effect was assessed using the curves in Ref. VI-10 and found to be negligible. If the crater were flattened, the observed cooling curve would remain.

H. Directional Lunar Surface Temperature Calculations

Surveyor III Compartment A and B outboard surface temperature profiles during lunar day were predicted on the basis of the Earth-based observed directional lunar surface temperature data described previously. The observed temperature of a specific area on the lunar surface is dependent on the Sun and elevation and azimuth angles of the observer (Fig. VI-23). When the azimuth angle is small, the compartment, looking into the Sun, sees higher temperatures; when the compartment looks against the Sun, lower temperatures are seen. In the mathematical model, 45 nodes were used. They were the compartment, the RADVS antennas, the cold space, the spacecraft shadow on the lunar surface and the sunlit lunar surface [Fig. VI-24(a)]. The lunar surface was divided into 41 nodes, each assumed to be flat and isothermal [Fig. VI-24(b)]. The JPL Thermal Analysis System computer program (Ref. VI-11) was used for the calculation. The spacecraft shadow on the lunar surface was neglected in this directional analysis.

The lunar surface form factors and associated directional temperatures (Tables VI-1 and VI-2) were computed for a horizontal, flat lunar surface with the spacecraft -Z axis tilted 0° toward the lunar surface for Compartment A and 11° toward the lunar surface for Compartment B.

Predicted compartment temperature profiles for Sun angles from 30 to 150° are plotted in Figs. VI-25 and VI-26. Comparison with the telemetered compartment temperatures indicates good agreement for both compartments between 30 and 90° Sun angles. During the lunar afternoon, both compartment temperatures are somewhat higher than predicted.

Also plotted in Figs. VI-25 and VI-26 are predicted compartment temperatures assuming increased solar absorptance, α_{1S}, values of 0.3 and 0.4. A value of approximately 0.35 brings Compartment B predicted and observed temperatures into reasonable agreement. However, this is not the case for Compartment A, which sees little Sun in the afternoon. This indicates that changing α_{1S} is not the explanation for the somewhat higher afternoon temperatures observed by both compartments.

Table VI-1. Compartment A directional temperatures[a]

Node	$F_{(1,x)}$ x(5→45)	Directional temperature, °F				
		ϕ = 30°	ϕ = 60°	ϕ = 90°	ϕ = 120°	ϕ = 150°
5	0.012	116	186	189	186	116
6	0.005	38	161	199	226	201
7	0.005	40	163	224	227	200
8	0.010	48	168	246	230	195
9	0.010	80	191	256	238	170
10	0.005	60	168	194	219	183
11	0.005	62	170	207	219	182
12	0.010	67	175	223	223	178
13	0.010	90	196	249	233	158
14	0.005	75	173	193	211	166
15	0.005	76	174	203	212	166
16	0.010	80	179	217	216	163
17	0.010	97	200	247	229	148
18	0.005	88	176	193	203	151
19	0.005	89	177	202	204	150
20	0.010	92	183	216	208	148
21	0.010	103	203	244	224	139
22	0.005	101	180	193	194	133
23	0.005	102	182	201	195	133
24	0.010	103	187	214	200	133
25	0.010	111	207	244	218	129
26	0.005	114	185	193	187	119
27	0.005	114	186	201	189	119
28	0.010	115	191	214	194	120
29	0.010	118	211	244	213	121
30	0.005	126	190	193	182	108
31	0.005	126	192	202	184	108
32	0.010	126	197	216	189	109
33	0.010	125	216	244	209	114
34	0.005	143	199	193	178	94
35	0.005	143	200	203	179	94
36	0.010	142	205	217	184	97
37	0.010	135	221	247	205	106
38	0.005	164	210	194	173	77
39	0.005	163	211	207	175	77
40	0.010	160	214	223	180	82
41	0.010	147	228	249	200	98
42	0.005	192	223	199	165	50
43	0.005	191	223	224	167	52
44	0.010	186	226	246	172	58
45	0.010	164	236	256	194	85

[a]Based on Ref. VI-8.

Table VI-2. Compartment B directional temperatures[a]

Node	$F_{(1,x)}$ x(5→45)	Directional temperature, °F				
		ϕ = 30°	ϕ = 60°	ϕ = 90°	ϕ = 120°	ϕ = 150°
5	0.005	116	186	180	186	116
6	0.005	143	199	194	178	94
7	0.000	142	202	210	182	96
8	0.001	139	212	233	193	101
9	0.003	129	228	255	216	113
10	0.005	163	209	194	173	78
11	0.005	161	212	210	177	81
12	0.004	154	220	233	189	89
13	0.003	135	232	255	212	109
14	0.010	186	220	194	167	57
15	0.010	183	222	210	171	61
16	0.011	173	229	233	183	74
17	0.010	143	236	255	208	104
18	0.014	200	226	194	162	40
19	0.016	196	228	210	166	46
20	0.016	185	233	233	178	62
21	0.015	148	238	255	205	101
22	0.015	202	226	194	161	37
23	0.018	198	228	210	165	43
24	0.019	186	234	233	177	60
25	0.019	149	239	255	205	100
26	0.015	193	223	194	165	49
27	0.018	189	225	210	169	54
28	0.019	179	231	233	180	68
29	0.019	145	237	255	207	102
30	0.014	173	214	194	171	70
31	0.016	170	217	210	175	73
32	0.016	162	224	233	186	83
33	0.015	138	233	255	210	107
34	0.001	147	201	194	177	91
35	0.010	145	204	210	181	93
36	0.011	142	213	233	192	99
37	0.010	130	228	255	215	112
38	0.005	121	188	194	184	112
39	0.005	121	192	210	188	113
40	0.004	122	203	233	199	115
41	0.003	122	223	255	220	119
42	0.005	99	179	194	195	136
43	0.000	101	183	210	199	135
44	0.001	105	195	233	209	133
45	0.003	114	217	255	226	126

[a]Based on Ref. VI-8.

I. Comparison of Surveyor I, III, and Earth-Based Lunar Surface Temperatures

From the analysis the following tentative conclusions may be drawn:

Lunation data

(1) Predicted and observed lunar surface temperatures from both compartments are in good agreement around noon and are compatible with the homogeneous surface model with thermal inertia, γ, greater than 400. Sunset data are not inconsistent with this picture.

(2) Differences in Compartment A and B temperatures during the morning may be explained by different local lunar surface Sun phase angles and by directional (non-Lambertian) thermal emission from the lunar surface.

(3) Correspondence in lunar surface brightness temperatures measured by Surveyors I and III indicates lack of any thermally significant dust on compartment faces.

(4) During the afternoon, compartment temperatures, especially that of Compartment A, are somewhat higher than expected from Earth-based data. Increased solar absorptance of the compartments does not account for the discrepancy. This is consistent with no thermal indication of dust on the compartment faces.

Eclipse data

(1) Compartments A and B saw the same lunar surface temperature throughout all of the umbral and almost all of both penumbral phases. This indicates Lambertian (i.e., nondirectional) lunar surface emission at low insolation.

(2) During both penumbral phases, observed lunar surface temperatures lagged those predicted from Earth-based data; umbral lunar surface temperatures were 50°K above those predicted. Both suggest an effective γ near 400.

REFERENCES

VI-1. Shorthill, R. W., and Saari, J. M., "Radiometric and Photometric Mapping of the Moon Through a Lunation," Ann. N. Y. Acad. Sci. 123, Art. 2, 722-739, 1965.

VI-2. Shorthill, R. W., and Saari, J. M., "Isothermal and Isophotic Atlas of the Moon: Contours Through a Lunation," to be published as a NASA publication, 1967.

VI-3. Jones, B. P., "Diurnal Lunar Temperatures," Paper 67-289 presented at AIAA Thermophysics Specialist Conference in New Orleans, April 17-20, 1967.

VI-4. Saari, J. M., and Shorthill, R. W., "Thermal Anomalies on the Totally Eclipsed Moon of December 19, 1965," Nature 205, 964-965, 1965.

VI-5. Shorthill, R. W., and Saari, J. M., "Non-uniform Cooling of the Eclipsed Moon: A Listing of Thirty Prominent Anomalies," Science 150, 210, 1965.

VI-6. Jaeger, J. L., "Surface Temperature of the Moon," Aust. J. Phys. 6, 10, 1953.

VI-7. Six, F., Montgomery, C., Saari, J. M., and Shorthill, R. W., paper presented at AIAA Thermophysics Specialist Conference, New Orleans, La., April 17-19, 1967.

VI-8. Sinton, W. M., "Temperatures of the Lunar Surface," Physics and Astronomy of the Moon (Z. Kopal, ed.), Chapter 11, Academic Press, New York, 1962.

VI-9. Lucas, J. W., Conel, J. E., Hagemeyer, W. A., Garipay, R. R., and Saari, J. M., "Lunar Surface Thermal Characteristics From Surveyor I," J. Geo. Res. 72, 2, 779-789, January 15, 1967. Also in Surveyor I Mission Report. Part II: Scientific Data and Results, Technical Report 32-1023, Jet Propulsion Laboratory, Pasadena, Calif., September 10, 1966.

VI-10. Kelly, F. J., and Moore, D. G., "A Test of Analytical Expression for the Thermal Emittance of Shallow Cylindrical Cavities," NASA SP-55, 1965.

VI-11. Hultberg, J. A., Porter, C. D., and O'Brien, P. F., "Thermal Analysis System I," JPL Space Programs Summary 37-43, Vol. IV, pp. 140-142, February 28, 1967.

ACKNOWLEDGMENT

Special appreciation is extended to all Jet Propulsion Laboratory and Hughes Aircraft Company Surveyor III development and flight operations engineers for obtaining raw data used; to R. Garipay of Hughes Aircraft Co., for providing spacecraft temperatures in real time; to W. Heathcote of Hughes Aircraft Co., for special positioning of solar panel during the shading experiment. Thanks are also extended to P. F. O'Brien of UCLA, for analysis consulting; and to G. Vitkus of Northrop Corporation for varied analytical support.

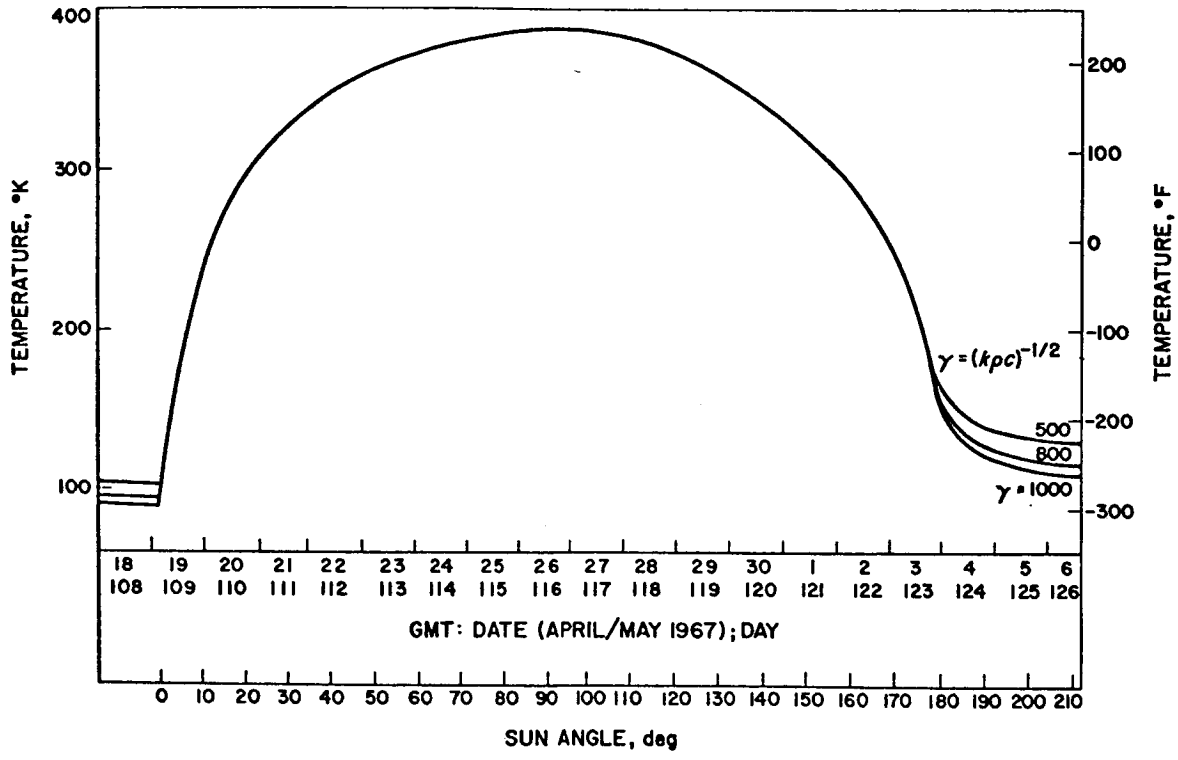

Fig. VI-1. Predicted lunar surface brightness temperatures on lunar equator

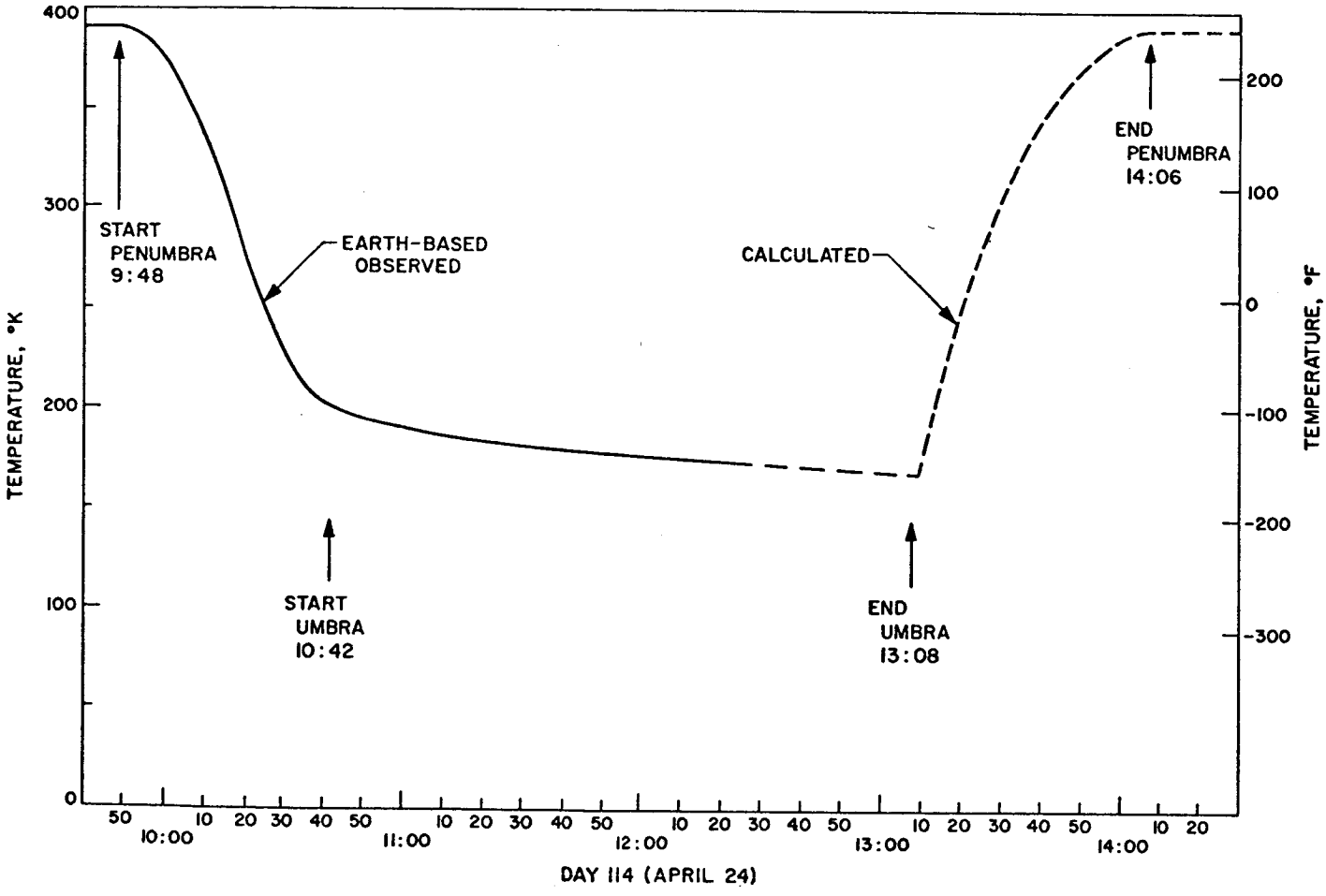

Fig. VI-2. Lunar surface brightness temperature at nominal Surveyor III landing site, during eclipse (data from December 1964 eclipse adjusted for times of April 1967 eclipse)

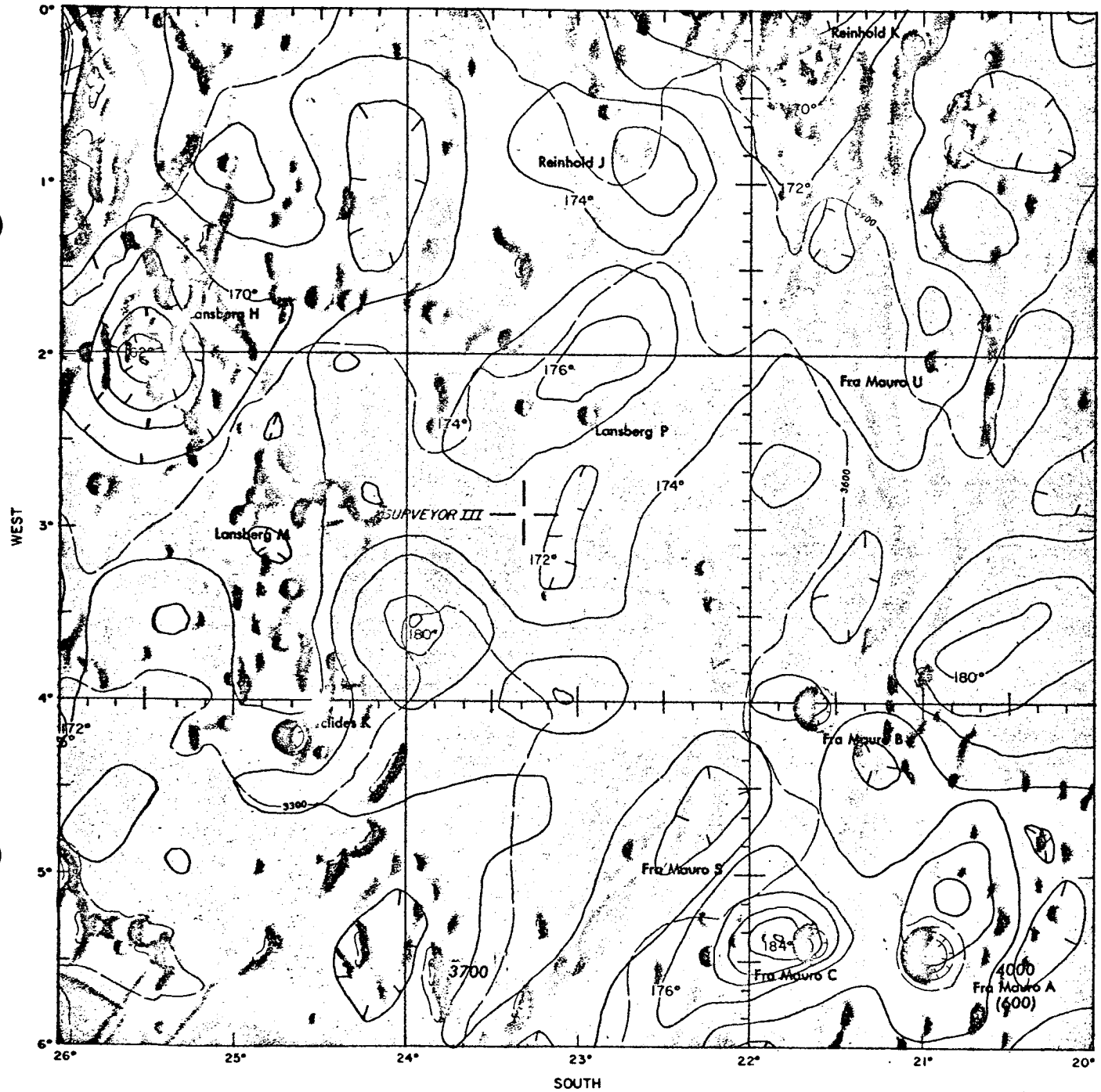

Fig. VI-3. Isothermal contours in Surveyor III landing region obtained during totality of lunar eclipse

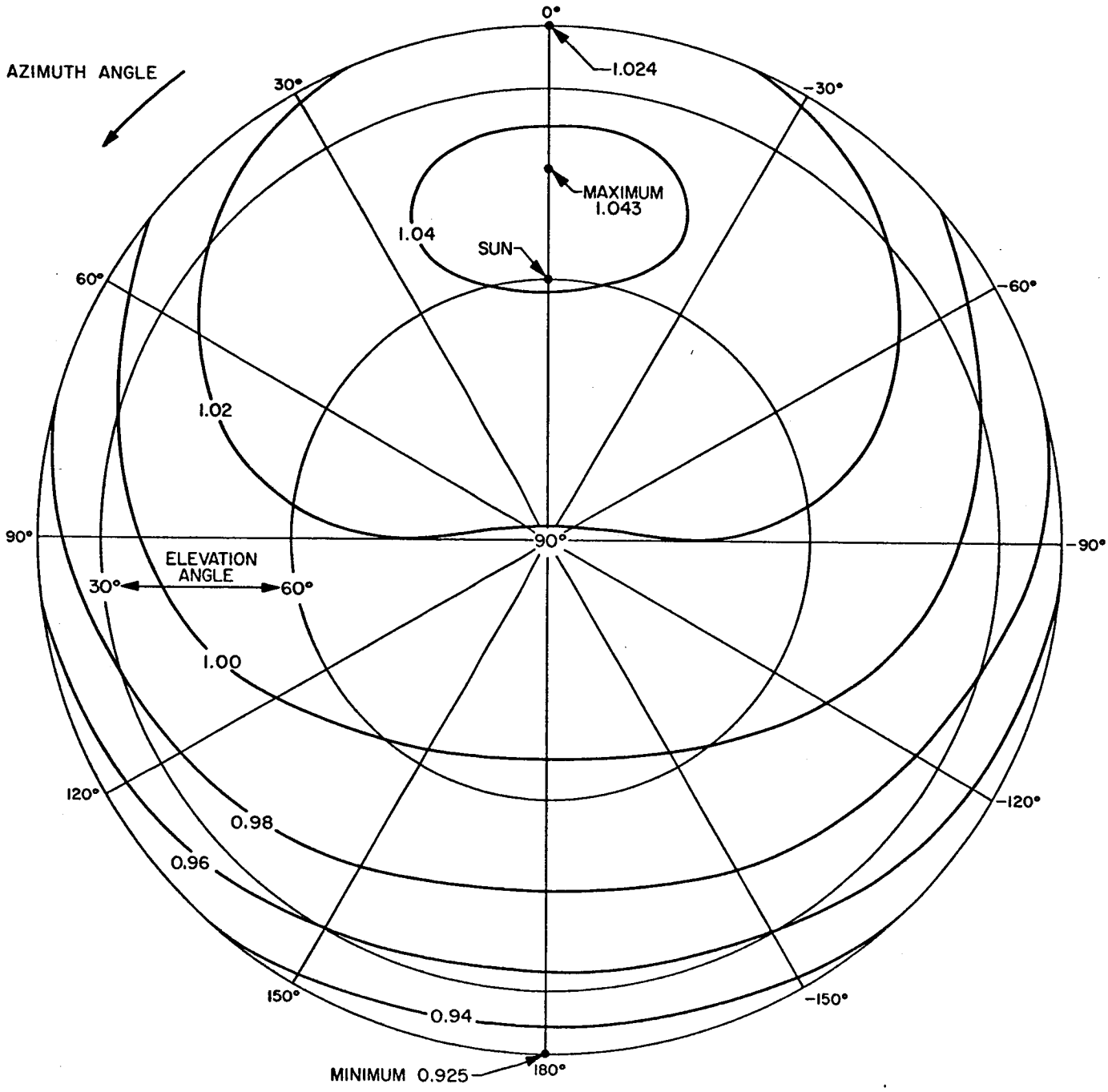

Fig. VI-4. Contours of directional factor for Sun elevation angle of 60°

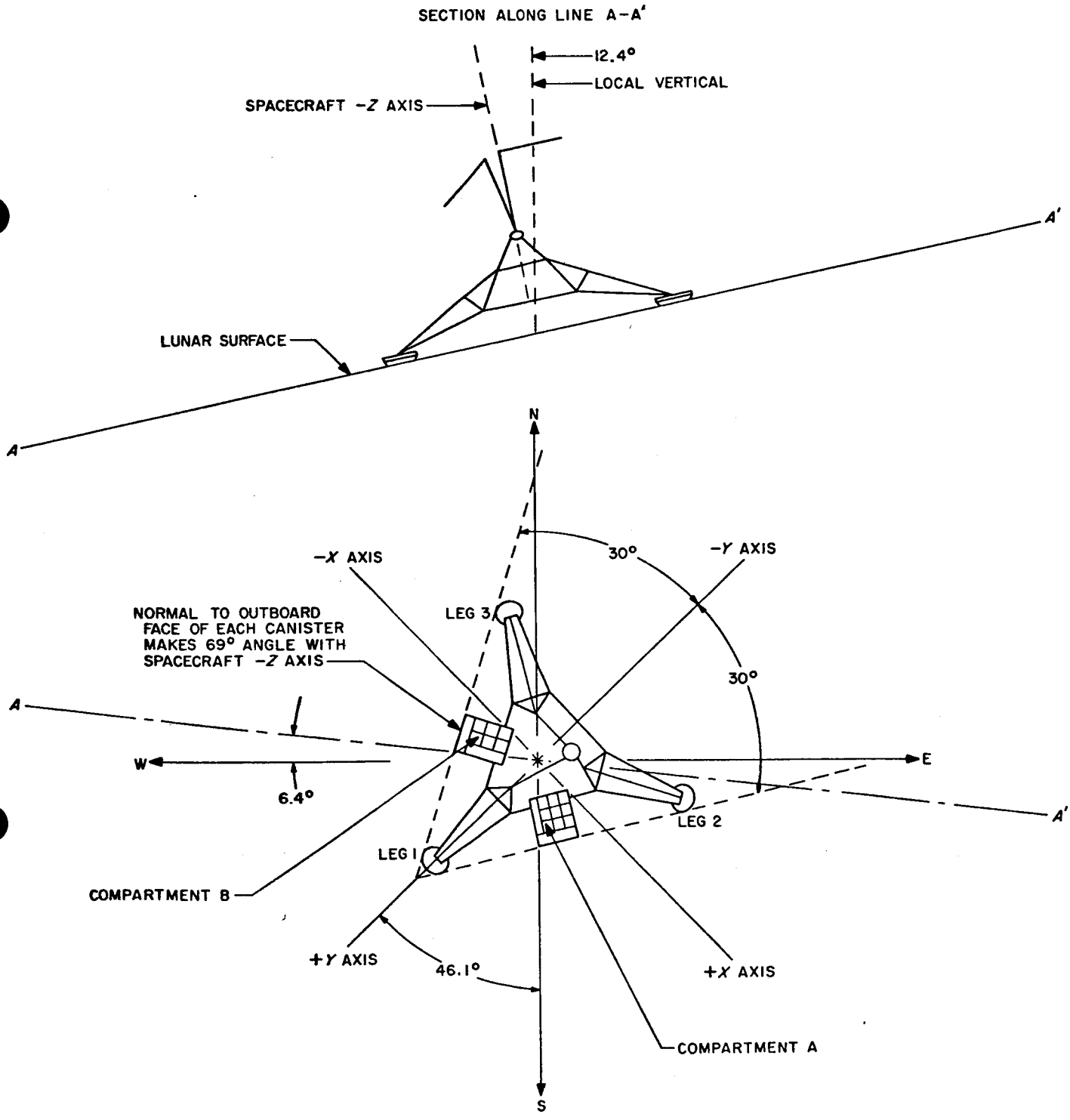

Fig. VI-5. Surveyor III landed orientation

Fig. VI-6. Surveyor III landing site (photograph taken by Lunar Orbiter III), showing sectors viewed by Compartments A and B

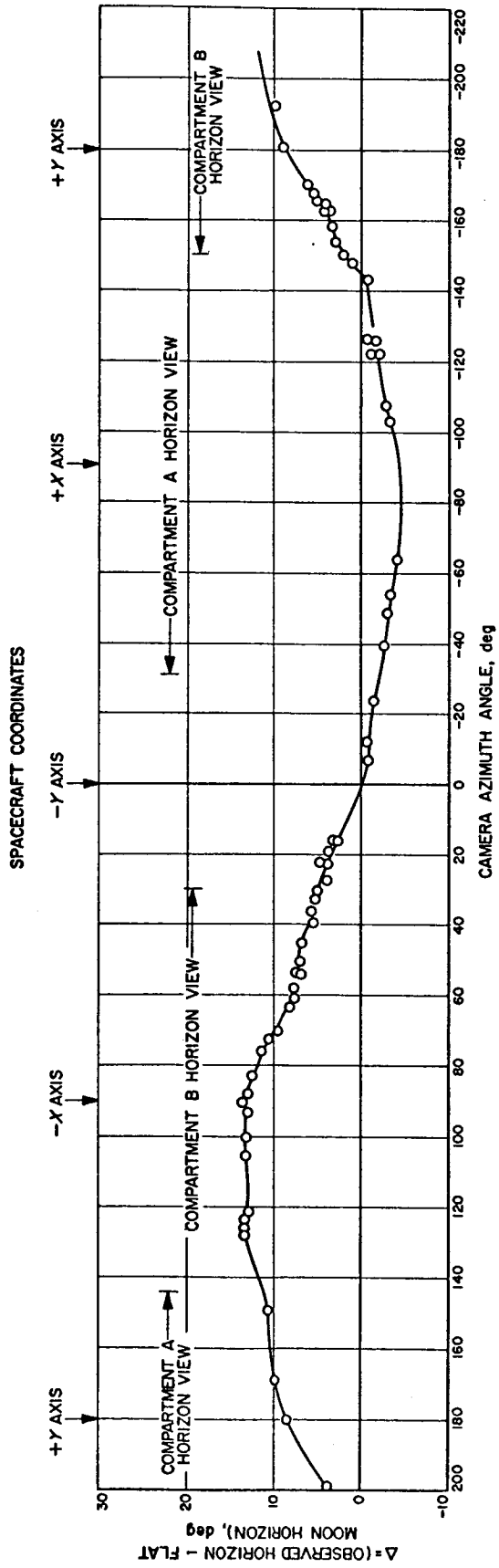

Fig. VI-7. Lunar horizon viewed from Surveyor III (data of E. A. Whitaker)

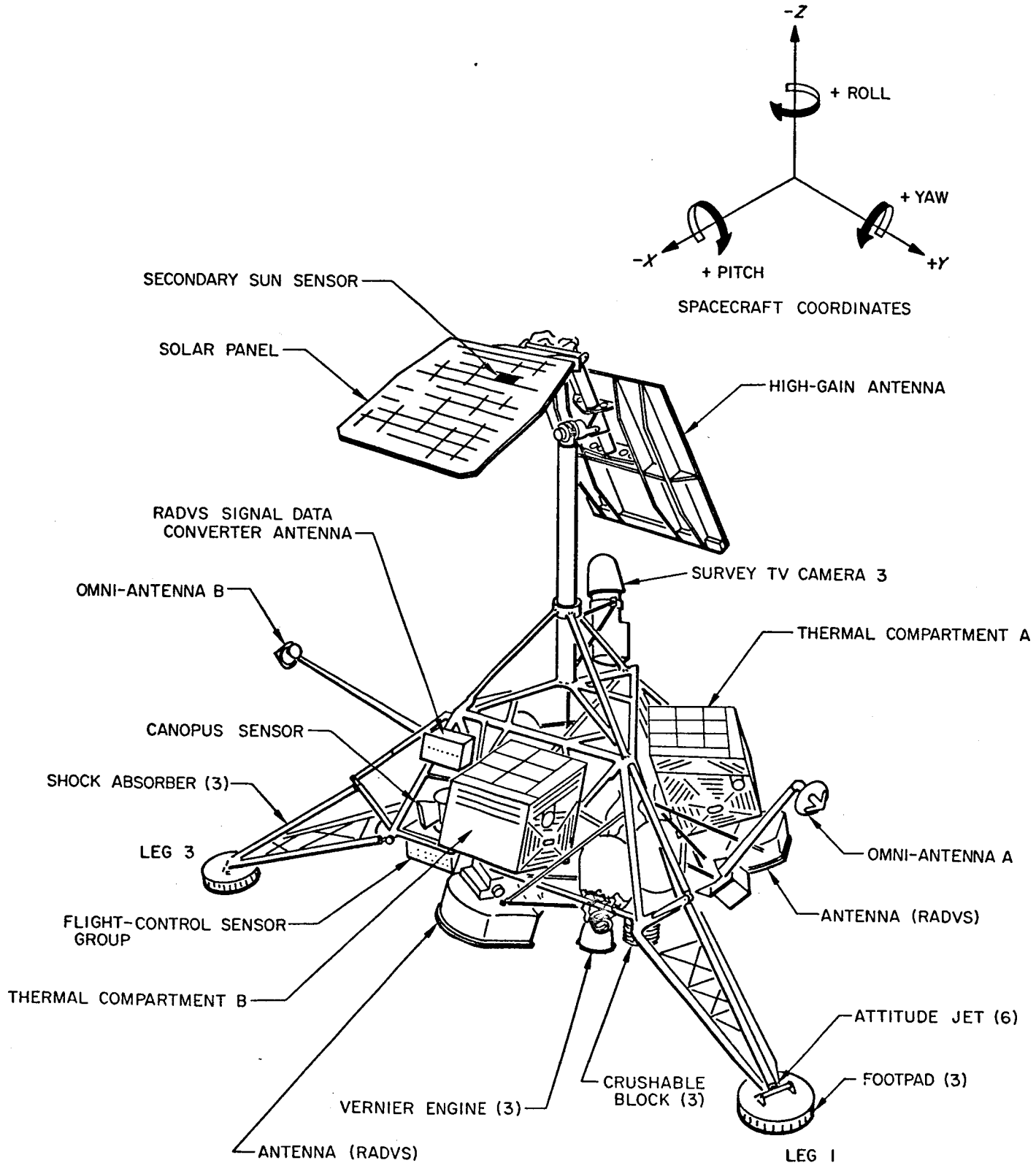

Fig. VI-8. Surveyor spacecraft configuration

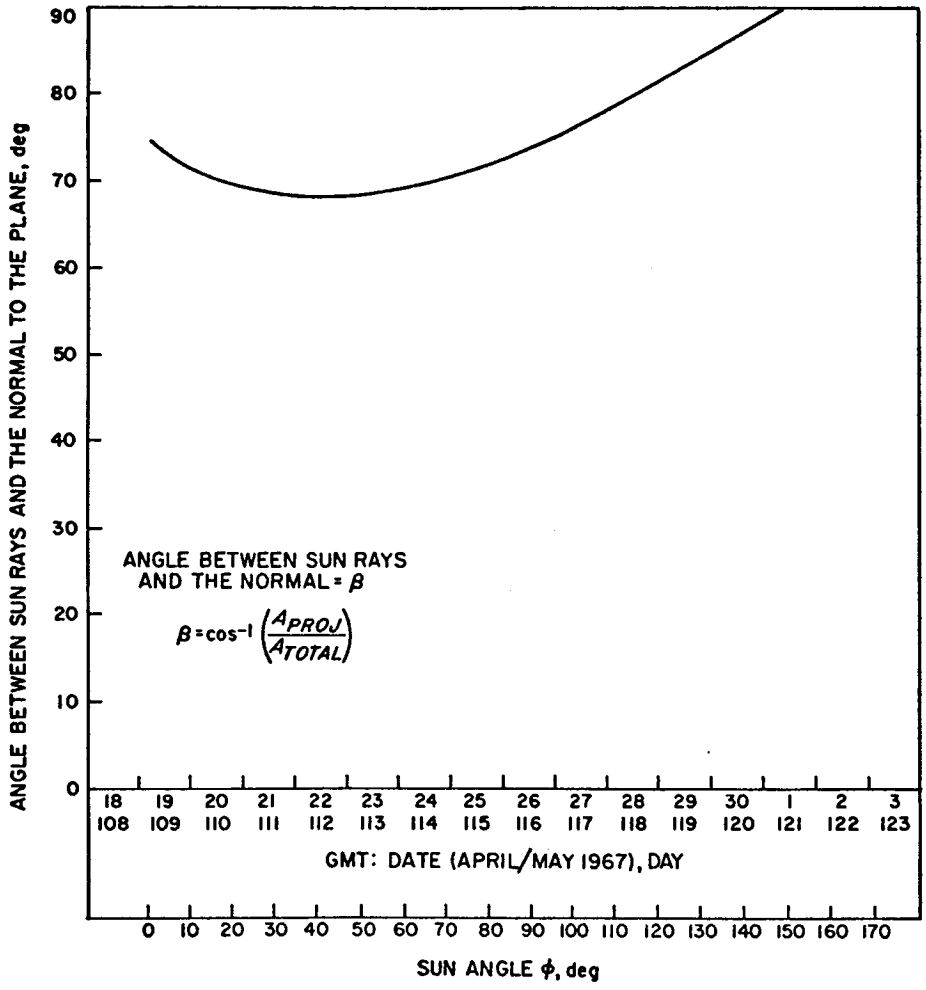

Fig. VI-9. Angle between direction of Sun and normal to outboard plane of Compartment A during first lunar day

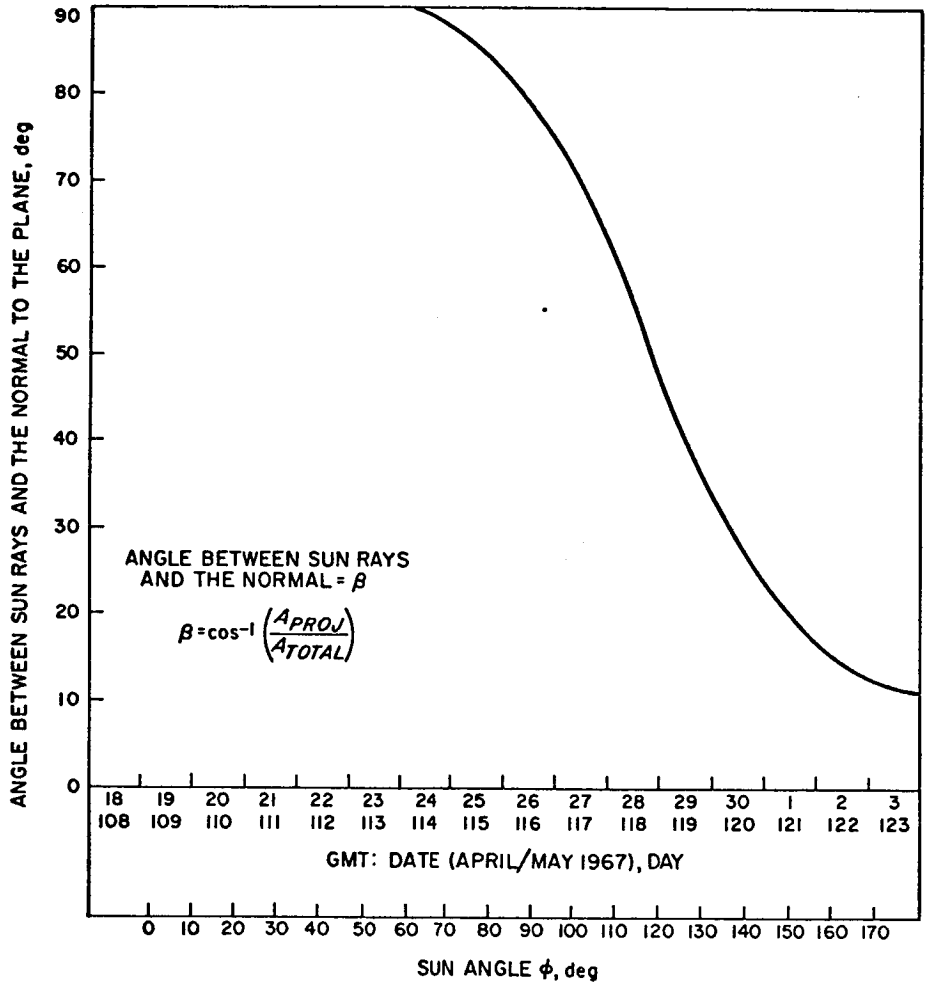

Fig. VI-10. Angle between direction of Sun and normal to outboard plane of Compartment B during first lunar day

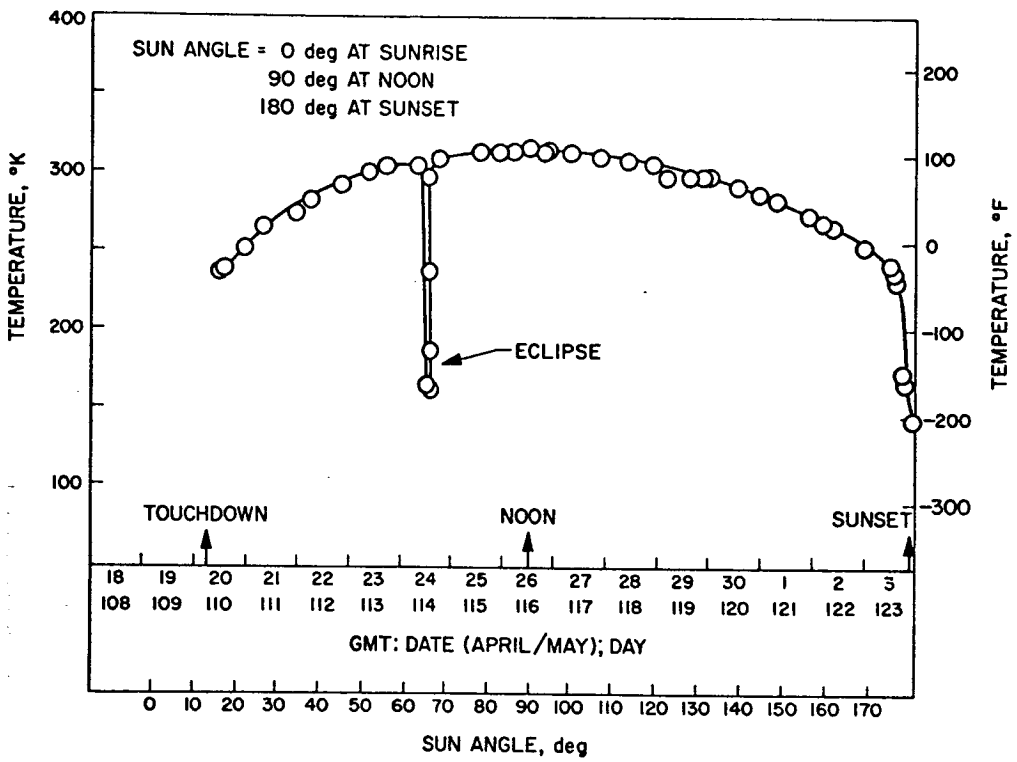

Fig. VI-11. Temperature of outboard face of Compartment A during lunation

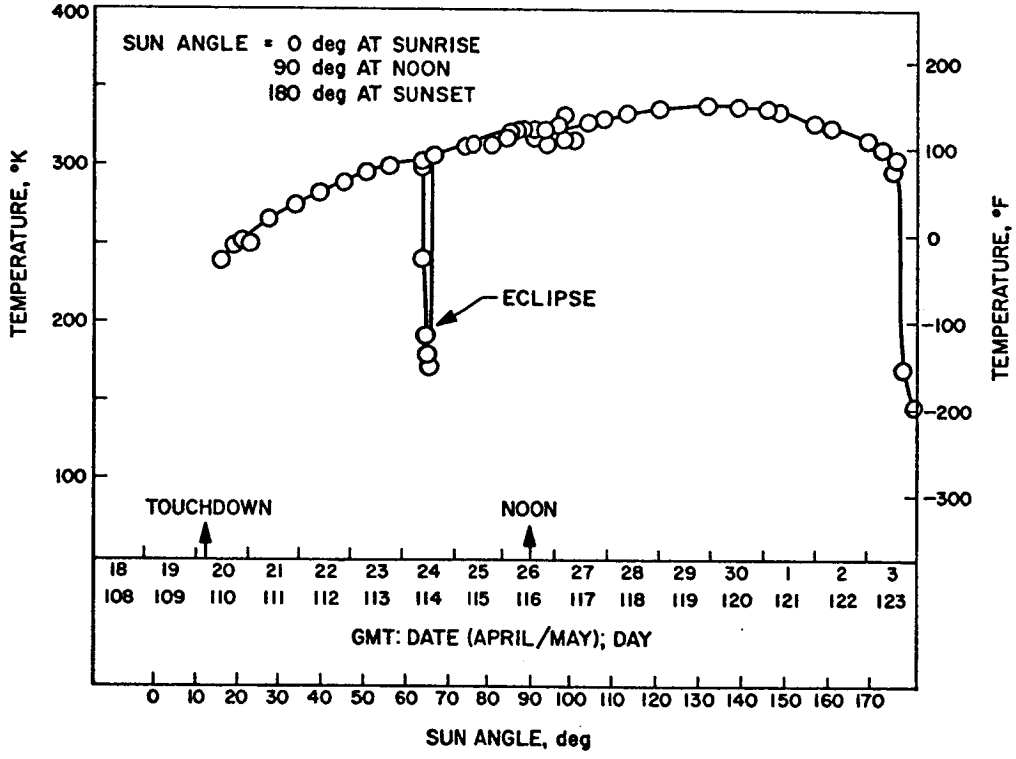

Fig. VI-12. Temperature of outboard face of Compartment B during lunation

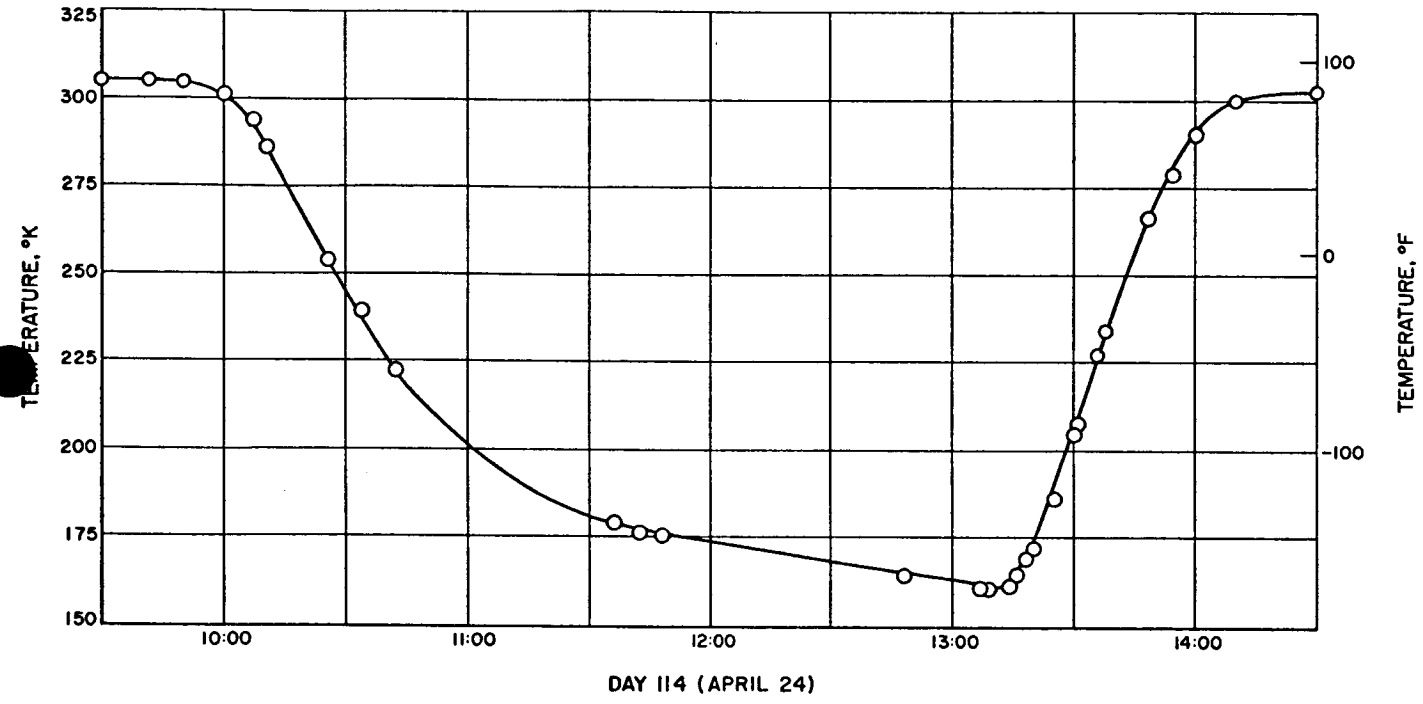

Fig. VI-13. Temperature of outboard face of Compartment A during eclipse

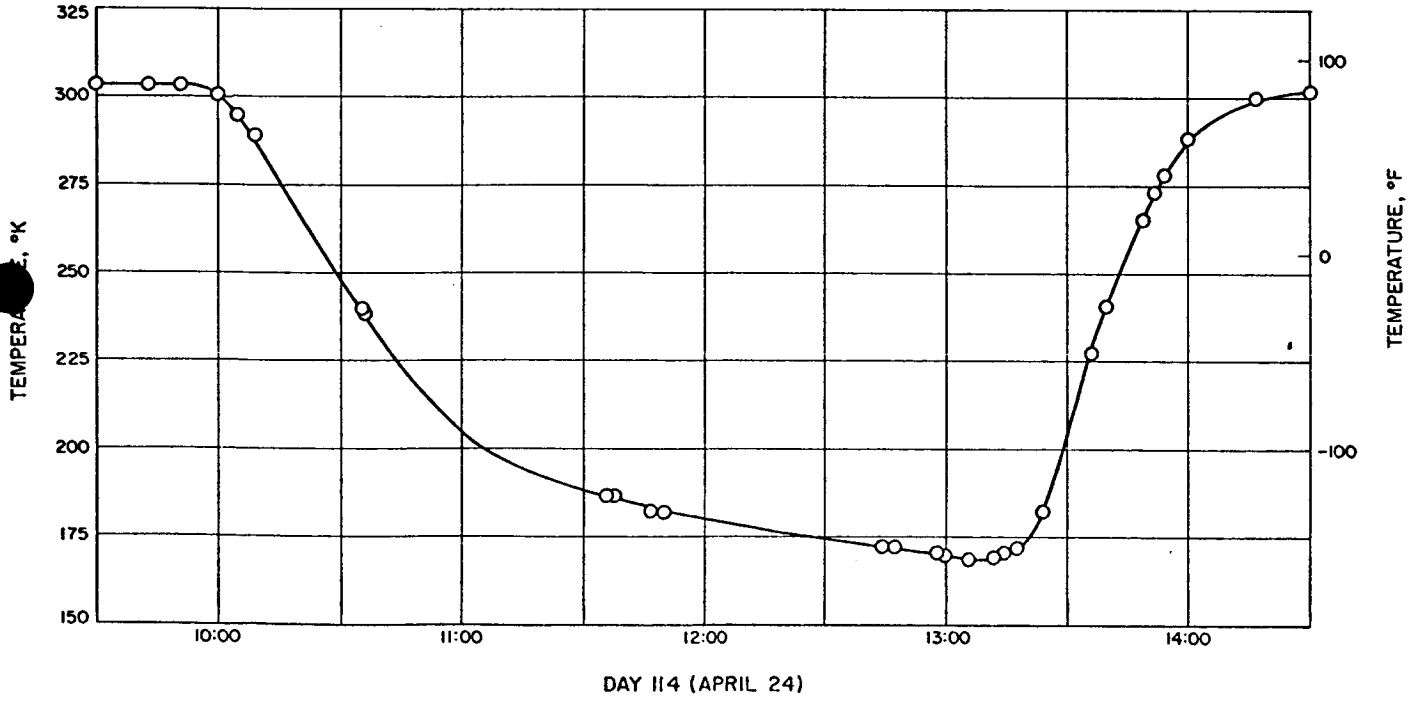

Fig. VI-14. Temperature of outboard face of Compartment B during eclipse

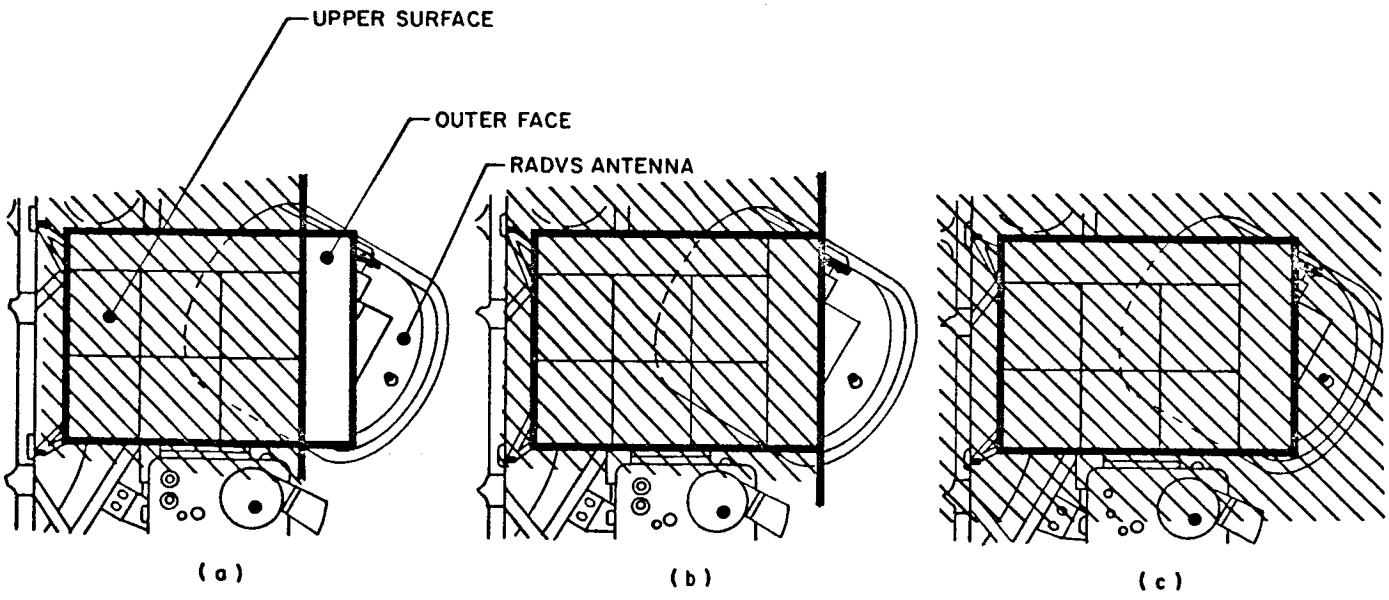

Fig. VI-15. Shading configurations for Compartment B

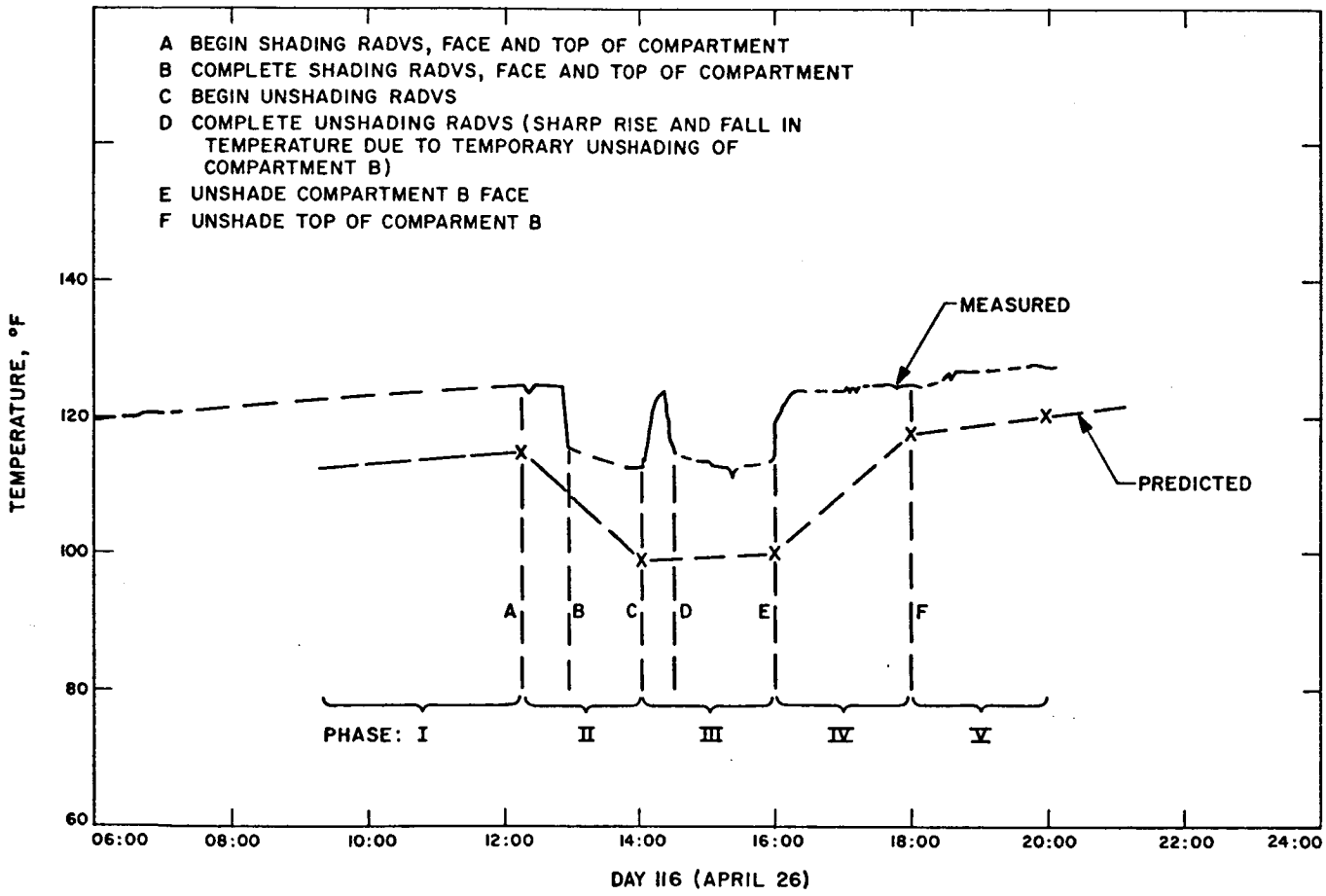

Fig. VI-16. Temperatures of Compartment B during shading experiment

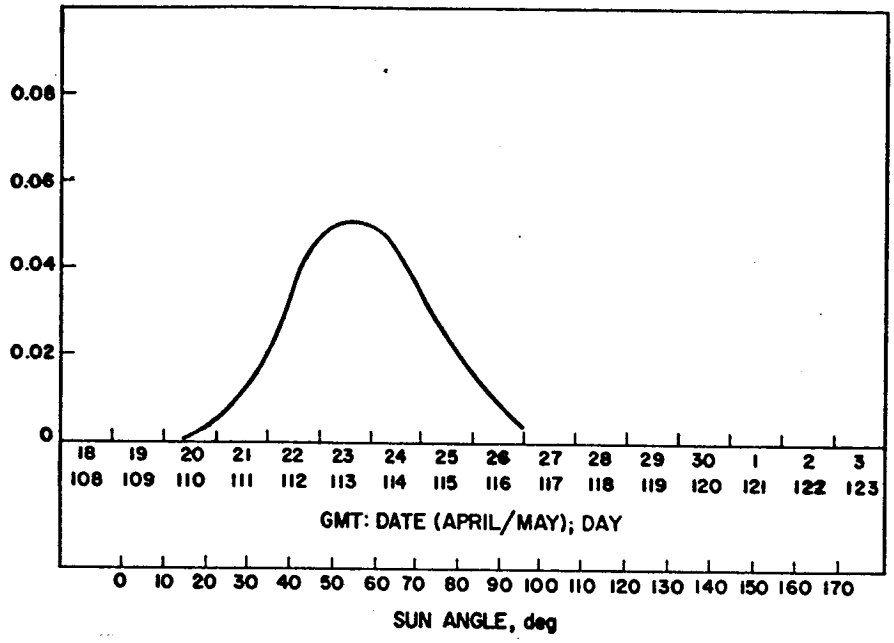

Fig. VI-17. F_{13} for Compartment B

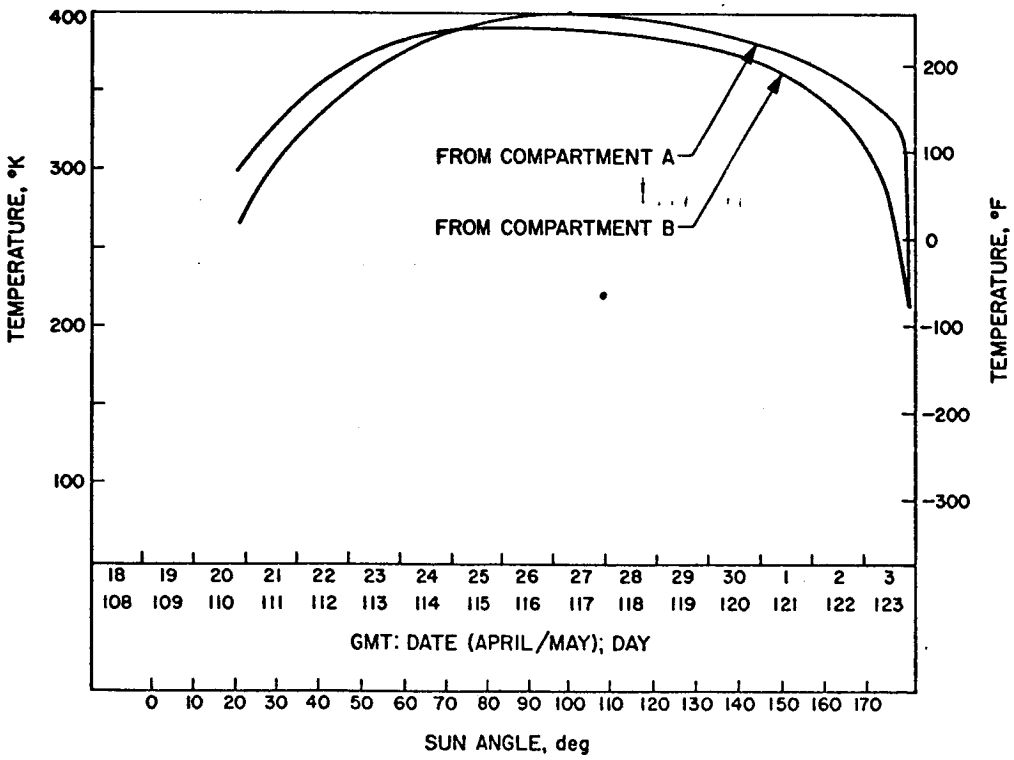

Fig. VI-18. Lunar surface temperatures, as calculated from telemetry data

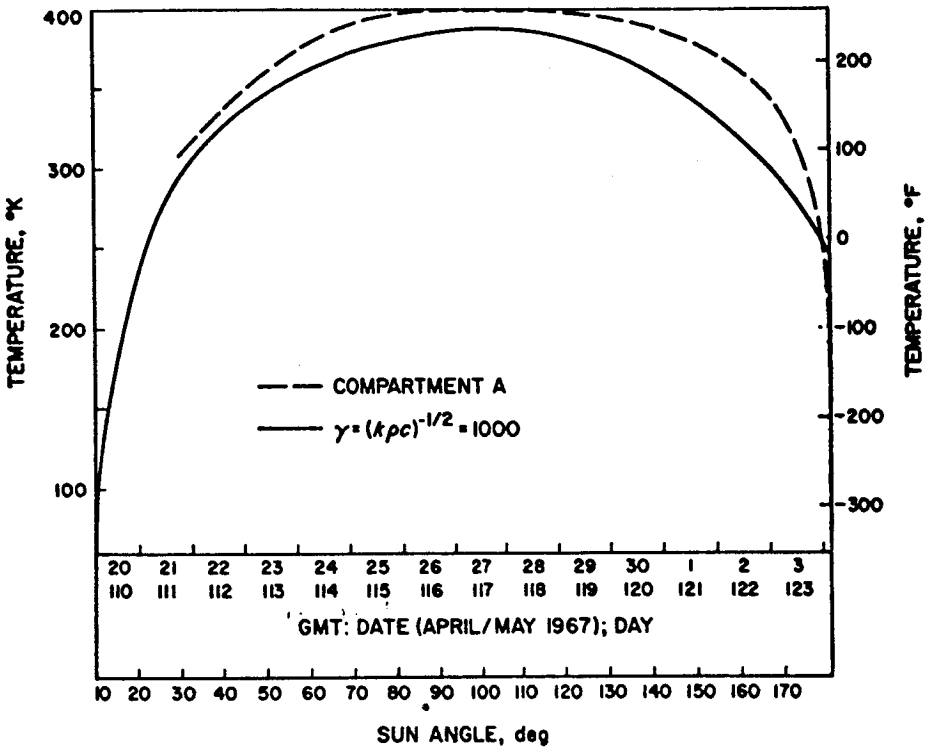

Fig. VI-19. Lunar surface brightness temperatures during lunation from Compartment A data compared with predicted temperatures

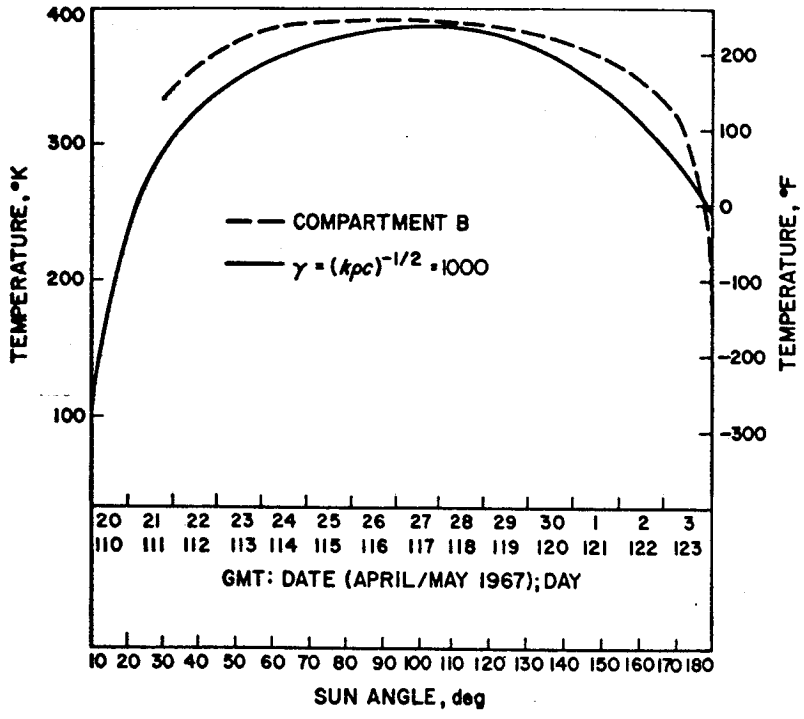

Fig. VI-20. Lunar surface brightness temperatures during lunation from Compartment B data compared with predicted temperatures

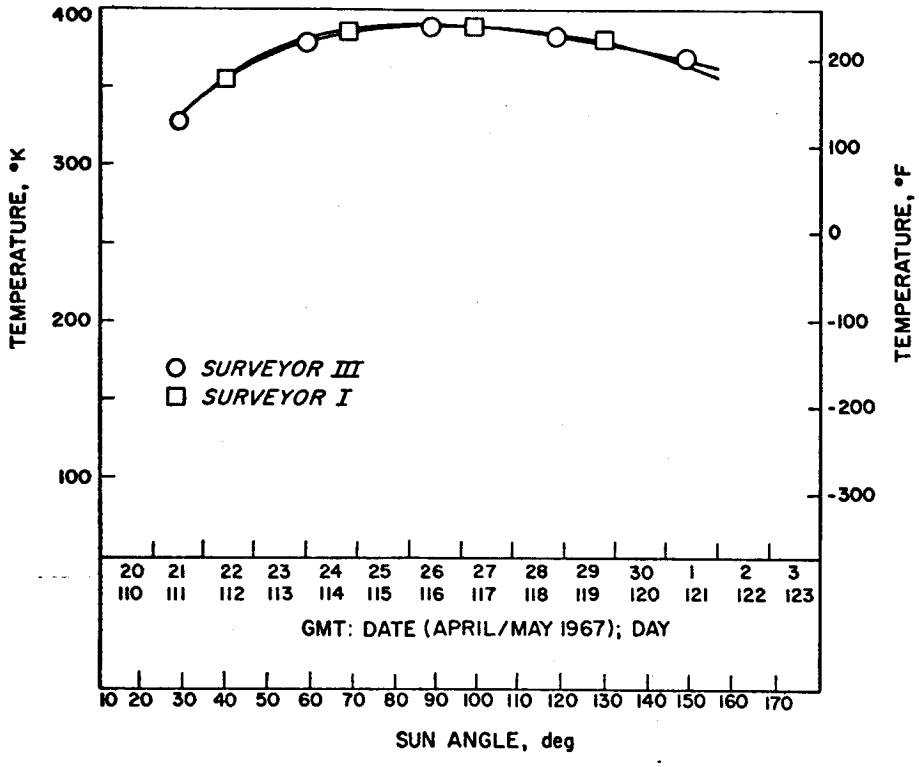

Fig. VI-21. Lunar surface brightness temperatures from Compartment B data on Surveyors I and III (Surveyor I curve adjusted time-wise to Surveyor III)

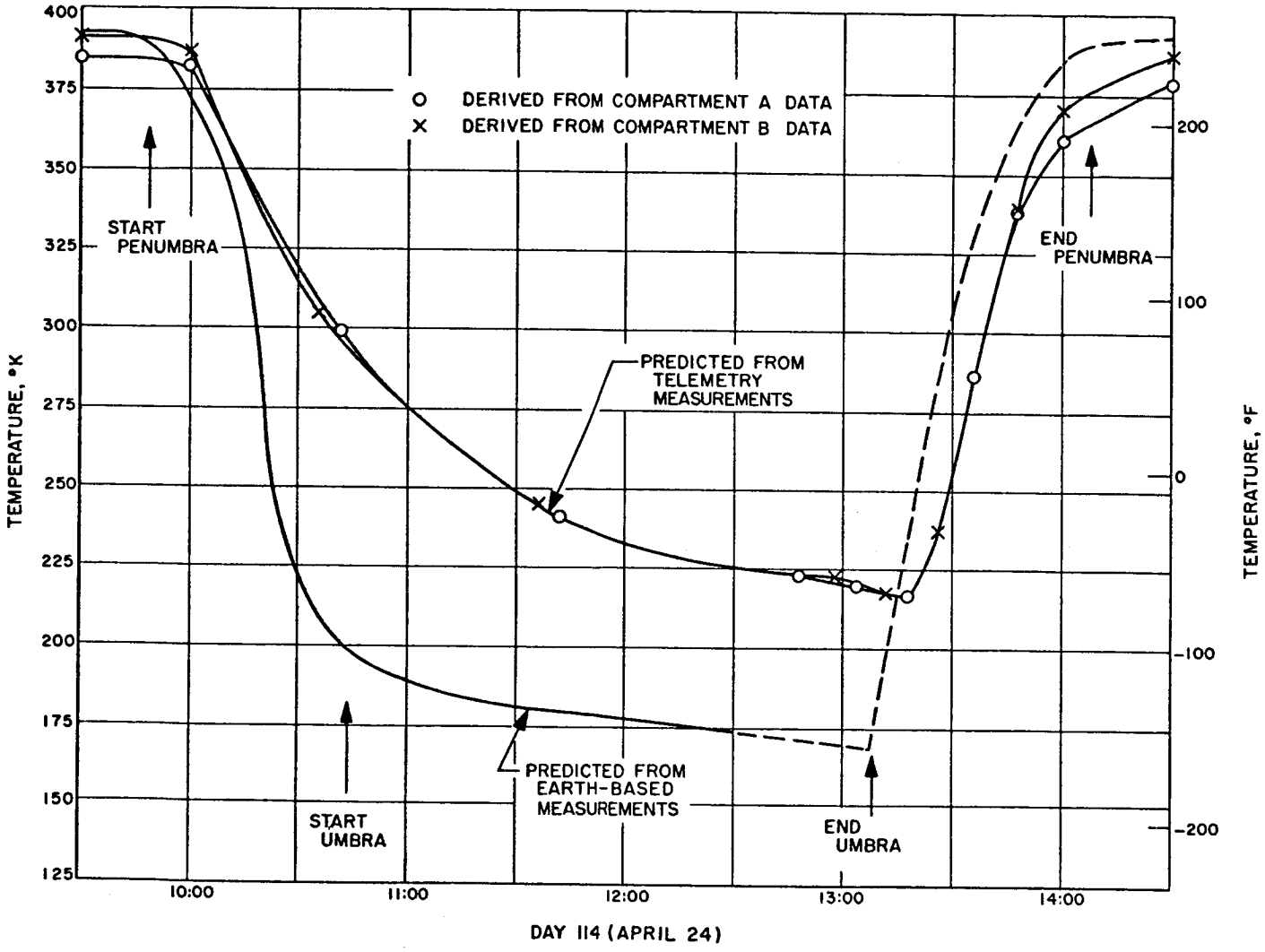

Fig. VI-22. Lunar surface brightness temperatures during eclipse

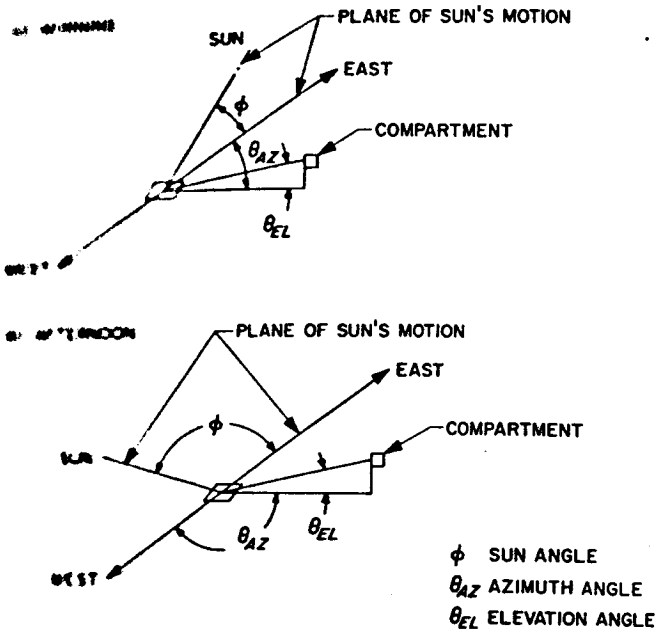

Fig. VI-23. Definition of angles

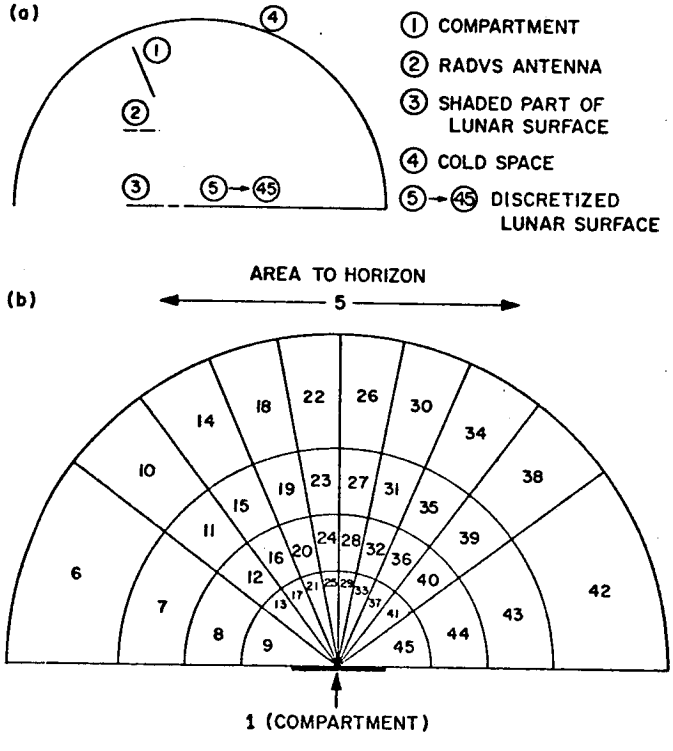

Fig. VI-24. (a) Mathematical model; (b) discretized lunar surface

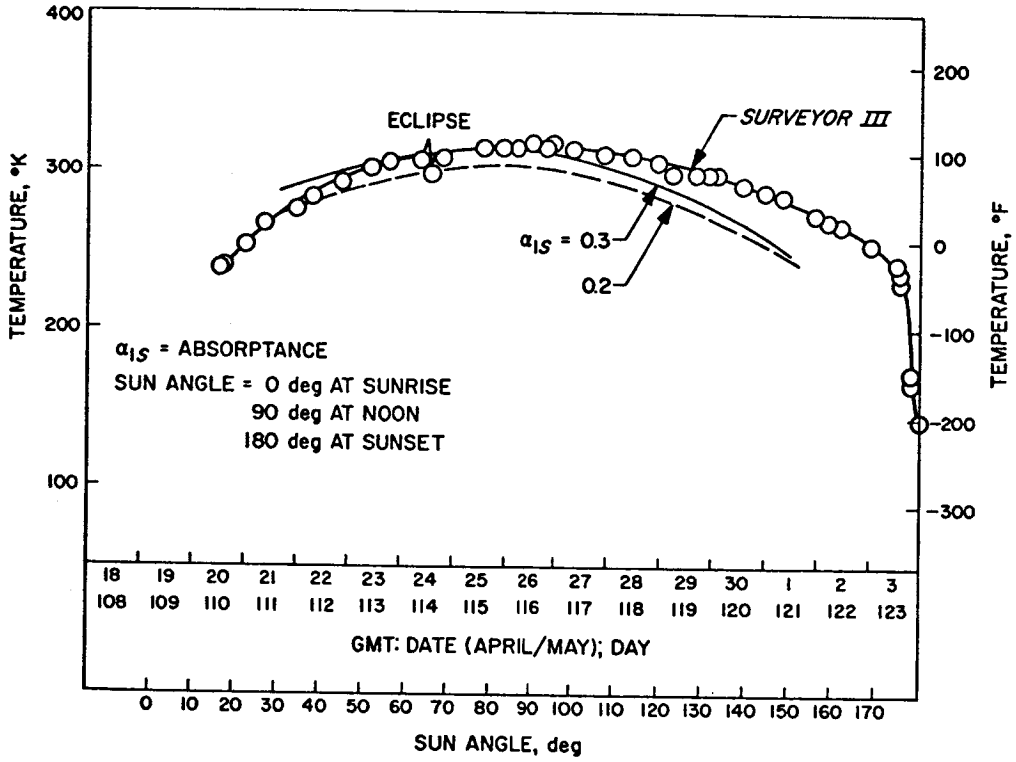

Fig. VI-25. Directional predicted and measured temperatures of outboard face of Compartment A

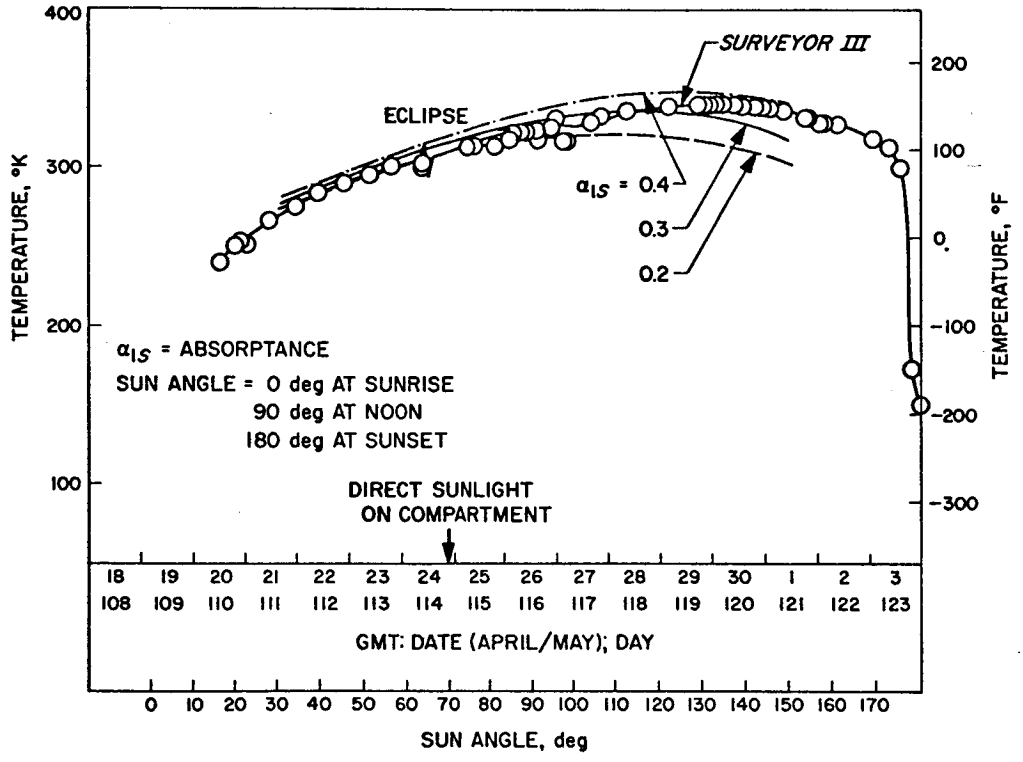

Fig. VI-26. Directional predicted and measured temperatures of outboard face of Compartment B

VII. TELEVISION OBSERVATIONS FROM SURVEYOR III

E. M. Shoemaker, R. M. Batson, H. E. Holt, E. C. Morris,
J. J. Rennilson, and E. A. Whitaker

Surveyor III landed on the lunar surface at 00:04 GMT, on Day 110 (April 20), 1967, approximately 23 hr after local sunrise on the Moon. The first pictures were taken by the television camera at 01:02 GMT. The camera was operated extensively for the first period of lunar visibility from the Goldstone Tracking Station of the Deep Space Network and, except on Day 115 (April 25), on each successive Goldstone pass of the Moon until the Sun set over the Surveyor III landing site on Day 123 (May 3). During this period, the Sun rose from an elevation angle of 11° in the east to within 3° of the zenith and then sank almost due west of the spacecraft. Many pictures were obtained of the illuminated eastern horizon in the period immediately preceding sunset. In addition to those received at the Goldstone Station, some were obtained at the Canberra, Australia, Station of the Deep Space Network. There were 6315 television pictures taken during the first lunar day of the Surveyor III mission.

The television camera on Surveyor III is closely similar to the survey camera carried on Surveyor I (Ref. VII-1). In the Surveyor survey camera, images are reflected from a rotatable mirror through a zoom lens onto the active element of a vidicon tube. The mirror can be rotated in azimuth and elevation relative to a line through the center of the vidicon tube and the zoom lens axis, which remain fixed in attitude. This rotation provides the capability of scanning the lunar scene and sky over a vertical angular range of 100° and a horizontal range of nearly 360°. The axis of the camera is inclined 16° to the nominal vertical axis of the spacecraft, which causes the horizon to vary in camera elevation angle as a function of the azimuth angle, when the spacecraft lands in an approximately level attitude. The variation of the horizon for a flat surface is very nearly a sine function of the azimuthal angular position and has a half amplitude of 16°.

The camera is normally operated with the zoom lens positioned for focal lengths at either the extreme long (100 mm) or short (25 mm) focal length. At the long focal length, or narrow-angle mode of operation, the field of view is 6.4°; at the short focal length or wide-angle mode, the field of view is 25.3°. The lens is capable of being set at varying focal positions, which are required in order to obtain focused pictures of parts of the lunar surface near

the spacecraft in the narrow-angle mode. In this mode, the camera has a calibrated angular resolution of 0.5 milliradian at 15% relative response. This resolution permits discrimination of objects on the lunar surface slightly less than 1 mm in diameter at the distance of the spacecraft footpads from the camera (1.6 m).

Between the zoom lens and the rotatable mirror is a filter wheel that may be positioned in four discrete positions. In one position, the optical path is intercepted by a clear piece of glass; in the other three positions, there are three color filters.

Within the zoom lens is a variable iris aperture that provides nominal focal ratios ranging from f/4 to f/22. The iris can be operated by command to six distinct calibrated positions. It can also be operated in an automatic mode in which the iris position is controlled by the integrated scene luminance detected by a photocell in the lens.

A focal plane shutter between the zoom lens and the faceplate of the vidicon tube provides exposures of 150 msec and 1.2 sec to many minutes. The camera is normally operated at the 150-msec exposure, which is calibrated for each camera and which is reproducible within about 2%. Long exposures are obtained by commanding the shutter open and later commanding it closed. This mode of operation is referred to as the integrating mode and was used to take pictures of faint objects, such as Venus and the spacecraft and lunar surface illuminated by refracted sunlight during an eclipse.

With a given aperture and filter position and 150-msec exposure, the dynamic range of the camera is approximately 25 to 1. The linear part of the function of the logarithm of video voltage versus logarithm of lunar scene luminance is somewhat less for the Surveyor III camera than for the Surveyor I camera. By combined use of various filters, apertures, and exposure times, the total range of response of the Surveyor III camera, like that of the Surveyor I camera, is about 1,000,000 to 1.

The image on the vidicon target can be scanned in two different modes: one produces a 200-line picture; the other produces a 600-line picture. The 200-line scan mode is employed when the video signal must be broadcast over the omnidirectional antenna and must be accommodated to the low bandwidth achievable during transmission from the omnidirectional antenna. The 600-line picture is transmitted over the planar array high-gain antenna after this antenna has been oriented so that the main beam from the antenna is intercepted at tracking stations on the Earth. The 200-line pictures are, therefore, usually taken shortly after

landing, before the planar array antenna has been oriented. For the remainder of the mission, the television pictures are normally taken and transmitted in the 600-line mode.

The principal differences between the Surveyor III camera and the Surveyor I camera are in the use of different colored filters, the different response of the vidicon tube, and the addition of a small visor attached to the hood of the camera. New color filters were used in the Surveyor III camera to obtain a closer match of the camera-filter spectral response functions to the standard CIE color-matching functions than was achieved with the filters used on Surveyor I. As shown in Fig. VII-1, a close match was achieved.

Because of technical difficulties involved in manufacture, each vidicon tube of the type employed in the Surveyor camera differs slightly from the others in sensitivity, dynamic range, erasure characteristics or retentivity of the image, shading, resolution, and imperfections which produce minute bright spots on the image. In addition, it is possible for dust to settle on the faceplate of the vidicon tube. The dust particles produce dark spots in the image. The vidicon tube employed in the Surveyor III camera displayed a higher retentivity of the image than that employed in Surveyor I and has a higher number of imperfections, which produce small bright spots. Slightly less dust appeared to be present on the vidicon faceplate of the Surveyor III camera after landing on the lunar surface than in the case of Surveyor I.

In order to reduce veiling glare, a visor was added to the hood of the camera to reduce the amount of sunlight falling directly on the mirror and inner parts of the camera optical train. The hood carries the mirror and is an integral part of the mirror rotation system, so that the visor maintains a fixed position in azimuth relative to the mirror. Degradation of the surface of the mirror during lunar landing so greatly increased the veiling glare, however, that the addition of the visor was of relatively little value.

During operation of the Surveyor III camera after touchdown, problems were encountered that may be attributed to the unusual circumstances of landing. Normally, the camera mirror is capable of being rotated in elevation to a position which essentially closes or seals the hood. The torque required to rotate the mirror to an open position after closure was close to the torque generated by the mirror elevation stepping motor on the Surveyor III camera, however. For this reason, the camera was flown to the Moon with the mirror open. The spacecraft touched down

three different times during landing on the lunar surface; during the first two touchdowns, the vernier engines, which control the descent of the spacecraft, continued to fire. After the first series of pictures was received from the television camera, it was found that many were partially or completely obscured by strong veiling glare. Evidently, the mirror and possibly other parts of the optical train of the camera were either partially coated with particles or rocket effluent or pitted by impact of particles entrained by the rocket effluent. If the glare is caused by deposited particles or pitting or both, we estimate that between one-half and two-thirds of the area of the mirror was significantly degraded. The particles or pits responsible for degradation of the mirror surface were too small to be detected by direct observation of the mirror at the 25-mm focal length (smaller than 0.5 mm).

Because of the glare, usable pictures could be obtained in only limited ranges of azimuth during the early lunar morning and late lunar afternoon. Whenever sunlight fell directly on the mirror, the image of the lunar surface was completely obscured where reflected through the directly illuminated part of the mirror. In addition, considerable glare is present in other pictures taken when the mirror is averted from the Sun, owing to light scattered from the lunar surface.

Because of operational difficulties in rotating the mirror, the camera was operated over an azimuth range extending only to one side of the +3° azimuth position during most of the lunar day. Because of requirements for time to operate the surface sampler on the spacecraft and for other experiments, limited time was available for systematic lunar surveys during each Goldstone pass. Much more time would have been required for the completion of systematic surveys than in the case for normal operation, and only a fraction of the planned operation of the camera was executed during each Goldstone pass.

The camera operated best during high Sun angles, but under high Sun the photometric conditions are less favorable for detecting relief features on the lunar surface. Craters and subtle relief features were almost impossible to observe at high Sun, although blocky fragments could be observed because they differ in albedo from the rest of the lunar surface material. Most of the details of the topography and geology of the Surveyor III landing site are extractable from the pictures only with considerable difficulty.

Of the 6315 pictures taken with the television camera, about 45% of the pictures were taken in the narrow-angle mode at sequential camera azimuth and elevation settings to provide high-resolution coverage of the entire area visible to the

camera. The wide-angle mode was used to take 8% of the total number of pictures, providing panoramas of the landing site at lower resolution than that of the narrow-angle pictures, but with one-tenth the number of frames. Immediately after touchdown, before the high-gain antenna had been oriented, 55 wide-angle pictures were taken in the 200-line, low-resolution television mode.

Special sequences of pictures were taken for a variety of purposes. Pictures were taken in wide- and narrow-angle modes, and with color filters of photometric and color target areas as well as other areas of special interest for photometric or color studies. Surveys were made along certain azimuths in which pictures were taken at several different focal settings at each elevation step. These pictures will be used to determine distance to points on the surface, from optimum focus, and will be used to construct focus ranging profiles out to about 10 m (33 ft) from the spacecraft. Other special surveys were obtained at varying Sun angles of the areas close to the visible footpads of the spacecraft and of areas directly beneath the crushable blocks of the spacecraft. In addition, special surveys were made of parts of the spacecraft itself to search for particles and possible structural damage.

A unique sequence of pictures was obtained of the Earth during an eclipse on Day 114 (April 24). During the eclipse, a picture was also obtained of Venus, and an attempt was made to photograph stars to gain precise information on the orientation of the camera and the spacecraft. All attempts to obtain pictures of stars both during the eclipse and later were unsuccessful, however, because of difficulties in commanding the camera mirror to rotate and because of the high background of veiling glare produced by scattering of light from the lunar surface onto the mirror.

The special surveys account for about 25% of the total number of pictures taken during the first lunar day; the remainder were taken in support of operations of the surface sampler experiment.

The television pictures have provided new information on the location of the landing site on the lunar surface, on the lunar surface itself, and on the appearance of the Earth as seen from the Moon, during eclipse and partial direct illumination by the Sun. Calculation of the trajectory of the spacecraft by the Flight Performance and Analysis Group, from information obtained by tracking the spacecraft on its translunar trajectory, led to a determination of the location of the spacecraft on the lunar surface, with an uncertainty of a few kilometers. By close comparison of the detailed features of the surface observed by the television camera on Surveyor III with features observed from lunar orbit in pictures acquired

by Lunar Orbiter III, it was possible to determine the precise location of the Surveyor III spacecraft with respect to the pictures shown in the Lunar Orbiter photographs. The evidence by which the location of Surveyor III has been determined and its relation to the larger features of the lunar surface are described by Whitaker.

Many kinds of new information on the small details of the lunar surface and the specific topographic and geologic features of the landing site are contained in the television pictures, as discussed in the sections on topography and geology by Shoemaker, Morris, Batson, and Holt. Some of the photometric observations of the lunar surface at the Surveyor III landing site have been reduced and are described in this report by Holt and Rennilson. In addition, preliminary evaluation of the color of various features on the lunar surface at the Surveyor III landing site is presented here by Rennilson.

Observations of Earth during the eclipse of the Sun by the Earth have provided the first direct observations of the distribution of refracted sunlight that weakly illuminates the lunar disk during this type of eclipse. The distribution and color of light in the refraction halo surrounding the Earth during the eclipse are described by Rennilson, Shoemaker, and Whitaker. Finally, the observations of the crescent Earth illuminated directly by the Sun are described by Whitaker and Rennilson. The pictures obtained from Surveyor III are the first that have been taken of the Earth from the distance of the Moon by methods permitting reproduction of pictures of the Earth in color.

A. Location of Surveyor III on Moon

The nominal target for Surveyor III was 3°S latitude, 23°W longitude, which is in a small but telescopically relatively crater-free part of the Oceanus Procellarum about 120 km (75 mi) southeast of the crater Lansberg and due north of the center of Mare Cognitum (Fig. VII-2). The area is crossed by the weak south end of a ray from Copernicus, and contains two very low segments of mare ridges (Figs. VII-3 and VII-4). The whole region is well covered by Lunar Orbiter III photographs, which reveal a fairly low density of sub-telescopic craters, closely resembling those observed around the Surveyor I landing site.

The best estimate of the position of the landing site obtained from pre-landing tracking data was 2.99°S, 23.37°W. This position was plotted on ACIC lunar chart AIC 76A, and the point transferred to Lunar Orbiter III medium-resolution photograph

M154 (Fig. VII-5), from which it was further transferred to high-resolution photograph H154. Noting that Surveyor I and Rangers VII through IX landed somewhat to the east of, and in three cases to the north of, the positions derived from tracking data, it was considered that Surveyor III would probably be located in the central third of H154.

A study of preliminary mosaics of wide-angle Surveyor III pictures showed that the spacecraft had landed on a west-facing surface sloping about 10° to the horizontal; the average level of the horizon was about 5° higher than nominal for a flat surface. These data implied that the spacecraft was situated on the inner east slope of a shallow crater.

A comparison with Surveyor I panoramas of narrow-angle surveys of areas to the north and south of the spacecraft suggested that the horizon lay at least 50 m away, indicating the crater in which the spacecraft landed had a diameter of 100 m or more. These surveys also showed several small, but distinct, craters and a number of blocks, estimated to be large enough to be visible on Lunar Orbiter III photograph H154. A rough plan of the crater and its details was drawn and memorized, and the general pattern searched for in all craters 50 to 250 m in diameter in the central third of H154.

A crater was found that seemed to have the correct disposition of small craters and rocks; measurements of azimuths of these features confirmed the identification. Figure VII-6, an enlargement of a part of H154, illustrates this crater and its immediate surroundings. The crater has a diameter of approximately 200 m, and a depth of the order of 15 m. The selenographic coordinates of Surveyor III determined from the Lunar Orbiter III photograph and the ACIC map are 2.94°S latitude, 23.34° W longitude.

B. Topography of Surveyor III Landing Site and Attitude of Spacecraft

The crater in which Surveyor III landed is one of a family of craters of subdued topographic form that occupies more than 50% of the surface of this part of the Oceanus Procellarum. The rim of the crater is low and gently convex upward; the position of its precise crest is difficult to define. Slopes within the crater range between about 10 and 15° on the steepest parts of the crater wall, exclusive of the walls of smaller superposed craters. The floor of the crater is gently concave upward and merges imperceptibly with the sloping walls. A profile

across the center of the crater shows a reversal of curvature approximately halfway between the center of the crater and the rim crest, both in vertical and radial positions (Fig. VII-7).

Photoclinometric profiles across the crater in which Surveyor III landed were derived from the Lunar Orbiter III high-resolution photograph III P-9C, H154, EI 79W, framelet 027. The photometric method of deriving a surface profile utilizes variations in scene brightness and an adopted mean photometric function of the lunar maria for determining components of slope in the phase plane. Scene brightness was measured from the photograph along phase plane traces with a microdensitometer. Digital density measurements were converted to normalized luminance by use of a luminance factor derived from comparison of the computed luminance to the measured density of several areas whose orientation was determined by means of subjective photointerpretation. A slope element was then computed from the normalized luminance for each image element along the phase plane traces, using the terrestrially measured mean lunar photometric function for the maria. Finally, the slope elements were connected to form profiles. Two profiles across the central part of the crater (shown in Fig. VII-7) exhibit local slopes as high as 16°. The crater depth (20 m) derived by the photoclinometric technique is somewhat greater than that found directly by use of vertical angle measurements from Surveyor III.

About 100 small craters resolved in the Lunar Orbiter III pictures are scattered over the floor, inner slopes, and rim of the larger crater in which the spacecraft is located. These small craters range in diameter from 1 to 25 m. Many of them are subdued in form with gentle interior slopes and rounded rims, but a few have sharp, raised rims and steep inner walls. In addition, the inner surface of the main crater is sparsely strewn with coarse blocks, most of which are spatially associated with three of the largest superimposed small craters.

By close comparison of the Surveyor III pictures with the Lunar Orbiter III photograph of the Surveyor III landing site, it is possible to identify more than 100 craters and large blocks that are recognizable in both the Surveyor and Lunar Orbiter pictures. Because the number of these features is so large, it was possible to use the information obtained from the two different sets of pictures to produce a topographic map of the crater by methods analogous to ordinary field surveying, after a solution was obtained of the orientation of the Surveyor III camera. The planimetric position of the camera was located by resection within

the main crater in which the spacecraft landed to within 0.5 m, relative to the objects identifiable in the Lunar Orbiter III photographs; the azimuthal orientation of the camera and the spacecraft was found to within 1°. Distances from the Surveyor III camera to objects identifiable in the Lunar Orbiter photographs were obtained directly from a Lunar Orbiter high-resolution photograph that was taken when the optic axis of a high-resolution Lunar Orbiter camera was pointed within about 2° of the vertical. Vertical angles from the Surveyor III camera to the objects identified in the field of view were then obtained from the camera mirror azimuth angle and elevation angle telemetry and from positions of objects within the Surveyor pictures. From these data, elevations of points on the lunar surface relative to the Surveyor camera were obtained by elementary trigonometry. A preliminary contour map prepared by this method is illustrated in Fig. VII-8.

Surveyor III landed on the west-facing east wall of the main crater southeast of the center of the crater. It lies almost half-way between the center of the crater and the rim crest; the mean elevation of the footpads is about 7 m below the mean elevation of the rim crest.

The attitude of the spacecraft has been estimated by three independent methods:

(1) Adjustment of the position of the planar array antenna of the spacecraft so that it provides the maximum signal transmitted to the Earth and the solar panel so that maximum rate of change is obtained. The attitude of the spacecraft can be estimated with the aid of the known radiation pattern of the antenna. The antenna was adjusted slightly from time to time to compensate for libration of the Moon, and the solar panel was adjusted to track the Sun. Several estimates of position were obtained. Observational data on fine adjustment or "tuning" of the antenna and the solar panel indicate the spacecraft is tilted 12.5 ±2° in a direction 6.6° north of west.[1]

(2) Preliminary reduction of the observations of the position of the Earth and Venus in the television pictures by Rennilson indicates the spacecraft is tilted 13 ±1.5° in a direction 6° north of west.

(3) Assumption that the rim crest of the crater in which the spacecraft is located is, on the average, horizontal. Observations of the lunar horizon as seen from the Surveyor III camera can then be reduced to

[1] Computation of attitude of spacecraft from orientations of planar array antenna was carried out by Robert Lackman at the Hughes Aircraft Company.

an attitude for the spacecraft, after corrections have been made for the departure of the horizon from the rim crest. These observations, as reduced by Shoemaker, indicate the spacecraft is tilted 14.8° in a direction 6° north of west.

The azimuth of tilt by all methods is found to be very nearly west. Observations of the position of the shadow of the western rim of the crater on the spacecraft and on the eastern wall of the crater, near the time of lunar sunset, provide a very sensitive test of the orientation of the spacecraft. Predictions of the times at which the shadow would be seen at various positions on the spacecraft, derived from observations of the horizon and the attitude derived by Shoemaker, were found to be accurate within about 10 to 15 min. The western component of tilt of the spacecraft was found to be 14.7 ±0.1° from observations of the shadow of the western rim. Thus, the spacecraft is tilted very nearly toward the center of the crater at an angle somewhat steeper than the mean local slope of the crater wall, which is 10°. The legs of the spacecraft appear to straddle a shallow crater about 2 m in diameter, tentatively identified in the Lunar Orbiter III photographs of the site (Fig VII-9); footpad 1, on the downhill side of the spacecraft, lies in a shallow north-trending trough.

Because of the convexity of the crater rim, only the western half of the crest of the rim of the crater in which the spacecraft is located is fully visible from the camera. The eastern horizon, as seen from the camera, lies 35 m from the camera and is about 1 m below the eastern rim crest. The trace of the horizon is approximately an ellipse tilted to the east; the horizon rises from a point nearest the camera on the eastern crater wall both to the north and to the south and approximately coincides with the rim crest west of the camera. The camera is inclined 23.5° in a direction 47° north of west; the horizon varies in angular elevation 24° above and 20° below the plane normal to the camera axis. When plotted on a cylindrical projection about the camera axis, the trace of the horizon in camera coordinates is very nearly a smooth sine wave of 44° amplitude and 360° wavelength (Fig. VII-10). The maximum of the sine wave lies approximately in the direction of maximum tilt of the camera.

C. Geology of Surveyor III Landing Site

Small morphologic elements of the landing site include small craters, linear ridges and troughs, and fragmental debris. Small craters account for the

irregularities of largest relief on the inner surface of the main crater in which Surveyor III landed; they are, however, difficult to observe in the pictures because of glare and because the best pictures were obtained under conditions of high Sun. A well developed system of low amplitude ridges and troughs was found on the walls of the main crater and is well portrayed in the Lunar Orbiter III photographs of the landing site. These ridges and troughs are part of the patterned ground characteristic of this part of the Oceanus Procellarum and are probably related to a set of subsurface fractures. The relief of the ridges and troughs is so small, however, that, at the time of writing, they have not been detected in the Surveyor III pictures.

Fragmental debris is readily observed on both the Lunar Orbiter III photographs and the Surveyor pictures of the landing site. Blocks ranging from half a meter to several meters across are detectable in the Lunar Orbiter III photographs, and grains and lumps as small as 1 mm are observable close to the spacecraft in the Surveyor III pictures. The most easily extracted information about the geology of the landing site in the Surveyor III pictures is related to the distribution and characteristics of the fragmental debris and of the layer of this debris, or regolith, which is inferred to underlie the observed surface.

The craters observed in the Surveyor III pictures range in diameter from about 10 cm to about 16 m. Most of the craters smaller than 3 m in diameter are relatively shallow and nearly rimless or have very subdued raised rims. Approximately 25% of the craters that range from 3 m to approximately 12 m in diameter have distinctly raised rims and relatively steep walls; the other craters in this size range are of subdued form. The rims of most craters are composed of material similar in texture to parts of the surface between the craters. It may be inferred that most of the small craters have been excavated in fragmental material similar to that exposed at the surface.

Most craters have a normal cup shape, with walls and floors concave upward; however, one prominent crater over 20 m across, located near the center of the main crater, is dimple-shaped. Most of the craters appear to be irregularly or nearly randomly distributed over the rim, walls, and floor of the main crater, but some of the very shallow rimless craters tend to be aligned approximately in the north-south direction, parallel to one of the major lineation directions of the patterned ground. These aligned craters are probably related in origin to the patterned ground; they may have been formed by subsidence or by drainage of fragmental debris into fractures or fissures. A few irregular, elongated

depressions up to 5 m long are present on the east wall of the main crater where the small craters are most easily observed. These irregular depressions are not parallel with the major lineation directions and are inferred to be of secondary impact origin.

The size/frequency distribution of craters on the rim and within the main crater in which Surveyor III landed has been estimated by combining data obtained from the Surveyor III pictures and from the Lunar Orbiter III photographs. The frequency distribution of craters ranging in size from 25 cm to 4 m was estimated from one sample area (Area 1, Fig. VII-11) on the northeast wall of the main crater for which usable Surveyor pictures were obtained in the early lunar morning. In an area of 450 m^2, 79 craters were counted. From the Lunar Orbiter photograph, 95 craters ranging in diameter from 4 to 25 m were counted in an area of 49,000 m^2. The combined distribution is compared in Fig. VII-12 with the mean crater frequency distribution obtained from Ranger VII through IX pictures and the crater distribution obtained from Surveyor I pictures. It can be seen that the crater size/frequency distribution of the Surveyor III landing site is closely similar to the mean distribution observed on lunar plains by Rangers VII through IX in the size range of 1 to 16 m. The low frequency observed for the Surveyor III site in the size range of 25 cm to 1 m probably is due to incompleteness of the observational data rather than to an actual crater deficiency at the Surveyor III landing site. An unusually large number of craters was observed per unit area at the Surveyor I landing site in the crater size range of 25 cm to 4 m. The difference in the observed distributions may be related primarily to the ease of recognition of very shallow craters in the Surveyor I pictures, as compared with Ranger and Surveyor III pictures.

Lunar patterned ground consists of one or more sets of parallel ridges and troughs, which generally have amplitudes of a few tens of centimeters and wavelengths on the order of 5 to 10 m. This pattern is well developed at the Surveyor III landing site, where the long axes of the ridges and troughs trend in two dominant directions, one slightly west of north and the other about 30° east of north. The intersection of these two ridge and trough sets gives a corrugated appearance to the surface when it is illuminated at very low angles by the Sun. The east wall of the crater was illuminated in such a manner at the time that Lunar Orbiter III photographs were taken; only in this part of the crater is the pattern detectable. Certain rows of subdued craters and more pronounced troughs are oriented parallel with the north-trending element of the patterned ground at the Surveyor landing site.

The pattern is inferred to be controlled by underlying fractures or joints; it may have been developed and sustained by mass movement of fragmental material on the surface, perhaps during seismic agitation, and by drainage of surficial fragmental debris into open joints. A majority of craters aligned in rows parallel with the pattern are inferred to have developed either by subsidence of joint blocks or, like the troughs in the patterned ground, by drainage of surficial debris into fissures that are opened and closed from time to time by shaking caused primarily by nearby impact events.

Bright angular-to-rounded pieces of fragmental debris are the most conspicuous features in the Surveyor III pictures. The observed fragments, which range in size from about 1 mm to 4 m in longest dimensions, are scattered somewhat irregularly and, in most places, sparsely over most of the visible parts of the lunar surface. Except in two prominent strewn fields of coarse blocks, the resolvable fragments occupy no more than about 14% of the surface.

Most of the observed fragments are relatively angular, but some well-rounded fragments are also present which, in most places, appear to be fairly deeply buried in the lunar surface. On the whole, the fragments tend to be equant in shape, but some are distinctly tabular and a few have the form of sharp, narrow wedges. In a few cases, the edge of a wedge-shaped fragment protrudes from the surface in such a way as to resemble a spike or hatchet blade protruding from the lunar surface (Fig. VII-13).

All of the recognizable fragments are conspicuously brighter at high Sun than the rest of the lunar surface. Although the brightness is, in part, dependent upon the orientation of the surface of the fragments, it is clear that the fragments have a higher albedo, in some cases perhaps as much as 30% higher than the average albedo of the rest of the surface.

Over much of the surface, the distribution of fragments appears to be nearly random; locally, however, strewn fields of blocks are present, and at least two examples were found of aligned rows of fragments. In one of these rows lying northeast of the camera, a conspicuously rounded group of fragments trends approximately east-west. These aligned groups of fragments may represent small elements of rays of nearby or distant craters.

The fragments exhibit all variations of apparent position with respect to the surface, from pieces that appear to rest almost entirely on top of the surface (Fig. VII-14) to pieces that appear to be almost completely buried, with only a

small part showing. From qualitative examination of the pictures, the impression is gained that, in the average case, about half of the fragment is buried beneath the surface and half protrudes above it. Rounded blocks, in most instances, seem to be more deeply buried than average.

As in Surveyor I, no examples were found in which a fragment seemed to be perched on a pedestal, as reported from the Luna IX pictures by Lebedinskiy (Ref. VII-2). We believe the pedestals reportedly observed in the Luna IX pictures are an illusion that is, in part, due to the lower resolution of the Luna IX pictures and to the particular conditions of illumination under which they were taken. This illusion can be experienced in observing some fragments in the Surveyor III pictures by viewing the pictures at certain angles and under poor conditions of lighting.

Most of the fragments close to the spacecraft have a peculiar grainy or knobby, or in some cases, pitted texture. The resolvable pits are generally shallow, but on at least one fragment (Fig. VII-15) close to the spacecraft they are nearly as deep as those observed in Rock B at the Surveyor I landing site. On this fragment, the pits may indicate the presence of vesicles in the fragment. Some fragments, notably pieces associated with a strewn field of blocks to the northeast of the spacecraft, have smooth, nearly planar, faces as though they were broken along pre-existing joints or fractures. A number of large blocks, most of which are tabular in form, appear to be laminated or contain planes of weakness parallel to the long dimensions of the blocks. The apparent lamination is expressed as grooves and ridges along the narrow sides of the blocks (Fig. VII-16).

The coarsest blocks scattered about the surface of the Surveyor III landing site occur mainly in two distinct strewn fields. One field (Area B, Fig. VII-17) is associated with a sharp, raised rim crater about 13 m across on the northeast rim of the main crater, and the other field (Area A, Fig. VII-18) with two adjacent subdued craters high on the southwest wall of the main crater. In the case of the strewn field associated with the crater to the northeast (Area B), the majority of the blocks are clearly related to the crater, as there is a rapid increase in spatial density of blocks toward the crater. The crater is also occupied by blocks. The blocks outside are inferred to have been ejected from this crater and to have been derived from material that underlies the rim of the main crater at depths only 2 or 3 m below the surface. The observed blocks are strikingly angular and range from a few centimeters (the limit of resolution) to more than 2 m across. Blocks associated with the more subdued craters to the southwest (Area A) show a similar

range in size, but are more rounded in appearance. The largest of the two southwesterly craters with which these blocks are associated is about 15 m in diameter; it is inferred that most of the blocks were ejected primarily from the larger crater.

In the northeastern and southwestern strewn fields, the size/frequency distribution of the blocks per unit area lies well above the size/frequency distribution for the more normal surface (Fig. VII-19). Because of the relatively large size and number of blocks in each strewn field that could be studied in the Surveyor III pictures, it has been possible to conduct a preliminary statistical investigation of the roundness and degree of burial of these blocks, and the relationship of roundness and burial to the characteristics of the principal crater associated with each strewn field.

In order to obtain a measure of roundness that could be used for statistical studies, a descriptive parameter, here called the roundness factor, was devised that may be obtained from the pictures as follows: Circles are fitted to all of the corners or curved parts of the outline of each block that occult the more distant lunar scene (Fig. VII-20). The geometric mean of the radius of curvature of these corners is then divided by the radius of that circle which just encloses the outline of the block. This ratio is the roundness factor, and, for blocks that are not deeply buried in the surface, it will vary between the limits of 0 and 1. For very round fragments whose tops are just exposed above the surface, it is possible to obtain values of the roundness factor larger than 1, although no values this high were observed for the blocks measured in the strewn fields.

The roundness factor was measured for 25 blocks located within a confined area in each strewn field (Fig. VII-21). Blocks associated with the sharply formed crater to the northeast exhibit a mean roundness of 0.17 with a standard deviation of roundness of 0.11. The blocks associated with the more subdued, rounded-rim crater to the southwest exhibit a mean roundness of 0.33 and a standard deviation of roundness of 0.17. The difference in roundness between these two samples of blocks is significant, by Student's t test, at the 0.999-probability level.

A measurement of degree of burial of blocks in the lunar surface was obtained by the following method. The angle between a line parallel with the horizon that meets the block, where its outline against the more distant lunar scene comes to the surface, and the tangent to the outline of the block at this point was measured on each side of each block (Fig. VII-22). The sum of these two angles for each block divided by 2π radians, here defined as the burial factor, can vary between 0 and 1.

Rounded fragments whose tops just barely show above the surface have burial factors that approach 1, whereas rocks that sit up on the surface and exhibit overhanging sides have burial factors that approach 0.

Measurement of the burial factor for the same 25 blocks in each strewn field that were studied for roundness gave the following results: The mean burial factor of blocks associated with the sharply formed crater to the northeast is 0.62 with a standard deviation of burial factor of 0.09 (Fig. VII-23). The blocks associated with the more subdued, rounded-rim crater to the southwest have a mean burial factor of 0.69 with a standard deviation of burial factor of 0.07 (Fig. VII-23). The difference between these means is significant, by Student's t test, at the 0.995-probability level.

No significant correlation was found between roundness and burial of individual blocks within each strewn field. The linear correlation coefficient between the roundness factor and burial factor for the blocks in the strewn field around the northwest crater is -0.07 and, for the blocks in the strewn field associated with the southwest crater, -0.16. Both of these coefficients are well below the 95% confidence level. If the blocks in both the strewn fields are examined as a single sample, the linear correlation coefficient between roundness factor and burial factor is +0.13, which is also below the level of significance. Examination of the scatter diagram (Fig. VII-24) of burial factor versus roundness factor shows that, while there is no significant linear correlation, there are relatively few blocks in the strewn fields that tend to have high roundness but a low burial factor.

While there is no significant linear correlation between roundness and burial for blocks in a given strewn field of presumably one age, it may be expected that, as individual fresh pieces are added to the regolith of the lunar surface, they start out with relatively high angularity and tend to be perched on top. In time, the fragments tend to become rounded and from time to time will show varying degrees of burial. Thus, for fragments generally mixed together in the debris layer or regolith, there should be a correlation between the roundness and degree of burial. Further studies of the Surveyor pictures will be required to confirm this hypothesis.

In summary, the blocks associated with the more subdued craters have twice as high a mean roundness factor as those associated with the crater with a sharp raised rim, and the blocks around the subdued crater are significantly more buried in the lunar surface than those around the crater with the sharp raised rim. These

results suggest that blocks freshly exposed on the lunar surface tend to be rounded off in the course of time by solid particle bombardment and possibly by evaporation of material by the solar wind or other high-energy radiation. Initially, the ejected blocks tend to be shallowly embedded in the lunar surface, but in time may become partly or completely covered up by ejecta arriving from other parts of the lunar surface. Progressive burial of blocks may take place also as a result of downhill movement of the debris layer by creep.

The size/frequency distribution of fragmental debris at the Surveyor III landing site was studied both in the strewn fields of blocks just described and in four sample areas that lie close to the spacecraft [Area C, Fig. VII-17; Area D, Fig. VII-25(a); Area E, Fig. VII-25(b); and Area F, Fig. VII-25(c)] These sample areas were chosen so that the resolution and area covered would provide particle counts spanning different, but overlapping, parts of the particle size range. All sharply formed, bright fragments recognizable in the relatively high Sun pictures in each sample area were measured and counted. A total of 2205 fragments and grains, ranging in diameter from 1 mm to more than 1 m, were measured.

The integral size/frequency distribution of measured fragments, normalized to an area 100 m^2 for each of the sample areas, is shown in Fig. VII-19. Fragments in the strewn fields associated with the northeast and southwest craters are, on the whole, an order of magnitude coarser than the fragments observed on the more characteristic parts of the landing site. The size distribution of the fragments in each strewn field resembles the size distribution of fragments ejected from impact craters formed in strong rock, such as at Meteor Crater, Arizona (Fig. VII-26).

The integral frequency of fragments for the average surface, outside of the strewn fields of blocks is approximately a simple power function of the grain size with an exponent of about -2.6. This distribution may be compared with a revised size/frequency distribution of fragments observed in the Surveyor I landing site (Figs. VII-27 and VII-28). The power function used to approximate the observational results for Surveyor III has a slightly lower exponent than that obtained for the particles studied at the Surveyor I landing site, which is -2.1. The observed difference between the size/frequency distribution of fragments in the two areas may be within the error of measurement.

We have carried out experimental studies of the relationship between the size/frequency distribution of particles obtained by measuring and counting fragments from a photograph of the surface of a fragmental debris layer and the distribution found by

mechanically sieving the entire layer. Among the different materials studied were samples of the ash and pumice from the volcanic ash flow deposited in the Valley of 10,000 Smokes in Alaska during the eruption of 1912 (Fig. VII-29). The difference between the particle distribution obtained by measurement and counting of grains from pictures and by mechanical sieving for this sample is shown in Fig. VII-30.

It may be seen that the number of small particles counted in pictures of the surface layer of fragments tends to be much lower than the number of small particles found by sieving the entire layer. A similar difference was observed in the study of fragment size distribution of dolomite ejecta from Meteor Crater, Arizona. Theoretically, for each decrease by a factor of ten in size, the number of small fragments per unit volume should increase ten times as much as the number of recognizable small fragments exposed at the surface per unit area. The volumetric size/frequency distribution of fragments in the debris layer of the lunar surface can be represented by a power function with an exponent of approximately -3.

If the volumetric particle size distribution is like the suggested distribution shown in Fig. VII-28, then it follows closely the size distribution of particles that would be expected to be produced by an incident flux upon the Moon of meteoroids with an integral mass frequency distribution which is a simple inverse function of the mass. The present evidence on the mass frequency distribution of interplanetary solid particles in the size range capable of producing the observed fragments on the lunar surface at the Surveyor I and III landing sites indicates that it is very close to a simple inverse function.

The fine-grained matrix of the lunar surface material at the Surveyor III landing site shows a peculiar patchiness of albedo like that observed at the Surveyor I landing site (see Sect. III of Ref. VII-1). Dark rubbly patches commonly occupy small shallow craters. These patches resemble, in some respects, the dark lumpy rims surrounding the imprints of the spacecraft footpads and the material disturbed by the surface sampler. We believe that these patches have probably been formed by breakup of fresh clots of fine-grained material that have been ejected from nearby small impact craters, and that the shallow craters they occupy are very young secondary craters produced by the low-speed impact of these relatively soft clots.

In places, fine-grained material appears to be banked up slightly against the sides of some of the larger blocks protruding above the lunar surface, both in the strewn fields of blocks and around blocks elsewhere with the main crater (Fig. VII-31). Similar banking up of fine material and partial covering of blocks by fine

material was observed around blocks at the Surveyor I landing site. The steep faces of coarse blocks can be considered ballistic traps for small particles sprayed out from nearby parts of the lunar surface, and it is inferred that the banks of fine-grained material have been deposited particle by particle from the particle spray from numerous small nearby impact events.

Imprints in the lunar surface material produced at several of the touchdown points of the footpads of the spacecraft are visible to the east of the camera (Fig. VII-32) and are of interest to compare with the natural disturbances of the surface, such as secondary impact craters. These disturbances also provide clues about the size distribution of fragments beneath the surface. Well developed imprints in the lunar surface lie just upslope from the present position of footpads 2 and 3. At 12, 14.5, and 15 m upslope from the camera are three other well-defined marks left at the site of the second touchdown of the spacecraft (Fig. VII-33). The mark at 12 m was formed by footpad 1 and the two marks at 14.5 and 15 m by footpad 2, which evidently touched the surface twice before the spacecraft lifted clear of the surface on its second ascent under power (see Sect. IV, this report). The imprint of footpad 3 is not clearly distinguishable at the site of second touchdown, although its position can be fairly accurately predicted; the position of this imprint is in a shallow crater, and only a small part of the imprint appears to be visible. The imprints left by the first touchdown do not appear to be visible from the present position of the camera. They lie either beyond the eastern horizon or on a part of the crater wall which is observed only at a grazing angle, where the imprints would be difficult to detect.

We have searched for marks produced by the vernier engine effluent at the second touchdown site of the spacecraft. One such mark may be present near the imprint at 15 m, which we believe was produced by footpad 2. It is possible that this disturbance of the surface was produced by the combined effects of the effluent from vernier engine 2 and the dragging of footpad 2.

The imprints just upslope from footpads 2 and 3 of the spacecraft are nearly flat-bottomed depressions, the floors of which lie a few centimeters deeper than the adjacent undisturbed parts of the lunar surface. Most of the observable parts of the walls of these two depressions are smooth, conical surfaces that conform approximately in shape to the tapered or chamfered part of the underside of each footpad. The wall of the imprint left by footpad 2 is not complete, however, and it is offset, in places, along short distinctive breaks.

The imprint of footpad 2 is nearly encompassed by a raised rim of lumpy material with an albedo significantly lower that that of the undisturbed surface. The raised rim and dark material are absent along a short sector of the edge of the imprint on the upslope side, the side from which the footpad approached the surface. On the downslope side, dark lumpy debris is spread out for an observable distance of at least 0.5 m. Along the east-southeast sector of the imprint, a smooth wall is not present, and dark lumpy material extends from the rim of the depression to the floor. Presumably a smooth sloping surface was produced during penetration of the footpad and later either collapsed or was covered over by dark material slumping down across it.

The dark lumpy rim of the imprint next to footpad 2 resembles the ejected dark rim material around footpads 2 and 3 at the Surveyor I landing site. Apparently, the lumps are mostly aggregates of finer particles formed by breakup of the slightly cohesive lunar surface debris. The observed lumps range from 1 mm to 5 cm across and have a mean diameter of about 1 cm.

The floor of the imprint near footpad 2 exhibits a regular series of very low mounds arranged in a pattern similar to that of a waffle iron. This pattern must have been produced by the bottom of the footpad, the skin of which was evidently pressed slightly into the honeycomb structure of the pad interior. Two small bumps in the depression probably are either small fragments lying on the floor of the imprint or reflect dents in the bottom of the footpad that may have been produced by a hard lunar fragment during the first, second, or third touchdown of the spacecraft. The breaks in the smooth wall are somewhat similar to chatter marks formed on glacial pavements and probably have been formed by downslope distortion of the wall as the spacecraft footpad pulled away in the downslope direction.

The smooth walls and floor of the imprint next to footpad 2 are different photometrically from the undisturbed lunar surface, as indicated in the following section on photometry. Observations of the imprint on several different days during the lunar morning and early afternoon indicate this smooth surface is more like a Lambertian surface than is the natural lunar surface. Much more light is scattered toward the eastward facing camera from the smooth imprint surface than from nearby undisturbed parts of the Moon in the early lunar morning, but in the lunar afternoon the imprint is not brighter than the undisturbed surface. This indicates that the very small irregularities between the grains have been partially smoothed out or filled in by pressure and by sliding of the smooth metallic footpad.

Only part of the imprint near footpad 3 is observable from the camera, but it appears to be somewhat smoother and more regular than the imprint next to footpad 2. Dark lumpy material also forms a partial rim around the imprint near footpad 3, and there are dark streaks in the walls of the depression, probably formed by collapse or drainage of particles down the upslope side of the depression.

The three clearly visible imprints at the site of second touchdown are much less regular in form than those next to the spacecraft. All three are formed on the walls of small craters. Two imprints were left by footpad 2 low on the northeast wall of a crater about 4 m across. The uppermost, and presumably first formed imprint of these two, has a well-defined rim on its upslope side, but none is clearly observable on the downslope side. The lower imprint looks as though it had been formed simply by dragging of the footpad along the crater wall during the second ascent of the spacecraft from the lunar surface. The imprint formed by footpad 1 at the second touchdown site is on the upper part of the east wall of a crater about 1 m across. This imprint, too, has a well-defined wall on the upslope side, formed of dark lumpy material, whereas the downslope side is open toward the center of the crater. The floors of all three of these imprints are relatively smooth and appear to have anomalous photometric properties like those of the footpad 2 imprint near the spacecraft.

Each of the four well-formed imprints observed is generally similar. It may be inferred that the mechanical properties of the lunar surface are rather similar at the positions of all four imprints and that the mechanical properties of the fragmental material at the Surveyor III landing site are closely similar to those of the material at the Surveyor I landing site. (For a detailed discussion of the similarities and differences, see Section IV of this report.)

Disturbances produced in the lunar surface by the surface sampler are similar in several ways to the disturbances produced by the footpads of the spacecraft. The disturbed material tends to form lumps or clots a millimeter to a few centimeters across, like those formed on the raised rims of the footpad imprints, and the disturbed lumpy material has a significantly lower albedo than the undisturbed surface. Where the surface sampler scoop was pressed into the surface in a bearing test, a raised ridge of lumpy material was formed around the depression, which has been interpreted (see Sect. V) to indicate that the fine-grained material at the lunar surface is relatively incompressible or only very moderately compressible. Smooth parts of the scoop left smooth marks or a smooth surface where pressed firmly against the fine-grained fragmental debris. The photometric properties of these artificially smoothed surfaces are like the smooth surfaces in the footpad imprints.

No bright angular hard fragments were uncovered in the trenching operations with the surface sampler, but they would be extremely difficult to detect, if they are scattered through the subsurface material as they are on the surface. The fact that smooth metallic surfaces leave smooth imprints in the lunar fragmental debris does not mean that coarse particles are absent. They are probably sufficiently well dispersed through the finer-grained matrix that they tend to yield when pressed against and tend to be concealed by the matrix in an imprint area.

From the geological standpoint, the most important conclusions to be drawn from the footpad imprints and areas disturbed by the surface sampler are that the lunar surface material is only moderately compressible and that it has relatively low cohesion. It is also important to note that all disturbances of the surface produced by Surveyors I and III exposed darker material at depths not greater than a few centimeters. In all likelihood, the fine-grained fragmental debris of the lunar surface is 20 to 30% lower in albedo at depths of only a fraction of a millimeter beneath the optically observed surface.

D. Interpretation of Geologic Observations

The observations of the lunar surface obtained from the Surveyor III mission, when combined with results obtained from Surveyor I, Ranger and Lunar Orbiter Programs, and observations at the telescope, can be used to infer hypotheses or amplify previous hypotheses about the geologic processes taking place on the lunar surface. The processes of most immediate interest are those which have produced the observed craters and the fragmental debris and which control the observed distribution of craters and fragmental debris. In addition, some inferences may be drawn about processes leading to the observed variations of albedo of the lunar surface and subsurface material.

It should be noted that the small features of the Surveyor III landing site are closely similar, in detail, to the features of the Surveyor I landing site. The characteristics of the craters and fragmental debris and the processes by which these features have been formed and modified are probably closely similar. In short, the lunar surface on the interior of a broad shallow crater on the maria is much like the surface on a relatively level area between the craters.

We infer that most craters observed at the Surveyor III landing site are of impact origin. The size/frequency distribution of the observed craters corresponds

to that which would be produced by repetitive bombardment of the lunar surface by meteoroids, a bombardment sufficiently prolonged that the crater population has reached a steady state or come to equilibrium (Refs. VII-3 through VII-5). In a steady-state population, old craters of a given size are destroyed as rapidly as new ones are formed. From investigations of Ranger and Lunar Orbiter pictures, the upper size limit of the steady-state or equilibrium crater population was found (Refs. VII-3 and VII-6) to be several hundred meters, much larger than any of the craters observed at the Surveyor III landing site.

Some direct evidence for the impact origin of two of the larger craters seen from the Surveyor III camera is provided by the size/frequency distribution of the blocks in the strewn fields associated with these craters. These blocks exhibit the type of size/frequency distribution that is produced by a single impact or explosion cratering event in relatively hard rock.

Some of the craters observed at the Surveyor III landing site are inferred to be of secondary impact origin; some apparently are structurally controlled and probably have been formed either by subsidence or by drainage of fragmental debris into cracks or fissures in the subsurface. Most of the shallow craters that contain patches of dark rubble resemble craters of secondary impact origin investigated by Moore at the White Sands Missile Range (Ref. III-7), which are produced by weakly cohesive clots ejected from primary craters. Some other irregular, elongated craters at the Surveyor III landing site may also be of secondary impact origin. Linear troughs and rows of shallow craters aligned parallel with troughs in the lunar patterned ground are probably produced by drainage or collapse. At the present writing, we have not been able to determine with confidence the number of craters of each different type and presumed different origin.

The observed fragmental debris is inferred to have been derived primarily by the same process of repetitive bombardment that has produced the majority of the craters. The fragments at the surface are evidently part of a layer of fragmental material of low cohesion that is at least as thick as 1 m along the upper parts of the wall of the main crater in which Surveyor landed and may be much thicker near the center of the crater. This layer we refer to as the lunar regolith. The inferred volumetric size/frequency distribution of fragments, derived from the observed size distribution of fragments on the surface, is similar to that which would be produced by repetitive bombardment of coherent rock by meteoroids with a mass frequency distribution like that found from observations of meteors and recovered meteorites on Earth.

Observed fragments in the regolith exhibit some diversity of surface texture and structure and probably have been derived from diverse sources, some nearby and some relatively distant from the Surveyor III landing site. Most fragments are massive, but a few are strikingly tabular in shape and appear to be laminated. Many fragments are pitted, and some may be vesicular. We infer that the large majority of the fragments have been derived from pre-existing relatively strong rock, possibly volcanic flows or lithified volcanic ash flows.

Evidence from the Surveyor III pictures suggests the regolith is subject to creep or mass movement down the slopes of the main crater. As observed in the pictures, blocks and finer fragments tend to "ride" at different levels with respect to the surface, or, to put it in different terms, blocks seem to be stuck into the surface at varying depths. Regardless of apparent depth of burial, the surface is not appreciably deflected as the side of a block is approached. Because of this relationship, we were able to obtain relatively unambiguous measurements of the burial factor for the coarser blocks.

The observed relationship of the blocks to the surface is not that which would be expected if the blocks had been buried to varying depths simply by penetration of the surface on impact or by later covering by fine-grained ejecta from nearby craters. In the former case, because the fine-grained material of the region is relatively incompressible, a small crater would tend to be formed around the blocks and, in the latter case, material would tend to be banked up around the blocks. Some banking of fine material against blocks is observed, but it is a relatively minor effect.

The varying degree of burial of the blocks is probably significantly influenced by slow or intermittent downhill creep or flow of the entire layer of debris. During the flow, blocks that are initially deposited on top of the regolith or buried at only slight depth will tend to sink, if their density is greater than the bulk density of the fine-grained debris and if coarse fragments are not too closely spaced within the fine-grained matrix. The surface of the fine-grained matrix will tend to become smooth during flow; small depressions will tend to be filled in and ridges or banks of debris will tend to be flattened out.

The regolith at the Surveyor III landing site can flow under relatively low stress because it has very low cohesion. This low cohesion is demonstrated by three independent lines of evidence:

(1) Deformation of the lunar surface by the spacecraft footpads, which is similar to the deformation produced by the Surveyor I footpads, is

consistent with the behavior of a near-surface material that is only weakly cohesive. A material with a cohesion between 10^3 and 10^4 dynes/cm^2 has been suggested to give a behavior representative of the lunar surface deformed by the footpads of Surveyor I (Ref. VII-1). Christensen et al. (Section IV of this report) conclude that the cohesion of the lunar soil at the Surveyor III site cannot exceed 7×10^4 dynes/cm^2.

(2) Tests of lunar surface material by the surface sampler show that the behavior of the fine-grained material near the spacecraft is consistent with a low cohesion, between 1×10^3 and 3×10^3 dynes/cm^2, according to Scott, Roberson, and Clary (see Section V of this report).

(3) Presence of raised rims consisting essentially of fine-grained debris around many of the small craters shows the cohesion is generally low at most places visible from the camera. Craters of the size observed with rims of this type can be formed experimentally only in material with a cohesion of about 10^4 dynes/cm^2 or less.

Because of this low cohesion, creep or flow will take place in the regolith on sloping surfaces, if it is shaken or agitated (Ref. VII-9). Agitation or shaking must occur from time to time as a consequence of impact events. Seismic waves are propagated a considerable distance beyond each impact crater that is formed, whether it is large or small. From field observations made by Shoemaker at the Atomic Energy Commission, Nevada Test Site, of mass movement induced by subsequent cratering experiments on the walls of experimental craters formed in alluvium, we estimate that significant creep of the lunar regolith may be induced on sloping surfaces at a distance at least as great as 10 times the crater radius, for each impact cratering event. Most of the seismic shaking that causes creep is probably due to relatively small nearby impact events; only rarely does a large distant impact take place that will induce creep at any given locality. The formation of impact crater present at the Surveyor landing site probably was accompanied by some downhill creep of the regolith over a small area surrounding the crater. In addition to seismic waves produced by impact, seismic waves of sufficient amplitude to cause creep may be produced by internal tectonic activity of the Moon.

Creep of a very thin layer at the top of the regolith may also take place as a result of the thermal expansion and contraction induced by insolation. During an insolation cycle, material tends to expand in a direction normal to the surface and to contract down the gravitational gradient. Because the thermal wave is damped

out rapidly with depth on the Moon, significant expansion and contraction are limited to a layer at most a few centimeters thick. Thermally induced creep may, however, tend to make fine debris near the surface flow around and past protruding blocks.

The main crater in which the spacecraft is located probably has been partially filled in by mass movement of the fragmental debris. The presence of coarse blocky ejecta from superposed craters on the northeast rim and high on the southwest wall show that the fine-grained debris layer is at most a few meters thick on or near the rim of the main crater. No strewn fields of blocks or blocky crater rims occur near the floor of the main crater, which indicates the base of the debris layer is deeper than any of the craters present there. The main crater probably is an old impact crater and initially had a significantly higher rim and deeper floor. Bombardment and mass movement may have reduced the height at the rim by many meters and filled in the floor with a deposit of fragmental debris several tens of meters thick at the center of the crater. The blocks in the northeast and southwest strewn fields are probably derived from the eroded remnants of the original fragmental rim deposit of the main crater, which evidently lies at shallow depth along the rim crest and is exposed from time to time by superposed craters. It is of interest that a relatively large dimple crater is located near the center of the main crater where a thick deposit of fine-grained debris may be present, a deposit required for a large crater to be developed by drainage.

On the basis of observations made from Surveyors I and III, it is now possible to draw two tentative new generalizations about photometric properties of material on the lunar surface: (1) protruding blocks, in all observed cases, have a higher albedo than the fine-grained matrix of the surface, and (2) freshly exposed fine-grained material derived from just beneath the surface has a lower albedo than the undisturbed fine-grained material at the surface. We present here a simple working hypothesis, based on the general model of surface processes given above and on geologic observations given earlier, which accounts for these two general photometric relationships.

From the studies of roundness, we concluded that some process or combination of processes leads to progressive rounding of blocks over the course of time. It was also noted that the angular blocks associated with a relatively sharply formed crater northeast of the spacecraft have smooth planar faces, whereas the surfaces of most other blocks are pitted. This suggests that most of the pits are produced by impact of small particles and that small particle bombardment may be a significant

process leading to the rounding of blocks. Other processes may also contribute to rounding. Sputtering of material from the blocks by solar protons may lead to significant mass loss and rounding. Professor Charles H. Townes has suggested to Shoemaker that ultraviolet radiation may cause appreciable evaporation of atoms from silicates on the lunar surface. We have observed ribs on rounded rocks at the Surveyor I landing site that may have been left by selective or different evaporation of the surfaces of these blocks. Whatever the processes contributing to rounding, it is probably significant that those surfaces from which material is evidently being worn or evaporated away are the brightest surfaces observed from Surveyors I and III.

The general photometric relationships can be explained if it is assumed that the surfaces of particles in the shallow lunar subsurface tend to become coated with a dark substance. This hypothetical substance we will call lunar varnish. On the surfaces of blocks or coarse fragments that have been exposed to space for some time, the lunar varnish is scrubbed off by the processes that produce rounding. Under this hypothesis, the observed albedo of a large block is essentially the same as the albedo that would be observed on a new surface cut through the interior of the block.

The exposed surfaces of the fine particles on the lunar surface also tend to be scrubbed. Because they are mixed fairly rapidly with coated particles just beneath the surface by mass movement and small cratering events, however, the scrubbing is incomplete and the fine-grained material at the surface has a lower albedo than the coarse blocks. In order for material just beneath the surface to remain dark and not have its albedo raised by mixing with scrubbed particles from above, deposition or coating of particles by lunar varnish must take place just beneath the surface. The process of coating may also take place at greater depths as well. Inasmuch as the particles on the lunar surface are turned over or mixed to depths on the order of 1 mm in a period of time on the order of 100 to 1000 yr by small meteroid bombardment, the deposition of lunar varnish must take place fairly rapidly.

The composition of the lunar varnish and the processes by which it might be deposited are problems that remained to be solved. Hapke (Ref. VII-9) has suggested that oxygen-depleted material derived by sputtering may be deposited on the under sides of grains on the lunar surface and on grains just beneath the surface. It now appears that the experiments on which this suggestion was based do not show that the effect can be produced by sputtering. Hapke's experiments did produce a coating

on the grains at very shallow depths, however, as required by our hypothesis. The lunar varnish may be deposited from gases escaping from depth or generated in the fragmental debris layer itself by high-energy charged particle radiation, or it may be deposited by some process or processes that we do not yet have sufficient clues to discover.

E. Photometric Observations of the Lunar Surface Material

Several special, as well as general, photometric studies of the local lunar surface have been undertaken by means of the Surveyor III pictures. Areas of special interest for photometric study were the footpad imprints and the material disturbed by the surface sampler. As in Surveyor I, the landing site was near the lunar equator, and the Sun passed almost directly overhead. The site was, therefore, suitable for a general study of the local photometric function of the surface.

For the purpose of photometric data collection, several observing programs were planned for the Surveyor III mission. The plan consisted of taking pictures at selected steps along the east-west line to obtain photometric measurements in the plane defined by the vectors from the camera to the Sun. Other target areas for pictures were selected at azimuths of ±45, ±90, and ±135° from the east-west line. Pictures taken at lunar noon were of special interest for study of the symmetry of the local photometric function. An additional objective was to measure the variation of the normal luminance factor (normal albedo) of the lunar surface from pictures taken of areas adjacent to the camera's shadow as it progressed (in the lunar afternoon) toward the east. Because of operational constraints and severe scattering of light from the mirror surface, only a small number of pictures suitable for photometric reduction were obtained.

Measurements and reduction of photometric data have been carried out in a manner similar to that used in the photometric analysis of Surveyor I pictures (Ref. VII-1). Film negatives from the television Ground Data Handling System of the Space Flight Operations Facility, Pasadena, California, were measured with a Macbeth spot densitometer. The transfer characteristics of the negatives used and the total television transfer characteristic function for Surveyor III are illustrated in Figs. VII-34 and VII-35. Measurements of the film density of each gray level in pictures of the photometric target on leg 2 of the spacecraft were used to determine the total television transfer characteristic function. This function was

then used to determine scene luminance of areas of interest from the measurements of film density. The photometric geometry was calculated in terms of the vector normal to the local surface, the vector to the camera, and the vector to the Sun. For convenience, these vectors were referred to lunar coordinates.

Several problems were encountered in the reduction of photometric data from the Surveyor III pictures. The most important and the most difficult problem to evaluate is the large amount of space light that was scattered from the camera mirror into the television images. The pattern of this scattered light varied as a function of the mirror azimuth and elevation angles and of the Sun's positions. Light scattered from the mirror was also present when the mirror was turned away from the Sun; thus a significant amount of scattered light was derived from the luminous flux re-emitted by the terrain. As a start toward evaluating the contribution of scattered light to television images, pictures were taken in wide angle of the photometric target on the omnidirectional antenna B, after stepping the mirror in both azimuth and elevation to position the photometric target in various parts of the pictures. An estimate of the contrast attenuation due to scattered light can be made from these pictures, if it is assumed that the luminance of the objects in the pictures remains constant over the short period in which they were taken. This attenuation is illustrated in a narrow-angle picture of the photometric target on leg 2 of the spacecraft, shown in Fig. VII-36. Measurements of the density of the spacecraft shadow observed in the lunar afternoon (Fig. VII-37) can also be used to provide information on the pattern and intensity of the scattered light.

Several areas of special interest were chosen for a preliminary reduction of film densities to photometric units. These areas include the undisturbed surface in the vicinity of footpad 2, the footpad imprint next to footpad 2, an area disturbed by the surface sampler, and the debris deposited on footpad 2 by the surface sampler.

Examination of 14 measurements of the luminance of a small undisturbed area of the surface in the vicinity of footpad 2 indicates the photometric function of this area is similar to that observed at the Surveyor I landing site and that of other mare areas observed at the telescope. The estimated normal luminance factor (normal albedo) of this area is 8.5%. This calculated value has an estimated uncertainty of at least 25% because of uncertainty in the correction required for light scatter from the mirror.

Pictures were taken several times during the lunar day of the floor of the imprint of footpad 2 next to the present position of the footpad; a few photometric

measurements from these pictures have been reduced. The photometric function of this smoothed surface is conspicuously different from that of the undisturbed lunar surface, but the extent to which the function has been changed has not as yet been determined. The calculated luminance factor of the imprint floor is 30% greater than that of the adjacent undisturbed surface, at phase angles of approximately 40 to 60°.

During operation of the surface sampler, a sample of fine-grained material from the subsurface was placed on footpad 2. The measured part of the photometric function of this material does not differ in form appreciably from the function measured on the undisturbed areas; the normal luminance factor for this material is estimated to be about 7.6, about 10% less than that of the undisturbed surface. An area on the lunar surface disturbed by the surface sampler, on the other hand, has an estimated normal luminance factor of 6.6, about 20% less than that of the undisturbed surface. It should be emphasized that these preliminary estimates have large possible errors because of uncertainties about the amount of light scattered from the mirror into the image formed on the vidicon target.

F. Colorimetric Observations of the Lunar Surface

Color is commonly used in terrestrial geological studies as an aid in discriminating between rock types and in distinguishing the weathering state of rocks. Color filters were incorporated in the Surveyor III television camera, essentially for the same purpose. Because only a limited number of filters could be used in the television camera, three-color colorimetry was selected as the best method for measuring and describing the colors observed with the camera (Ref. VII-10).

A technique suggested by Davies and Wyszecki (Ref. VII-11) was utilized for selecting color filters to fit the response of the television camera approximately to the $\bar{x}(\lambda)$, $\bar{y}(\lambda)$, $\bar{z}(\lambda)$ color-matching functions of colorimetry. Two filters are used in series in the optical train of the camera. The filter glass components had to be 1 mm or more in thickness in order to withstand the vibration and rigors of space flight. Because of weight constraints, the filter pairs were limited to a total thickness of 3.0 mm. A special computer program was used for determining the ideal thicknesses and combinations of filters required to fit the Surveyor III camera system spectral response to the CIE color-matching functions; the fit obtained is fairly good (Fig. VII-1). The filters were coated with a neutral density deposit of Inconel so that, without varying the aperture, approximately equal video signals would be produced by exposure to a daylight source.

In order to measure color from the television pictures, it is necessary to determine the camera tristimulus values, which are proportional to the video voltage. The proportionality factors may be determined by measuring the video signal when the camera is exposed to object colors of known spectral radiance. Tristimulus values for the Surveyor III camera were determined by observing a 3 x 3 matrix of filter-source combinations prior to launch; the proportionality factors were obtained by least-squares solution. The chromaticity coordinates of these nine filter-source combinations were calibrated with a spectroradiometer.

The spectral response of the vidicon tubes used in the Surveyor television cameras is sensitive to temperature. Variation of the spectral response of the Surveyor III television camera with temperature was not calibrated prior to flight; thus, tristimulus values obtained from measurements of pictures of calibrated color targets, taken on the lunar surface at the operating temperature of the camera, must be used for accurate calculation of color. The color targets were provided as parts of the two photometric targets mounted on the spacecraft. Three colors are present on each target; they were calibrated with a spectroradiometer while irradiated by a known spectral source at various angles of incidence. Because of the contribution of scattered light to the Surveyor III pictures, the measurements of the photometric targets in the pictures must be carefully analyzed by computer techniques before a final interpretation of color is made.

Approximately 50 sets of pictures were obtained for colorimetric measurement during the first lunar day of Surveyor III television operations. Each set consists of multiple pictures taken through each of the three color filters. Experience in reducing color measurements from the Surveyor I pictures indicated there were significant variations between the video signals for pictures of the same scene taken in succession. The greatest difference occurred between the first and second pictures. After the third picture the differences were negligible. Therefore, three pictures were taken through each color filter on Surveyor III; the first two are not used for color measurement. All of the pictures in a given set were taken by positioning the camera at one azimuth and elevation setting and rotating the filter wheel through the color sequence in order to avoid incorrect picture registration. The neutral density coatings on the filters permitted all pictures in a set to be taken without change in iris, thus eliminating errors in color measurement due to uncertainty in aperture.

Sets of pictures for colorimetric measurement were taken of various parts of the lunar surface. Some of the larger blocks and the material disturbed by the surface sampler were of special interest. A first attempt to look for color differences has been made by preparing color pictures, by color reconstitution methods, using the preflight calibration for control. Figure VII-38 shows three black and white pictures, taken through the $\bar{x}'$ (red), $\bar{y}'$ (green), and $\bar{z}'$ (blue) filters, that were used to prepare a color picture of the footpad, the photometric target, and the debris placed on the pad by the surface sampler. The known colors on the photometric target, the white surface of the footpad, and the gold tip of the attitude control jet were reproduced fairly well in the reconstituted color picture; the debris is dark gray in color. Figure VII-39 illustrates three pictures taken through each of the color filters of a surface sampler trench and the adjacent disturbed fine-grained material on the lunar surface. The light blue color of the surface sampler was reproduced well in a reconstituted color picture, although the color is somewhat washed out because the image of the sampler was nearly saturated in parts of the pictures; the disturbed material of the lunar surface is a relatively uniform dark gray. No demonstrable differences in color have been observed on any of the coarse blocks so far examined, which are all gray, but lighter than the fine-grained gray matrix of the surface. It will be necessary to digitize the television pictures and analyze the color by computer methods to determine whether subtle color differences are present among the materials observed.

G. Eclipse of the Sun by the Earth as Seen From Surveyor III

An unusual opportunity occurred late in the lunar morning to observe an eclipse of the Sun by the Earth, which took place on Day 114 during the Goldstone pass of the Moon. Were it not for the fact that the spacecraft was tilted as much as 14.7° to the west and was oriented favorably with respect to azimuth, it would not have been possible to observe the Earth from a landing site at 23° W longitude because of the limited range of elevation angles through which the mirror can be stepped. In order to observe the Earth, the mirror was pointed upward, positioned at its highest permissible elevation step, and a wide-angle picture of the eclipse was obtained. The image of the Earth was reflected from a part of the mirror very close to its upper edge. During the eclipse, two series of pictures (20 pictures total) were obtained through the color filters. The first series of pictures was obtained at approximately

11:24 GMT; the second set was obtained approximately 37 min later. The pictures were taken at two iris positions and multiple pictures were taken through each filter.

During the eclipse, the Sun passed behind the Earth along a path that brought the position of the center of the Sun, as seen from the Moon, to within 15 min of the sublunar point on the Earth (Fig. VII-40). At the time the Sun was most nearly centered behind the Earth the projected center of the Sun lay northeast of the sublunar point. The sublunar point was at about 172° W longitude and 12.5°S latitude at the time the first series of pictures was taken, and at about 179°E longitude and 12.5°S latitude at the time the second series of pictures was taken. These positions are in the southwest Pacific. The limb of the Earth lay along western North America, the eastern Pacific, eastern Antarctica, the central Indian Ocean, southeast Asia, central China, eastern Siberia, and a short arc across the western Arctic Ocean.

In the first series of eclipse pictures, the Earth is partially surrounded by a halo of refracted light that varies greatly in brightness from one position to another along the limb (Fig. VII-41). A very bright region, approximately 60° in arc length, lies along the northern part of the limb, nearest the position of the Sun. In the majority of pictures taken, parts of the image of the halo in this region are saturated. On either side of this bright region, the halo has a beaded appearance; small bright areas of short arc length are separated from other bright areas by sectors of the halo that are relatively faint. Most of these bright areas or beads are only a few degrees in length, but one relatively bright sector about 20° long is present that cannot be resolved into separate beads. At least 12 beads can be distinguished in the halo.

A gap ranging from about 50° to more than 90° is present in the images of the halo along the eastern limb of Earth. Over most of the arc length of the gap, the halo was too faint to be detected with the exposures used, but over a short sector of the gap the image of the Earth may have been cut off by the edge of the camera mirror.

In the second series of eclipse pictures, the very bright region in the halo shifted to the northeastern part of the limb, following the Sun (Fig. VII-41). More of the eastern limb was bright enough to be detected in the second series of television pictures, and the gap was reduced to an arc length no greater than 40°. At least 18 beads can be distinguished in the halo in the best exposed pictures. Many of these beads occur at nearly the same angular position, relative to the projection of the

Earth's axis, as the beads observed in the first series of pictures (Fig. VII-41). The beads are clearly related to features in the Earth's atmosphere, in contrast to the brightest region in the halo, which is related to the position of the Sun.

In order to identify the atmospheric features controlling the distribution of the beads, each bead's position in the second series of pictures was measured relative to the projection of the Earth's axis. These positions were plotted on the trace of the limb on stereographic projections of the northern and southern hemispheres of the Earth. The plotted positions of the beads were then compared directly with stereographic mosaics of ESSA 3 pictures of the Earth taken on the day preceding the eclipse [Fig. VII-42 (a) and (b)]. Even though there was some shift in cloud patterns between the time the ESSA 3 pictures were taken and the time of the eclipse, it can be seen that the beads occur predominantly over clear or largely clear regions between the clouds. Clouds tend to occult the refracted rays of the Sun, most of which pass through the low atmosphere at the limb; the beads are localized over clear areas, which can be considered depressions in the optical silhouette of the Earth.

Preliminary reduction has been started on the colorimetric information contained in the pictures. Six pictures, one taken through each of the three color filters during each of the two periods of observation (Fig. VII-43), were digitized using equipment at the Jet Propulsion Laboratory. The video voltage recorded on magnetic tape was divided into 64 equally spaced levels. For calibration, the preflight recording of the 3 x 3 filter matrix was also digitized. Equations for computing tristimulus values were derived from the digital printout of the preflight calibration tape.

The digitization procedure adopted for the television pictures generates a larger number of digital picture elements along a scan line than there are scan lines in the picture; the digital picture is a rectangular matrix of 600 x 684 elements. In the first series of pictures, the image of the refraction halo is 54 lines high and 61 picture elements wide. The total number of picture elements yielding colorimetric data in each of the digitized pictures from this series was 644. Chromaticity coordinates for selected picture elements were calculated, by means of the tristimulus value equations, from the digital voltages of corresponding elements in pictures taken through each of the three color pictures. Because of present uncertainties about the preflight calibration tapes and because of possible jitter or other displacement of image points in corresponding pictures, the calculated chromaticity coordinates may have an error as much as 0.03 in x and y.

Chromaticity coordinates were calculated for 18 points on the images in the first series of eclipse pictures and were plotted on a chromaticity diagram (Fig. VII-44). The location of these colorimetric measurements with respect to the eclipse images is shown in Fig. VII-45. Also plotted on the chromaticity diagram are the locus of color temperatures for a body which obeys Planck's law (a blackbody) and the locus of color temperatures for natural daylight as far as 4800°K. Loci of correlated color temperature (Ref. VII-12) are shown in Fig. VII-44 crossing the Planckian locus.

Most of the colorimetric measurements were taken in the bright region of the halo controlled by the position of the Sun. The majority of measurements in this region have a correlated color temperature close to 4800°K. Beads in the halo exhibit lower correlated color temperatures. The center of bead G, close to the bright region, has a correlated color temperature of about 4000°K, and the center of bead A, which lies over Anarctica, farthest from the projected position of the Sun, has a correlated color temperature of approximately 2850°K. The correlated color temperature tends to decrease in directions away from the projected position of the Sun and also tends to decrease toward the inner edge of the halo. As would be expected, the color temperature tends to be lower for light that followed paths of greater atmospheric absorbtion. Most of the colors present in the images had purities less than 50%.

H. Partially Illuminated Earth as Seen From Surveyor III

During the period from 10:29 to 11:06 GMT on Day 120, 25 pictures of Earth were taken with the Surveyor III camera in the wide-angle mode. The angle of elevation was too great for pictures of the Earth to be taken in the narrow-angle mode. The images were obtained using the three color filters (red, blue, green), and a color picture of the Earth has been reconstituted from a selected set of three pictures. A diagram of the orientation of Earth and the theoretical position of the sunrise line and corresponding series of pictures taken through each filter position are shown in Fig. VII-46. The bright areas in the pictures are cloud covered; clouds can be seen to extend over most of the Atlantic Ocean and the northern coast of South America. Parts of the Caribbean Sea and southwestern Brazil appear to be free of clouds.

As the distance between centers of the television lines is about 2.5 minutes of arc, the details shown in the Surveyor III pictures of the Earth are comparable to

the details recorded in good quality telescopic photographs of Mars, near opposition, or observed visually with a telescope of about 8-in. aperture.

A preliminary analysis of the Earth pictures by color reconstitution indicates the clouds are white, whereas the areas free of clouds vary in hue from greenish blue to purplish blue. The colors are similar to those recorded and seen by the Mercury and Gemini astronauts.

REFERENCES

VII-1. Surveyor I Mission Report. Part II: Scientific data and Results, Technical Report 32-1023, Jet Propulsion Laboratory, Pasadena, California, September 10, 1966.

VII-2. Lebedinskiy, A. I., Scientific Results of Processing of Panoramas from Photographs of the Lunar Surface Taken from Luna-9, from reprint of the USSR Academy of Sciences Izdatel'stvo NAUKA. National Aeronautics and Space Administration, Goddard Space Flight Center, Contract No. NAS-5-9299. ST-LPS-10493/Revision 1, 1966.

VII-3. Shoemaker, E. M., Preliminary Analysis of Fine Structure of the Lunar Surface in Mare Cognitum, in The Nature of the Lunar Surface, Proceedings of the 1965 IAU-NASA Symposium, The John Hopkins Press, (Hess, W. N., Menzel, D. H., O'Keefe, J. A., editors), p. 23-78, 1966.

VII-4. Trask, N. J., 1966, "Progress in the Analysis of the Fine Structure and Geology of the Lunar Surface From the Ranger VIII and IX Photographs," Rangers VIII and IX. Part II: Experimenters' Analyses and Interpretations, Jet Propulsion Laboratory, California Institute of Technology, Technical Report 32-800, p. 252-267, March 15, 1966.

VII-5. Marcus, Allen, "A Stochastic Model of the Formation and Survival of Lunar Craters. V. Approximate Diameter Distribution of Primary and Secondary Craters," Icarus 5, No. 6, pp. 590-605, 1966.

VII-6. Gault, D. E. et al.,"Criteria for Equilibrium Crater Distribution on Lunar Surface," to be published.

VII-7. Moore, H. J., and Lugn, R. V., A Missile Impact in Water-Saturated Sediments, in Astrogeologic Studies Annual Progress Report, July 1964-July 1965, Part B: p. 101-126. U. S. Geological Survey Open-File Report, 1965.

VII-8. Titley, S. R., 1967, "Seismic Energy as an Agent of Morphologic Modification on the Moon," in Astrogeologic Studies Annual Progress Report, July 1965-1966, Part A: U. S. Geological Survey Open-File Report, 1966.

VII-9. Hapke, B. W., Optical Properties of the Moon's Surface, The Nature of the Lunar Surface, proceedings of the 1965 IAU-NASA Symposium, The John Hopkins Press, p. 141-154, 1966.

VII-10. Rennilson, J. J., 1965, "A Television Colorimeter for Lunar Exploration," proceedings of the 8th International Colour Meeting, Lucerne, Switzerland, Centre d'Information de la Couleur, 23 Rue Notre-Dame-des-Victories, Paris, June 1965.

VII-11. Davies, W. E., and Wyszecki, G., "Physical Approximation of Color-Mixture-Functions," J. Opt. Soc. Am. 52, N. 6., p. 679-685, June 1962.

VII-12. Judd, D. B., MacAdam, D. L., and Wyszecki, G., Spectral Distribution of Typical Daylite as a Function of Correlated Color Temperature, J. Opt. Soc. Am. 54, N. 8, p. 1030-1040, 1964.

VII-13. Nayatani, Y., and Wyszecki, G., Color of Daylight from North Sky, J. Opt. Soc. Am. 53, N. 5, p. 626-629.

ACKNOWLEDGMENT

Special appreciation is extended to Raymond Jordan, Jo Anne Jordan, and S. G. Priebe of the U. S. Geological Survey, and Sayuri Harami and Patricia B. Fisher of the Jet Propulsion Laboratory for help in the reduction of the television data and in the preparation of this report.

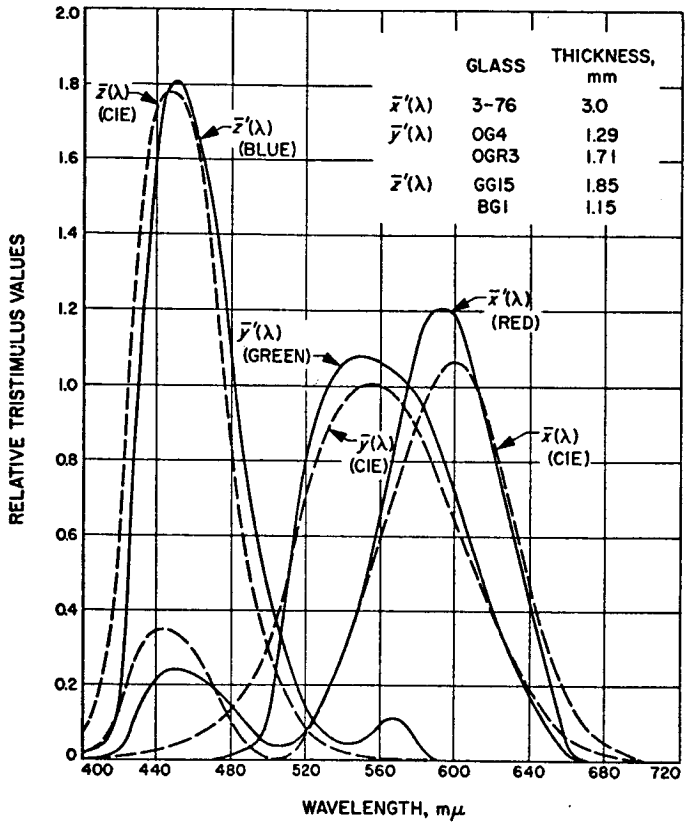

Fig. VII-1. Camera-filter spectral response functions of Surveyor III camera compared with CIE (Commission Internationale l'Eclarage 1931) color-matching functions. Camera-filter spectral response functions shown with solid line. CIE color-matching functions shown with dashed line.

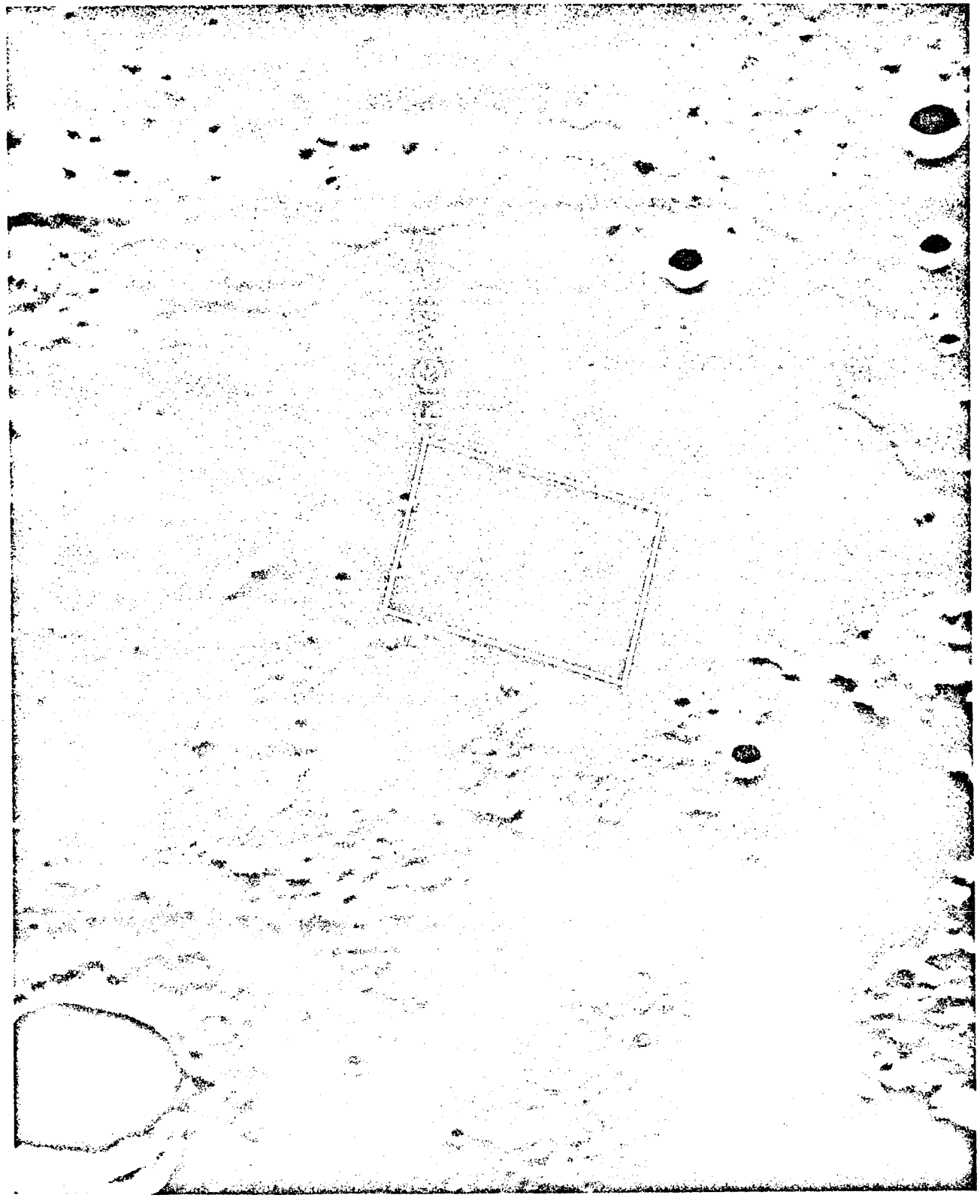

Fig. VII-2. The crater Lansberg and region to southeast, showing Surveyor III location (small circle) and outline of Lunar Orbiter III photograph M154 (University of Arizona Lunar and Planetary Laboratory 61-in. reflector photograph)

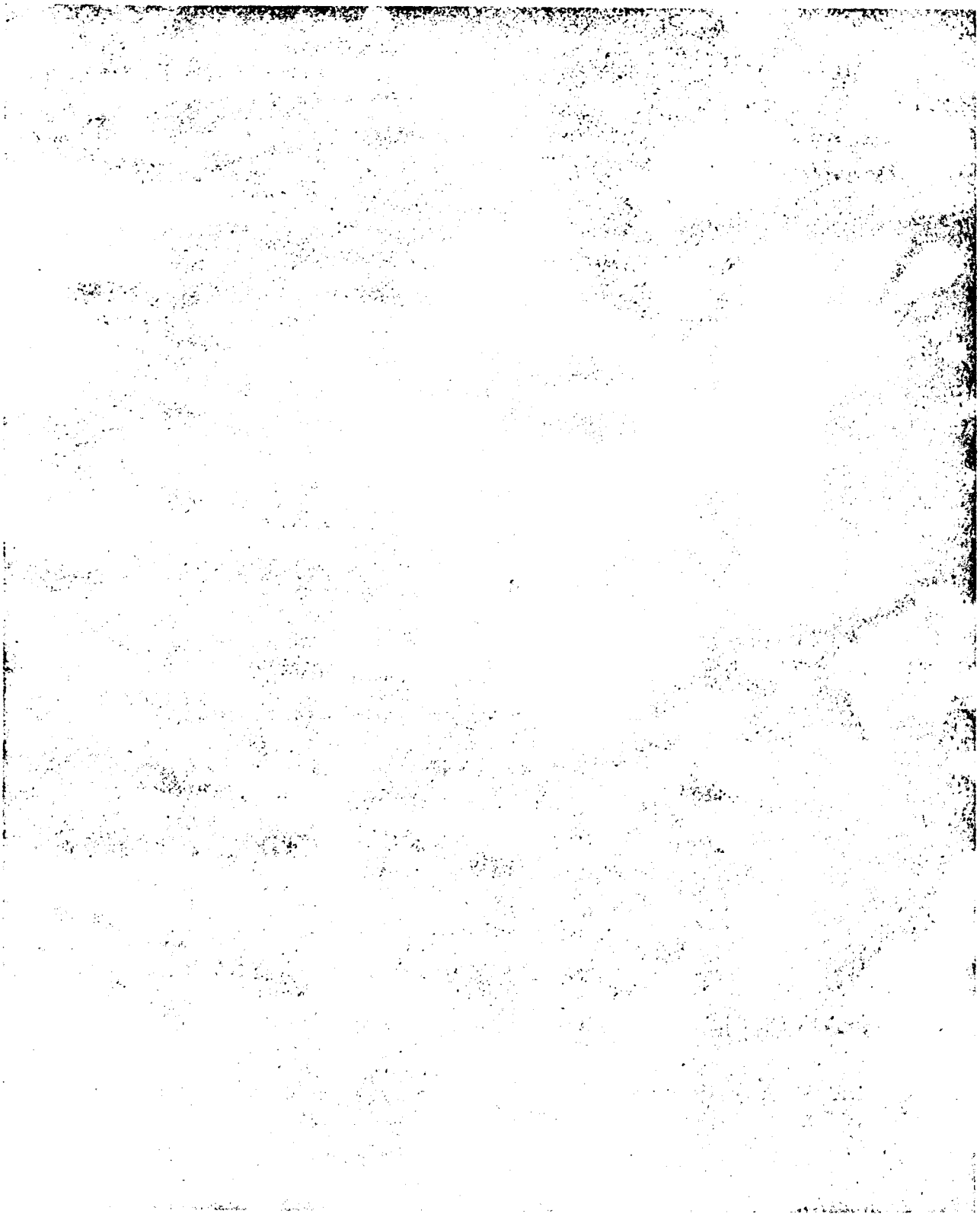

Fig. VII-3. Same region as Fig. VII-2 with full Moon illumination, showing relationship between Surveyor III location (small circle) and Copernicus rays (Yerkes Observatory 40-in. refractor photograph)

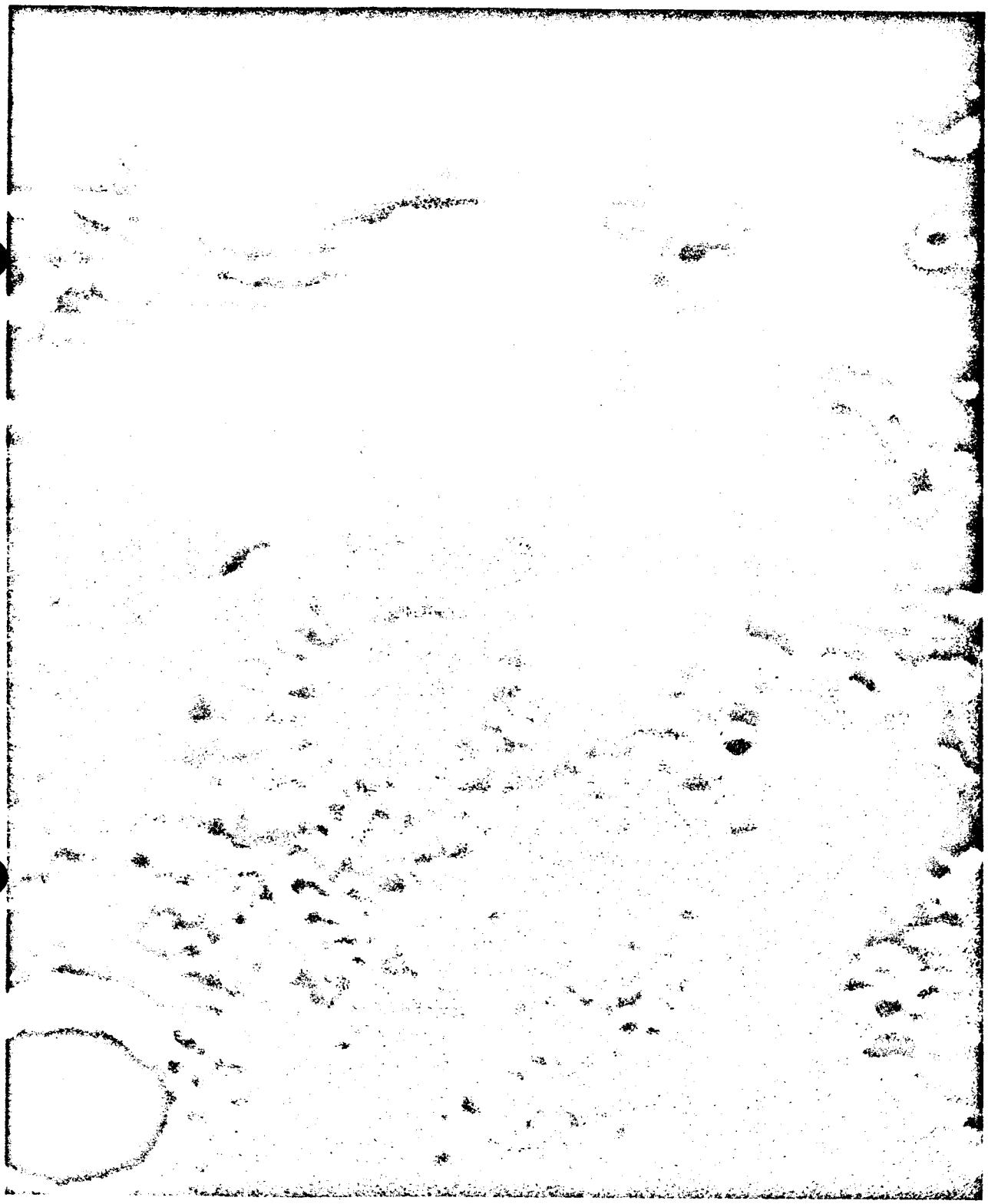

Fig. VII-4. Same region as Figs. VII-2 and VII-3 with low evening illumination, showing low mare ridge segments northeast of Surveyor III (McDonald Observatory 82-in. reflector photograph)

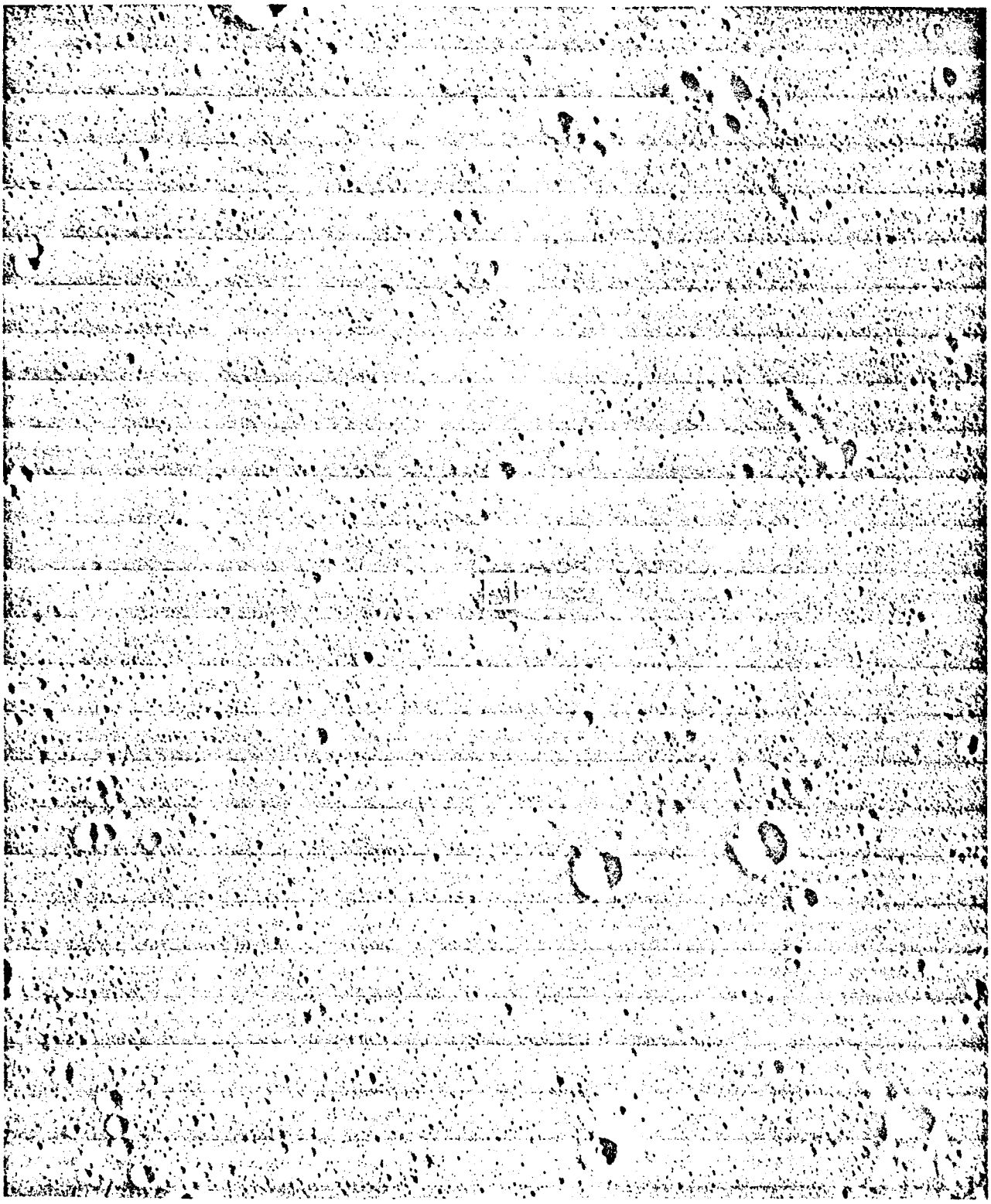

Fig. VII-5. Lunar Orbiter III medium-resolution photograph M154, showing outline of Fig. VII-6

Fig. VII-6. Small part of Lunar Orbiter III high-resolution photograph H154, showing location of Surveyor III in 200-m-diameter crater. The small triangle represents the true size and orientation of the spacecraft.

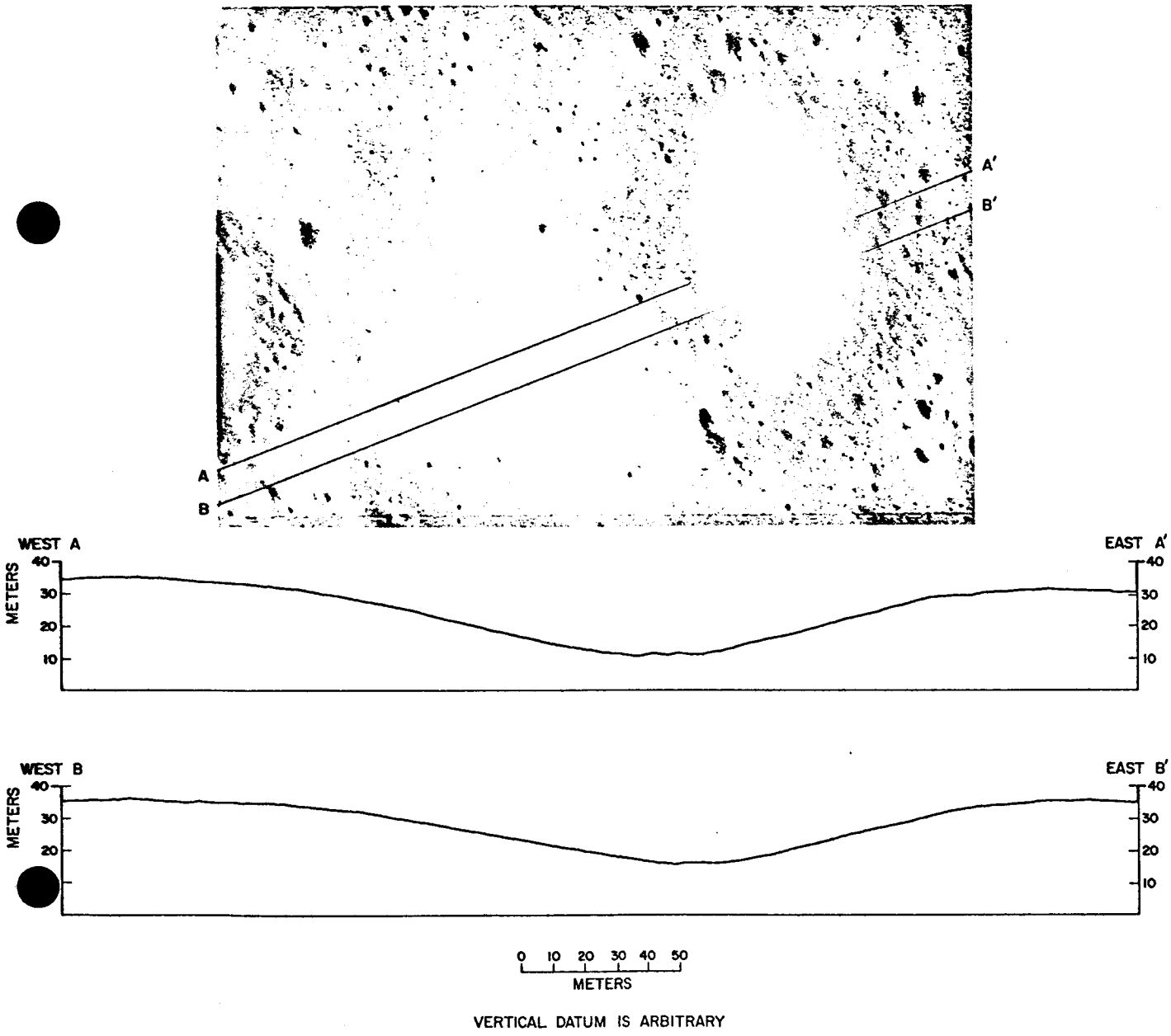

Fig. VII-7. Photoclinometric profiles of the Surveyor III landing site. Profiles were calculated from photometric measurements of Lunar Orbiter III photograph H154, framelet 27, along lines AA' and BB' (photoclinometry by H. E. Holt and S. G. Priebe).

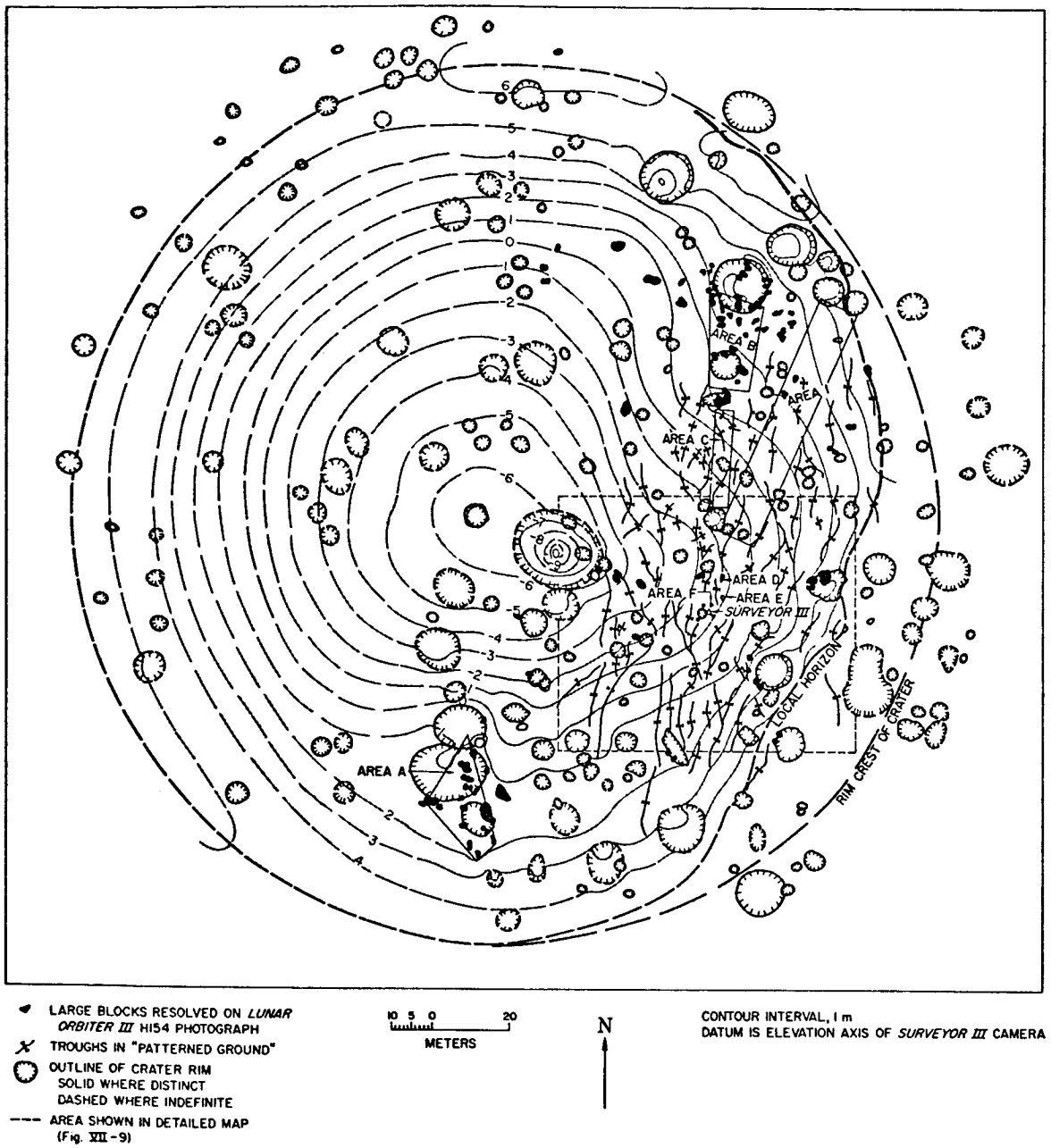

Fig. VII-8. Contour map of Surveyor III landing site, showing craters and blocks resolved in Lunar Orbiter III photographs, the local horizon as observed from the Surveyor III camera, the rim crest of the main crater, and areas studied in detail with the Surveyor III pictures. Contours were plotted using information obtained from Lunar Orbiter III photographs and from Surveyor III pictures (topography by R. M. Batson and Raymond Jordan; geology by E. C. Morris and E. M. Shoemaker).

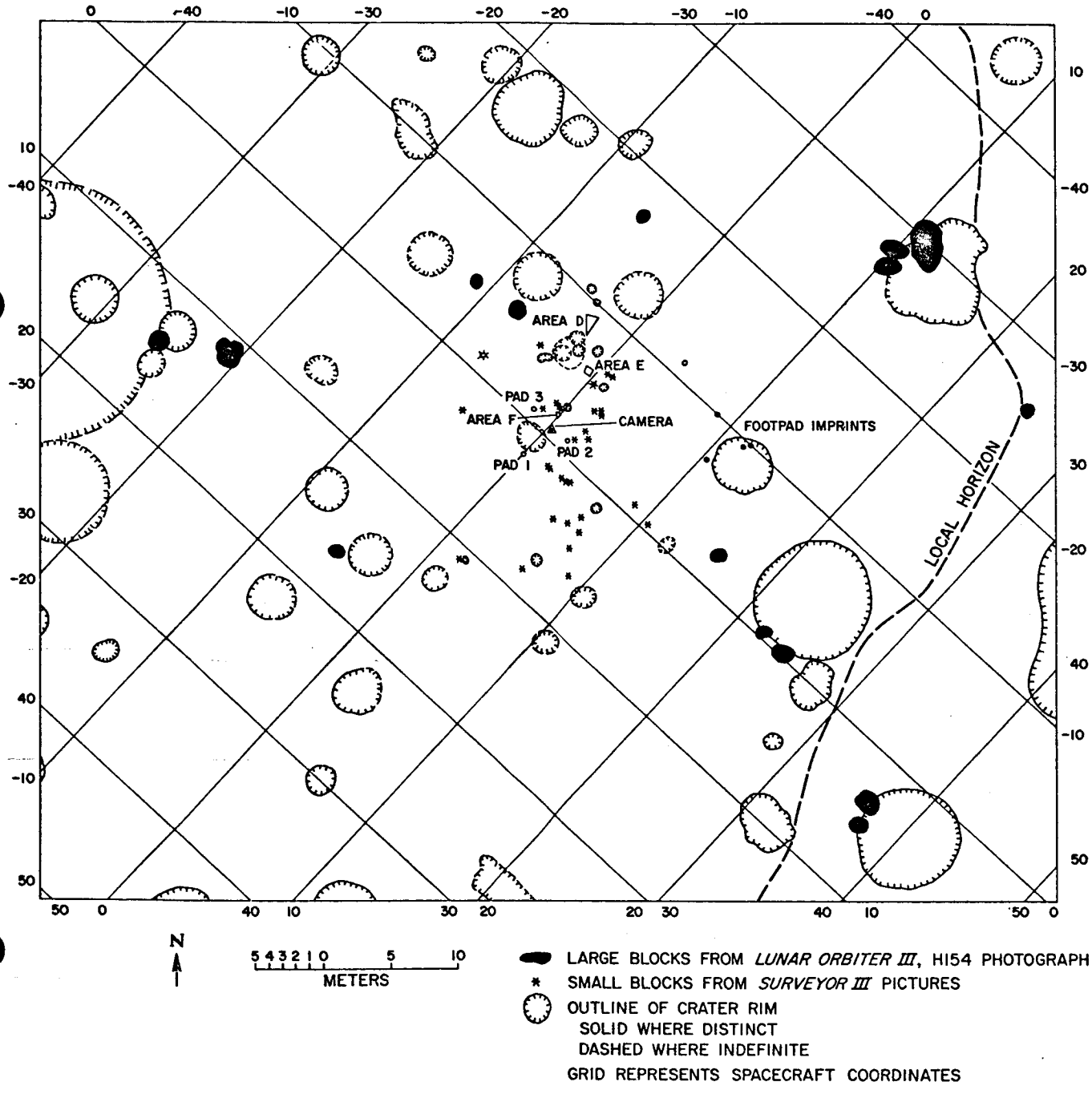

Fig. VII-9. Detailed planimetric map of area around Surveyor III spacecraft, showing craters and blocks, the local horizon, areas studied for size distribution of fragmental debris, the present position of the footpads and camera of Surveyor III and the position of footpad imprints made during the second touchdown of the spacecraft. The position of the spacecraft is known to within about 0.5 m (1.5 ft) relative to craters and blocks resolved on the Lunar Orbiter III photographs.

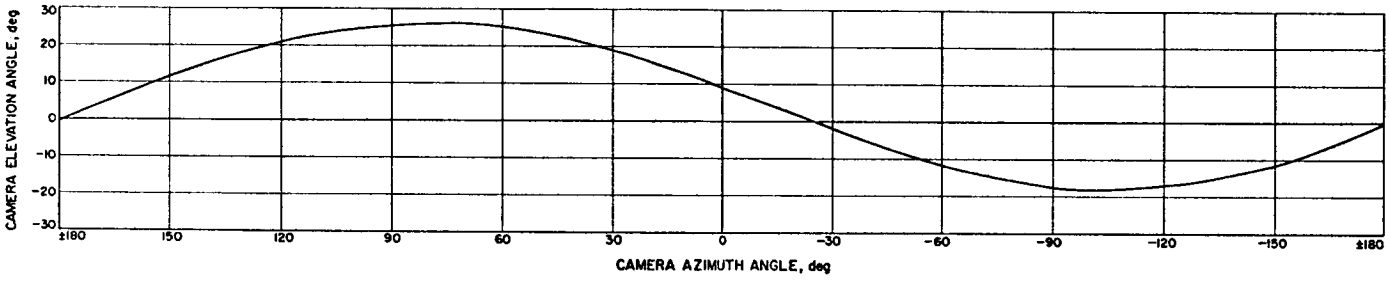

Fig. VII-10. Running average trace of the horizon seen from Surveyor III camera, plotted on cylindrical projection in camera coordinates

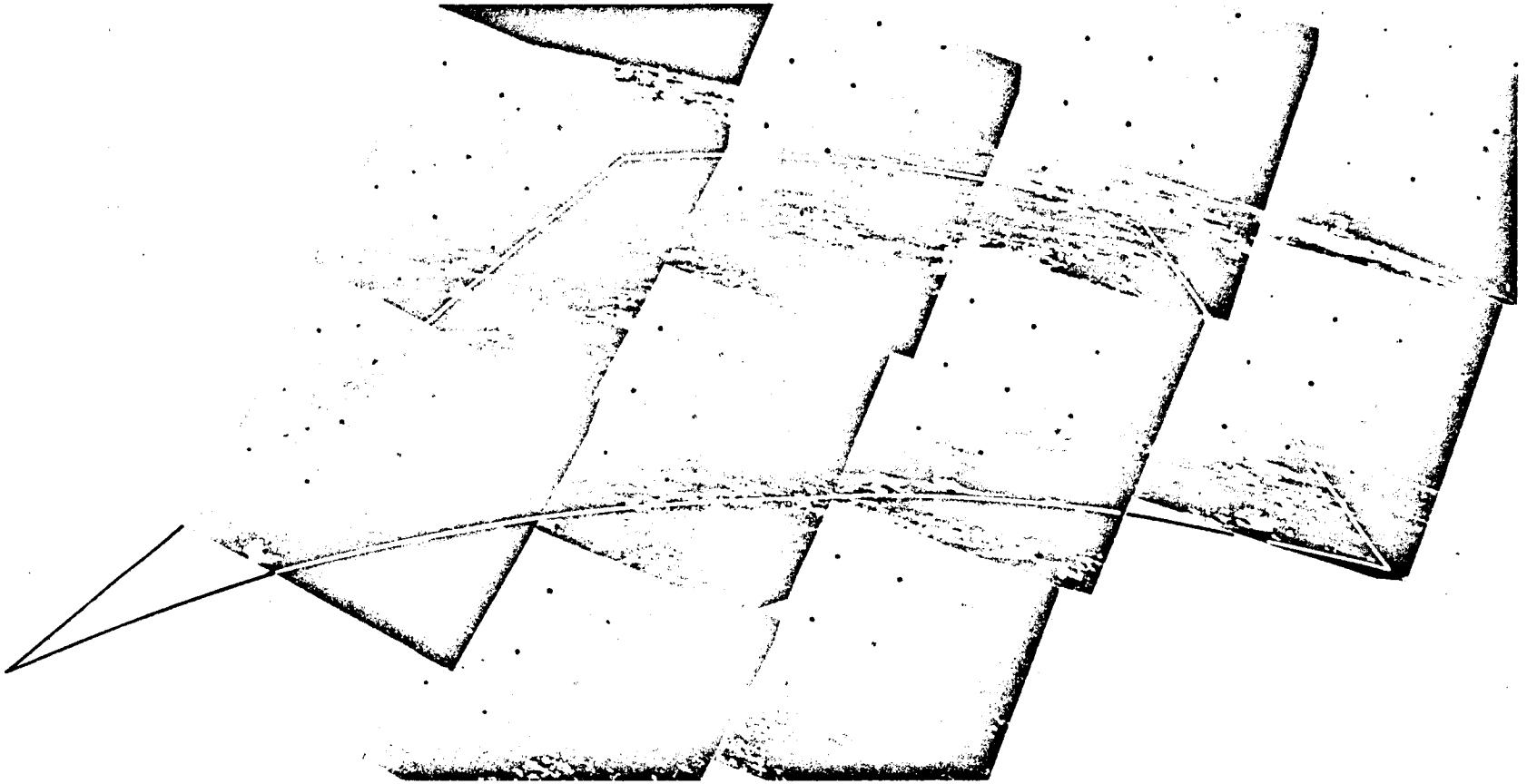

Fig. VII-11. Mosaic of narrow-angle Surveyor III pictures, showing part of northeast wall of crater in which the spacecraft is located. The crater wall is illuminated by the glancing rays of the early morning Sun, which reveal a large number of small craters and many angular fragments of debris strewn across the wall of the main crater. Outline shows boundary of Area 1, which was studied for the size/frequency distribution of small craters (Day 110, 09:37:21 to 09:37:56 GMT).

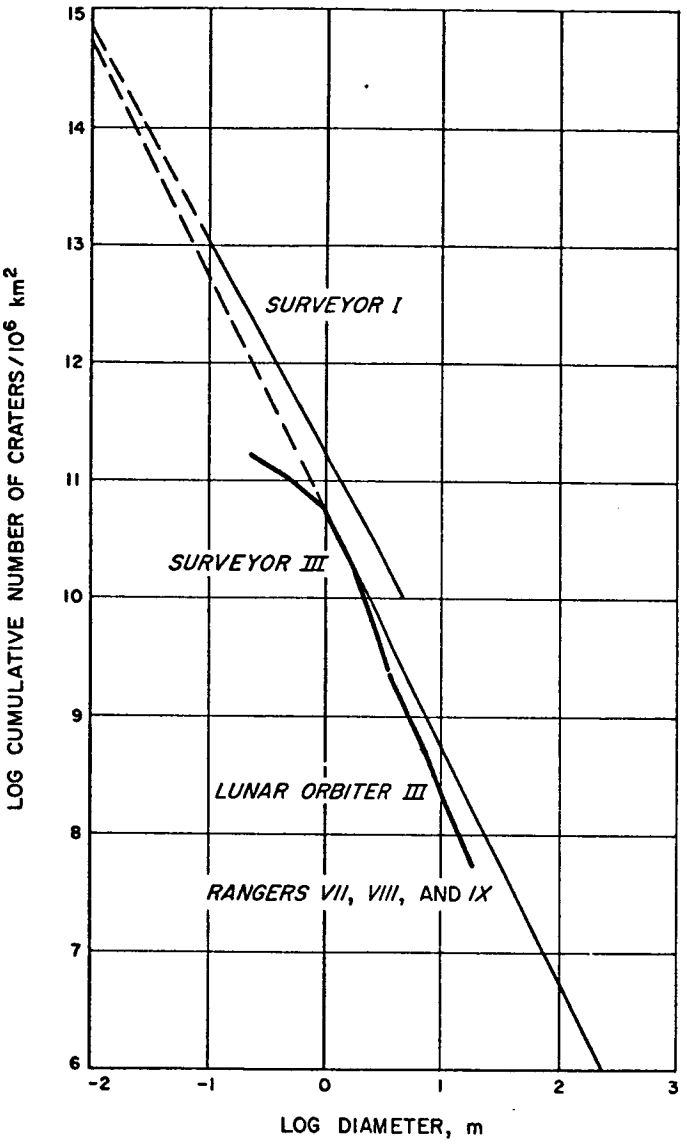

Fig. VII-12. Size/frequency distribution of small craters at Surveyor III landing site compared with the size/frequency distribution of craters estimated for the Surveyor I landing site and the mean size/frequency distribution of small craters on lunar plains determined from Ranger VII, VIII, and IX pictures. The size/frequency distribution of craters at Surveyor III landing site was measured from Surveyor III and Lunar Orbiter III pictures.

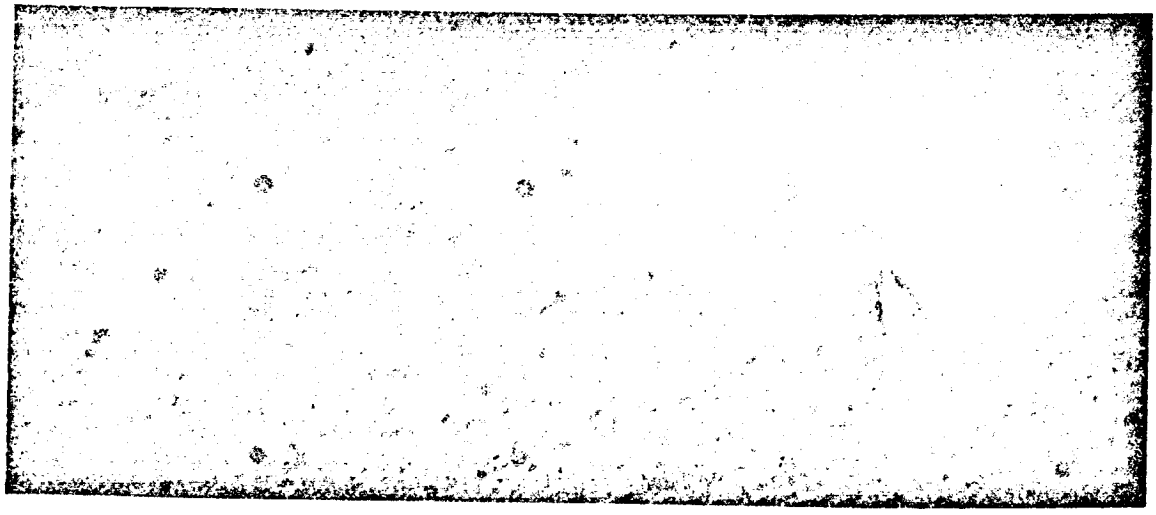

Fig. VII-13. Part of narrow-angle Surveyor III picture, showing area on northeast wall of crater in which the spacecraft is located. Two craters about 1.5 and 2 m in diameter and a wedge-shaped fragment protruding 20 cm above the surface are shown in the picture (Day 120, 14:37:00 GMT).

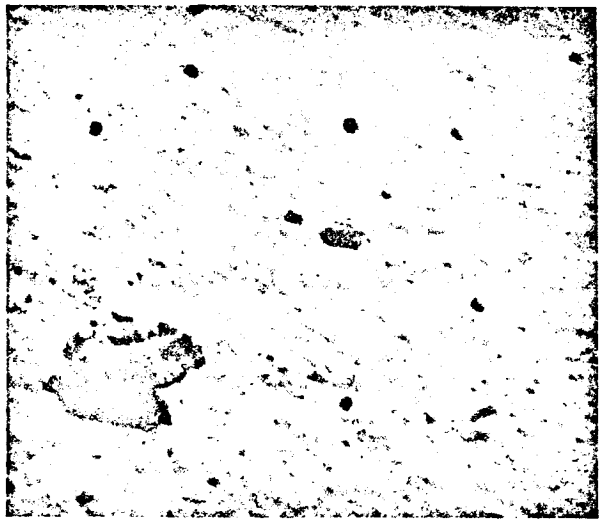

Fig. VII-14. Part of wide-angle Surveyor III picture, showing rounded fragment 20 cm across lying on top of fragmental debris (Day 116, 09:07:06 GMT)

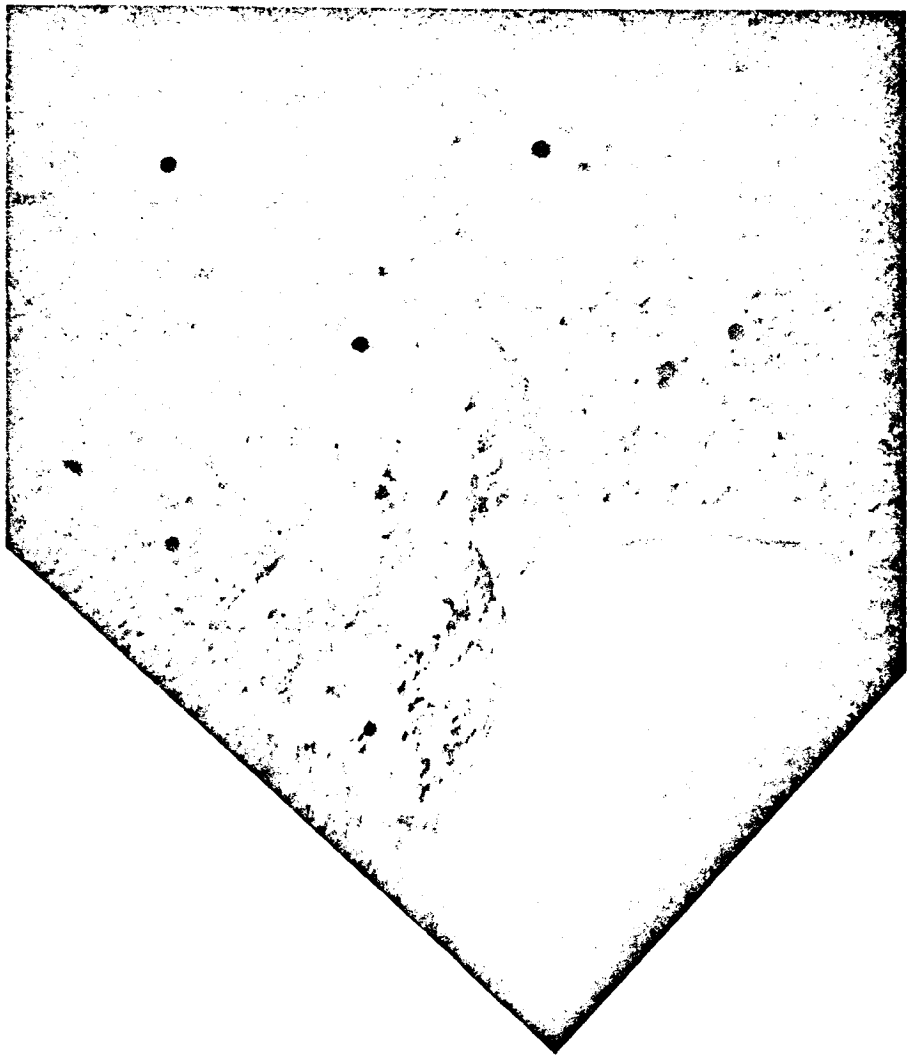

Fig. VII-15. Part of narrow-angle Surveyor III picture, showing rounded fragment lying close to the spacecraft. Fragment is 13 cm high and has small deep pits on the surface. This fragment, like rock "B" seen at the Surveyor I landing site, may be vesicular (Day 120, 14:51:59 GMT).

Fig. VII-16. Part of narrow-angle Surveyor III picture, showing abundant blocky fragments on north wall of crater in which the spacecraft is located. Some of the largest blocks shown are tabular in shape and appear to be laminated (Day 120, 14:52:35 GMT).

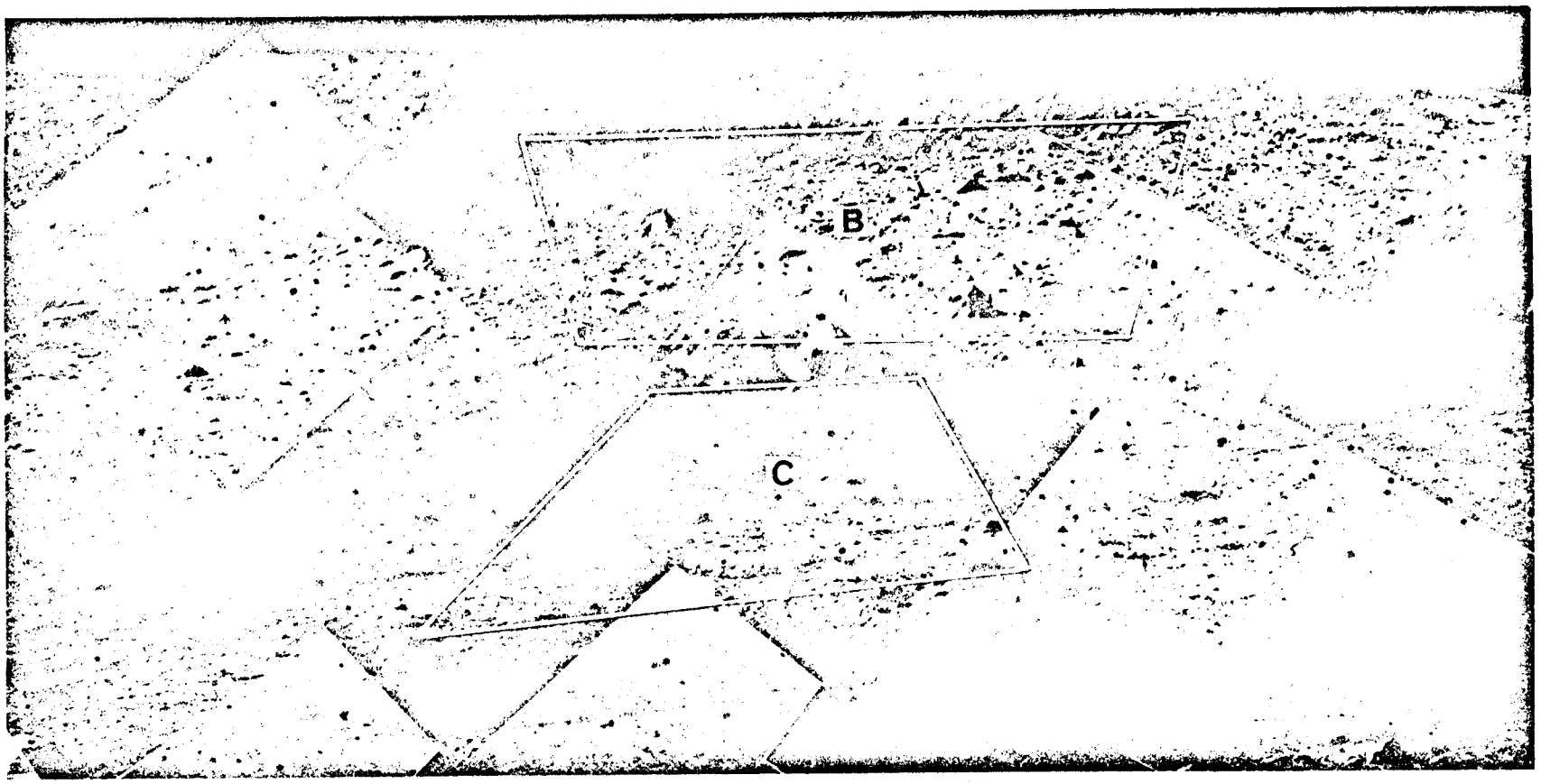

Fig. VII-17. Mosaic of narrow-angle Surveyor III pictures, showing crater 13 m across and associated strewn field of blocks on northeast wall of main crater in which the spacecraft is located. Outlines show boundary of Area B, in which roundness factor and burial factor of blocks were measured, and boundary of Area C, in which size/frequency distribution of fragments was measured (Catalog No. 88SI).

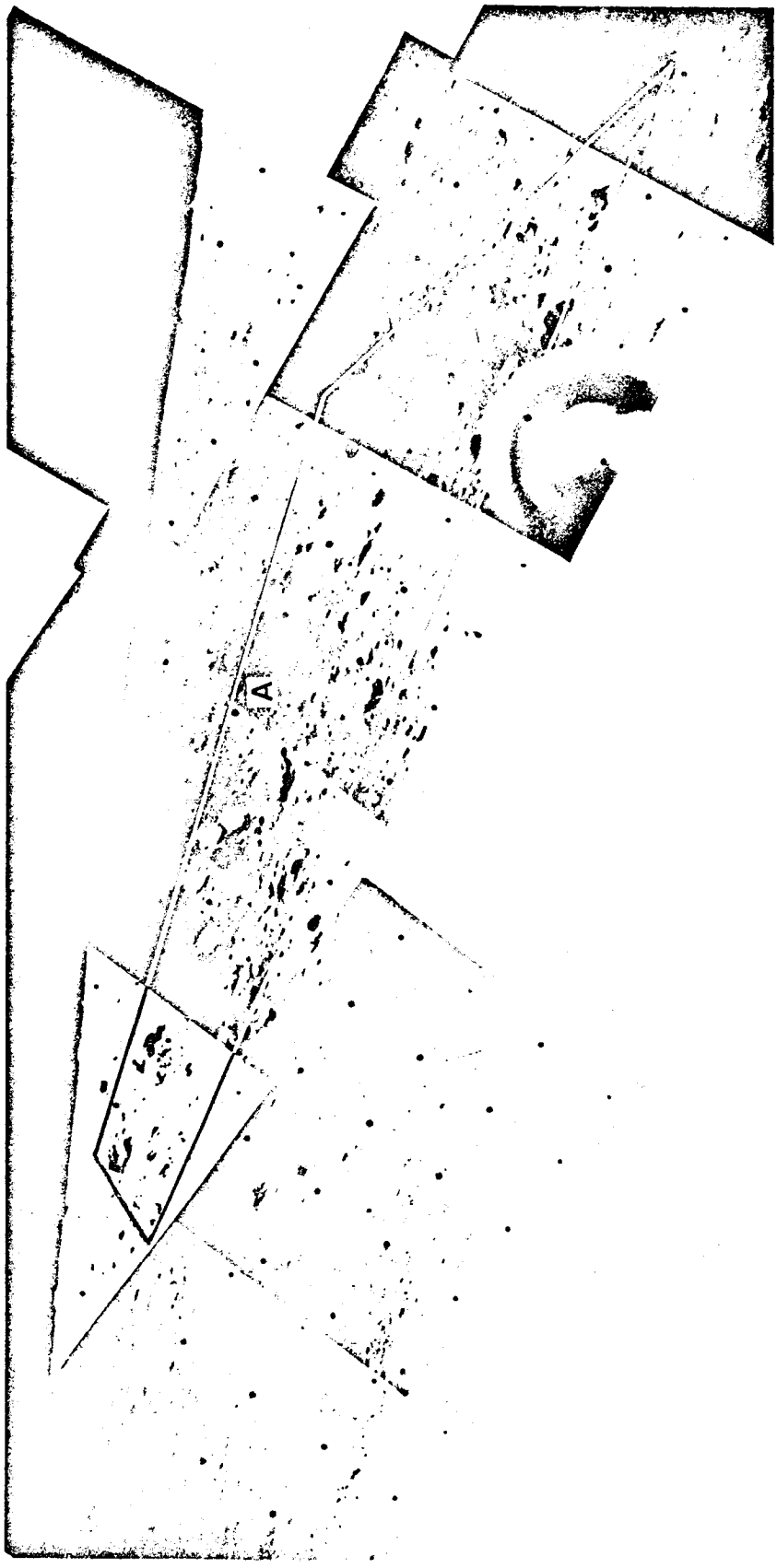

Fig. VII-18. Mosaic of narrow-angle Surveyor III pictures, showing part of southwest wall of main crater and strewn field of blocks. Outline shows boundary of Area A, in which roundness factor and burial factor of blocks were measured. Two subdued rim craters with which the blocks are associated are present, but difficult to discern in these pictures because of high Sun illumination (Catalog No. 87SI, Day 117, 12:49:25 to 13:01:21 GMT).

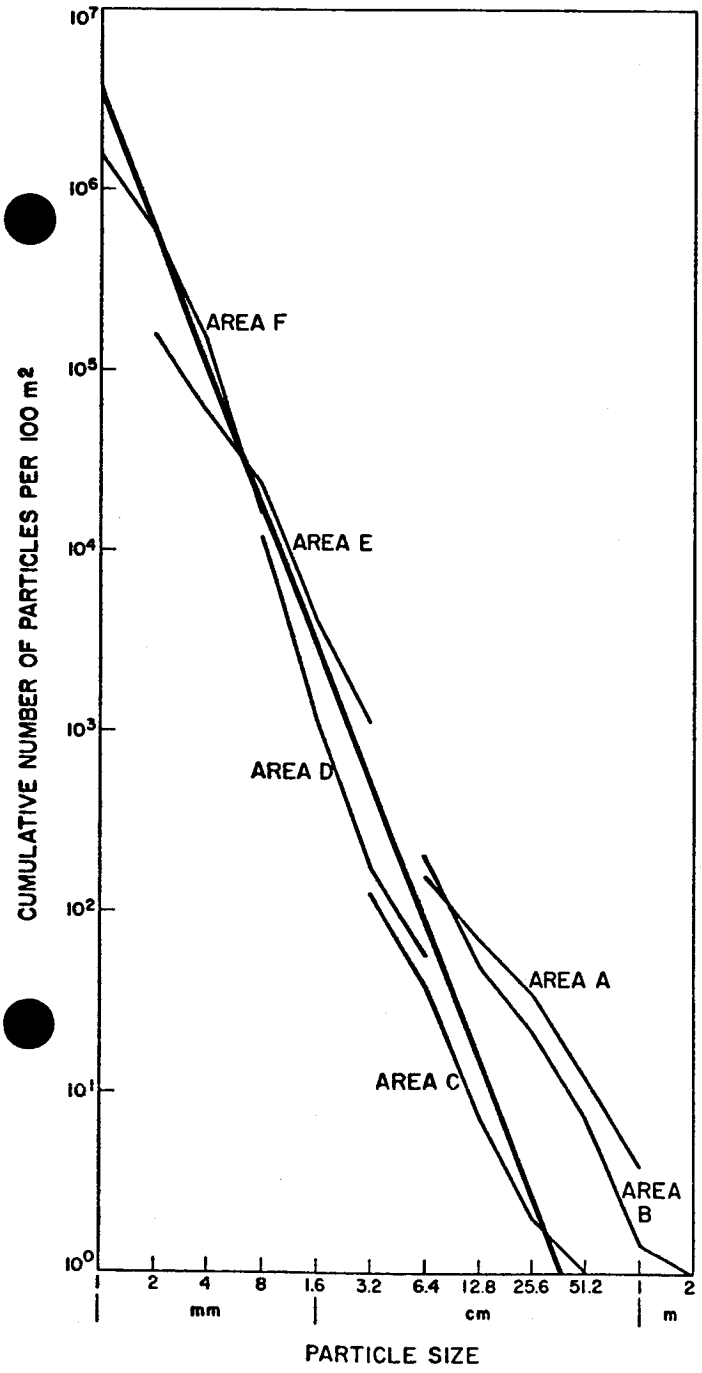

Fig. VII-19. Size/frequency distribution of fragments at the Surveyor III landing site. Location of Areas A, B, C, D, E, and F, in which the size/frequency distribution of fragments was measured, are shown in Figs. VII-8 and VII-9. Mean cumulative size/frequency distribution of fragments on characteristic parts of lunar surface at Surveyor III landing site is shown with heavy line. This line is the plot of the equation $N = 3 \times 10^{6} y^{-2.56}$, where N is the cumulative number of fragments and y is the diameter of fragments in millimeters. Fragments in strewn fields of Areas A and B are larger than those observed in the more characteristic parts of the lunar surface.

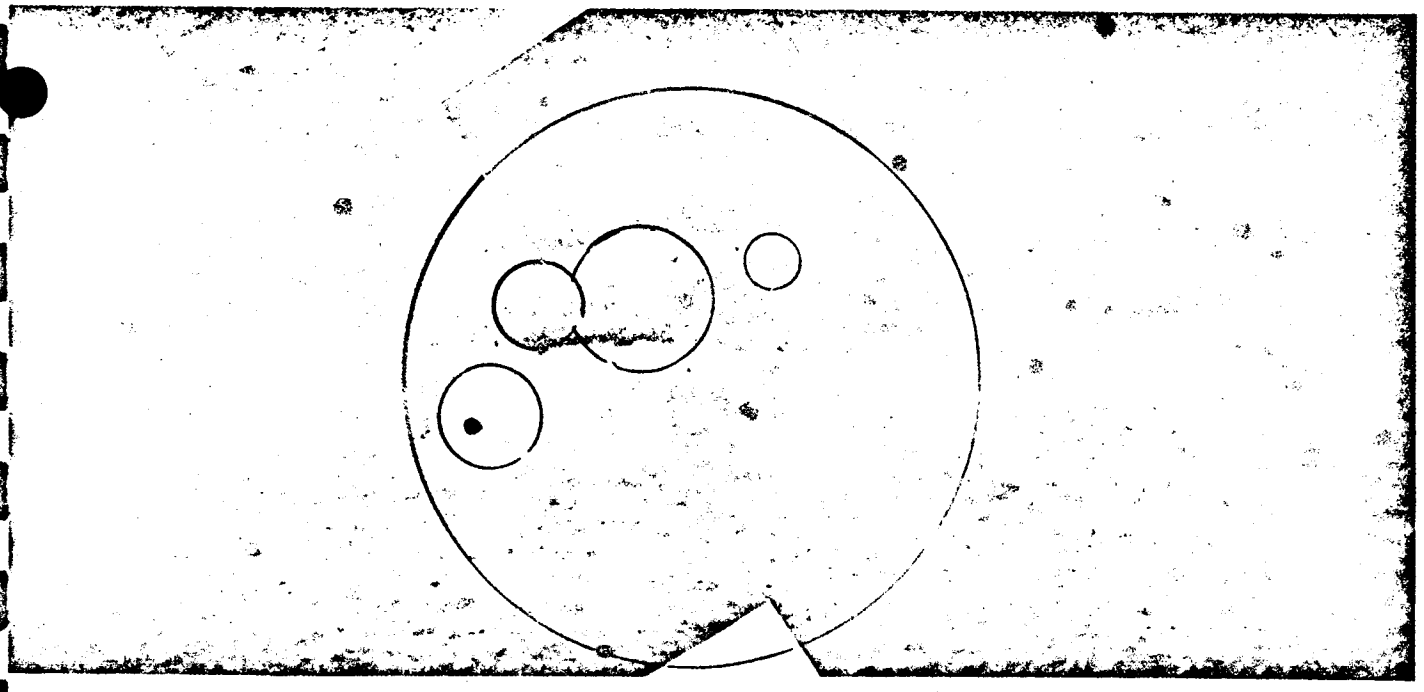

Fig. VII-20. Mosaic of two narrow-angle Surveyor III pictures, showing block about 0.5 m across close to spacecraft and position and size of circles used in measuring roundness factor. Largest circle encompasses entire block. Smaller circles are fitted to corners and rounded parts of the outline of block that occults the distant lunar scene. The geometric mean of the radii of the small circles divided by the radius of the large circle is defined as the roundness factor (Day 120, 14:54:23 and 14:52:22 GMT).

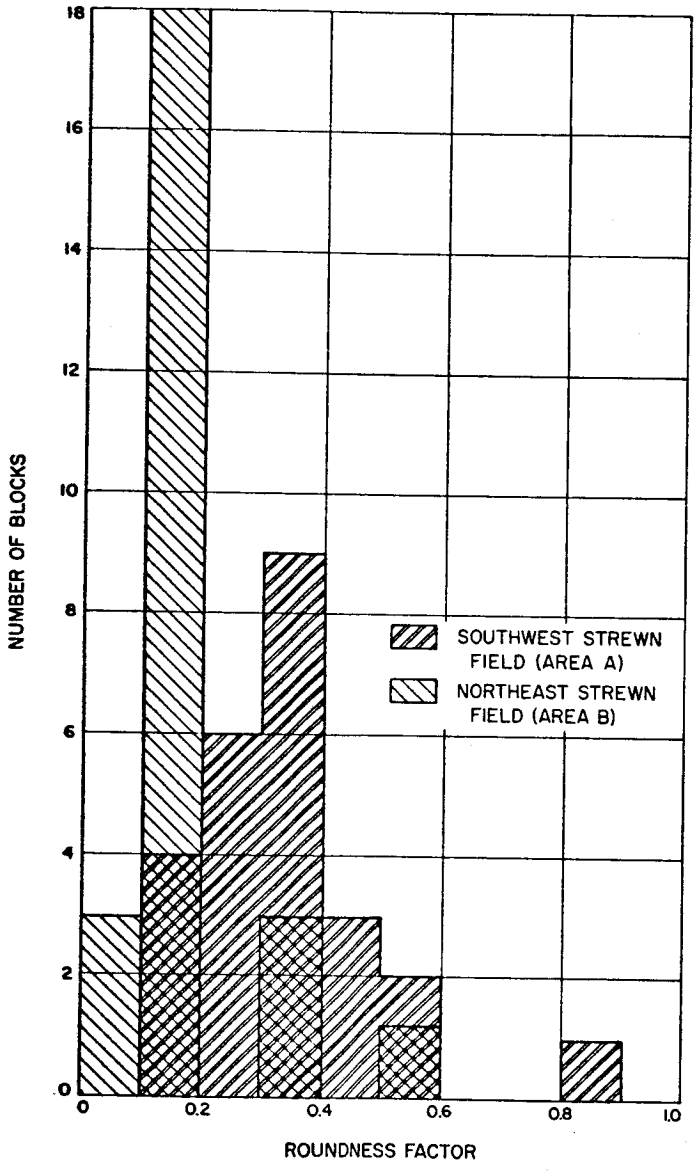

Fig. VII-21. Histograms showing frequency distribution of roundness factors for 25 blocks in Area A and 25 blocks in Area B. Blocks in Area A, associated with subdued rim craters, are significantly more rounded than blocks in Area B, associated with a sharp rim crater.

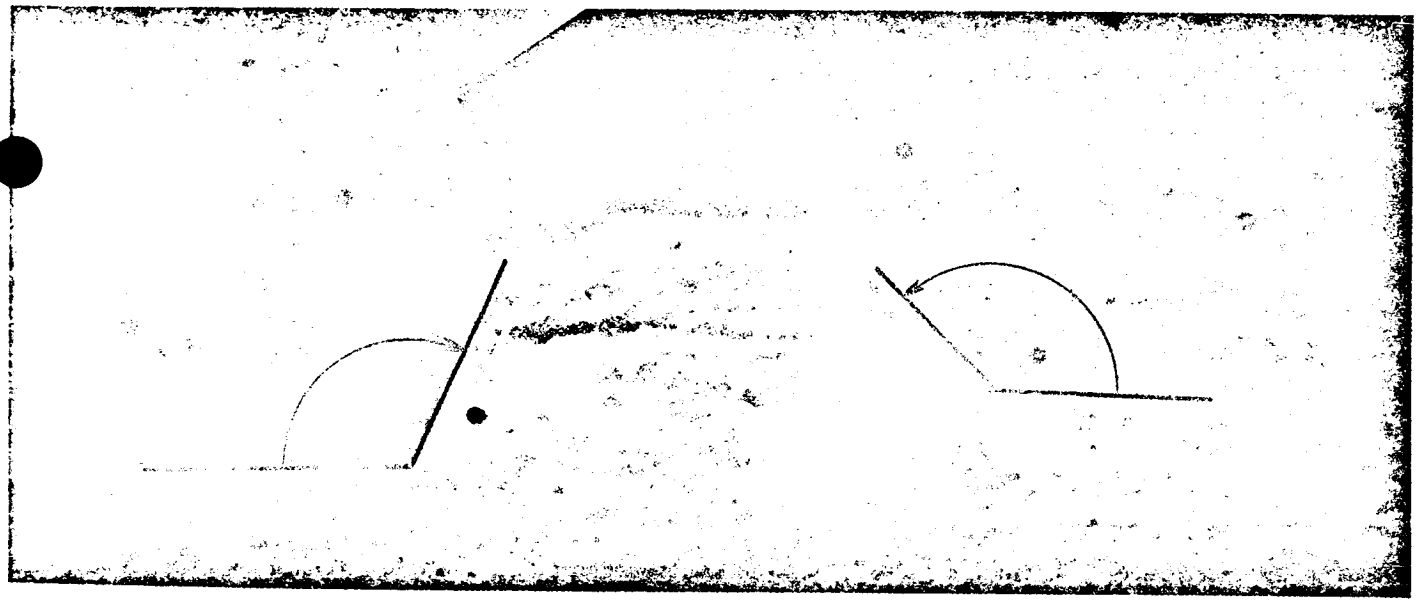

Fig. VII-22. Mosaic of two narrow-angle Surveyor III pictures, showing block about 0.5 m across close to spacecraft and angles measured to determine burial factor. Angles are measured between lines parallel with the horizon and the tangents to the outline of the block, where the outline of the block against the more distant lunar scene meets the surface. The sum of the two angles divided by 2π radians is defined as the burial factor (Day 120, 14:54:23 and 14:52:22 GMT).

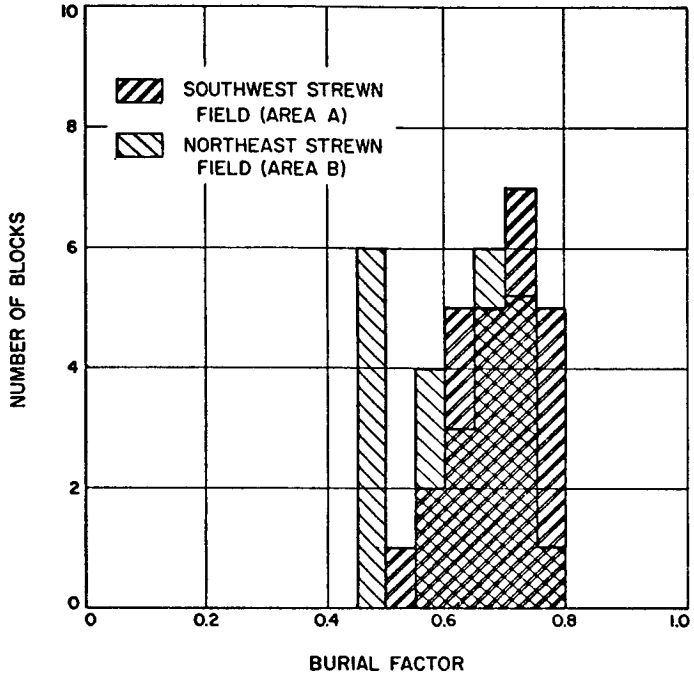

Fig. VII-23. Histograms showing frequency distribution of burial factors for 25 blocks in Area A and 25 blocks in Area B. Blocks in Area A, associated with subdued rim craters, are significantly more deeply buried in the surface than the blocks in Area B, associated with a sharp rim crater.

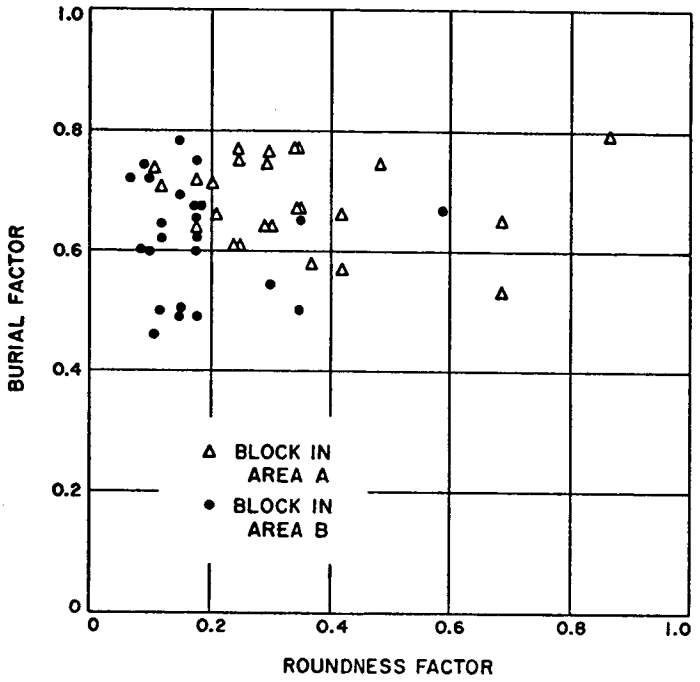

Fig. VII-24. Scatter diagram of roundness factor versus burial factor for 50 blocks in Areas A and B. The roundness factor and burial factor have no significant linear correlation; relatively few blocks, however, exhibit roundness and low burial.

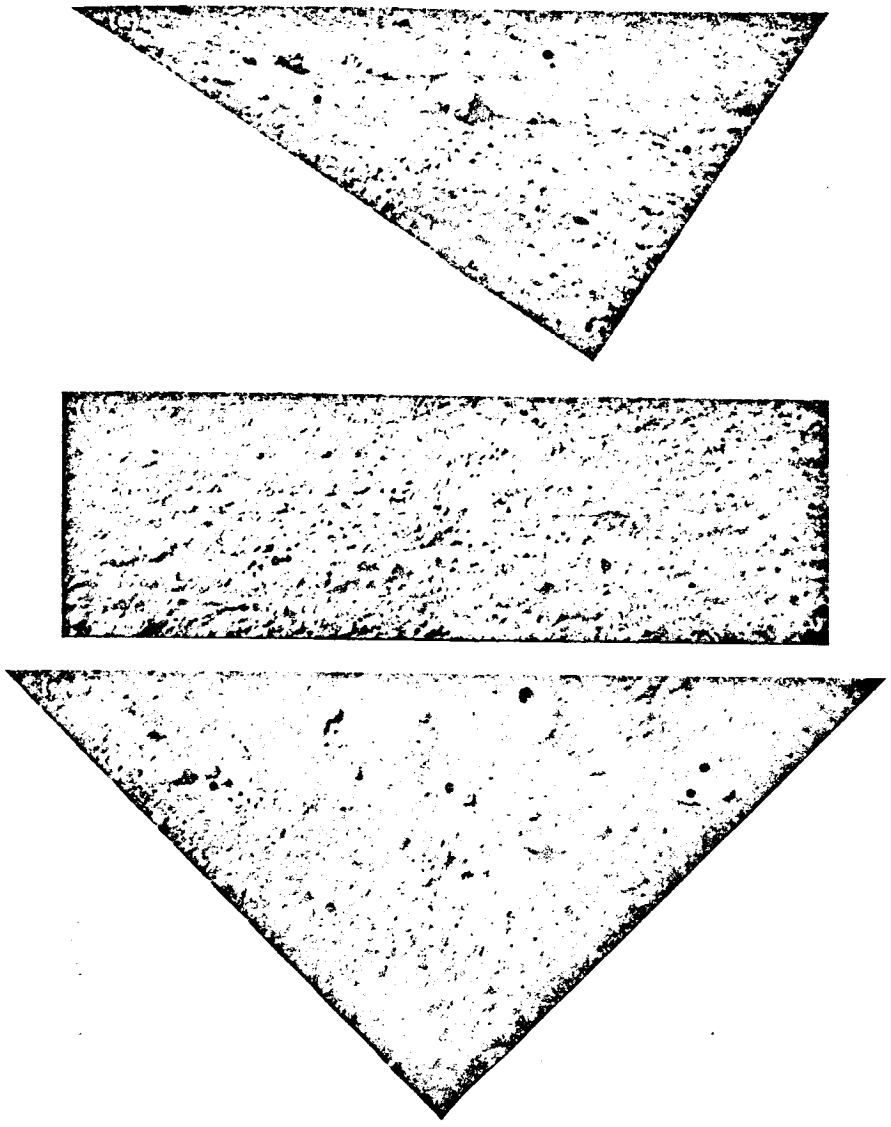

Fig. VII-25. Parts of narrow-angle Surveyor III pictures, showing small areas on the lunar surface close to the spacecraft in which the size/frequency distribution of fragments was measured. (a) Area D: smallest fragments resolved in this picture are about 8 mm across; largest fragments present are 6 to 12 cm across (Day 120, 14:38:45 GMT). (b) Area E: smallest fragments resolved in this picture are about 2 mm across; largest fragments present are 3 to 4 cm across (Day 120, 14:32:01 GMT). (c) Area F: smallest fragments resolved in this picture are about 1 mm across; largest fragments present are 8 mm across (Day 120, 14:38:08 GMT).

Fig. VII-26. Sample of ejected fragmental debris collected from the rim of Meteor Crater, Arizona. Area of floor of box in which sample has been placed is 1 square meter. Fragments are sandy dolomite from the Kaibab Formation of Permian age. Coarsest piece is 12 cm across, and finest grains identifiable in the picture are about 1 mm across. Spacing between coarser fragments resembles that observed for blocks in strewn fields around small craters at the Surveyor III landing site.

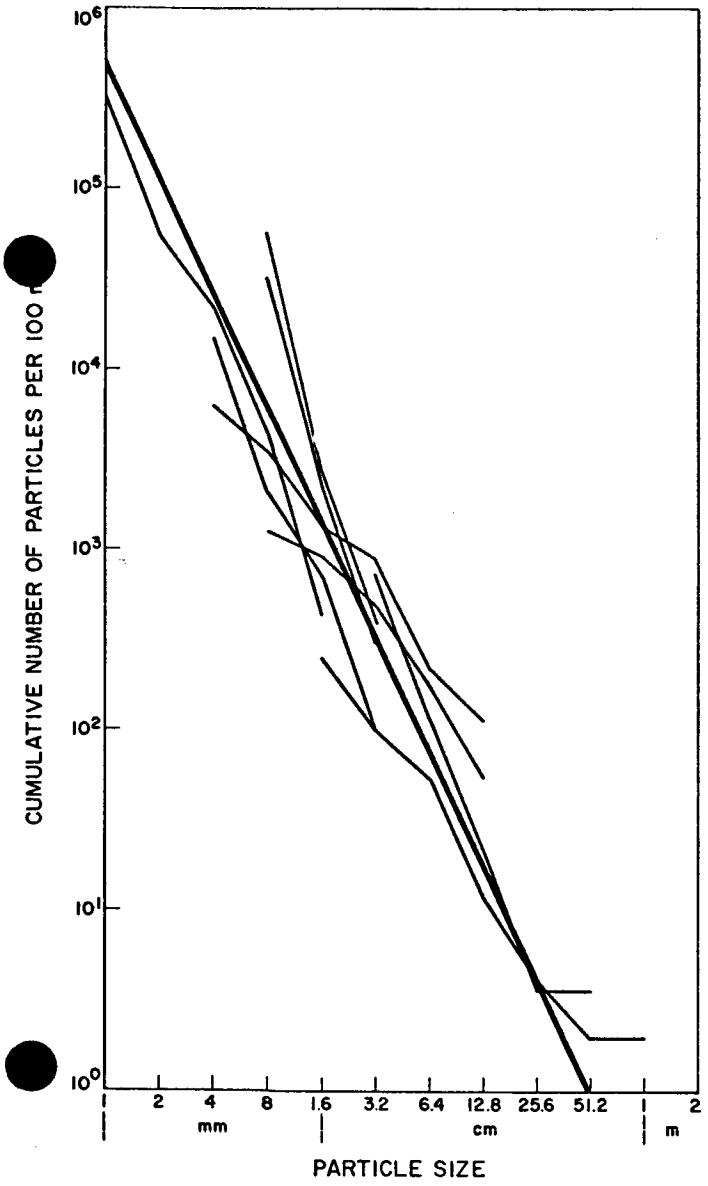

Fig. VII-27. Mean cumulative size/frequency distribution of fragment on characteristic parts of lunar surface at Surveyor I landing site (revised). Heavy solid line represents the general size/frequency distribution determined from eight sample areas. This line is the plot of the equation $N = 5 \times 10^5 y^{-2.11}$, where N is the cumulative number of fragments and y is the diameter of fragments in millimeters.

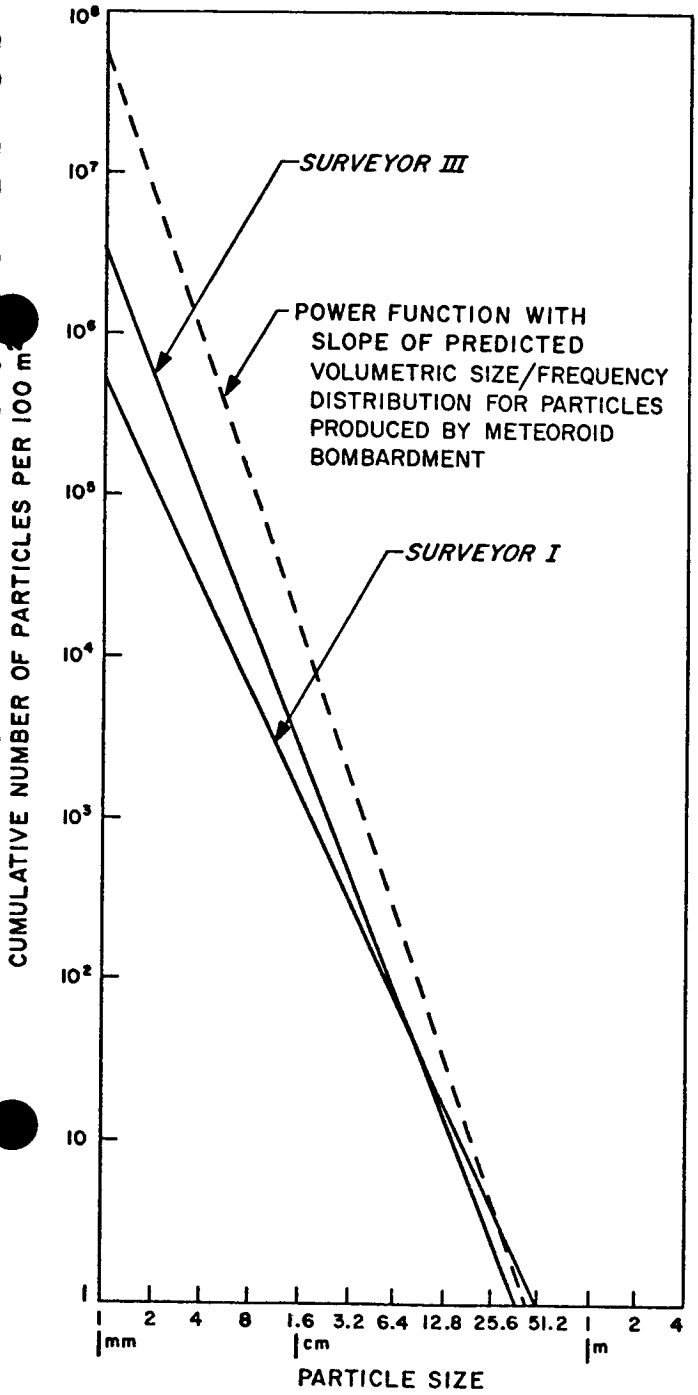

Fig. VII-28. Mean cumulative size/frequency distribution of fragments on characteristic parts of the lunar surface at Surveyor III landing site compared with mean cumulative size/frequency distribution of fragments observed at Surveyor I landing site. The volumetric size/frequency distribution of fragments expected to be produced by incident flux of meteoroids on the lunar surface is shown with dashed line. The volumetric fragment size/frequency distribution is measured to a depth equal to one-half the diameter of the coarsest fragments. The volumetric fragment size/distribution at both Surveyor I and Surveyor III landing sites probably is close to this predicted distribution.

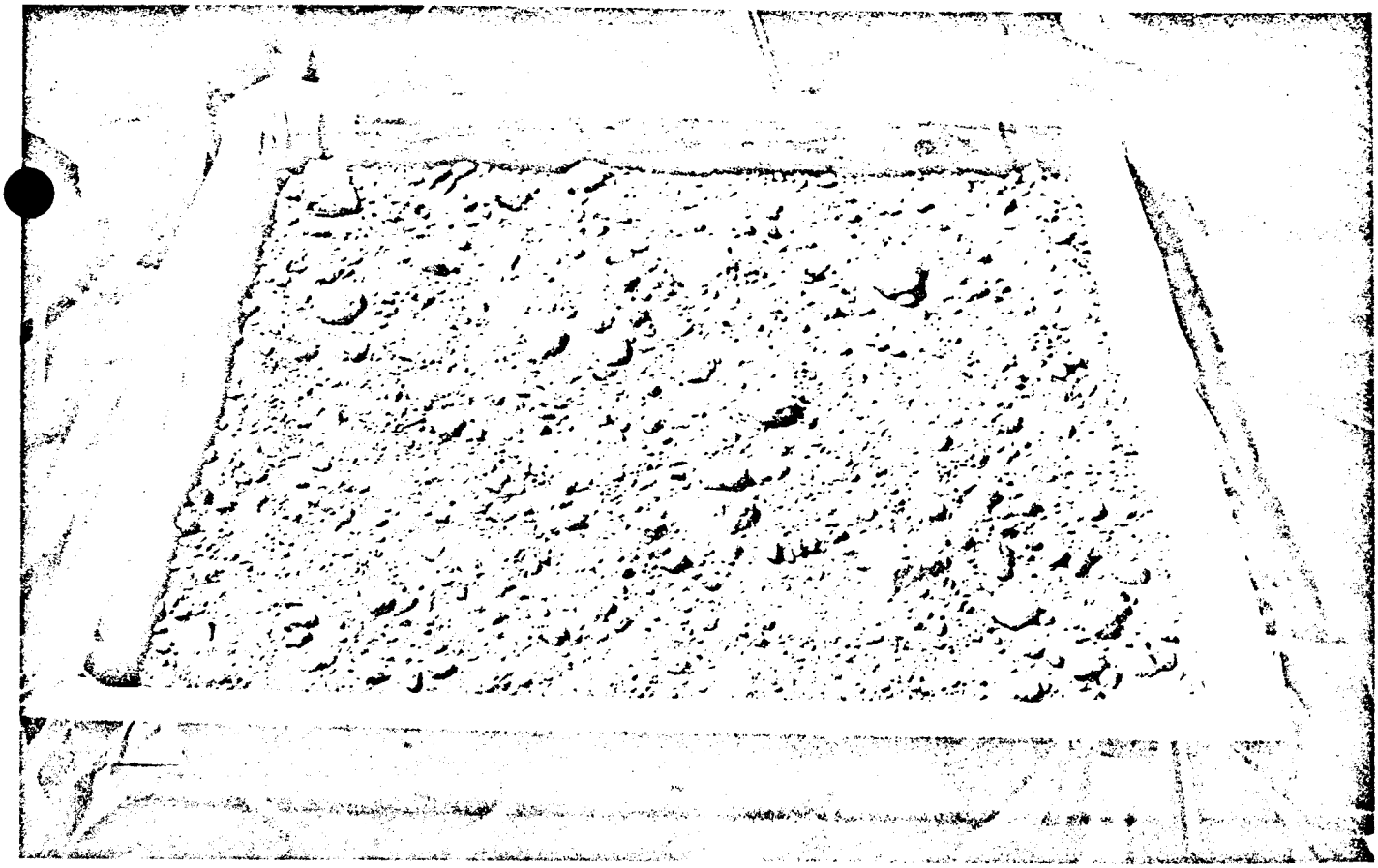

Fig. VII-29. Sample of ash and pumice from volcanic ash flow deposited in the Valley of 10,000 Smokes, Alaska, during the eruption of 1912. Area of floor of box in which sample has been placed is 1 square meter. Coarsest fragments of pumice in sample are 4 to 5 cm across; finest grains identifiable in the picture are about 1 mm across.

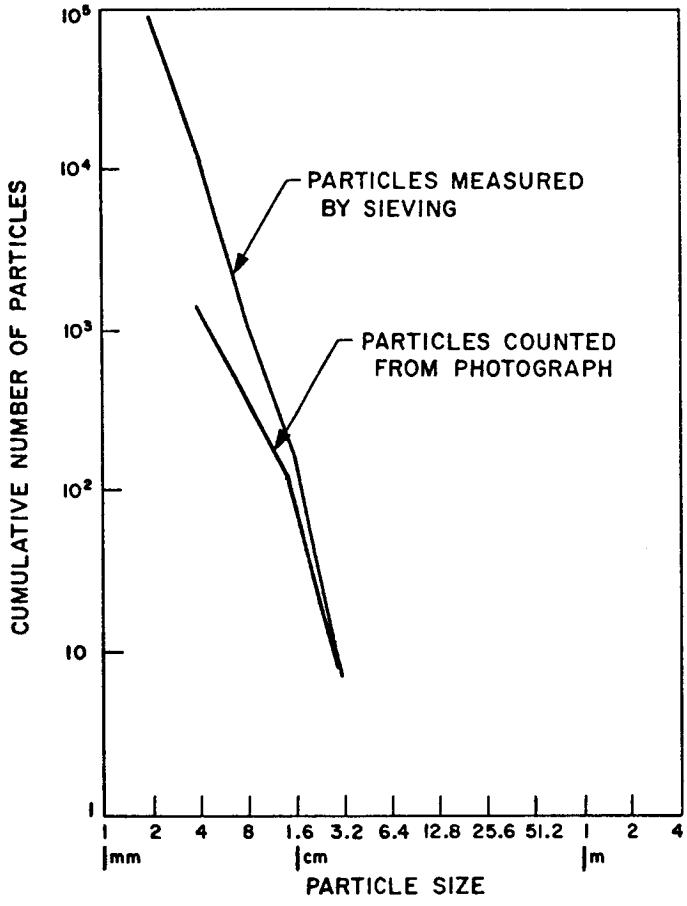

Fig. VII-30. Size/frequency distribution of particles in sample of ash and pumice from the volcanic ash flow deposited in the Valley of 10,000 Smokes, Alaska, during the eruption of 1912. Upper curve shows size/frequency distribution obtained by sieving the entire sample shown in Fig. VII-29. Lower curve shows size/frequency distribution of particles identifiable in Fig. VII-29. The difference in these two curves illustrates the difference between the volumetric size/frequency distribution of fragmental debris and the size/frequency distribution of identifiable fragments on the surface of the debris layer.

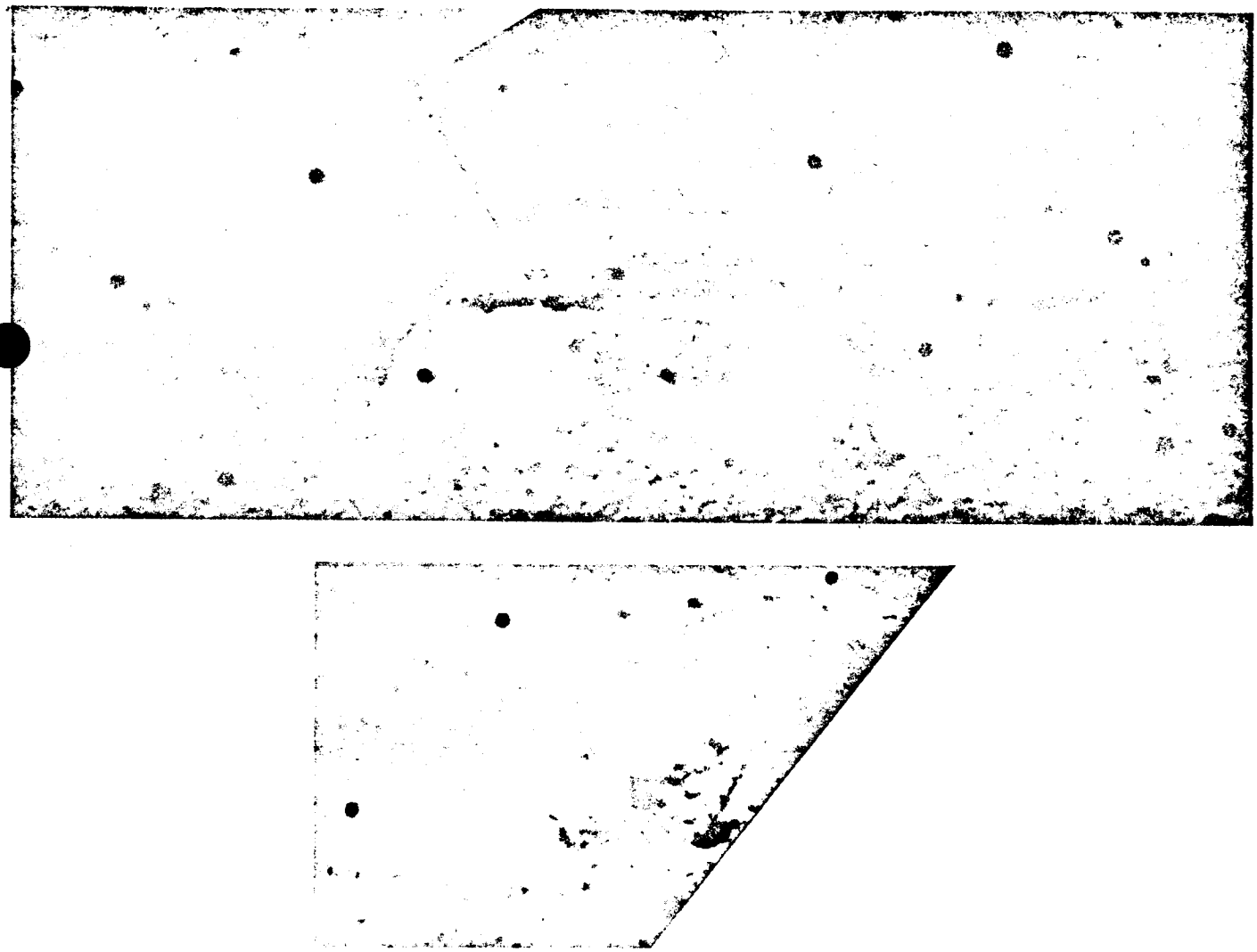

Fig. VII-31. (a) Mosaic of two narrow-angle Surveyor III pictures, showing block about 0.5 m across close to spacecraft, and fine-grained material banked up against side of block. Note nearly horizontal groove in side of block facing camera. This groove may have been produced by differential erosion of the surface along a bedding plane or a comparatively easily eroded layer (Day 120, 14:54:23 and 14:52:22 GMT). (b) Portion of narrow-angle Surveyor III picture, showing angular block close to spacecraft and fine-grained material banked up against the side of the block facing the camera. Block is 7 cm across. Note small particles 1 to 5 mm in diameter that can be resolved in the fine-grained debris (Day 118, 14:30:51 GMT).

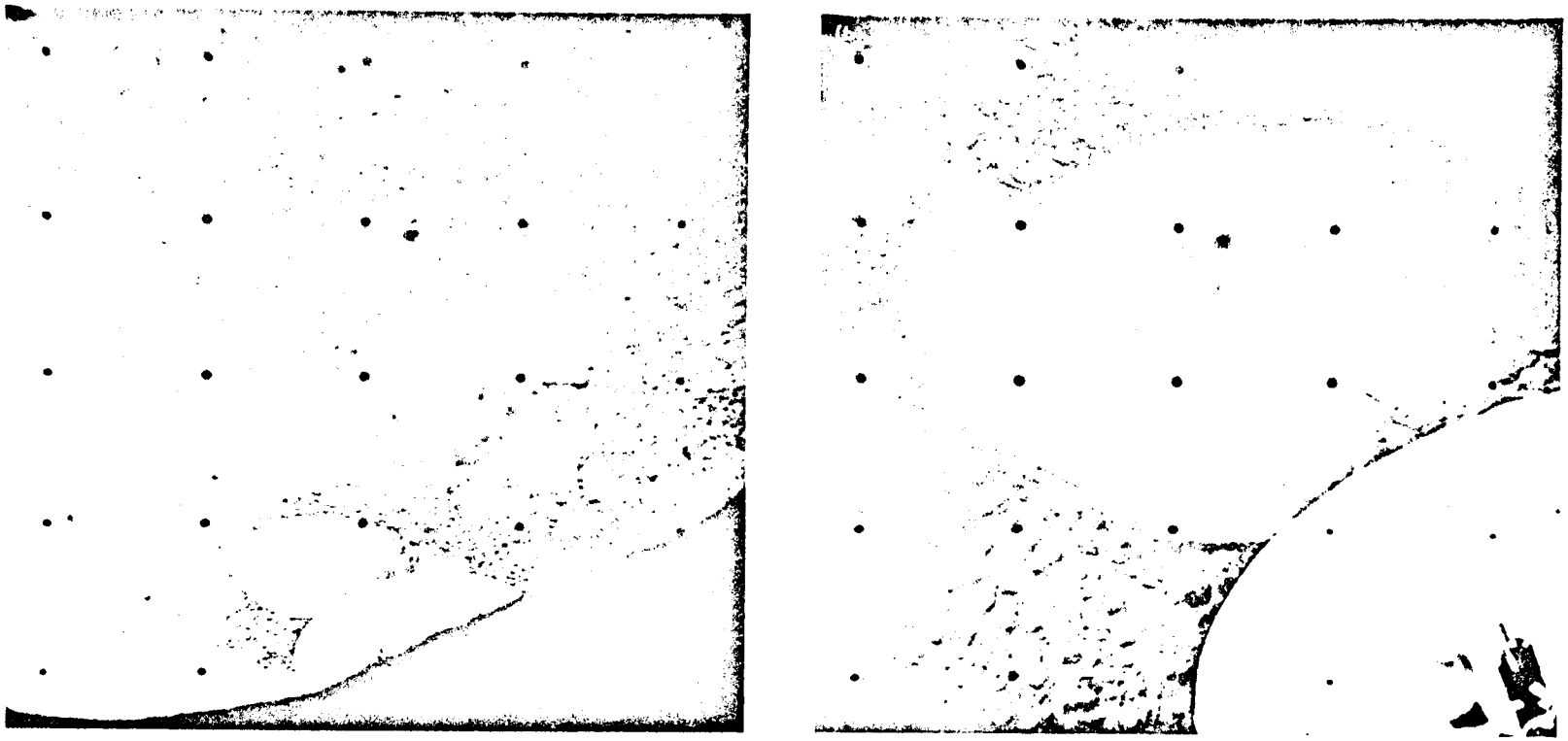

Fig. VII-32. (a) Wide-angle Surveyor III picture, showing imprint in lunar surface produced by footpad 2 of the spacecraft. Part of the top of footpad 2 may be seen next to the imprint. Note the smooth bottom and sloping walls of the imprint and the dark raised rim of lumpy material around the imprint (Day 116, 05:54:53 GMT). (b) Narrow-angle Surveyor III picture, showing imprint in lunar surface produced by footpad 2. Part of the top of footpad 2 is visible in the lower right-hand corner of the picture. Note breaks in smooth wall of imprint resembling chatter marks. Rim of dark lumpy material is absent near upper left-hand corner of the picture. The dark lumpy material appears to have collapsed or slumped across the sector of the imprint wall near the top of the picture and extends down to the floor of the imprint (Day 116, 06:05:55 GMT).

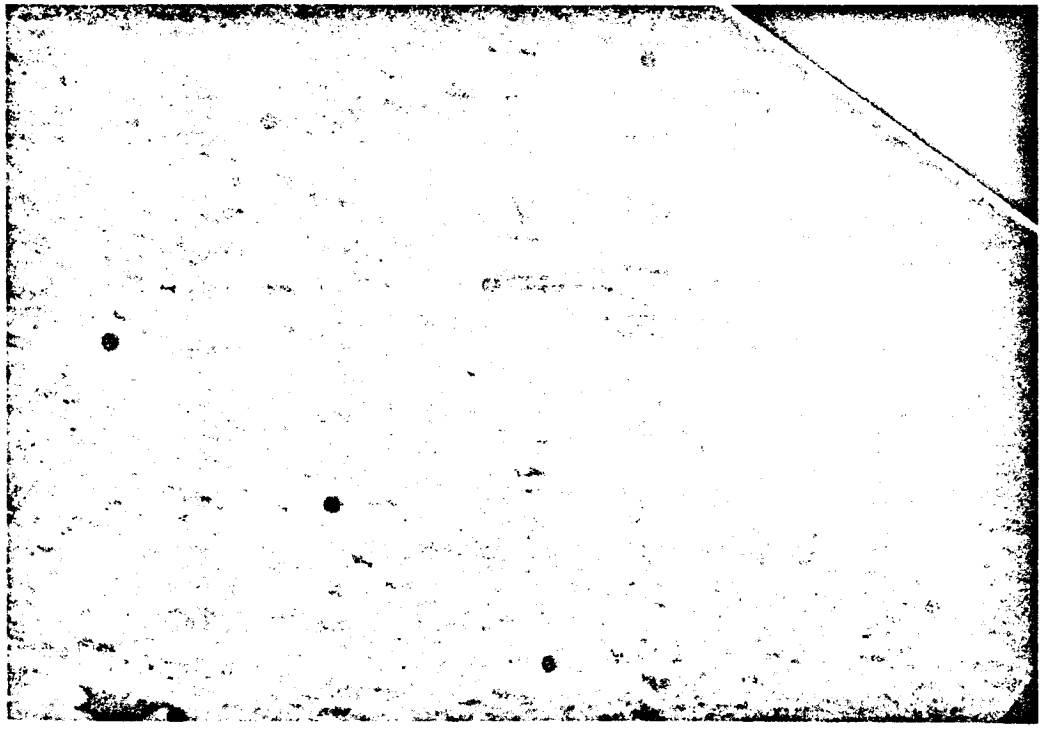

Fig. VII-33. Portion of narrow-angle Surveyor III picture, showing imprint in lunar surface produced by footpad 1 of the spacecraft during the second touchdown of the landing sequence. The imprint occurs on a small crater wall facing the camera, and the imprint is stepped down along several breaks toward the camera and toward the center of the small crater. The crater in which the imprint is formed is about 1 m across (Day 116, 08:37:36 GMT).

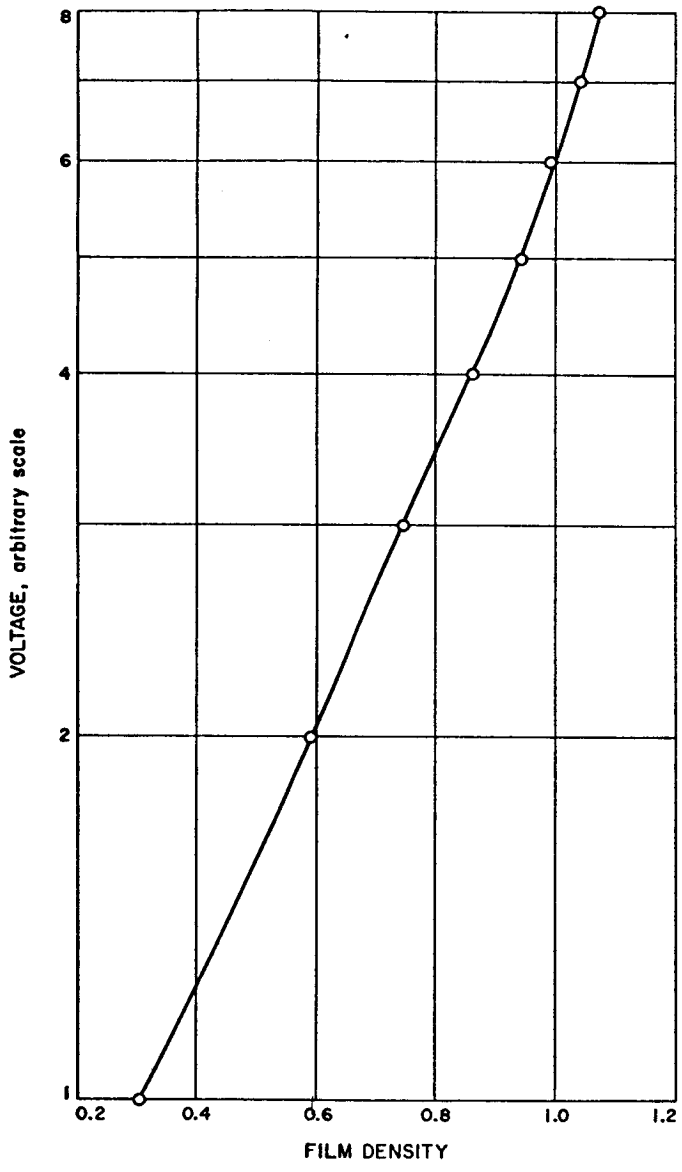

Figure VII-34. Typical plot of measured film density versus voltage from electronic gray scale on negatives produced by Ground Data Handling System at the Space Flight Operations Facility in Jet Propulsion Laboratory. Electronic gray scale is added to each frame by the Ground Data Handling System to provide system photometric control.

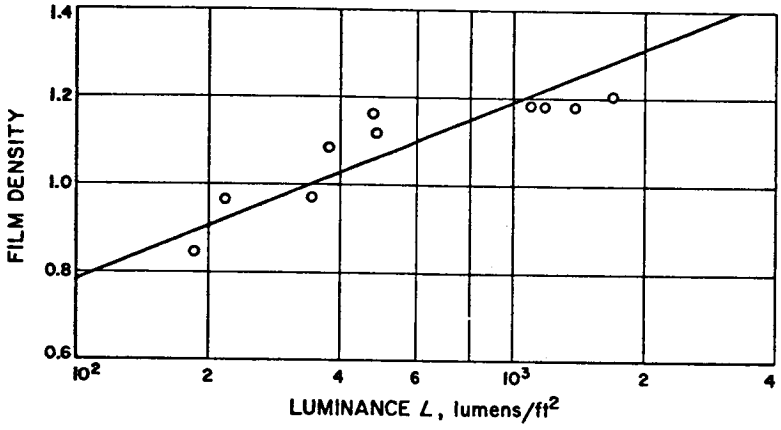

Fig. VII-35. Total television system transfer characteristic function determined from observation of the photometric target on the spacecraft leg during lunar operations. This function is used to convert film density to scene luminance.

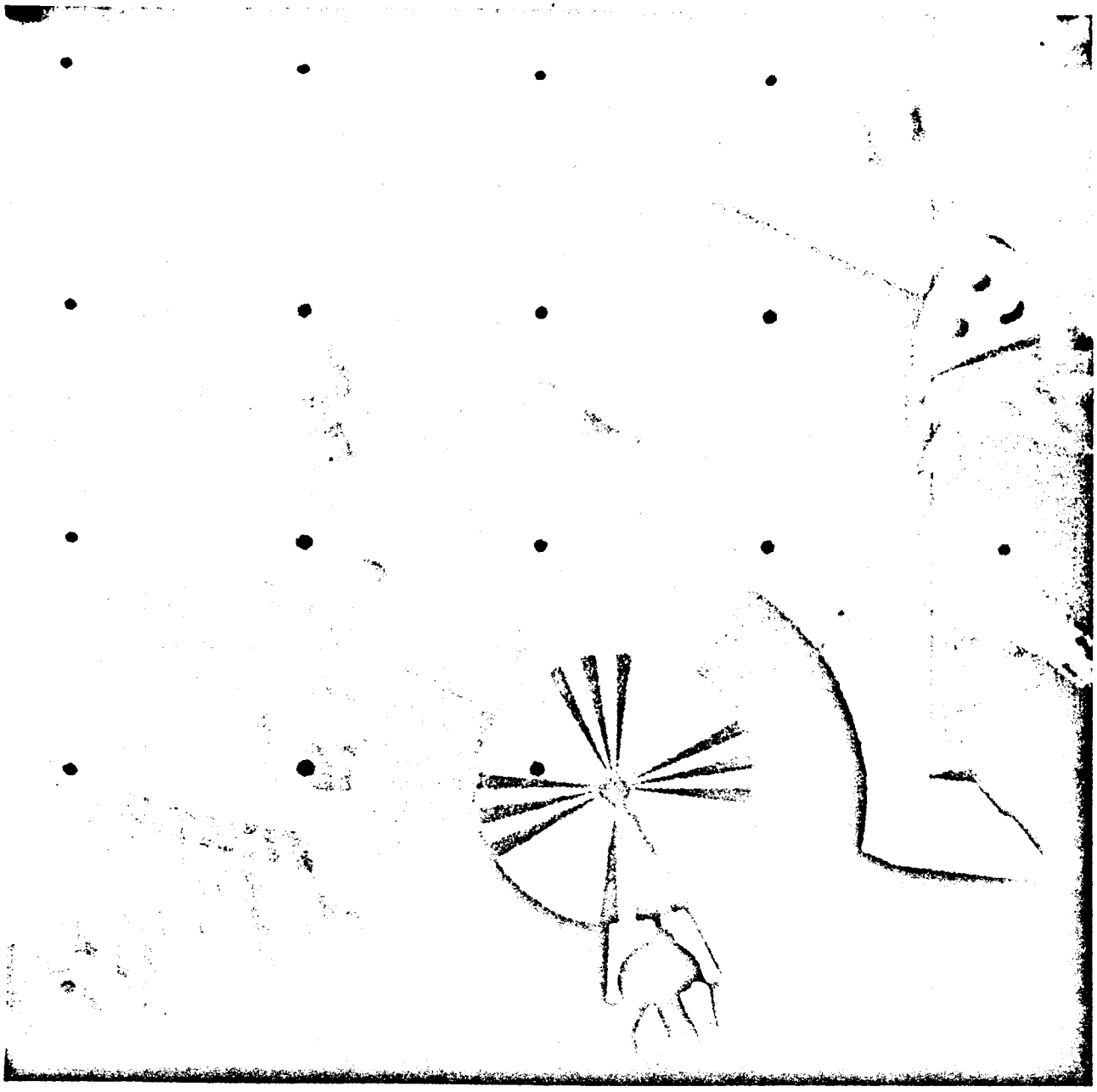

Fig. VII-36. Narrow-angle Surveyor III picture of photometric target on leg 2. Note contrast attenuation and additional increase in light level in the upper half of the picture (Day 116, 05:59:33 GMT).

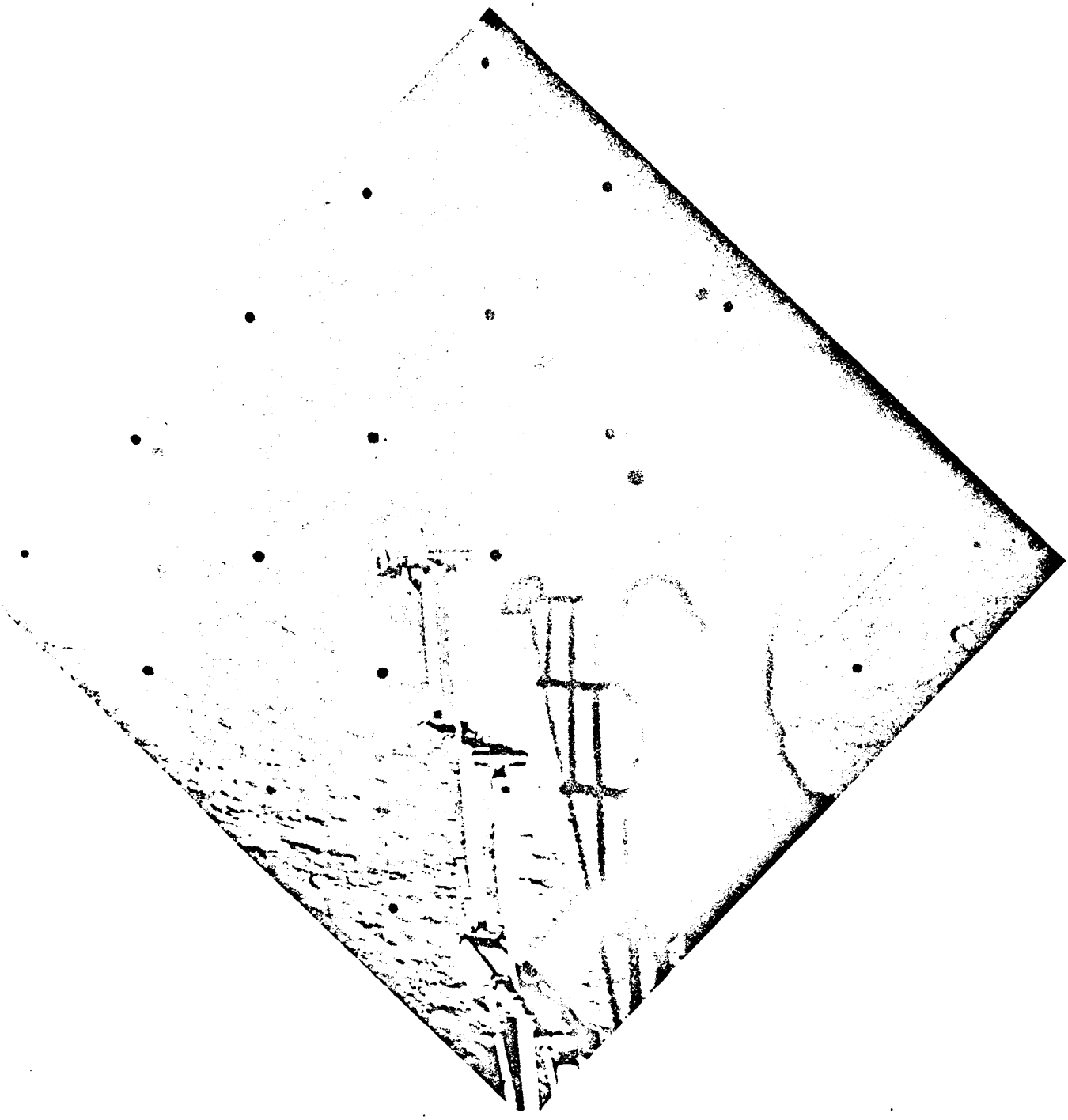

Fig. VII-37. Wide-angle Surveyor III picture, showing shadow of camera and solar panel. The shadows are washed out in the upper right half of the picture because of glare from camera mirror (Day 122, 14:37:01 GMT).

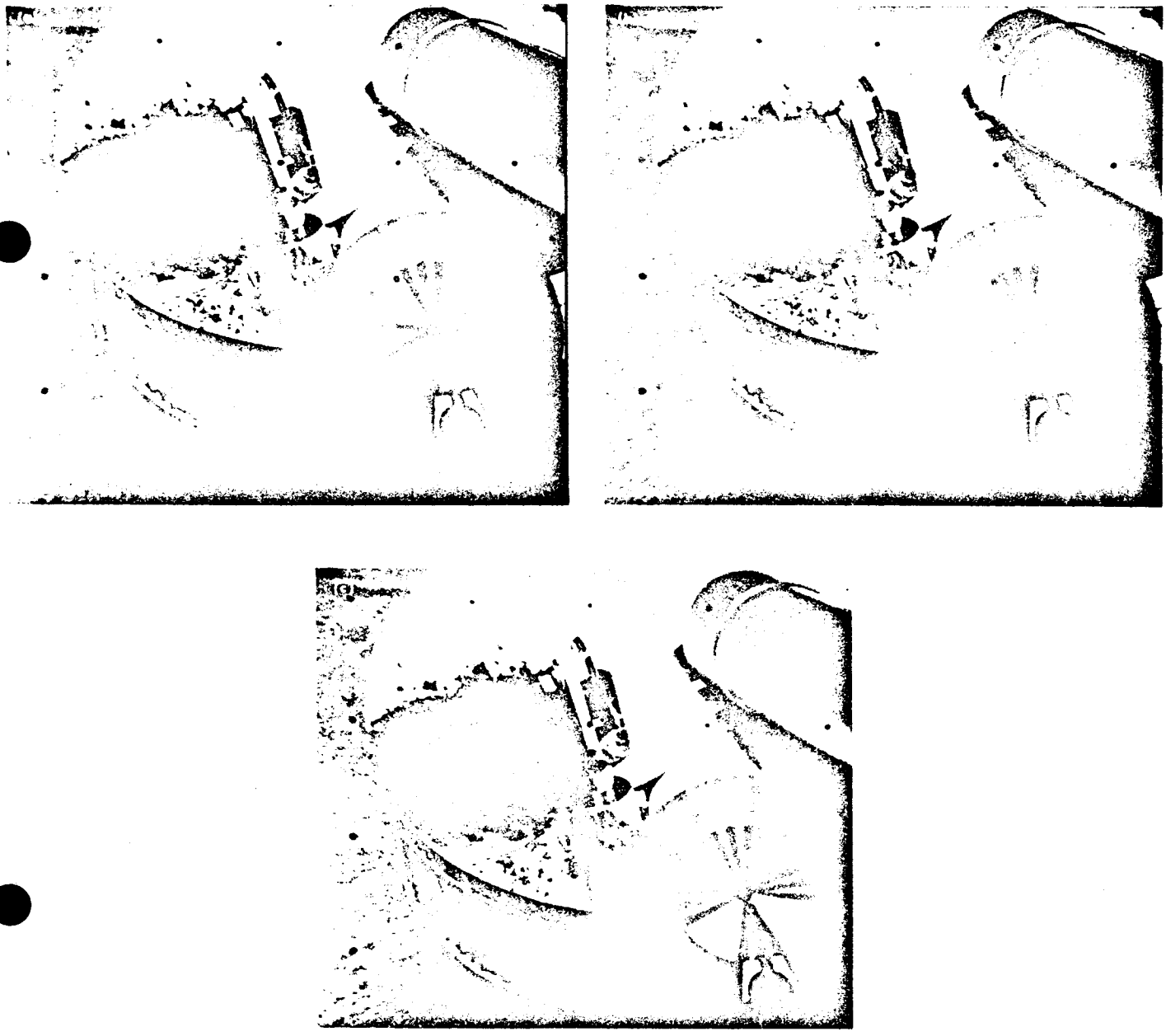

Fig. VII-38. Narrow-angle Surveyor III pictures showing photometric target and debris on footpad 2. Target observed on Day 116: (a) through $\bar{x}'$ filter (red), 12:00:54 GMT; (b) through $\bar{y}'$ filter (green), 12:02:14 GMT; and (c) through $\bar{z}'$ filter (blue), 12:01:27 GMT.

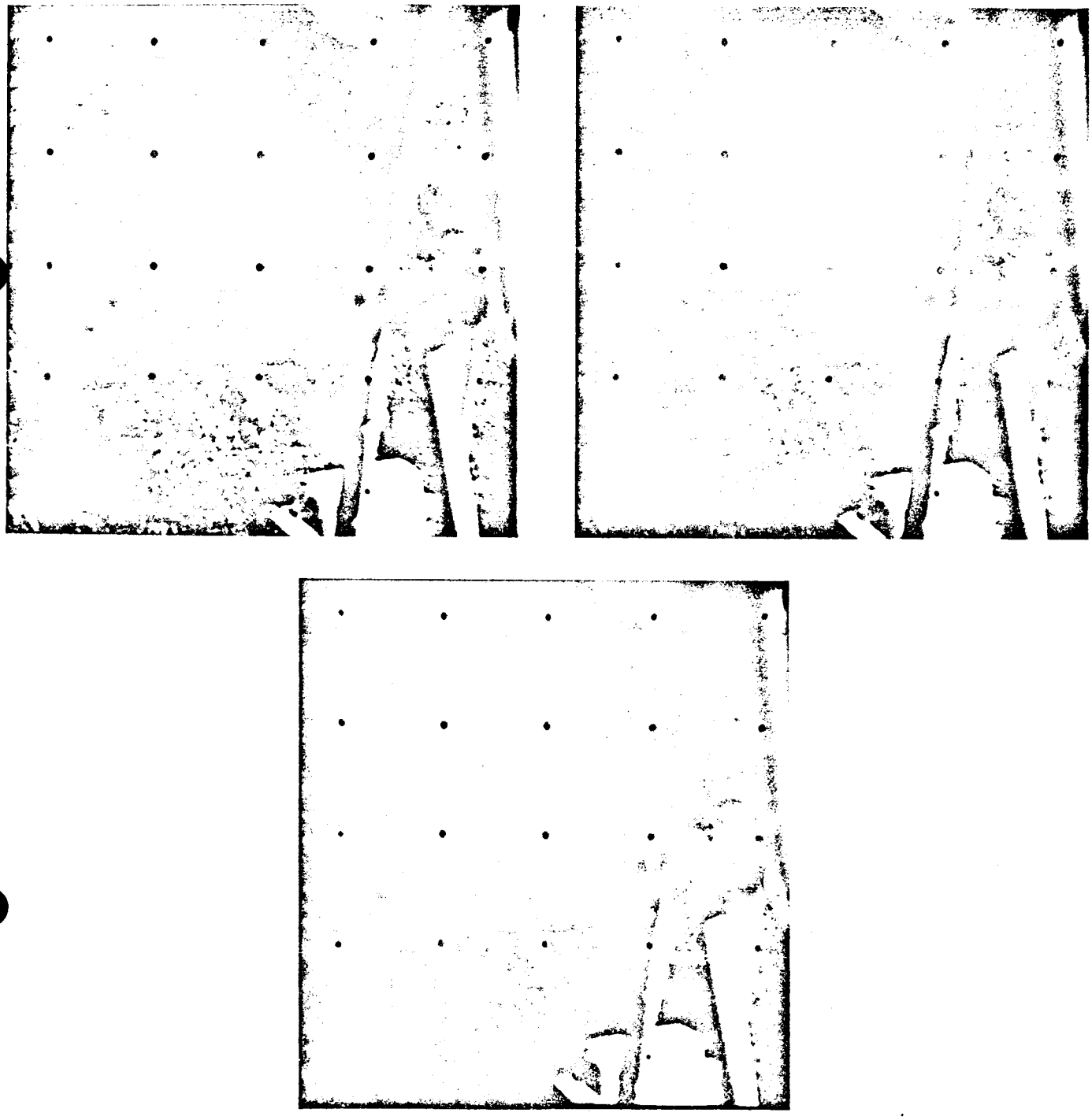

Fig. VII-39. Narrow-angle Surveyor III pictures of surface sampler trench observed on Day 114; (a) through $\overline{x}'$ filter (red), 05:19:23 GMT; (b) $\overline{y}'$ filter (green), 05:15:18 GMT; and (c) $\overline{z}'$ filter (blue), 05:20:20 GMT.

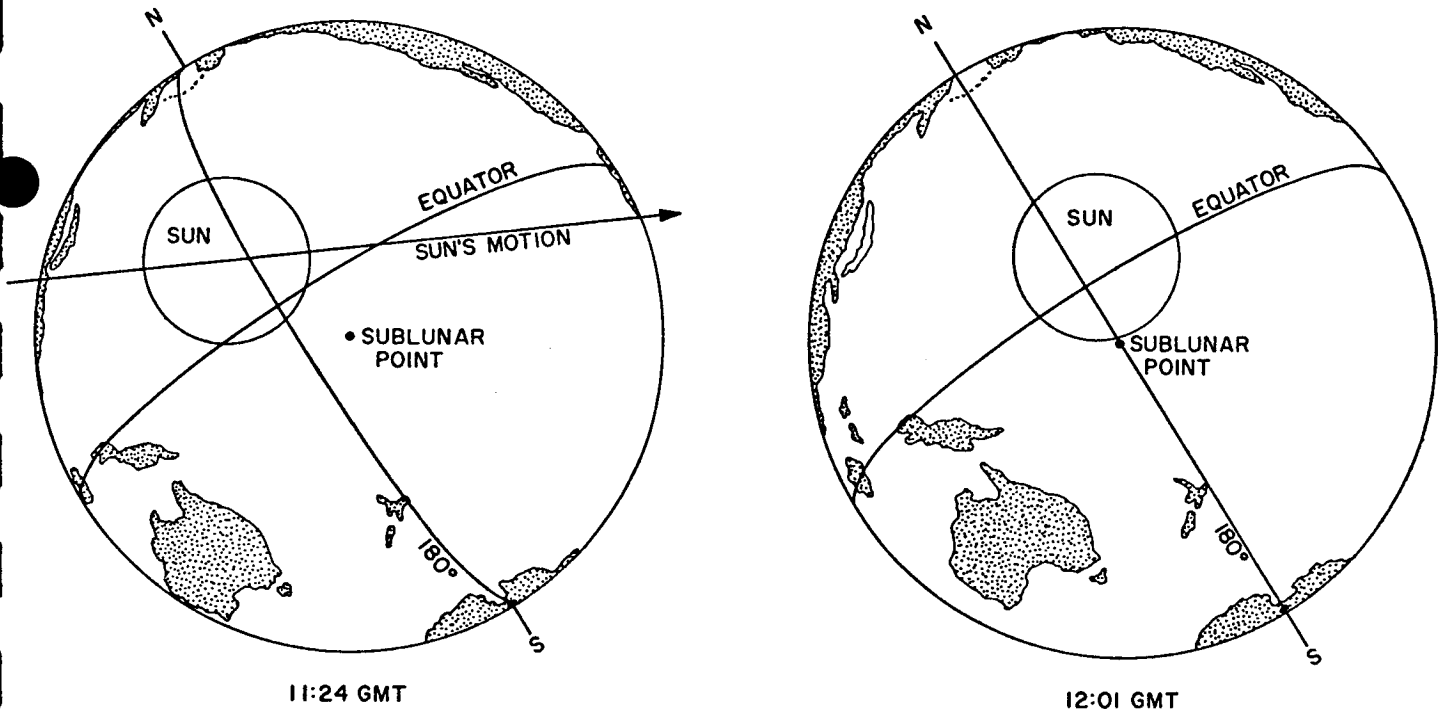

Fig. VII-40. Diagrams showing orientation of Earth and position of the Sun, as seen from the Moon on Day 116, at 11:24 GMT and 12:01 GMT. A series of pictures of the eclipse of the Sun by the Earth was taken with the Surveyor III television camera at approximately the times illustrated.

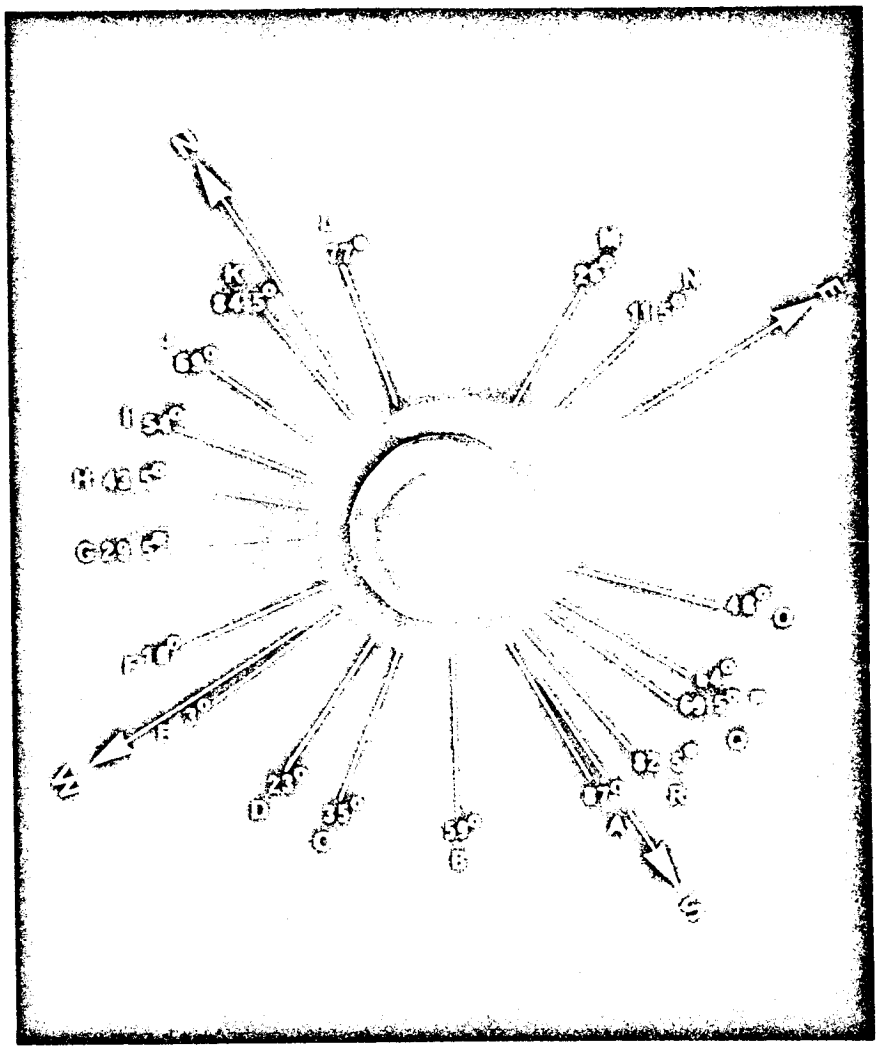

Fig. VII-41. Superimposed Surveyor III pictures illustrating distribution of light in the refraction halo of the Earth at the time the first series of eclipse pictures was taken and at the time the second series was taken. An eclipse image taken from the first series of pictures had been reduced in size and shown nested within an eclipse image taken from the second series of eclipse pictures. The angular orientation of both images is the same. Line marked N-S shows projection of Earth's axis on plane of pictures. Eighteen beads, identified by letters, can be distinguished. Note the angular position of beads in the refraction halo tends to remain the same, but the bright region nearest the Sun changes position between the time of the first series of pictures and the second series, following the Sun.

Fig. VII-42. Stereographic mosaics of ESSA 3 pictures of (a) northern and (b) the eclipse. Bright areas are clouds and, in mountainous regions and the Arcti which may be seen in the clear areas on the right-hand side of (a). The trace o bright region in the refraction halo of the Earth, observed in the second series circles that extend from 90°W to 90°E. Beads occur in areas that are largely c of beads in Fig. VII-41 (mosaic of ESSA 3 pictures provided through the courte ESSA).

IT

DAY

outhern hemispheres of the Earth. Pictures taken on the day preceding
snow fields; dark areas are clear. Note position of African continent,
he limb of Earth, as seen from the Moon, and positions of beads and the
eclipse pictures taken by Surveyor III, are shown by the white lines and
ar. Letters beside symbols for beads correspond to letter identification
y of Dr. David S. Johnson, National Environmental Satellite Center,

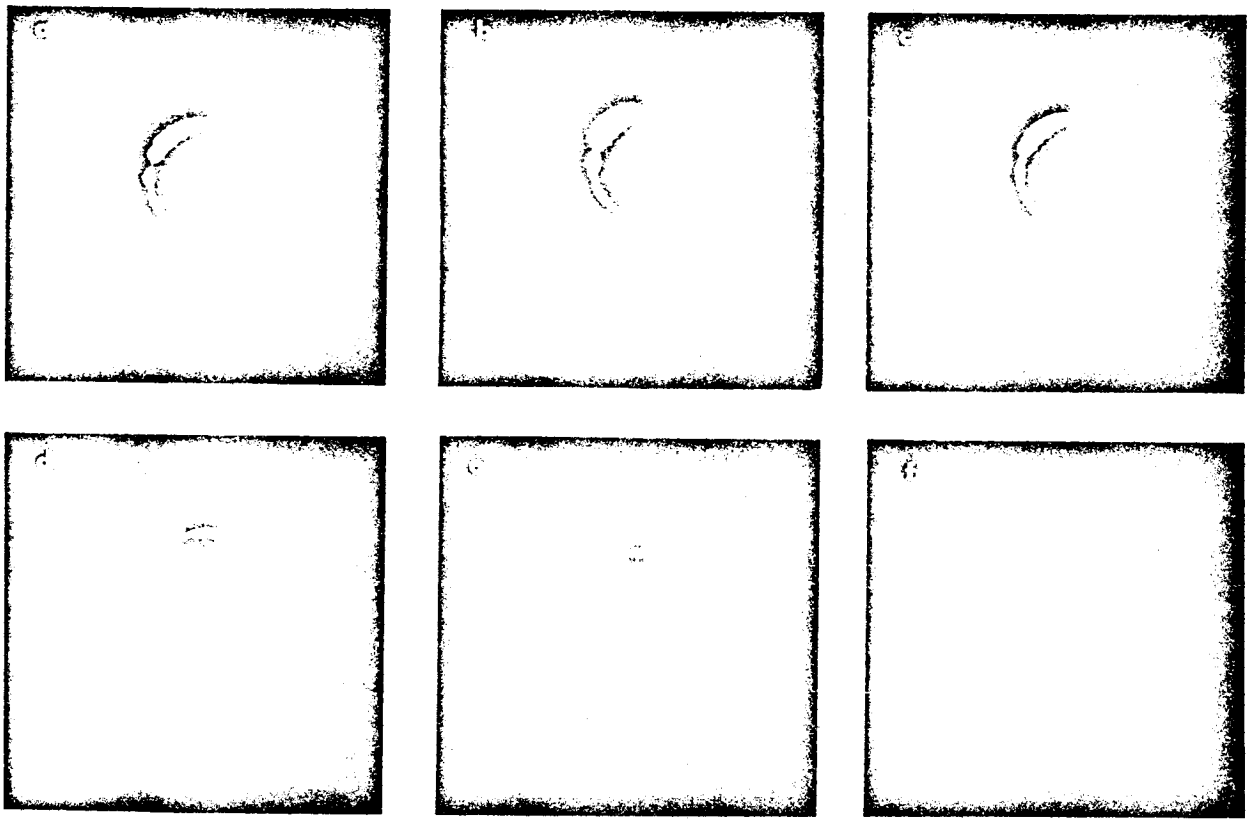

Fig. VII-43. Wide-angle Surveyor III pictures showing eclipse of Sun by Earth as observed on Day 114 through the filters indicated: (a) $\overline{x}'$ (red), 11:31:40 GMT; (b) $\overline{y}'$ (green), 11:23:06 GMT; (c) $\overline{z}'$ (blue), 11:24:01 GMT; (d) $\overline{x}'$, 12:02:10 GMT; (e) $\overline{y}'$, 12:03:10 GMT; and (f) $\overline{z}'$, 12:02:44 GMT. (First set of figures includes (a), (b), and (c); second set of figures includes (d), (e), and (f).)

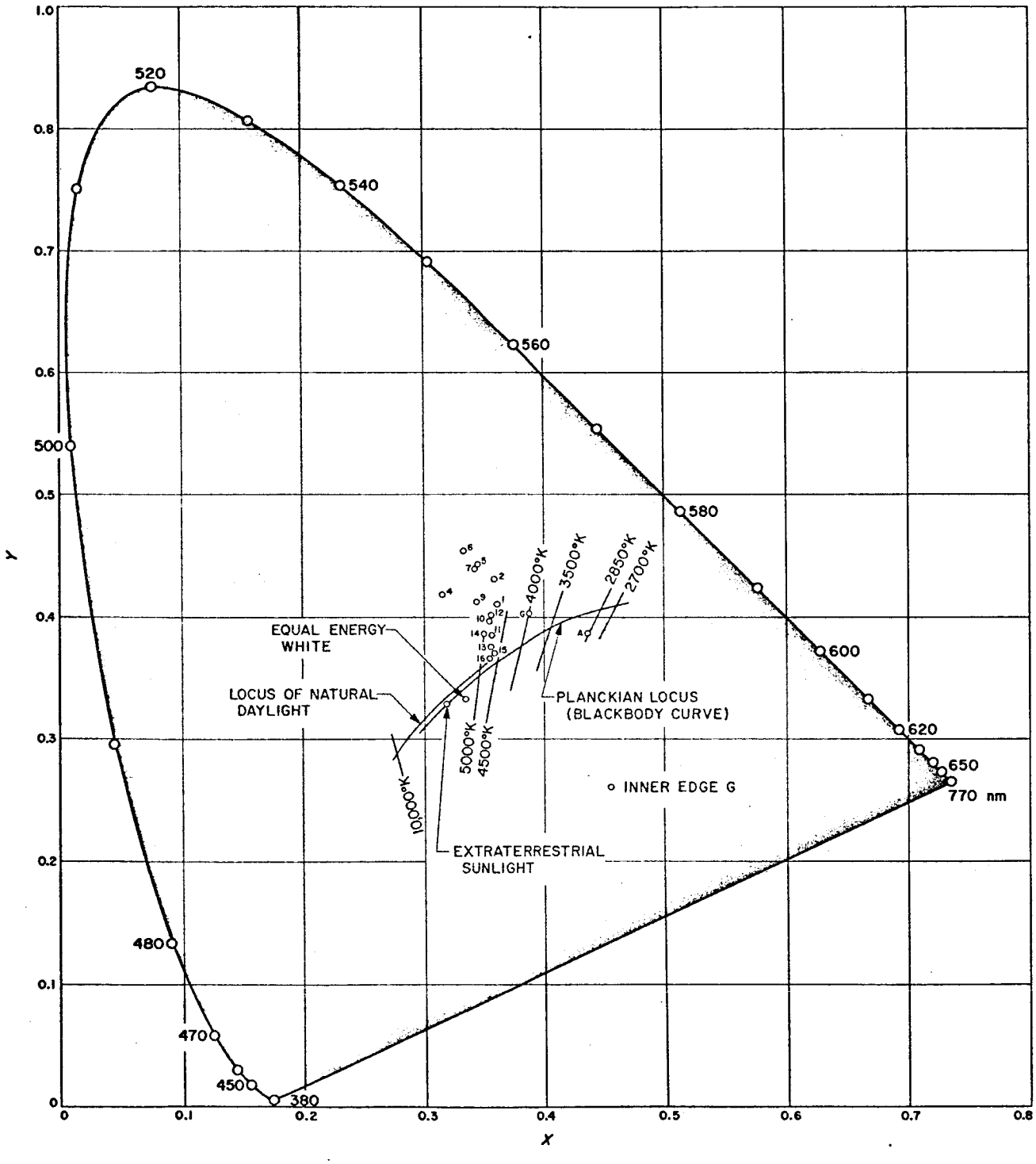

Fig. VII-44. Chromaticity coordinates of selected points from the first series of Surveyor eclipse pictures. For comparison purposes, the Planckian locus with correlated color temperature lines is shown together with the locus of natural daylight as measured by Y. Nayatin and G. Wyszecki (Ref. VII-13).

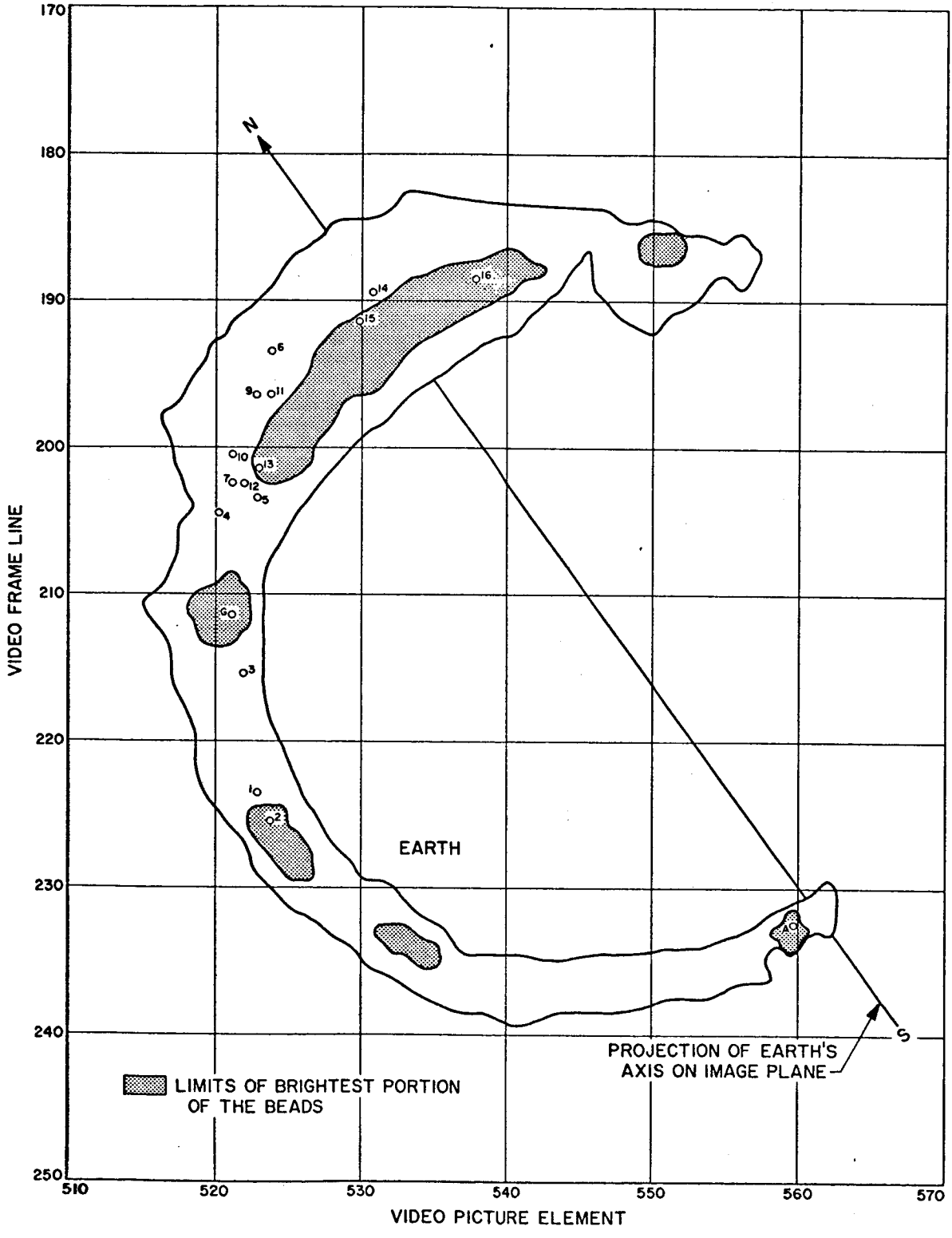

Fig. VII-45. Diagram of the solar eclipse, showing positions of points on the color composite image that were measured for color. The letters refer to the beads.

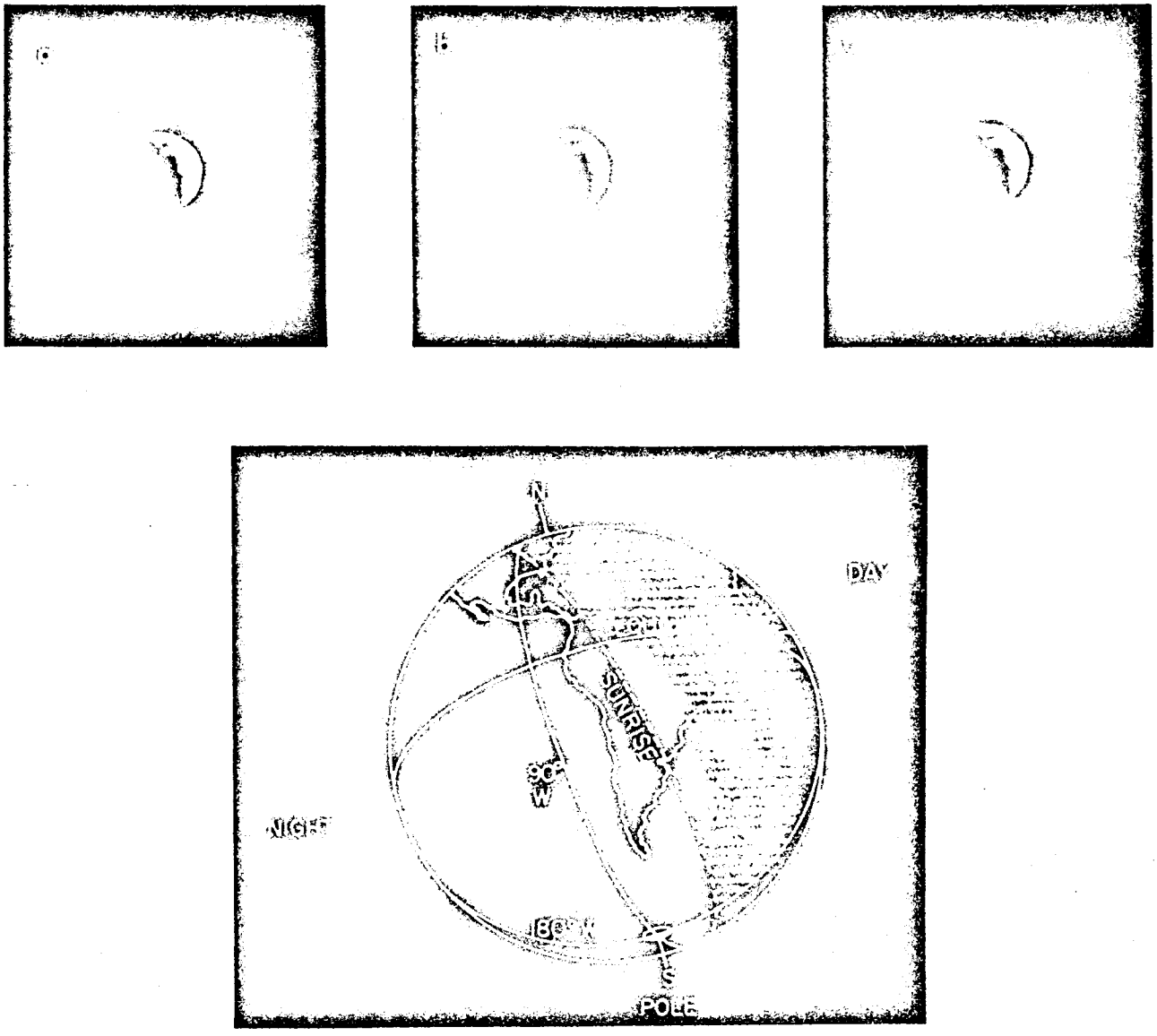

Fig. VII-46. Wide-angle Surveyor III pictures of Earth as observed on Day 120 through: (a) $\overline{x}'$ filter (red), 10:39:29 GMT; (b) $\overline{y}'$ filter (green), 10:37:18 GMT; and (c) $\overline{z}'$ filter (blue), 10:38:15 GMT. The lunar libration had caused a favorable movement of the Earth's position, giving an unobstructed view of Earth from Surveyor III. Diagram shows orientation of Earth when pictures were taken.

VIII. LUNAR THEORY AND PROCESSES

D. Gault, R. Collins, T. Gold, J. Green, G. P. Kuiper, H. Masursky, J. O'Keefe, R. Phinney, and E. M. Shoemaker

A. Some Implications of Surveyor III Results

Significant new information has been provided by Surveyor III's successful landing and operation on the lunar surface; some of the most significant and interesting events are presented here. Pending completion of data reduction and more detailed analysis of the information available from the Surveyor mission, only limited interpretive discussion is included at this time.

1. Position of Surveyor III on the Lunar Surface

The location of the spacecraft is shown in Fig. VIII-1, and discussed in detail in Section VII of this preliminary report. Features are indicated in this figure for reference in the following discussion. Approximate crater profiles, based on photometry of Lunar Orbiter III records, are shown in Fig. VIII-2; approximate spacecraft position is indicated on the profile BB'.[1] Crater profiles indicate that the crater is 22 to 25 m deep and that the slope component in the phase plane at the position of the spacecraft touchdown point is about 13°. The latter value corrects to a true slope of about 14°. This value is not consistent with results presented in Section VII, and additional analysis is required to resolve the difference. Nevertheless, these results indicate that the eye of the spacecraft (rotating mirror on the television camera system) is about 10 to 12 m below the rim crest of the crater and about 12 to 13 m above the crater bottom. Figure VIII-3 is a stereoscopic view of the crater composed of two convergent, high-resolution frames from Lunar Orbiter III. The right-hand frame is a near-vertical photograph; the other is rectified from a 37° tilted photograph.

[1] Photometric profiles necessary to generate these contours were developed by G. R. Taylor and J. J. Lambiotte, NASA, Langley Research Center.

It is important to note that the rim of the crater is everywhere higher than the television camera on the spacecraft. Thus, the only lunar terrain visible to the Surveyor III camera system is restricted to the interior walls of the crater. Differences between the Surveyor III site and locations photographed by Surveyor I, as well as Luna IX and Luna XIII, may be attributed to the landing location of Surveyor III. Both differences and similarities have fundamental implications in lunar theory and processes.

2. Degradation of Pictures

Quality of some pictures, and thus the information obtained during this mission, has been seriously decreased as a result of the degradation of the pictures due to scattered light in the optical system. In all cases in which the mirror was exposed to direct sunlight, the pictures are poor. When the mirror was not exposed to sunlight, the pictures improve in quality, but still suffer from a general glare, which results in a severe loss of contrast in detail.

Regions of maximum degradation observed in the pictures appear to rotate about the center of the frame as the camera is moved in azimuth. In each case, this degradation is oriented on the frame in such a way that it corresponds to a direction from the camera lens associated with light scattered from the upper half of the mirror. The direction of the Sun affects the degree of the degradation, but not its position. The effect is readily apparent in most of the pictures, but is demonstrated most clearly in Fig. VIII-4,[2] which is a time exposure of the crescent Earth obtained as part of observations conducted to determine spacecraft orientation. Figure VIII-4 was taken looking approximately due east with the Sun setting directly behind at an angle of approximately 40° above the western horizon. The approximate 6° field of view is centered about 60° above the horizon; the only strong source of light incident on the mirror is that reflected from the lunar surface and from Earth. The dark stripe in the upper right-hand corner and the bright stripe in the lower left-hand corner define the upper and lower edges of the mirror, respectively. The entire field of view should be dark except for the crescent Earth. The broad diffuse white band over the upper half of the mirror appears to be consistent with the glare

[2]This was brought to our attention by R. H. Steinbacher, Jet Propulsion Laboratory, Pasadena, California.

observed in the photographic images, and is apparently the result of either surface abrasion caused by the impact of fine particulate material that became entrained in the vernier exhaust or a deposit of fine particles and/or effluent from the vernier engines on the surface of the mirror. No such effect was observed in the case of Surveyor I.

It seems reasonable to assume that these effects were caused by some difference between Surveyor I and III missions. In both cases, the mirror was open, and thus exposed to the ambient environment during cislunar flight and touchdown. Exhaust gases from midcourse guidance and main retro maneuvers are not a likely source of contaminant, since the conditions there seem to have been the same as in the case of Surveyor I. The principal difference between the two missions occurred during the landing maneuver, when the bipropellant vernier engines (using nitrogen tetroxide and hydrazine derivative as fuel) continued to fire after landing and throughout the time of the first two contacts of the vehicle with the lunar surface. The relatively sharp boundary of the degraded region on the mirror does not seem consistent with deposition of effluent from the vernier engines. The most likely cause of degradation, therefore, seems to be fine particulate material from the lunar surface sprayed up by the vernier engines. Particles dislodged from the surface by the vernier blast could either pit the surface of the mirror or adhere to the surface if they were small enough. The most exposed portion of the mirror was, in fact, the upper half during touchdown; the glare pattern shown in Fig. VIII-4 is entirely consistent with such an orientation of the mirror.

It is possible to estimate the fraction of the surface of the mirror that must be covered with small particles in order to produce the observed degradation. Under the assumption that the particles on the surface of the mirror have the same albedo as the particles on the lunar surface, preliminary estimates suggest that more than 30% of the surface of the upper half of the mirror is covered with small particles. More detailed studies of the photometric properties of the diffused light and the amount of obscuration when the mirror was in the shade are required before more detailed conclusions can be drawn. It is significant, however, that if fine particles have adhered to the mirror it is corroborating evidence for the existence of fine particulate material in the upper surface layers of the Moon.

3. Properties of the Lunar Surface Layer

Important new data on the physical and mechanical properties of the surficial layer of the lunar surface were obtained from two different sources. The principal

source of new information was the soil mechanics surface sampler experiment described in Section V of this report. Valuable information was also obtained as a result of the unprogrammed multiple landing sequence.

Despite the moderate cohesion exhibited by the material of the lunar surface to a depth greater than 15 cm, there is no conclusive evidence that the lunar material adhered to the surface sampler. The material that spilled from the surface sampler subsequent to trenching operations may have been "jammed" in the scoop rather than physically adhering to the interior surfaces. Indeed, within the limits of resolution (1 mm) of the television camera system, it appears that the external surface of the sampler remained clean throughout its digging operation. This fact seems at first difficult to reconcile with the adhesion of small particles to the mirror of the television camera. However, it is possible that a layer of fine material such as that believed to exist on the mirror also existed on the surface sampler. It is significant that no clots or clumps of surface material adhered to the external surface of the sampler even though brought into intimate contact during the digging operation. The absence of adhesion forces was also displayed by the failure of the darker, fine-grained lunar surface material to adhere to the small white-colored rock excavated by the surface sampler [Fig. VIII-5(a)].

An additional observation of potential significance, in spite of the limited area observed and photographed, is the apparent absence of a raisin-bread texture in the fine particulate material, which was exposed by the soil sampler as it first penetrated into the surface. The resultant smooth-textured surface [Fig. VIII-5(b)] gives no evidence for inclusions of rocks or hard grains large enough to be resolved by the television system.

As described previously, the final landing of the spacecraft was preceded by two other touchdowns (Landing Events 1 and 2), which preceded the final landing by about 36 and 12 sec, respectively. The imprints of landing pads belonging to Landing Event 2 have been identified in the pictures.

In addition to providing information on the particle size of the material comprising the lunar surface layer, as discussed in Section V, the footpad imprints provide further information on the photometric properties of the lunar surface. The bright conical rim seen under some lighting conditions on the imprint of footpad 3 demonstrates that the photometric properties of the disturbed surface material differ from those of the undisturbed surface. Photographs of the imprint formed by footpad 2 for Days 110, 111, 112, and 116 (Fig. VIII-6) show the variation of imprint

brightness relative to the background of the undisturbed surface over a large range of solar phase angles. Photometric measurements are not yet available, and photographic records for Days 113, 114, and 115 were not obtained due to operational limitations of the spacecraft. However, examination of the pictures in Fig. VIII-6 gives a strong impression that the surface became markedly brighter as the solar phase angle approached the angle near that for specular reflection, and thereafter the brightness decreased after passing through the zero phase angle. A change in the photometric properties of the imprint area suggests that an important change has occurred in the state of the material. The usual photometric law for the Moon has been attributed to intricate surface structure which casts many shadows. This intricate structure has to be at the millimeter, or smaller, scale. The destruction of the usual photometric properties of the Moon makes it clear that the complex open structure has been crushed and the particles packed more densely. The range of scales between the resolvable millimeter and the wavelength of light (0.5 micron), therefore, has to have contained the intricate shadow-casting structure on the lunar surface. In practice, this cannot be accomplished with particles much larger than the order of 10 microns.

4. General Morphology of the Landing Site

Although landing pad imprints and soil sampler experiments suggest that the lunar surface layer is composed of very fine particulate material, an inspection of the entire 200-m-diameter (660 ft-diameter) crater bowl shows the presence of many scattered "rocks". Despite the fact that Surveyor III landed in a crater, the general appearance of the surrounding terrain in the vicinity of the spacecraft is not unlike that revealed by the Surveyor I pictures. The general area for both landing sites was selected for the apparent smoothness and suitability as a landing site for Apollo. Judging from the similarity of the appearance of the mare surfaces in Lunar Orbiter photographs, it now appears that most of the upper layers of the mare surfaces of the Moon have the general character noted at the Surveyor I and III sites.

The area surrounding the spacecraft is shown in Figs. VIII-1, VIII-7, and VIII-8. In Fig. VIII-1, the Lunar Orbiter high-resolution frame is displayed at "normal" gain; that is, a nominal amplifier gain setting was used to convert the magnetic tape record to film. In contrast, Fig. VIII-7 shows the same scene at low gain to show detail in the shadows and high gain to show detail in the highlighted areas.

Figure VIII-8 is a mosaic of the region to the north of the spacecraft and illustrates the general types of rocky debris observable inside the crater. Small craters, as well as a scattering of rock fragments not obviously associated with them, may also be seen in this figure. The slopes and rims of these small craters suggest that they were formed in essentially homogeneous material presumably similar in nature to that disturbed by the soil sampler and the footpads of the spacecraft. Crater B of intermediate size (diameter: 5 m; depth: 1 to 1.5 m) appears also to have been formed in the fine-grained surface material. Two craters 16 m north-northeast of crater B (craters C in Figs. VIII-1 and VIII-8), each 2 m (6 ft) in diameter, have no rocks directly associated with them. Thus, it would appear that the finely particulate surface material extends below the approximately 15 cm (5 in.) excavated by the soil sampling experiment to a depth of as much as 1.5 m (5 ft). Below this depth, it would seem the consistency of the lunar material changes to one not unlike terrestrial rock that fractures into angular pieces. This result is essentially the same as that observed at the Surveyor I landing site.

A crater 12 to 13 m (40 to 43 ft) in diameter (marked A in Fig. VIII-1) may be seen 80 m (250 ft) due north of the spacecraft. This crater is surrounded by angular rocks, the largest of which are visible at the scale of the Lunar Orbiter photographs. Surveyor images of examples of these rocks are reproduced in greater detail in Figs. VIII-9 and VIII-10. Figure VIII-9 is a mosaic of three adjacent frames showing crater A and surrounding area. This small crater is approximately 2 to 2.5 m deep, based on estimates from the Lunar Orbiter photograph. The blocky rocks on its rim are, by their distribution, clearly ejecta from the crater.

Surveyor pictures show that positions of rocks on the lunar surface vary from lying almost completely on the surface to being almost completely buried. These rocks appear to belong to at least three classes:

(1) Sharp, jointed, or fractured or angular blocks found principally north of the spacecraft in the sector containing crater A. These are distinguished from class 2 objects by the presence of sharp corners and distinctly planar faces. Their association with, and origin from, crater A is unmistakable, although the more widely strewn fragments found in the area to the west of the crater may come from another source. Many of the smaller fragments found in this north quadrant are unmistakably sharp-edged and belong to this population of rocks. The small fragments are typically tabular with irregular outlines and

lie flat on the surface, although the few exceptions are spectacular [a sharp, tabular stone at least half buried, protruding upward, Fig. VIII-10(d)]. Among the larger blocks, several appear to be partially buried in this position. Where visible, the walls and rim of crater A are composed almost entirely of large angular blocks in a random jumble.

(2) Large, subrounded to subangular blocks resting on the surface or partially buried only [Fig. VIII-11(a)]. Despite the lack of clean fractures and sharp corners, many of these rocks appear to be internally heterogeneous as evidenced by albedo contrasts, parallel layering indicated by the projection of more or less resistant edges of layers [Fig. VIII-11(b)], and poorly developed joints, many of which are parallel to the layers [Fig. VIII-10(d)]. The larger (non-vesicular) rock in Surveyor I is, perhaps, a member of this class. Other rocks such as the one illustrated in Fig. VIII-11(a) show evidence of pitting or vesiculation, also similar to an object observed in Surveyor I pictures.

(3) Low, rounded rocks appearing to be partially to almost totally buried. Many have a blanket of apparently very fine material built along the uphill side [Fig. VIII-10(c)]. These rocks have a rough, mottled texture not unlike that of the lunar surface material and give the distinct impression of being the eroded remnants of blocks (say, population 1 and 2) partially mottled with fine particulate material from the lunar surface.

Type (2) blocks seem to make up nearly all those visible in the survey, but are a minority in the area to the north near crater A, since they are outnumbered there by the type (1) sharp blocks. Type (2) rocks may be rather uniformly distributed over the surface on all quadrants, while the type (1) rocks show association with crater A and a concentration toward it. The more widely strewn material may have another local source. There is a lack of this angular blanket to the northeast and east of the spacecraft; it apparently terminates toward the north at 10 to 15 m (30 to 50 ft) from the spacecraft, since the near surveys show only dark lunar material.

5. Evidence for Material Transport

The fine-grained material of the lunar surface shows a remarkable tendency to develop and maintain a smooth surface. In the case of Surveyor I, the mean surface was essentially horizontal; for Surveyor III, the mean surface level is inclined at an angle of approximately 14 to 15°. Most rocks seen in Surveyor I and III pictures appear to be partly submerged with the contact line between the rock and the lunar surface, nearly in the same plane as the lunar surface. Thus, if trenches or craters were made by the rocks as they fell into their observed positions, subsequent processes must have been at work to fill in and smooth over such scars. On the other hand, these processes have not piled up the material in the vicinity of the rock so as to produce a raised line of contact. There is at most a small fillet, centimeters high, that smooths the transition from the general surface to the rock face. The transportation mechanism of the material must be one that works toward smooth deposition. This transportation mechanism must, however, be as effective on a sloping surface as on a level surface.

Camera azimuths looking north-northeast and south-southwest from Surveyor III view the wall of the crater across the downhill slope. Thus, rocks viewed in these two directions permit one to examine and compare the uphill and downhill ends of the rocks (Fig. VIII-10). There is a definite indication of the downhill movement of material comprising the fine material of the lunar surface layer. A fillet of material encompasses the base of most rocks at the contact line with the fine-grained surface material; this fillet tends to be higher on the uphill end than on the downhill end. On some large rocks a well-developed fillet is observed that laps several centimeters up onto the uphill face of the rock. This enhanced fillet can be explained, regardless of the mechanism which sets the particles in motion, only as the accumulation of fragments arrested in place during downhill motion.

6. Lunar Dielectric Constant

The dielectric constant of the lunar surface materials derived from terrestrial observations, k_{obs}, lies in the range 1.8 to 2.8 (Ref. VIII-1). This figure refers to the bulk dielectric constant, including the effects of porosity. To obtain the dielectric constant, k, of the individual grains, use may be made of the formulas of Twersky (Ref. VIII-1), Betner (Ref. VIII-2), and Odelevskii and Levin (Ref. VIII-2).

To give an idea of the relative values these formulas provide we find, for $k_{obs} = 2.4$ and porosity of 0.5, the following: Twersky, k = 5.8; Betner, k = 4.7; and Odelevskii and Levin, k = 4.4.

Twersky's formula is stated to apply to granular material in which the grains are well separated; that of Betner to granular material; that of Odelevskii and Levin applies to vesicular material. Data presented in Ref. VIII-1 support the formula of Odelevskii and Levin. Data presented by Krotikov (Ref. VIII-2) support an interpolation formula between the Betner formula and that of Odelevskii and Levin. The Betner formula was adopted for this paper; it appears to give conservative values (i.e., high values) of the grain dielectric constant.

The formula of Betner is:

$$\frac{k_{obs} - 1}{3k_{obs}} = \frac{k - 1}{k + 2k_{obs}} (1 - \eta)$$

where η is the porosity, i.e., the ratio of intergranular void space to total volume. The formula is presented graphically in Fig. VIII-12.

The data presented in Ref. VIII-3 was used to check Fig. VIII-12; the only points falling on this plot, and corresponding to known values of the solid dielectric constant are:

(1) Sand, true dielectric constant of solid material probably 4.2 (handbook value for crystalline quartz) rather than 3.8 as quoted in Ref. VIII-3; the latter value is for fused silica.

k_{obs}	η	k of grains, (Fig. VIII-12)
2.92	0.343	4.5
2.68	0..400	4.5
2.36	0.503	4.5
2.19	0.560	4.5
1.94	0.645	5.2
1.90	0.637	4.8

(2) Plate glass, true dielectric constant of solid material 7.3.

k_{obs}	η	k of grains, (Fig. VIII-12)
3.01	0.559	8.4
2.27	0.680	8.2
1.96	0.739	8.1

It appears that Fig. VIII-12 is conservative.

The minimum value of the dielectric constant for plausible lunar materials in the solid form is that for clear silica glass, namely 3.8 (Chemical Rubber Handbook, 44th edition, p. 2626).

At this writing, data on the porosity are not available from Surveyor III measurements of the lunar soil. It is possible to sketch the lines of constant bulk density on Fig. VIII-12, using the porosities shown and the accepted values of the bulk densities of the rocks. These values are indicated by dashed lines. When reliable values of the porosity and/or density become available, it may be possible to draw some conclusions about the nature of the lunar surface. It must be kept in mind, however, that the grains themselves may be vesicular; in this case they may appear to be more acid than they are. This is more important for basalts than for chondritic materials; to this date, no cases of vesicular chondritic material have been pointed out.

7. Concluding Remarks

Surveyor III results at this preliminary evaluation of data give valuable information about the relation between the surface skin of under-dense material responsible for the photometric properties and the deeper layers of material whose properties resemble those of ordinary terrestrial soils. In addition, they provide new insight into the relation between the general lunar surface as seen by Surveyor I and the interior of a large subdued crater. The new results have also contributed to our understanding of the mechanism of downhill transport. Many critical questions cannot, however, be answered until final reduction of experimental data.

REFERENCES

VIII-1. Radar Studies of the Moon, Quarterly Report, Lincoln Laboratories, Lexington, Mass.

VIII-2. Krotikov, V. L., "Some Electrical Properties of Earth Rocks and Their Comparison With Those of the Lunar Surface Layer," Proceedings of the High Scientific Institute, Radiophysics Series 5, pp. 1057-1061, 1962.

VIII-3. Fensler, W. E., Knott, E. F., Olte, A., and Siegel, K. M., "The Electromagnetic Parameters of Selected Terrestrial and Extra-terrestrial Rocks and Glasses," from The Moon, pp. 545-565, ed. by Z. Kopal and Z. K. Mikhailov, Academic Press, New York, 1962.

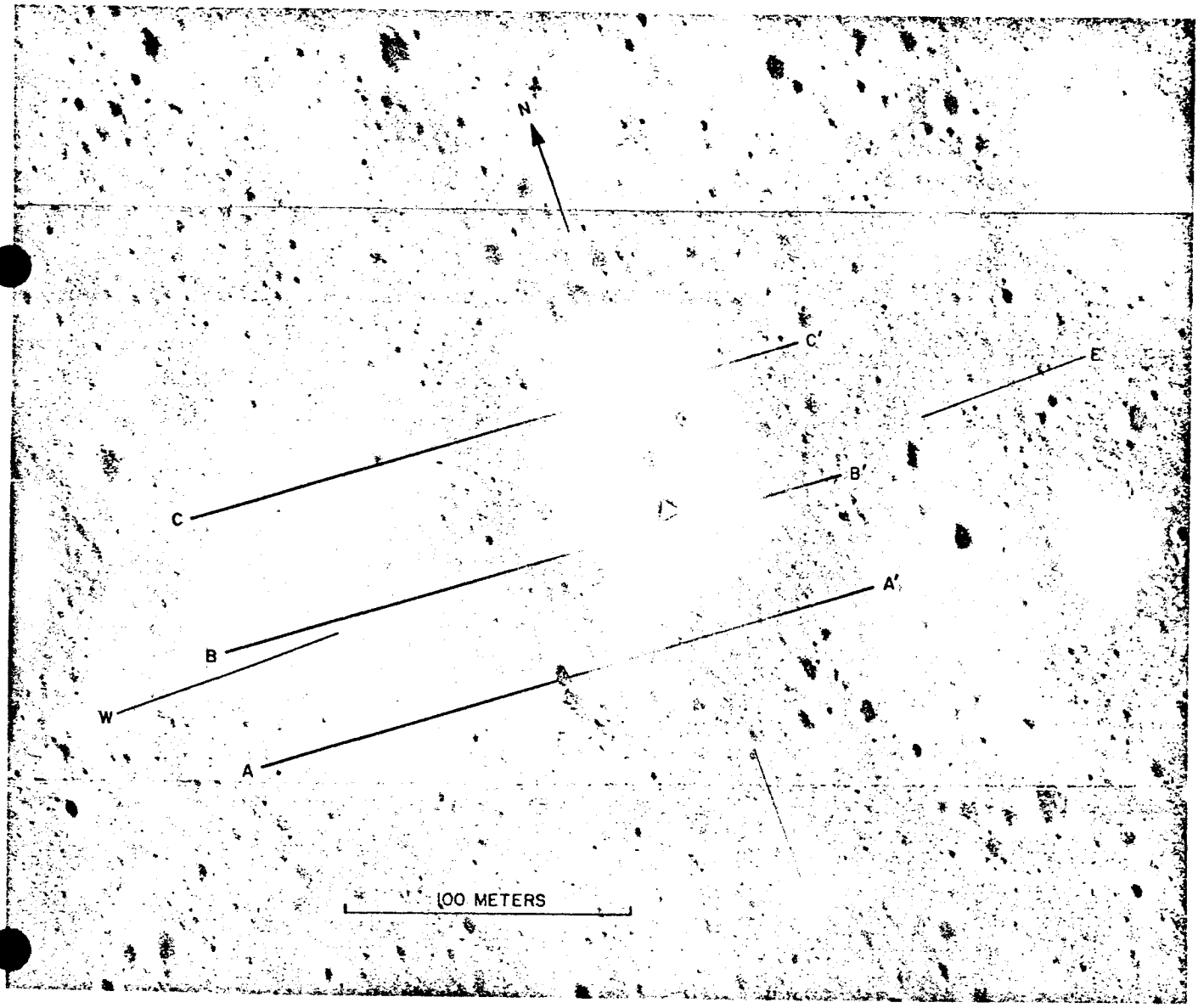

Fig. VIII-1. Portion of Lunar Orbiter III, P9, frame H154, showing the crater in which Surveyor III landed. The approximate position of the spacecraft is indicated by the triangular spot, and features mentioned in the text are identified with letters and numbers. The lines AA', BB', and CC' define the traces for the photometric determinations used to estimate crater profiles shown in Fig. VIII-2.

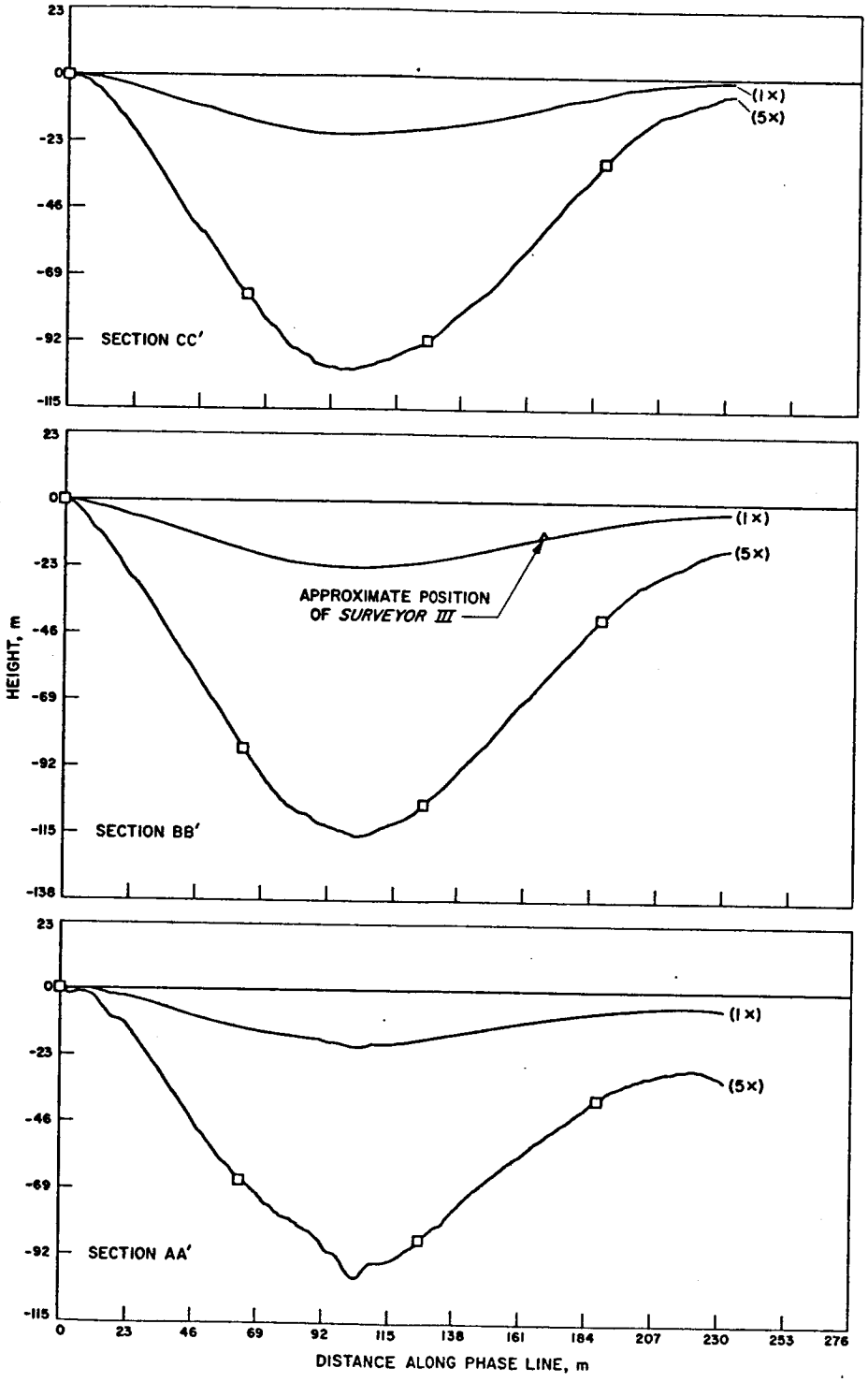

Fig. VIII-2. Topographic profiles of Surveyor III crater drawn by photometric methods from Lunar Orbiter III, P9, frame H154 (profiles obtained by G. R. Taylor and J. J. Lambiotte, NASA, Langley Research Center).

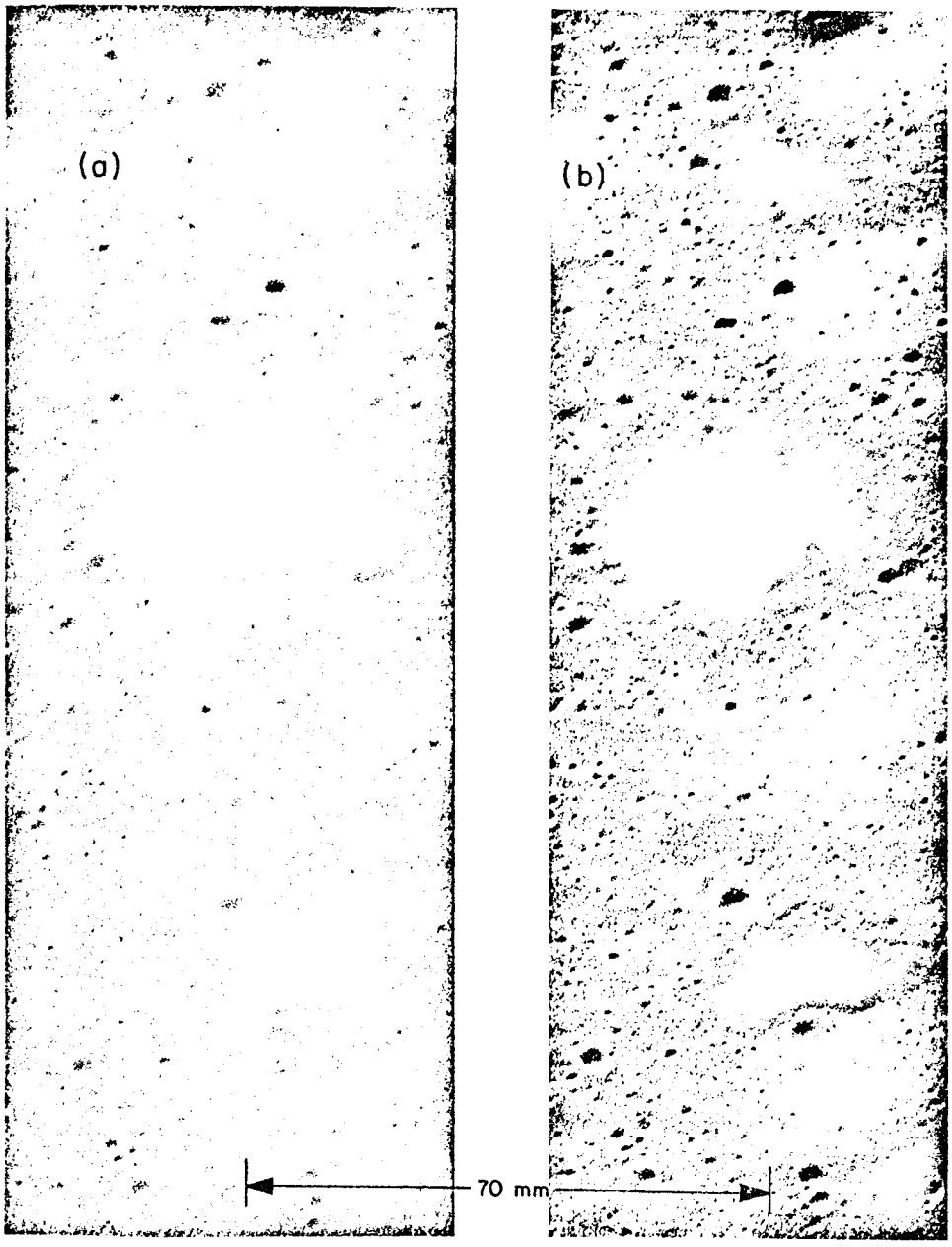

Fig. VIII-3. Stereoscopic pair of Lunar Orbiter III photographs of the crater in which Surveyor III landed: (a) site 9A, frame H137, rectified by R. A. Altenhofer, USGS; (b) site 9C, frame H154.

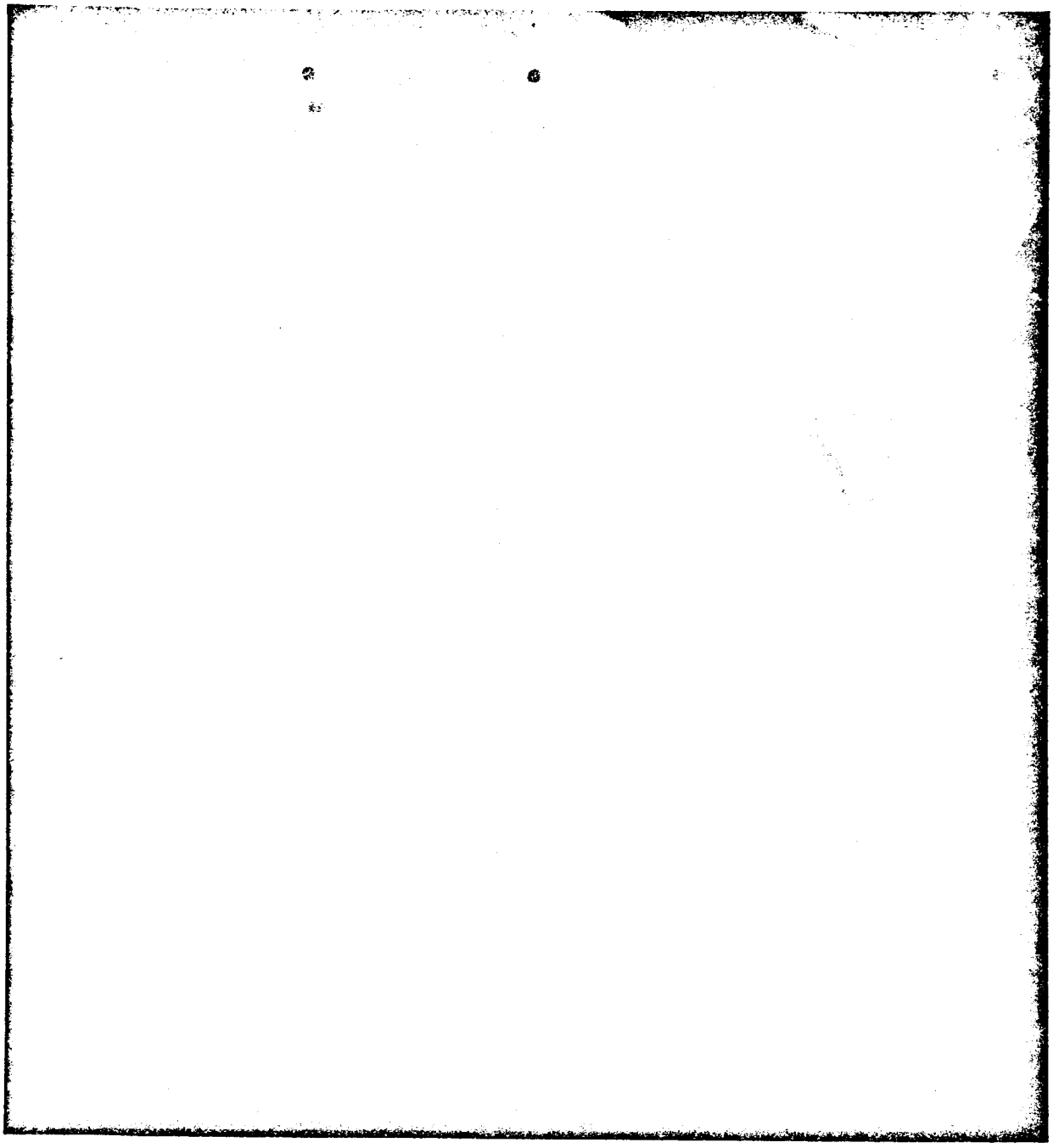

Fig. VIII-4. Time exposure of Earth. The broad diffuse band of light extending from the lower right to the upper left is attributed to scattered light from fine particles adhering to the surface of the mirror (Day 120, 10:47:02 GMT).

Fig. VIII-5(a). View of the small rock-like object that was excavated from the lunar surface during the course of the surface sampler experiment (Day 120, 16:54:48 GMT).

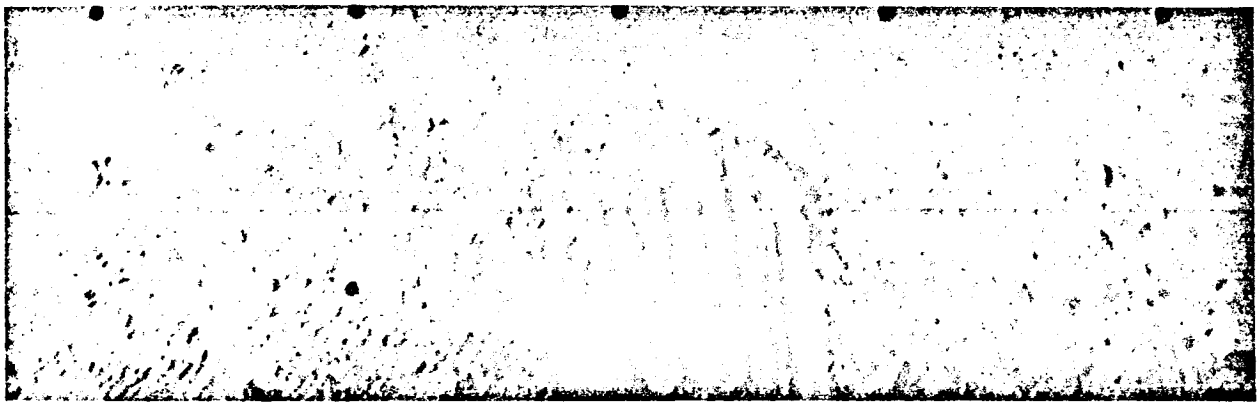

Fig. VIII-5(b). Smooth surface that resulted from an initial penetration of the surface sampler scoop into the lunar surface (Day 120, 14:28:03 GMT).

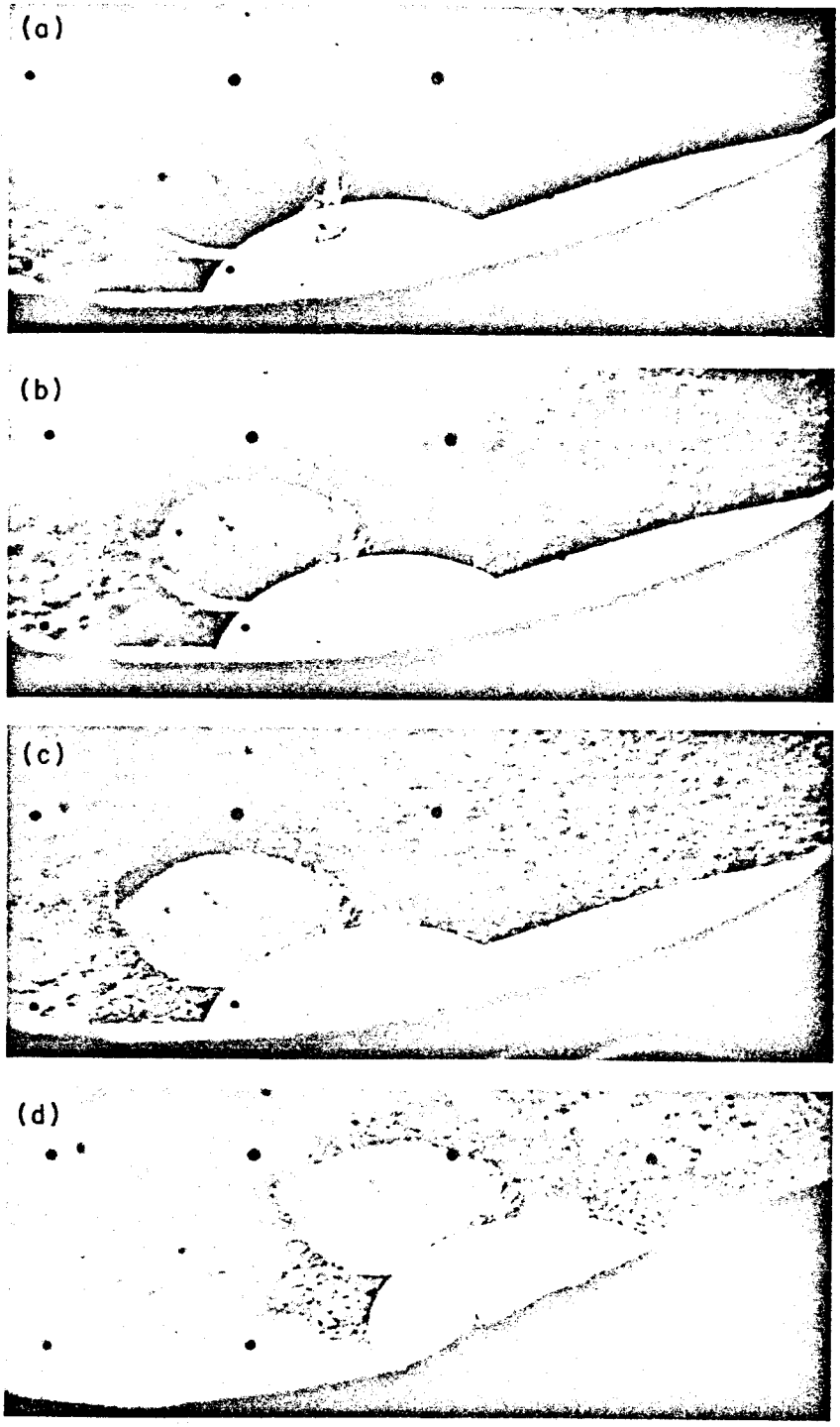

Fig. VIII-6. Photographs of the imprint formed by footpad 2:
(a) Day 110, 09:05:17 GMT; phase angle approximately 134°;
(b) Day 111, 02:39:32 GMT; phase angle approximately 126°;
(c) Day 112, 00:49:30 GMT; phase angle approximately 114°;
(d) Day 116, 05:54:53 GMT; phase angle approximately 66°.

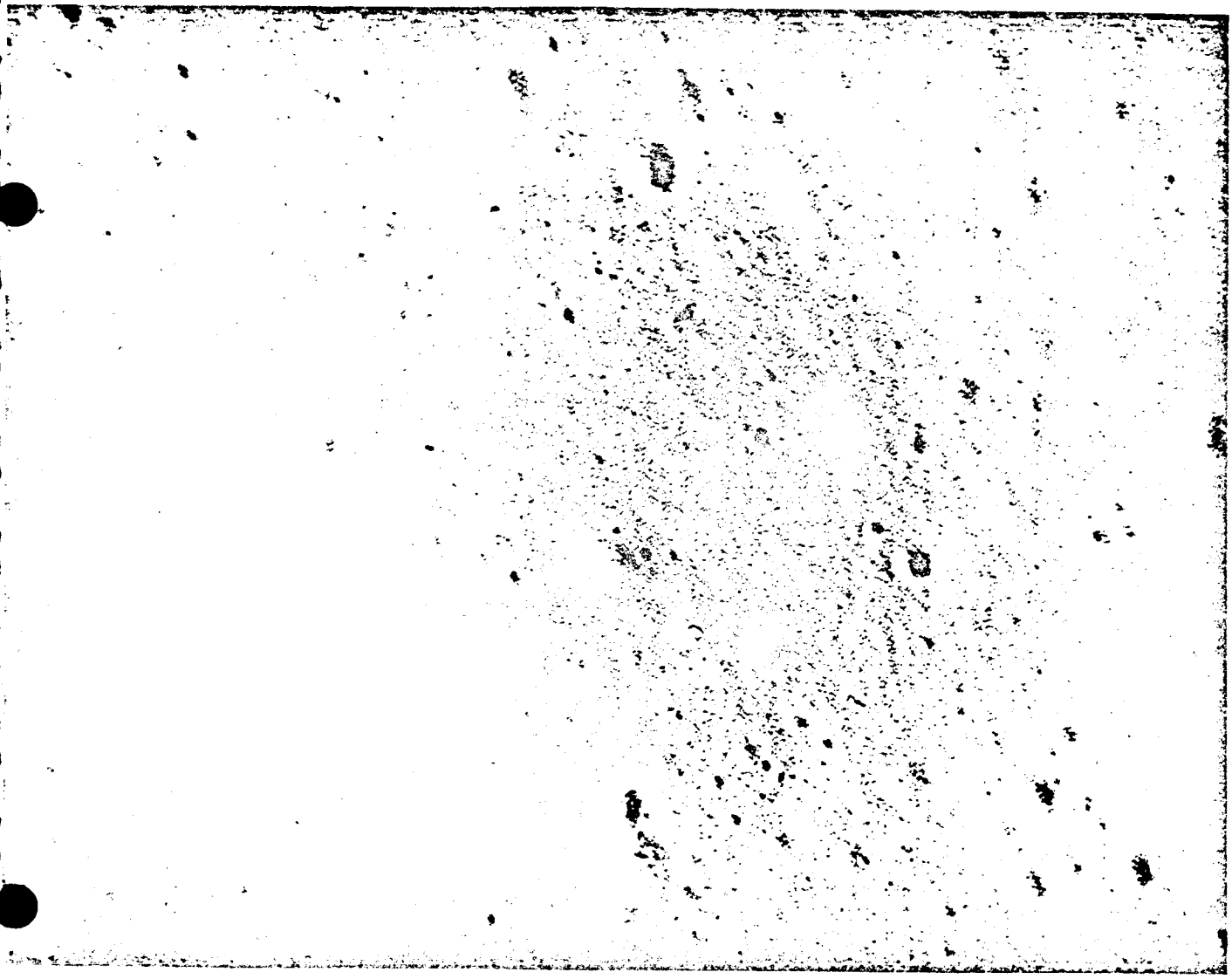

Fig. VIII-7(a). Portion of photograph from Lunar Orbiter III (site 9C, frame H154, framelet 27). In contrast to Fig. VIII-1, a low amplifier gain setting was employed to convert the magnetic tape record to film (photograph courtesy of I. G. Recant, NASA, Langley Research Center).

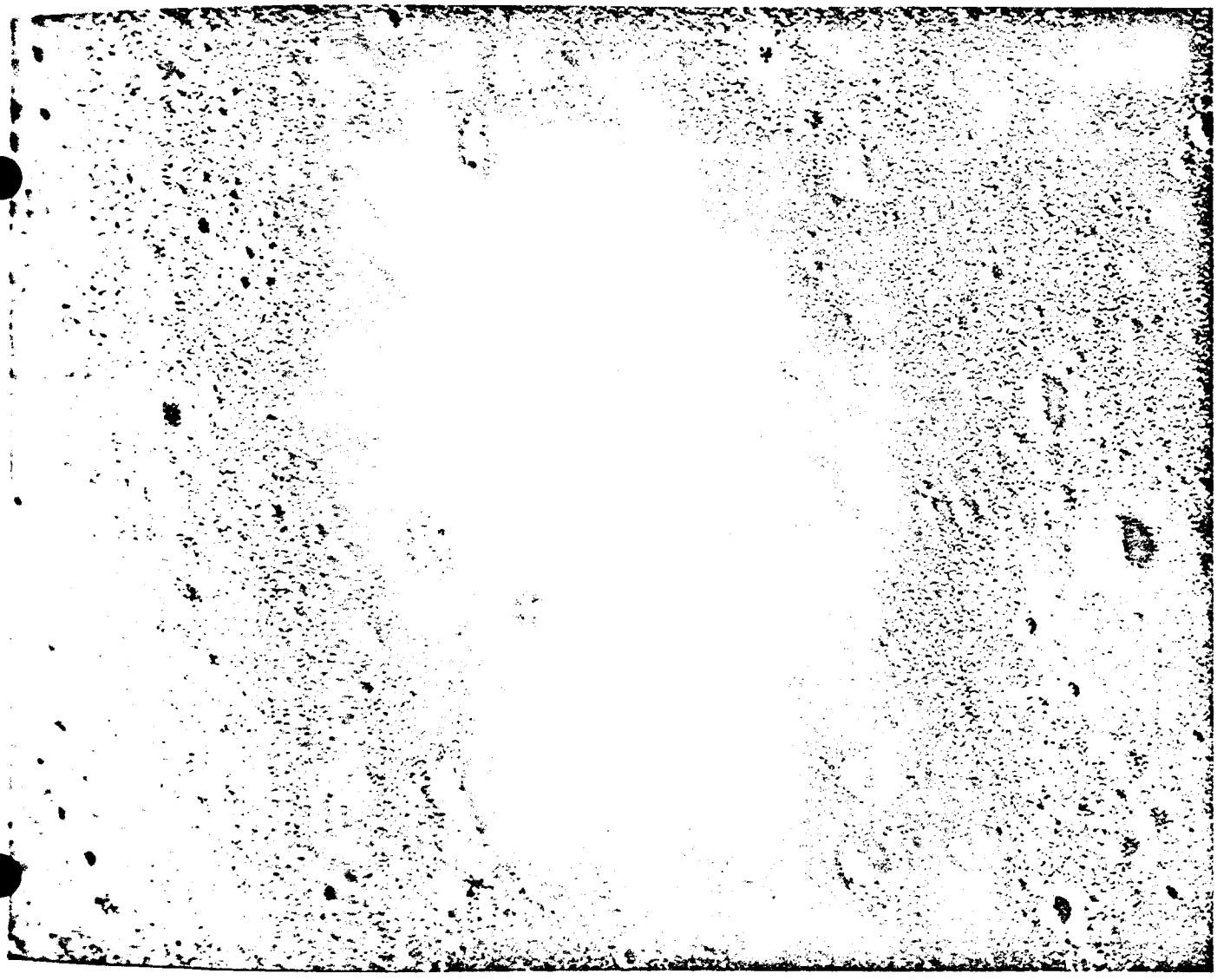

Fig. VIII-7(b). Portion of photograph from Lunar Orbiter III (site 9C, frame H154, framelet 27). In contrast to Fig. VIII-1, a high amplifier gain setting was employed to convert the magnetic tape record to film (photograph courtesy of I. G. Recant, NASA, Langley Research Center).

Fig. VIII-8. Mosaic of the crater wall to the north of the spacecraft (Catalog No. 90SI, Day 120, 14:38:57 to 15:07:45 GMT).

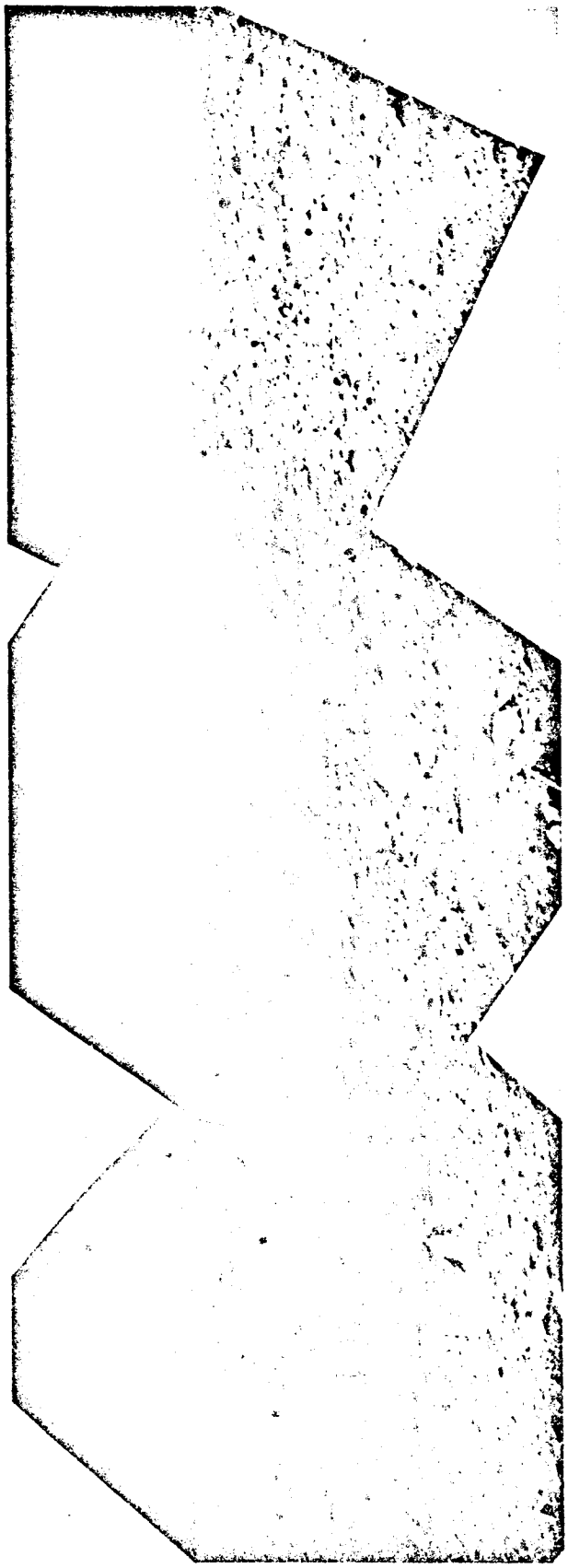

Fig. VIII-9. Mosaic of three narrow-angle frames, showing details of Crater A and surrounding area (Day 120: left to right, 14:47:09, 14:45:05, and 14:41:04 GMT).

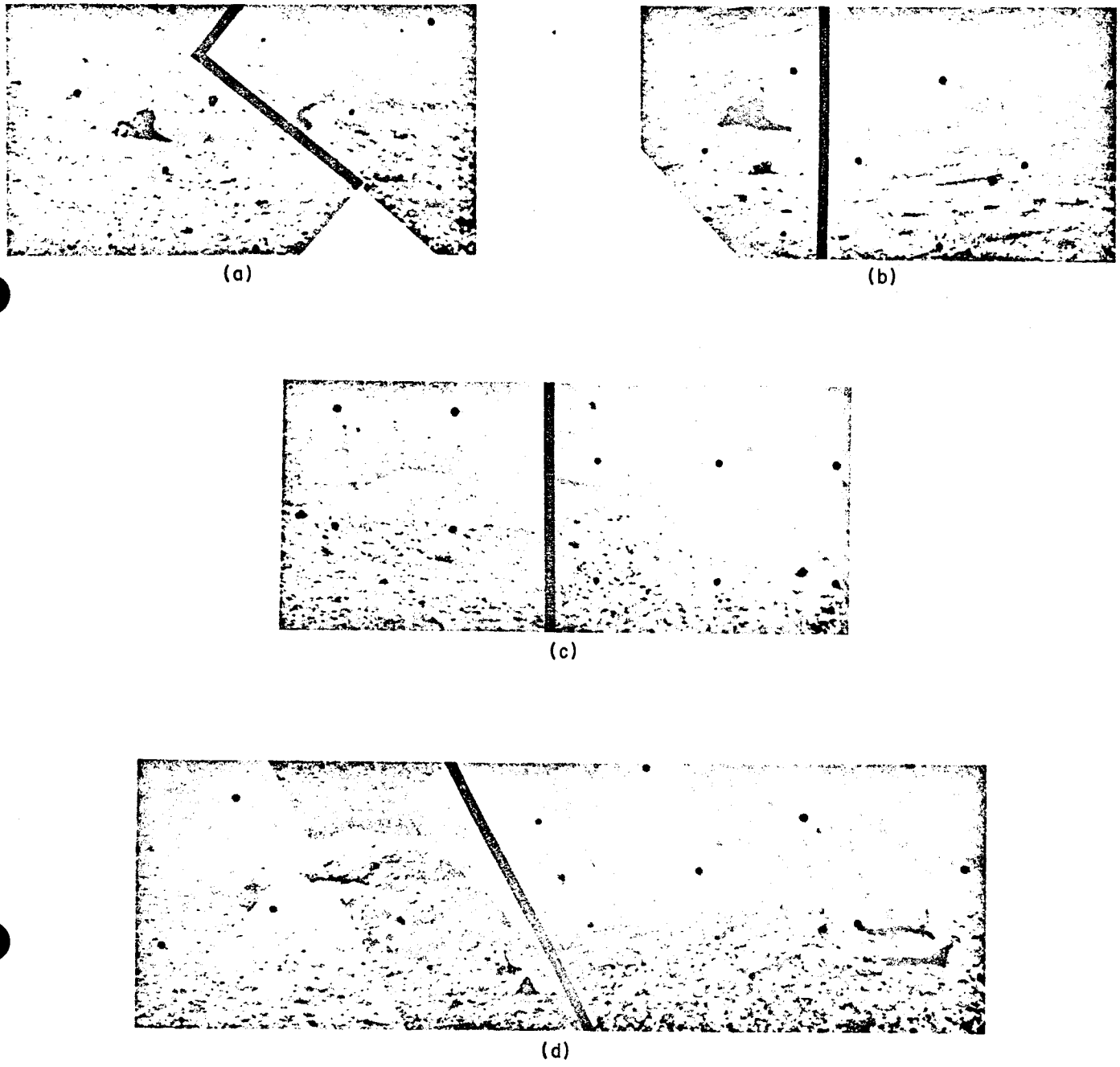

Fig. VIII-10. Selected rocks on wall of crater with lunar afternoon and early morning illumination (left and right views, respectively). Note absence of a fillet or accumulation of material on downhill (left) side of objects: (a) Day 120, 14:41:09 GMT; Day 111, 05:59:07 GMT; (b) Day 120, 14:47:03 GMT; Day 111, 05:59:25 GMT; (c) Day 120, 15:00:51 GMT; Day 111 05:15:03 GMT; (d) Day 120, 14:54:23 and 14:52:22 GMT; Day 111 05:14:55 GMT.

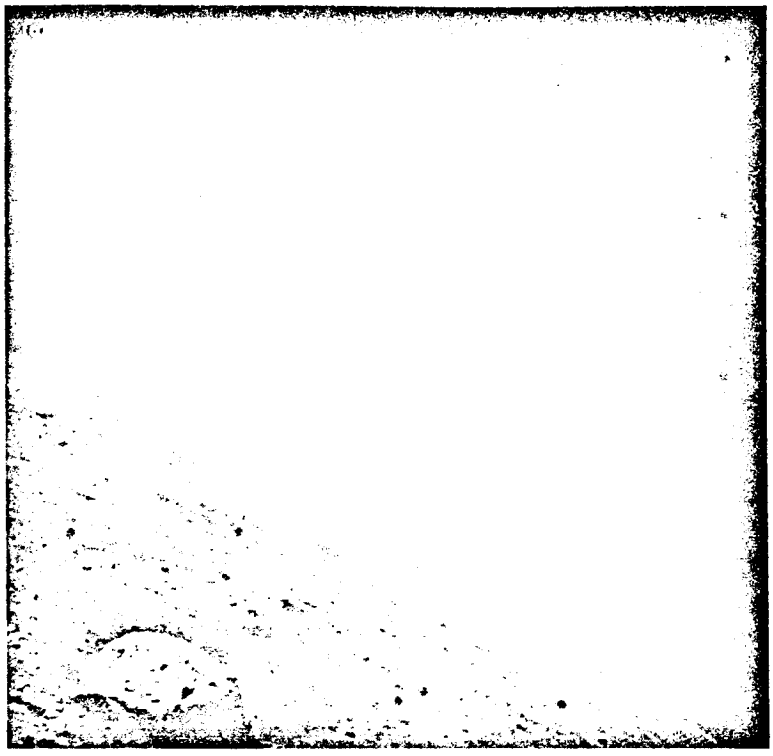

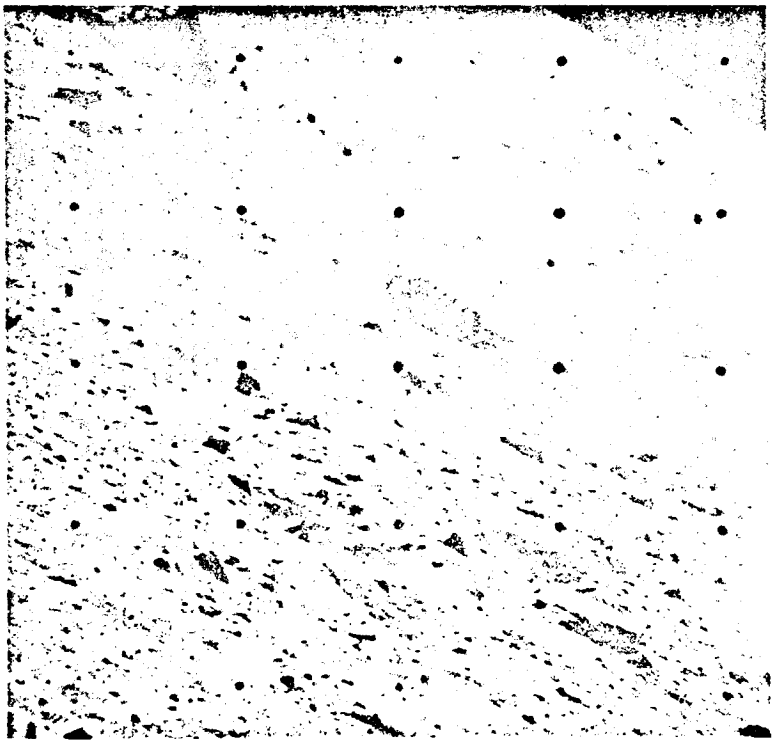

Fig. VIII-11. Details of (a) Rock 1 (Day 120, 15:07:16 GMT), and (b) Rock 2 (Day 120, 14:52:35 GMT).

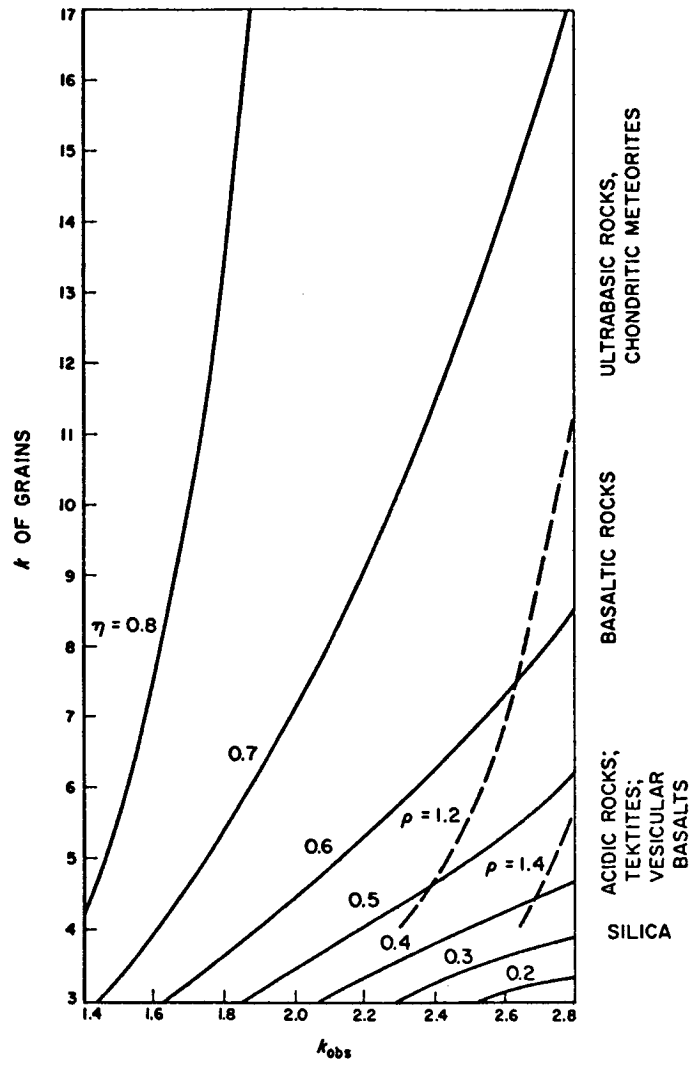

Fig. VIII-12. Relation between the bulk dielectric constant, k_{obs}, and the dielectric constant of the grains, k, according to the Betner formula. η is the porosity, ρ is the density.

JPL Project Document 125

ON-LAB DISTRIBUTION LIST

Surveyor Project Distribution List 120, A's and E's only, and the following additional personnel:

Adams, B.
Allen, D.
Alper, M.
Alper, W. E.
Anderson, A. T.
Anderson, T.
Arcand, A.
Baker, G.
Barath, F. T.
Bartz, D.
Bayley, W. H.
Berdahl, C. M.
Bilbo, T. S.
Billingsley, F.
Bode, C.
Brandt, R.
Bratenahl, A.
Brereton, R. G.
Bristow, F.
Brown, W. E., Jr.
Burcham, D. P.
Burlarge, J.
Calkins, J. E.
Cannon, M.
Carpenter, R. L.
Casani, J.
Cole, C. W.
Colella, F. J.
Collier, W. A.
Communtzis, M.
Conel, J. E.
Cutting, E.
Despain, L. G.
Dipprey, D.
Dobies, E.
Douglas, D.
Dunk, A. C.
Eckman, P. K.
Estabrook, F. B.
Fawcett, W. G.
Felberg, F.
Filice, A.
Ford, H.
Foster, C. F.
Frederickson, C. D.
Fujikawa, C. D.
Gates, C. R.
Gerpheide, J. H.
Giffin, C. E.
Gin, W.
Goddard, F. E.
Goforth, L.
Goldfine, M. T.
Goldsmith, C.
Goldsmith, P.
Goldstein, R.
Goranson, G.
Grotch, S.
Gunn, J.
Haddock, G.
Hamilton, T.
Harami, S.
Haurlan, P. N.
Heacock, R.
Henry, M.
Hobby, G. L.
Holdridge, M.
Hotz, G. M.
Howard, W. R.
Huber, B.
Irving, A.
James, J. N.
Johnson, E.
Jones, D. E.
Kaplan, L. D.
Kautz, G.
Kindt, G. H.
Kistler, A. L.
Kohlhase, C. E.
Koukol, J. F.
Ladner, G.
Lairmore, G. E.
Landel, R.
La Porte, D. D.
Larkin, W. E.
Lawrence, H. R.
Levoe, G. E.
Linnes, K. W.
Loomis, A.
Lucas, J. W.
Luedecke, A. R.
Mack, L. M.
Mackin, R. J.
Margetts, D. R.
McDonald, W. S.
McFee, R. H.
Meghreblian, R. V.
Merrick, W. D.
Metzger, A.
Morris, B. T.
Morris, R. V.
Nash, D. B.
Nathan, R.
Neiswanger, G.
Neugebauer, M. M.
Newburn, R. L.
Norris, D. D.
Norton, R.
Parker, T. H.
Parks, R.
Paulson, J. J.
Peer, W.
Peterson, G.
Pickering, W. H.
Plescia, A.
Port, D.
Pounder, E.
Putnam, R.
Raggio, C. W.
Rechtin, E.
Roberson, F. I.
Robillard, G.
Rose, R. F.
Rosenberg, H.
Rygh, P. H.
Schneider, W. J.
Schneiderman, D.
Schurmeier, H. M.
Scull, J. R.
Sheldon, E. L.
Shipley, W.
Sirri, N.
Slaughter, D. W.
Sloan, R. K.
Small, J. G.
Smith, E. J.
Smith, G. M.
Smith, K.

ON-LAB DISTRIBUTION LIST (Cont'd)

Soffen, G. A.
Sparks, D.
Spencer, D. F.
Spencer, R.
Stallkamp, J. A.
Starks, L.
Stevens, R.
Stewart, H. J.
Stuart, J. L.
Sturm, A. G.
Sweetnam, G. E.
Thatcher, J. W.
Theis, T.
Trostle, H. G.
Vango, S. P.
van der Wyk, E.
Vescelus, G.
Victor, W. K.
Williams, N.
Wilson, J. N.
Wyckoff, R. C.

OFF-LAB DISTRIBUTION LIST

G. Abell	UCLA
A. Adel	Arizona State College
I. Adler	Goddard Space Flight Center
W. M. Alexander	Temple University
R. C. Allenby	NASA
L. H. Aller	UCLA
C. O. Alley	University of Maryland
D. Alter	Berkeley, California
E. Anders	University of Chicago
D. Anderson	Cold Region Engineering Labs
J. Arnold	Scripps Institute of Oceanography
J. Ashbrook	Massachusetts
H. W. Babcock	Mt. Wilson and Palomar Universities
R. B. Baldwin	Grand Rapids, Michigan
J. Balsley	Wesleyan University
A. R. Barringer	Barringer Research, Ltd.
W. R. Beardsley	Allegheny Observatory
J. G. Beckersley	Cambridge, Massachusetts
M. G. Bekker	GM Defense Research Laboratories
P. R. Bell	Oak Ridge National Laboratory
H. S. Bennett	University of Chicago
H. E. Benson	Manned Spacecraft Center
R. Benzwi	General Dynamics/Convair
L. V. Berkner	Southwest Center for Advanced Studies
N. Bhandari	University of California at San Diego
R. Bideaux	Harvard University
K. Biemann	Massachusetts Institute of Technology
J. L. Bohn	Temple University
M. L. Bottino	Old Dominion College
C. Bowen	Woods Hole Oceanographic Institution
I. S. Bowen	Mt. Palomar Observatory
J. Bronowski	Salk Institute for Biological Studies

OFF-LAB DISTRIBUTION LIST (Cont'd)

G. Brooks	Langley Research Center
D. Brouwer	Yale University Observatory
A. Brown	University of Pennsylvania
H. Brown	CIT
M. Calvin	University of California at Berkeley
A. G. W. Cameron	Institute for Space Studies
E. N. Cameron	University of Wisconsin
W. S. Cameron	Goddard Space Flight Center
J. T. Campbell	Goddard Space Flight Center
W. D. Cannell	Lowell Observatory
R. R. Carder	Air Force Aeronautical Chart and Information Center
W. A. Cassidy	Lamont Geological Observatory
L. D. Carlson	University of California, Davis
E. Chao	USGS
D. Chapman	Ames Research Center
S. P. Clark	Yale University
F. H. Clauser	University of California, Santa Cruz
J. D. Cloud	Hughes Aircraft Company
A. Code	University of Wisconsin
P. Coleman	University of California at Los Angeles
R. J. Collins	University of Minnesota
J. Copeland	University of South Alabama
N. Crabhill	Langley Research Center
C. L. Critchfield	Los Alamos, Scientific Laboratory
H. D. Culver	TRW Systems
D. Currie	Northeastern University at Boston
G. D. Derbyshire	National Academy of Sciences
W. C. De Marcus	University of Kentucky
G. D. Vaucouleurs	University of Texas
R. A. Dibos	Hughes Aircraft Company
R. H. Dicke	Princeton University
J. Dietrich	Manned Spacecraft Center
M. Di Mercurio	Hughes Aircraft Company
G. Z. Dimitroff	Dartmouth College, New Hampshire
F. Drake	Cornell University
J. L. Dragg	Manned Spacecraft Center
L. DuBridge	CIT
S. E. Dwornik	NASA
F. Dyson	Princeton University
W. J. Eckert	Watson Scientific Computing Bureau
F. K. Edmonsen	University of Indiana
R. E. Eggleton	USGS
E. Elston	University of New Mexico
R. B. Erb	Manned Spacecraft Center
J. W. Evans	MIT
M. Ewing	Columbia University, New York
J. Faller	Wesleyan University, Conn.
E. O. Felkel	Hughes Aircraft Company
G. B. Field	University of California at Berkeley

OFF-LAB DISTRIBUTION LIST (Cont'd)

J. W. Findlay	Arecibo Iononspheric Observatory, Puerto Rico
W. Fisher	USGS
W. Fitch	University of Arizona
S. Flateau	Hughes Aircraft Company
W. Fowler	CIT
S. Fox	University of Miami, Florida
L. W. Frederick	University of Virginia
J. Freeman	Rice University, Texas
J. French	UCLA
H. Friedman	U. S. Naval Research Laboratory
C. Frondel	Harvard University
R. R. Garipay	Hughes Aircraft Company
P. W. Gast	St. Paul, Minn.
D. E. Gault	Ames Research Center
T. Gehrels	University of Arizona
M. Gellman	CIT
G. B. Gibson	Manned Spacecraft Center
H. L. Giclas	Lowell Observatory
J. Gillis	Mapping and Intelligence Agency
J. J. Gilvarry	Ames Research Center
P. Glaser	Arthur D. Little Company
W. R. Gockel	Hughes Aircraft Company
E. N. Goddard	University of Michigan, Ann Arbor
T. Gold	Cornell University
L. Goldberg	Harvard College Observatory
J. S. Goldstein	Brandeis University, Mass.
C. D. Goodman	University of Houston
T. G. Goodman	Loras College, Iowa
R. H. Gray	Unmanned Launch Operations, Kennedy Space Center
J. Green	Douglas Aircraft
J. L. Greenstein	Mt. Wilson and Palomar Observatories
R. R. Gunter	Hughes Aircraft Company
W. H. Haas	Lunar and Planetary Observatory, New Mexico
R. T. Hackman	USGS
T. Hagfors	Lincoln Laboratory, MIT
J. D. Halajian	Grumman Aircraft Engineering Company
B. Hall	Department of the Army, Washington, D. C.
J. S. Hall	Lowell Observatory, Arizona
R. G. Hall	U. S. Naval Observatory, Washington D. C.
B. Hapke	Cornell University
R. Hardie	Dyer Observatory
J. C. Harrison	University of Colorado, Boulder
H. K. Hartline	Rockefeller University, New York
W. K. Hartmann	University of Arizona
G. S. Hawkins	Boston University Observatory
L. J. Haworth	National Science Foundation, Washington, D. C.
E. I. Hawthorne	Hughes Aircraft Company
R. M. Haythornthwaite	University of Michigan
H. D. Hedberg	Princeton University

OFF-LAB DISTRIBUTION LIST (Cont'd)

R. T. Hedden	ACIC
D. S. Heeschen	National Radio Observatory
P. Hergret	University of Cincinnati
K. Herring	University of Arizona
O. N. Hertzmann	Hughes Aircraft Company
H. H. Hess	Princeton University
W. N. Hess	Goddard Space Flight Center
F. J. Heyden	Georgetown College Observatory, Washington, D. C.
R. Hide	MIT
J. E. Hill	Rand Corporation
W. A. Hiltner	Yerkes Observatory
R. Hofstadter	Stanford University
D. F. Hornig	Office of Science and Technology, Washington, D.C.
M. Hunt	Air Force Cambridge Research Labs
J. A. Hynek	Northwestern University
H. C. Ingrao	Harvard University
D. James	Bellcomm, Inc.
J. Jamieson	University of Chicago
R. Jastrow	Goddard Institute for Space Studies
A. H. Jay	CIT
F. S. Johnson	Southwest Center for Advanced Studies
E. R. Jonash	NASA Lewis Research Center
W. Jones	Marshall Space Flight Center
R. Jones	Hughes Aircraft Company
J. Kaplan	University of California, Los Angeles
S. Katzoff	Langley Research Center
W. M. Kaula	University of California, Los Angeles
W. W. Kellogg	National Center for Atmospheric Research
C. Kenknight	Litton Industries
Z. Kopal	Boeing Research Laboratories
R. Kovach	Stanford University
W. R. Krafft	Hughes Aircraft Company
G. P. Kuiper	University of Arizona
A. Lachenbruch	USGS
W. Lamb	Yale University
T. W. Lambe	MIT
C. J. Lambertsen	University of Pennsylvania
M. C. Langseth	Columbia University
G. Latham	Columbia University
J. H. Lawrence	University of California, Berkeley
J. Lederberg	Stanford University
R. Leighton	CIT
W. Libby	University of California, Los Angeles
S. Lipsky	Yale University
W. C. Livingstone	Kitt Peak National Observatory
H. C. Lord	University of California, San Diego
P. Lowman	Goddard Space Flight Center
R. P. Lyon	Stanford Research Institute
G. J. F. MacDonald	University of California, Los Angeles

OFF-LAB DISTRIBUTION LIST (Cont'd)

J. H. Mackin	University of Texas, Austin
W. Manning	Patrick Air Force Base
W. Markowitz	Marquette University, Wisconsin
F. Marmo	Geophysics Corporation of America
C. H. Marshall	USGS
H. Masursky	USGS
N. U. Mayall	Kitt Peak National Observatory, Arizona
C. H. Mayer	U. S. Naval Research Laboratory
J. McCauley	USGS
S. W. McCuskey	Warner and Swazey Observatories, Ohio
D. N. Menzel	Harvard College Observatory
M. Meridith	Hughes Aircraft Company
F. Curtis Michel	Manned Spacecraft Center, Texas
F. G. Miller	Hughes Aircraft Company
B. Milwitzky	NASA
O. C. Mohler	University of Michigan
G. A. Moore	National Bureau of Standards
R. K. Moore	University of Kansas
W. W. Morgan	Yerkes Observatory
E. Morris	USGS
D. O. Muhleman	Cornell University
B. Murray	CIT
C. Murtaugh	Bendix Corporation, Michigan
C. H. Nelson	Langley Research Center
G. A. Newkirk	High Altitude Observatory
H. H. Nininger	Sedona's Meteorite Museum
B. O'Brien	Rice University, Texas
H. Odishaw	National Academy of Sciences
J. J. O'Donnell	Hughes Aircraft Company
E. Opik	University of Maryland
J. Oro	University of Houston
E. Parker	University of Chicago
J. Patterson	Argonne Natural Laboratory
R. C. Peavey	Southwest Center for Advanced Studies
V. J. Peohls	Ryan Aeronautical Company
Perkins Observatory Library, Ohio	
C. D. Perkins	Princeton University
G. K. Pettengill	MIT
R. A. Phinney	Princeton University
F. H. Pickering	Army Map Service
C. S. Pittendrigh	Princeton University
M. A. Pomerantz	Franklin Institute, Penn.
R. W. Porter	General Electric Company
C. A. Privette	Ames Research Center
W. A. Quaide	Ames Research Center
N. F. Ramsey	Harvard University
D. Rea	University of California, Berkeley
I. Recant	Langley Research Center
J. Reynolds	University of California, Berkeley

OFF-LAB DISTRIBUTION LIST (Cont'd)

P. C. Ricks	Hughes Aircraft Company
F. E. Roach	Department of Commerce
W. O. Roberts	National Center for Atmospheric Research
R. L. Roderick	Hughes Aircraft Company
B. B. Rossi	MIT
J. A. Ryan	Douglas Aircraft Company
J. M. Saari	Boeing Scientific Research Labs
C. Sagan	Harvard College Observatory
J. W. Salisbury	AF Cambridge Research Laboratory
L. I. Schiff	Stanford University
H. H. Schmitt	Manned Spacecraft Center
M. Schwarzchild	Princeton University Observatory
R. L. Sears	Hughes Aircraft Company
F. Seitz	National Academy of Sciences
T. B. Senior	University of Michigan
S. Shallon	Hughes Aircraft Company
A. H. Shapley	Institute for Telecommunication Sciences and Aeronomy
H. Shapley	Cambridge, Massachusetts
W. G. Shepherd	University of Minnesota
W. Shockley	Stanford University
E. M. Shoemaker	USGS
R. Shorthill	Seattle, Washington
R. Q. Shotts	University of Alabama
E. N. Shipley	Bellcomm, Inc.
K. M. Suegekm	University of Michigan
M. G. Simmons	Southern Methodist University, Texas
J. A. Simpson	University of Chicago
A. G. Smith	University of Florida
E. Smith	University of Maryland
H. J. Smith	McDonald Observatory
H. T. U. Smith	University of Massachusetts
R. Smoluchowski	Princeton University
S. P. Sonett	Ames Research Center
D. C. Spencer	Stanford University
L. Spitzer	Princeton University Observatory
L. H. Spradley	ACIC
E. Steinghoff	Holloman Air Force Base
J. Strand	U. S. Naval Observatory
A. Strickler	Beckman Instruments, Inc.
J. D. Strong	Johns Hopkins University, Md.
E. Stuhlinger	Marshall Space Flight Center
G. Sutton	University of Hawaii
G. Thompson	Stanford University
C. W. Tombaugh	New Mexico State University
C. Townes	MIT
K. Turekian	Yale University
A. Turkevich	University of Chicago
H. C. Urey	University of California, San Diego
J. A. Van Allen	University of Iowa

OFF-LAB DISTRIBUTION LIST (Cont'd)

P. Van de Kamp	Swarthmore College, Pa.
J. Van Lopik	Texas Instruments, Inc.
O. H. Vaughn	Marshall Space Flight Center
E. Vey	IIT Research Institute
O. G. Villare, Jr.	Stanford University
J. Waak	U. S. Naval Research Laboratory
F. A. Wade	Texas Tech.
L. B. Walter	Goddard Space Flight Center
C. R. Warren	USGS
G. J. Wasserberg	CIT
A. C. Waters	University of California, Santa Barbara
C. B. Watts	U. S. Naval Observatory
G. K. Wehner	General Mills, Inc.
G. Westerhout	University of Maryland
J. R. Whinnery	University of California, Berkeley
F. L. Whipple	Smithsonian Institution
E. A. Whitaker	University of Chicago
A. E. Whitford	Lick Observatory
R. L. Wildey	CIT
R. Wildt	Yale University Observatory
A. G. Wilson	Topanga, California
J. T. Wilson	University of Michigan
D. U. Wise	Franklin and Marshall College, Pa.
F. C. Wolf	Hughes Aircraft Company
F. Wood	University of Pennsylvania
G. P. Woollard	University of Hawaii
H. Zirin	Mt. Wilson and Palomar Observatories
G. Zuidema	Johns Hopkins Hospital, Md.